MULTIMODE INTERFERENCE DEVICES AND INTEGRATION WITH ELECTROABSORPTION MODULATORS FOR PHOTONIC INTEGRATED CIRCUITS

LEE SHUH YING

School of Electrical and Electronic Engineering
Nanyang Technological University
Singapore

A thesis submitted to the Nanyang Technological University
in fulfillment of the requirements for the degree of
Doctor of Philosophy

2009

Statement of Originality

I declare that this thesis entitled "*Multimode Interference Devices and Integration with Electroabsorption Modulators for Photonic Integrated Circuits*" is the result of my own original research except as cited in the references. The thesis has not been accepted for a higher degree to any other University or Institution.

Signature : .....

Name : LEE SHUH YING

Date : 15 OCTOBER 2010

Acknowledgements

This thesis would not have been realized without the assistance of many parties. I would like to thank my first advisor, the late Prof. Chin Mee Koy for making everything possible in the first place by accepting me as his student. Throughout my first five years, under his kind tutelage and advice, the project had taken form and blossomed to what it is today. I am also very grateful to Dr. Mei Ting for taking me under his wings for the remainder of my PhD and under his guidance, this dissertation is finally completed. I am also eternally grateful for the great team of researchers I have been working with, namely, Lee Chee Wei, my 'senior' by half a year, whose patience and calm outlook has a force of its own to temper down my often more rash and impulsive actions; Stevanus Darmawan, whose inquisitive nature had influenced me greatly to be more adventurous in my research. His attention to details and perseverance in investigating his projects has taught me to take pride in fine-tuning things, be it in research or in perfecting a figure. Landobasa Y.M.A.T., an enigma when it comes to his high grasp of all things mathematical and theoretical, has also greatly motivated me to overcome my fears of equations. His infinite streams of ideas are often the tide that has saved me, be it in getting unstuck from a dead end or infusing new angle of approach and research.

Research fellows Dr. Xu Chendong and Dr.Yang Hua are the lifelines that I have often cling to in matters regarding fabrication. Their vast amount of practical experience has also helped reveal to me the solutions to many a problem.

Although my years in NTU had been peppered with ephemeral acquaintances, the short time with them had also been wonderful, our brief conversations and co-operations often stirring the calm waters and bringing in a breath of fresh air at 'old' things. These wonderful people are Mohd. Hanif Ibrahim of USM (Malaysia), Dr Zhang Xiao of SimTech and Li Yicen and Zhao Qiu Ji of NTU, among many others. Thank you.

Table of Contents

7. Conclusions and Recommendations

Author's Publications

Journals/Letters:

1. **S. Y. Lee**, S. Darmawan, C. W. Lee, M. K. Chin, "Transformation between directional couplers and multi-mode interferometers based on ridge waveguides," *Optics Express*, 12 (14): JULY 12, 2004,ref. 3079
2. S. Darmawan, **S. Y. Lee**, C. W. Lee, M. K. Chin, "A rigorous comparative analysis of directional couplers and multimode interferometers based on ridge waveguides" *IEEE J. Selected Topics In Quantum Electronics (JSTQE)*, 11 (2): 466-475 MAR-APR 2005
3. S. Darmawan, **S. Y. Lee**, C. W. Lee, M. K. Chin, "Transformation of Directional Couplers to Multi-Mode Interferometers Based On Ridge Waveguides and Its Applications," *J. Non-linear Optics and Material (JNOPM)* 14 (2): 221-235 JUN 2005
4. M. K. Chin, C. W. Lee, **S. Y. Lee**, S. Darmawan, "High Index Contrast Waveguides and Devices," *Applied Optics*, 44 (15): 3077-3086 MAY 20 2005
5. X. Zhang, M. Qian, **S. Y. Lee**, M. K. Chin, X. Zeng, D. K. Y. Low, A. C. W. , P. Plante, "Planar waveguide devices based on sol-gel-derived photopatternable hybrid material**,"** *J. Of Crystal Growth*, 288 (1): 176-179 FEB 2 2006
6. M. H. Ibrahim, **S. Y. Lee**, M. K. Chin, N. M. Kassim, A. B. Mohammad, "Multimode interference optical splitter based on photodefinable benzocyclobutene, (BCB 4024-40) polymer," *Optical Engineering*, 46 (1): Art. No. 013401 JAN 2007
7. Y. Hua, M. K. Chin, J. Zhou, **S. Y. Lee**, W. Chen, and H. Zhu, "A traveling-wave electroabsorption modulator with a large optical cavity and intrastep quantum wells," *Semiconductor Science and Technology*, vol. 23, pp. 105011, 2008.
8. Thomas Y. L Ang, S. T. Lim, **S. Y. Lee**, C. E. Png and M. K. Chin, "How small can a micro-ring resonator be and yet be polarization-independent?" *Applied Optics,* **48**(15): p. 2821-2835 MAY 20 2009
9. **S.Y. Lee**, H. Yang, Y.C. Li, C.W. Lee, T. Mei *Senior Member,* "Integrated twin modulator switches through MMI splitting and electroabsorption modulation," *Semiconductor Science and Technology,* vol 24, pp 125004 (5pp), 2009.

Conference Proceedings:

1. S. Darmawan, **S. Y. Lee**, C. W. Lee, M. K. Chin, "Transformation between directional couplers and multi-mode interferometers based on ridge waveguides," *4th International Symposium on Modern Optics and its Applications (ISMOA)*, 2004, Bandung, Indonesia.
2. S. Darmawan, **S. Y. Lee**, C. W. Lee, M. K. Chin, "Transition and comparison between directional couplers and multimode interference couplers based on ridge waveguides," *4th Photonics Asia (SPIE) Conference*, 2004, Beijing, China.
3. S. Darmawan, Y. M. Landobasa, C. W. Lee, **S. Y. Lee**, and M. K. Chin**,** "Scattering Matrix Analysis for Cascaded Ring Enhanced Mach-Zehnder Interferometers," *IPRA, OSA Topical Meeting,* 2005, San Diego, US.
4. Chee Wei, Lee, Stevanus Darmawan, **Shuh Ying, Lee**, and Mee Koy, Chin "Design of Polarization-Independent Wavelength Splitter Based on Single Directional Coupler," *IPRA, OSA Topical Meeting,* 2005, San Diego, US.
5. Hua Yang, Mee Koy Chin, Desmond C.S. Lim, Jingtao Zhou, **Shuhying Lee**, Yuanbing Cheng, HongLiang Zhu, Weixi Chen, "Design and fabrication of high-performance InGaAsP/InP electroabsorption modulator," *Proceedings of SPIE*, 6782(67820U): 2007.
6. **S.Y. Lee**, Y. M. Landobasa, S. Darmawan, Y.C. Li, T. Mei "Ultra compact SOI Tapered MMI," *ICMAT, 2009.*

Summary

Photonic integration is a critical emerging trend in the development of photonic devices. Its significance parallels that of the microelectronic integrated circuits (IC) albeit it has developed slower due to its diversity and often contrasting requirements. Photonic integrated circuits (PIC) is basically made up of small but important building blocks combined to realize even more complex circuits so that it may perform wider range of functionalities on optical signals used in various applications, such as optical communication, instrumentation, sensing, and signal processing.

Integration reduces the number of parts and hence the level of packaging and assembly required. It also results in parts with smaller footprints. Integrated components tend to be more reliable and power efficient and hence cut down operating cost. Because of these advantages, photonic integration is considered a key to opening the floodgate of low-cost optical subsystems that will make long-term sustainable investment in optical networks possible.

One of the fundamental issues of PIC is the interconnection from one active device to another. This is generally done using waveguides. Waveguides are also used to split or combine light. With the introduction of multimode interference (MMI) couplers, the splitting and coupling of light in integrated optics has become much more compact. The MMI device also has the advantage of being robust and polarization insensitive therefore making it one of the most elegant and versatile passive devices in photonic circuits.

In this thesis, we introduce and develop many functional circuits based on MMI couplers. Although the MMI device can be integrated with many other devices which are either passive or active, the MMI device on its own is also a versatile building block that can perform many functions, such as switching, multiplexing, and polarization splitting. I have studied the fundamentals of MMI and linked its modal properties to those of directional couplers, and established the transformation relationship between them.

Traditionally, 1:N MMI splitters have been accomplished with rib-waveguides. Our approach of using highly guiding ridge waveguides however, helps constrain the size and subsequently, the loss of our 1:N devices. We have demonstrated 1:N splitters for N up to 8 and achieved a 1:2 MMI splitter with ±5% uniformity for up to 35nm wavelength bandwidth based on the InP platform.

We then diversified our research scope to encompass other possible integration platform and successfully demonstrated coarse wavelength splitting of 1310nm and 1550nm wavelength bands on a polymer benzocyclobutene (BCB) platform. We realized too, the importance of silicon-on-insulator (SOI) as an alternative platform due to its vast similarity in fabrication technology (complementary metal–oxide–semiconductor (CMOS) based deep UV lithography) to the microelectronic counterpart. Therefore, in collaboration with Dr. Pieter Dumon and Prof. Roel Baets from University of Ghent, IMEC of Belgium, and with assistance from Dr. Jean-Marc Fedeli of CEA LETI (France), we have also produced prototype MMIs which is as small as 8.8μm for light splitting. In the case of these much smaller devices, the design of MMI shape, width and length becomes more critical to how efficiently the light can be coupled and switched. Even slight modifications in gaps and length can spell the difference between an appreciable 3dB splitting and excessive loss.

The X device that this thesis focuses on integrating with the MMI is the electroabsorption modulators (EAM). Although the vast amount of electroabsorption modulators around these days makes it hard to appreciate the lumped element EAM which is simpler in design and fabrication, our introduction of InGaAlAs/InGaAlAs MQW double depletion region (DDR) combined with large optical cavity (LOC) have helped lower the driving voltage to about 1V for a standalone EAM device.

However, since the EAM is an active device, integration of MMI to the EAM would need quantum well intermixing (QWI), a technique which, although is comparatively simpler than other integration alternatives, still needs meticulous study on its effects on different material structures. By retaining an area of active material isolated with a shallow trench, we were able to modulate two beams of light which have been separated by a 1:2 MMI. These individual arms have been able to exhibit 10dB extinction ratio modulation with a driving voltage of 4V.

List of Figures

List of Tables

List of Acronyms

Acronym	Full-text	Page first appear
AW	access waveguide	9
AWG	Arrayed waveguide gratings	11
BCB	bisbenzocyclobutene	13
BPM	Beam Propagation Method	18
BRAQWET	Blockaded reservoir and quantum-well electron transfer structure	7
DC	direct current	106
DC	directional coupler	3
DDR	dual depletion region	100
DFB	distributed feedback laser	7
DUT	device under test	82
EAM	electro absorption modulator	7
FD	Finite Difference	18
FIB	focused ion-beam implantation	5
FP	Fabry Perot	31
G-S-G	ground-signal-ground	110
HH	heavy hole	108
ICP	inductively coupled plasma (machine)	5
IFVD	impurity-free vacancy diffusion	5
IID	impurity-induced disordering	5
IMEC	Interuniversity Microelectronics Centre	17
IQW	intrastep quantum wells	99
LH	light hole	108
LOC	large optical cavity	17
MMI	Multimode inteference	3
MMIC	multimode inteference coupler	69
MQW	multiple quantum wells	7
MZI	Mach-Zehnder Interferometer	7
NTU	Nanyang Technological University	37
QW	quantum well	5
QWI	quantum well intermixing	4
RF	radio frequency	94
RIE	reactive ion etching	36
Sample A	InGaAlAs/InGaAlAs MQW DDR LOC EAM	105

Acronym	Full-text	Page first appear
Sample B	InGaAsP/InGaAsP MQW DDR LOC EAM	105
Sample C	InGaAsP/InGaAsP IQW LOC EAM	105
SOA	semiconductor optical amplifier	139
SOI	silicon on insulator	2
TE	transverse electric	17
TM	transverse magnetic	17
WDM	Wavelength Demultiplexer	11

Chapter 1

An Overview of the Thesis: Background, Objectives, and Significant Contributions

This chapter gives an overview of the dissertation, introduces the key concepts, devices, and materials, gives a literature survey of relevant devices, and summarizes the research objectives and contributions.

1.1. Motivation

The first photonic devices (including the laser diode) were large by today's standard. They were discrete devices designed to be joined together either through free space or by using optical fibers. As for electronic devices that had developed earlier, there was a natural trend to make devices smaller and integrate them together as a single integrated circuit (IC). Photonic IC (PIC for short) provides many of the same advantages as electronic IC, including lower cost per device and per functionality, lower operating cost (because of lower power requirement and smaller form factors), lower power loss and higher reliability (because of smaller part counts). The monolithic integration of components also holds the promise of increasing network functionality aside from reducing packaging expenses. Unfortunately, integration also drives down yield due to manufacturing complexity and the compounding of failures across devices. Historically, certain bottlenecks have prevented integrated optics from being more widely adopted but over recent years, these challenges have been rapidly overcome with the assistance of intense research worldwide, technical improvements and crossover technology from the semiconductor industry.

However, with integration comes complexity in design and processing. Although integration gives us better overall products, the process also places more steps in series during fabrication and these extra steps do affect the yield. The complexity of the integration process will affect the incidence of performance and processing failures which translates into higher costs. Hence

we will need to consider devices that do not require complex fabrication and whenever possible, to alter and reduce the process steps.

Another challenge faced is in the active-passive integration, which is the stringing together of active devices (e.g. detectors and lasers) and passive devices (switches, S-bends, couplers), which typically have different material requirements and physical dimensions, on the *same* material platform. The divergent characteristics of the devices impose severe restrictions on the range of material systems that can provide a uniform material platform. Indeed, the best material that allows monolithic integration of both active and passive devices for optical communication wavelength is the Indium Phosphide (InP) based compound semiconductor. Hence, we have focused on devices based on InP. The method of quantum well intermixing for integrating active and passive devices is an essential part of the integration platform, and will be briefly discussed in Chapter 4.

Nonetheless, we could not dismiss the silicon material as a possible PIC platform as well. The unprecedented maturity of silicon materials, processing and device technologies, which stems from international R&D investments that now exceeds $40B annually [1] has offered many opportunities in leveraging photonics applications and markets. Silicon-on-Insulator (SOI) also provides many inherent physical benefits for optics that can be advantageous in ultra-compact, high-performance communications, signal processing and sensor circuits. However, much research regarding active and passive integration and providing on-chip light sources need to be done towards achieving this aim. Among interesting on-going work are the silicon-compatible lasers which include the intrinsic, extrinsic and hybrid materials technologies and the active plasma index mechanisms. Design issues associated with certain passive SOI devices will be discussed in this work.

The interconnections between devices- active and passive- require passive low-loss waveguides. These waveguides also form the basic devices for spatially splitting or combining lightpaths. As we will show, various forms of waveguides can also be designed to perform functions such as wavelength and polarization splitting.

The most common passive waveguide device is probably the multi-mode interference (MMI) coupler, which, in its general form, consists of a multimode (slab) waveguide with M input waveguides and N output waveguides, where light from any of the inputs is coupled to all the outputs, and through multimode interference, results in single or multiple images of the input field mode being reproduced at periodic distances along the multimode waveguide, in a process called *self-imaging* [2]. Thus, the device can be designed for use as 1:N splitter, M:N coupler, spatial switch, or filter, all important devices for processing optical signals.

The simplest MMI device is the 1:2 coupler which can be used to split an optical beam into two waveguides in various ratios much like a directional coupler (denoted as DC, this device consists of two parallel, adjacent waveguides). It has been shown that MMI is more immune to fabrication variations, less sensitive to wavelength variations and more polarization independent than the DC counterpart. Thus, there are many potential advantages in using MMI as a building block for more complicated devices.

1.2. A brief survey of methods for Photonic Integrated Circuits (PIC)

In this thesis, PIC is defined as optical IC that consists predominantly of photonic devices. The integration techniques can be largely divided into two groups: (i) monolithic, and (ii) hybrid.

Monolithic integration refers to the case where all devices are fabricated in the same material substrate yielding a single "chip". The traditional optical IC involves both electronic and optical functions for optical communication applications, known as optoelectronic integrated circuit (OEIC), has developed and matured largely based on the Indium Phosphide (InP) material family. The requisite material's bandgap energy spans across the optical communication wavelengths (1.1-1.6 μm), and is one of the semiconductor materials that have both the required electronic and optical properties as it supports light generation,

amplification, modulation and detection. It enables all the key high-value optoelectronic functions required in an optical transport to be integrated on a simple substrate and maximizes potential cost reduction in optical transport systems. Passive optical functions such as wavelength multiplexing, demultiplexing, variable optical attenuation, switching and dispersion compensation can also be implemented in InP. To integrate both active and passive devices together requires a local tuning of the material bandgap to suit the different requirements for active and passive devices. Quantum well intermixing (QWI) is one of the techniques for doing so and is a relatively simple procedure compared with other methods. A survey of QWI is given in a later section.

An alternative technique for monolithic integration is selective-area-growth (SAG) [3-7] which tunes the bandgap energy by controlling the layer thickness grown (usually by MOCVD) through the width of a dielectric mask deposited on the substrate before growth has also been reported to offer good integration of modulator and laser. The process controls the integration of different layers. Most of the butt-joint regrowth process refers to this method.

Hybrid integration involves different materials which are usually bonded together. It can also involve wire-bonding a chip onto a separate wafer or carrier. One such form of integration which is gaining popularity is the Hybrid Integration of III-V lasers on Si. There are many established methods how this may be done. Although there are attempts in making active silicon materials, the easiest way to realize a Si-PIC presently is by bonding a III-V die to an SOI circuit [8, 9]. The bonding can be accomplished either by die-to-wafer, wafer-to-wafer or heteroepitaxy (III-V to Si/ SiGe material).

Another example of hybid integration involves bonding thin lithium niobate slices onto a bigger substrate using polymer [10]. It makes use of a new cutting technique which is able to produce thin slices of lithium niobate ($LiNbO_3$) which are then bonded onto a bigger substrate for integration purposes.

1.3. Quantum Well Intermixing (QWI)

QWI [3, 11-18] is a technique of integration between active and passive devices which was first proposed by Miller [18] by making use of the metastable nature of the compositional gradient found at heterointerfaces. Unlike other integration method which combines materials of different characteristics, QWI is accomplished by altering certain properties on selected areas of a wafer to render it passive. This means that there are no regrowth or joining of two or more different materials needed. The natural tendency for materials to interdiffuse is the basis of the intermixing process. The intermixing technique which comprises of ion implantation followed by selected rapid-thermal-annealing (RTA) modifies the bandgap energy across the selected areas on a single substrate [19]. Since QWI does not change the average composition but only slightly changes the compositional profile, there is a negligible index discontinuity at the interface between adjacent sections. This eliminates parasitic reflections that can degrade performance.

There are other intermixing techniques which can achieve energy band gap tuning in postgrowth process, such as the impurity-induced disordering (IID) [20], focused ion-beam (FIB) implantation [21] and sputter silica-induced intermixing [3, 22]. Our interest lies only on the plasma-enhanced (PE) QWI [11, 13-15, 23] method and the impurity-free vacancy diffusion (IFVD) [24-26] method. The PE-QWI technique, which uses the inductively coupled plasma (ICP) machine, enables the use of low-ion bombardment energy with high-ion fluxes, which is favorable in generating near surface point defects to promote intermixing in QW samples.

Using the argon (Ar) plasma-enhanced (PE) QWI method, the integration of active devices such as electroabsorption modulators with passive waveguide structures such as MMI devices can be realized. In the following sections, both of these devices are surveyed. Fig.1.1.1 gives a schematic idea of how the PE-QWI process was achieved.

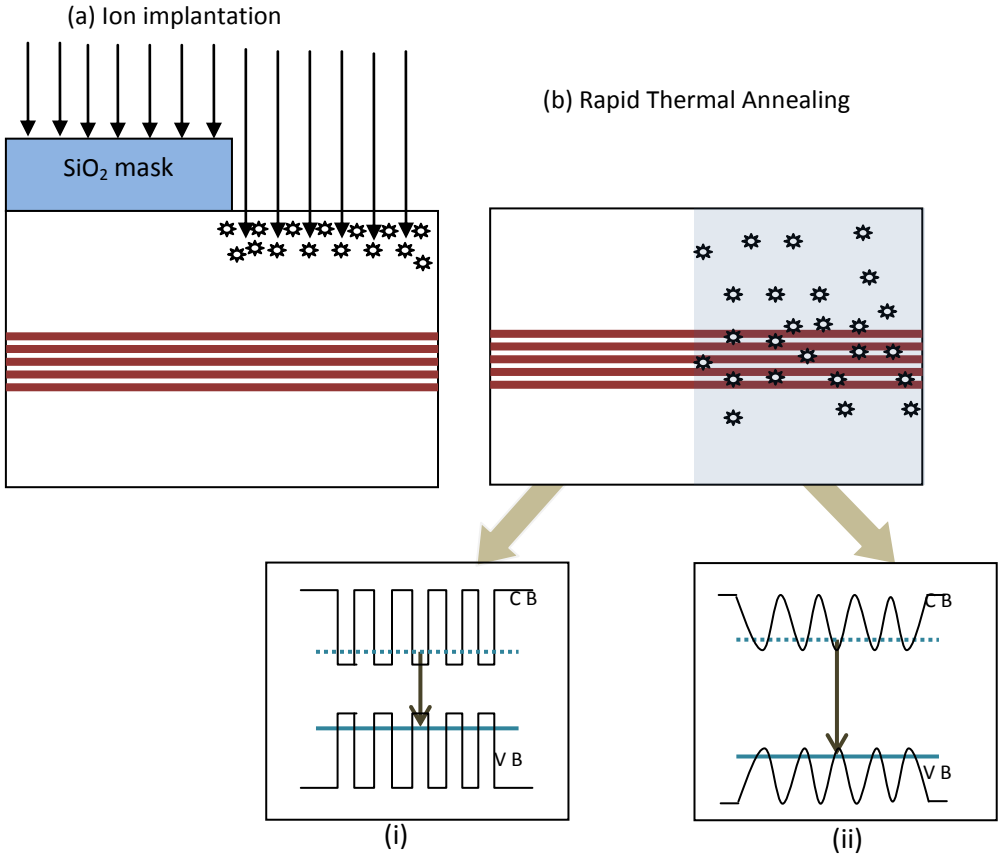

Fig.1.1.1. Schematic diagram of the QWI process which consists of (a) the ion implantation process, where the active area which is NOT intermixed is protected with a SiO_2 mask and (b) the Rapid Thermal Annealing (RTA) process after the SiO_2 mask has been removed. The un-shaded area is the area which is NOT intermixed. (i) The QW "square" shapes does not suffer any modification. The shaded area is the intermixed area. (ii) The bandgap energies are increased due to the change in the QW shape.

IFVD is another promising method. It is simple and it does not induce excessive crystal damage to the material, i.e., less optical loss to the device. IFVD involves the deposition of a dielectric cap layer, such as SiO_2 or Si_3N_4, onto the quantum well structure, followed by RTA which promotes the inter-diffusion between the vacancies and atoms. The type of dielectric material would determine whether it could encourage or inhibit the intermixing. Such difference depends on the thermal expansion coefficients of the dielectric and the top layer of the substrate. For instance, the thermal expansion coefficient, α_{th} of the dielectric SiO_2 is $0.52\times10^{-6}/^{\circ}C$ and a III-V compound semiconductor cap (which is usually p^{+}-InGaAs lattice-matched to InP in our case) is $\sim1.0852\times10^{-6}/^{\circ}C$. If the substrate surface is under compressive stress during annealing, i.e., the thermal expansion coefficient of the dielectric cap is smaller than that of the top layer of the sample, thus, the vacancies will diffuse across

the quantum well region and promote intermixing. If it is under tensile stress, the vacancies will be trapped and hence, the intermixing is limited [27].

1.4. Electroabsorption Modulator (EAM)

There are generally two types of operation mechanism for external modulators: the electro-optic (EO) modulators and the electroabsorption (EA) modulators. EO modulators operate on the basic idea that the material refraction index will change under the influence of an electric field. Materials with higher optical refractive index sensitivity are electro-optic materials such as $LiNbO_3$, KH_2PO_4, GaAs and ZnS semiconductors. When the electric field is modulated, the optical phase or polarization is modulated too, therefore making a phase modulator. When a Mach-Zehnder interferometer (MZI) configuration is used, an intensity modulator is made. The MZI modulator is usually made with travelling-wave electrode structures to achieve high-speed operations.

EA modulators on the other hand, are based on the electroabsorption effect, which is defined as the change of material absorption in the presence of an electric field. This effect is known as the Franz-Keldysh effect in bulk materials and the quantum-confined Stark effect (QCSE) in quantum-well materials. While the Franz-Keldysh effect were mostly observed at low temperature, the QCSE is easily observed even at room temperature due to the enhanced exciton binding energy in a quasi-two-dimensional structure using multiple quantum wells (MQW).

EAM is more attractive because of its compactness, which makes it more suitable for monolithic integration with DFB lasers [6, 28-30]. It also has a reduced chirp, larger extinction ratio and lower driving voltage, which is important in ensuring lesser power consumption and enabling integration. EAMs are typically shorter that 200μm and have driving voltage of lesser than $3V_{pp}$[1]. Their extinction ratios (ERs) are also generally higher than 8dB. Many material systems have been used for making QW EAMs, some of which are InGaAs/InAlAs[31], InGaAlAs/InP[32], GaAs/AlGaAs[33, 34],

[1] V_{pp} is the drive voltage for the electroabsorption modulators, and half wave phase shift voltage for electro-optic modulators (in V)

InGaAlAs/InAlAs[35-37] and the InGaAsP/InGaAsP[[4, 7, 29, 38, 39] systems. These III/V materials all offer the possibilities of integration via QWI. The various key parameters of recent publications on quantum well EAMs are summarized in the table below.

Table 1.1 Summary of multi-quantum well electroabsorption modulators in recent years.

PIC Method (if any)	Ref.	V_{PP}	f_{3dB} [GHz]	L [μm]	W [μm]	ER [dB]
QWI method						
Raring, 2007	[19]	1.0-1.5	35-39	125	-	>8.7
SAG method						
Zhao, 2006	[29]	-	>10	-	-	>16
Okayasu, 2004	[6]	2.5	~40	120	-	10
Cheng, 2007	[7]	1.0	23	50	50	12
Shared active layer						
Saravanan, 2006	[40]	2.5	-	115	-	≥8
Stand-alone device						
Fukano, 2006	[36]	0.79	46	200	-	10.5
Tamura, 2004	[37]	2.0	>50	75	-	18
Choi, 2002	[41]	3.0	>38	900	-	11.5
Mason, 2002	[42]	2.5	40-60	80-120	-	13
Ido, 1996	[31]	1.2	>20	150	3	>13
Chiu, 2005	[43]	0.6	25	300	-	~15

ER: Extinction Ratio

As this dissertation is focused on the integration of passive (MMI) and active devices, we give below a literature review of the MMI device.

1.5. Multimode Interference Devices (MMI)

The central structure of an MMI device is a waveguide designed to support a large number of modes [2]. Compared to more conventional devices like directional coupler, for instance, those based on multimode interference are shorter and more compact, and preserve the balanced output characteristics [44]. Other unique properties possessed by MMIs include low loss, stable splitting ratio, low cross talk and imbalance, large optical bandwidth, insensitivity to polarization, ease of production and good fabrication tolerance [45]. Due to all these advantages, many studies have been made to understand its characteristics. Earlier literature on MMIs concentrated on the formulation of equations to give a theoretical prediction of its properties [2, 44-46] although research and fabrication of devices that utilize MMI devices were also reported

[47]. Except for a few cases where testing of actual designs were still impeded by the problems of fabrications, MMI devices have largely been successfully tested and integrated with many devices.

The various types of MMI devices fabricated on three different material base of interest, namely, the InP, SOI and polymer platform have been summarized below. The dimensions of these MMIs are stated along with their function and patterning method.

Table 1.2 Summary of multi-mode interference devices on three different material platforms.

Material Type	Ref.	MMI function	Patterning method	AW width, W_{AG} [μm]	MMI width, W_{MMI} [μm]	MMI length, L_{MMI} [μm]
InGaAsP/InP						
Spiekman, 1994	[48]	2x2 3-dB coupler	Std. photolitho.	1.1	9	107
Besse, 1996	[49]	2x2 power splitter 1x3 power splitter	N.M. N.M.	N.M.	12~18 * 24*	308~920 612~1224
Levy, 1999	[50]	2x2 3-dB coupler	-ve E-beam resist & E-beam exposure	2.0	5.8*	66
Ma, 2000	[51]	2x2 3-dB coupler	E-beam litho.	0.4~ 0.8	2~ 3.2	17.15~48.2 3
Rabus, 2001	[52]	2x2 3-dB coupler for RR	Std. photolitho.	1.8	6	150
Leuthold, 2001	[53]	2x2 tunable power splitting ratio (active)	N.M.	1.3	11.3	200
Hyun, 2003	[54]	1x4:4x4 splitter for MZI	Std. photolitho.	2	20	221.9;847.6
SOI						
Lai, 1996	[55]	2x2 arbitraty ratio pwer splitters	N.M.	10.5	47.4	1432
Yu, 2003	[56]	1x2:2x1 splitter for MZI 1x2:2x2 splitter for switch	Std. photolitho.	4	45 50	3200 3200;5000
Xu, 2007	[57]	2x2 3-dB coupler for RR	E-beam litho.	0.45	3	9
Polymer						
Jiang, 2005	[58]	1x1 MMI for VOA (active)	Std. photolitho.	17.7	56	3600
Zhu, 2006	[59]	2x1 coupler integrated with Bragg grating	-ve E-beam resist & E-beam exposure	1.5	6	95
Choi, 2007	[60]	1x4 splitter	UV embossing	4	60	855
Seo, 2007	[61]	1x4 splitter integrated with laser	Std. photolitho.	20	160	7480

AW: Access Waveguide; N.M.: Not Mentioned; RR: Ring Resonator; E-beam litho.: Electron beam lithography; Std. photolitho.: Standard photolithography; *: tapered (minimum width); VOA: variable optical attenuator

1.5.1. Application of MMI devices

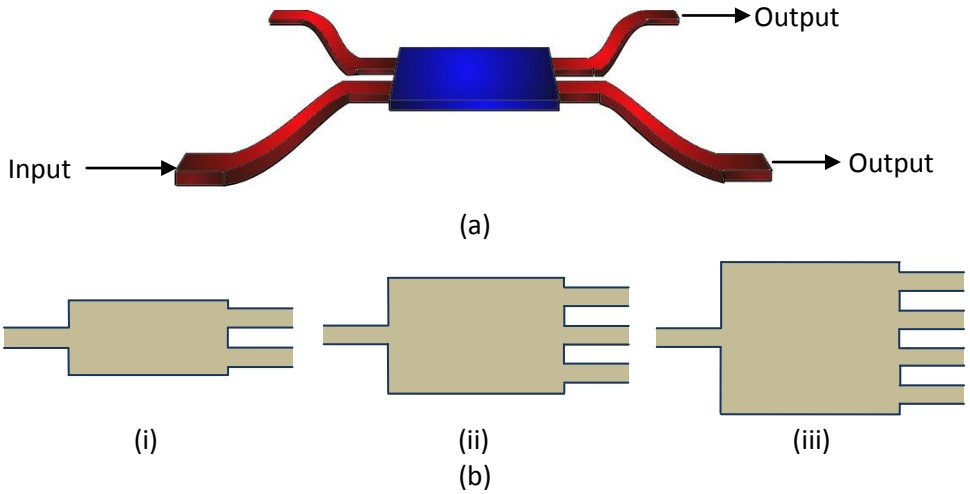

Fig.1.5.1. (a)Schematic view of a NxN MMI coupler (where N=2). The waveguides are joined to S-bends to allow a larger separation between the waveguides; (b) Schematic views of 1xN MMI couplers where N=(i)2, (ii)3 and (iii)4

Depending on how the MMI is designed, it can be used for many different applications. The most common one is a 3dB coupler. The design issues of a multimode interference-based 3-dB splitter have been studied in detail, including the effects of waveguide shifts, and variations in the MMI width, length and wavelength for the three types of interference mechanisms [62]. Other applications include the 1xN splitters, splitters with different power ratios and cross coupling devices. Multimode interference couplers can also be used as mode-combiners for fundamental and first-order modes [63]. These devices are capable of converting a fundamental mode into a transversal first-order mode and combining it with a second fundamental mode. These components have been successfully integrated into all-optical switches and were found to have advantageous characteristics in all-optical devices.

MMI devices that are used as wavelength splitters are usually integrated with other components for instance, the Mach-Zehnder Interferometer (MZI) [64-68]. Standalone MMI optical filters with rib [69], ridge [70] and deeply-etched rib [71] waveguide have also been simulated. MMI can also be used as an optical router [72]. This MMI has a slightly different structure, where the body of the MMI has a thicker rib structure than the input and output pathways. This structure is called the strip-loaded MMI structure. Researchers have noted

a much shorter *first* cross state when a weak-guiding MMI structure was used. This first image for weak-guiding structures could be useful in constructing an optical router. With their proposed MMI body which is thicker at the centre, the output signal can be improved by 10 percent. This optical router works in such a way that the interference in the MMI would cause a cross output when no bias is applied, and when an electric field is applied on the middle section of the multimode waveguide, the effective index of the body would drop until it resembles more of a directional coupler, and the output is in the bar state. The negative change in the refractive index is achieved using the blockaded reservoir and quantum-well electron transfer (BRAQWET) structure as shown in Fig.1.5.2.

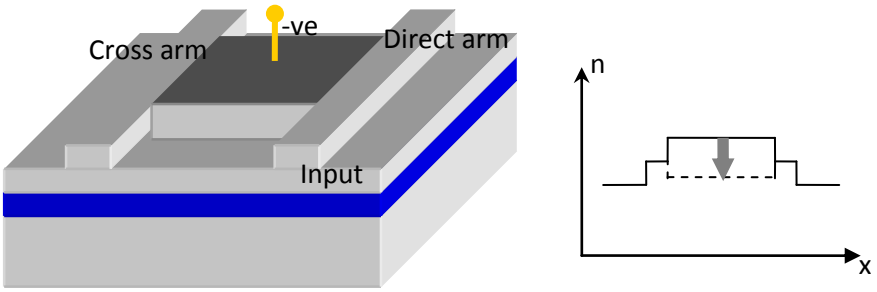

Fig.1.5.2. (a) A strip-loaded MMI structure (b) The refractive index distribution of the multimode section under no bias (solid) and with -9V (dashed line). (Ref[72])

MMI device as polarization separator/combiner based on self-imaging that uses the $LiNbO_3$ material [73] has been discussed. There has also been success in the design and fabrication of significantly shortened MMI coupler for application in polarization splitter, using a phenomenon that was termed the "quasi-state" (QS) imaging effect. This effect is formed by a particular four-mode interference condition. This concept shortens the split length to about 1/5 of the typical length by redefining the optical power field function [74].

The MMI device can also be used as a wavelength filter. Wavelength or optical filters[75-77] are essential components in wavelength division multiplexing (WDM) communication systems in which wavelengths are combined and separated to enable the transfer and routing of information. The wavelength of interest in telecommunication is in the 1.3- and 1.55-μm range. Various types of filter based on different mechanisms have been demonstrated.

These include (1) Mach-Zehnder interferometers (with unbalanced arms) [64-68], (2) directional couplers [78-81], (3) vertical couplers [78, 79] and grating-assisted couplers [82-85], (4) asymmetric Y branches [86], (5) MMI [69-71], (6) ring resonators [87, 88], (7) arrayed waveguide gratings (AWG) [89-94] and (8) Echelles gratings [95-102]. (1) to (6) are devices for filtering single wavelengths and many devices can be cascaded to filter or demultiplex multiple wavelengths. (6) and (7) are more complex optical integrated circuits that can demultiplex (or multiplex) multiple, closely spaced wavelengths simultaneously. Some filters are designed to separate wavelengths spaced very closely, and are called dense WDM (DWDM) filters. Other filters can only separate wavelengths spaced far apart, and are called coarse WDM filters. We will discuss only those filters based on MMI to illustrate the difference in our design which will be presented in the next chapters. (Note: MMI filter is an example of CWDM filter).

MMI filters are attractive because they are compact in size, low loss and allow large fabrication tolerances. Since the MMI effect is quite wavelength-insensitive, it is only applicable to cases where the interested wavelengths are >500nm apart [70]. MMI filters that have been proposed are formed by either Si/Ge [69] or SiON/SiO_2 [70, 71] layers. To our knowledge, actual devices have not been reported in the literature.

1.5.2. Design Variations for MMI Devices

Due to its popularity, many researchers have come up with different designs of MMI, some of which are discussed below.

Tapered MMI devices have been proposed by some researchers for their abilities in giving a broader optical bandwidth [103]. Another reason for utilizing tapered MMI devices is because they help to circumvent the proximity limitations in ultra-compact MMIs [104]. These have been successfully fabricated [105] and proven. The investigation has also shown that the tapered 3-dB 2x2 MMI devices fabricated are up to 40% shorter than all previously fabricated MMIs. The tapered structure enables the MMI to have a smaller

effective width without requiring a smaller input waveguide separation, thereby giving a substantial decrease in device length while maintaining the conventional imaging, or power splitting properties. Another geometric variation is the butterfly design. It is said to be polarization-insensitive and offers flexible choices of power splitting ratio [49]. Some of the proposed MMI shapes are shown in Fig.1.5.3.

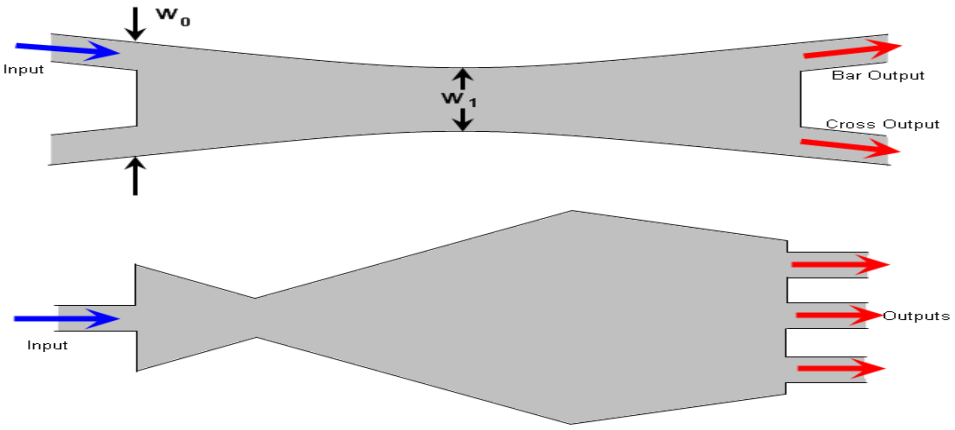

Fig.1.5.3. MMI structures. The top picture is designed using non-linear taper [109] whereas the bottom structure is made of a few linear tapers [53].

MMI couplers with tunable power splitting ratios have also been realized [53]. This is done by applying different voltages at the centre of the MMI device length, thus causing the effective index of the area to be altered. This alteration will then cause a different magnitude of output power in both the output waveguides. The idea actually exploits the fact that within an MMI, the input field is reproduced in single or multiple images at certain periodic intervals along the propagation direction of the light. The interference patterns of the self-images at one interval lead to the formation of a new set of self-images at the next interval and finally to the output images. Consequently, the output images can be changed by modifying the refractive index around some selected spots within one interval of the MMI where such self-images occur. This will lead to new phase relations between the self-images at the next interval and with that to a modified set of output images. The area where the tuning is done is where the most dominant self-images appear, wich is simply halfway along the propagation direction of an MMI. The effect of this tuning is quite big, for example, by inducing a negative refractive index change of as

little as 0.15% at edges halfway along the MMI, the splitting ratios of the bar to cross output ports turns from a 50:50 into a 20:80 ratio.

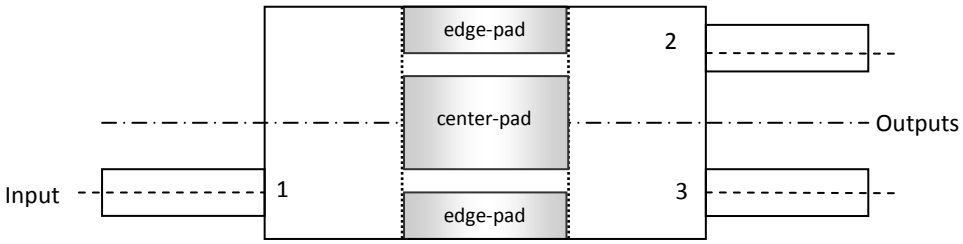

Fig. 1.5.4. Geometry of a symmetric 2x2 MMI with locations of the pads where a negative refractive index change was induced in order to tune the splitting ratios.

MMI have been fabricated in various materials. Since III-V materials and its related fabrication techniques are more costly in general, polymers [106] and sol-gel materials [107] have been offered as alternative choices. Polymeric optical waveguides are fabricated by using optical polymer benzocyclobutene (BCB). The properties of BCB include good thermal stability and high optical transmission (transparency at intended optical wavelength). Anisotropic etching of BCB is achieved by reactive ion etching. Superior properties such as low excess loss and good tolerance to the variation of wavelength were reported.

1.5.3 MMI in photonic integrated circuits

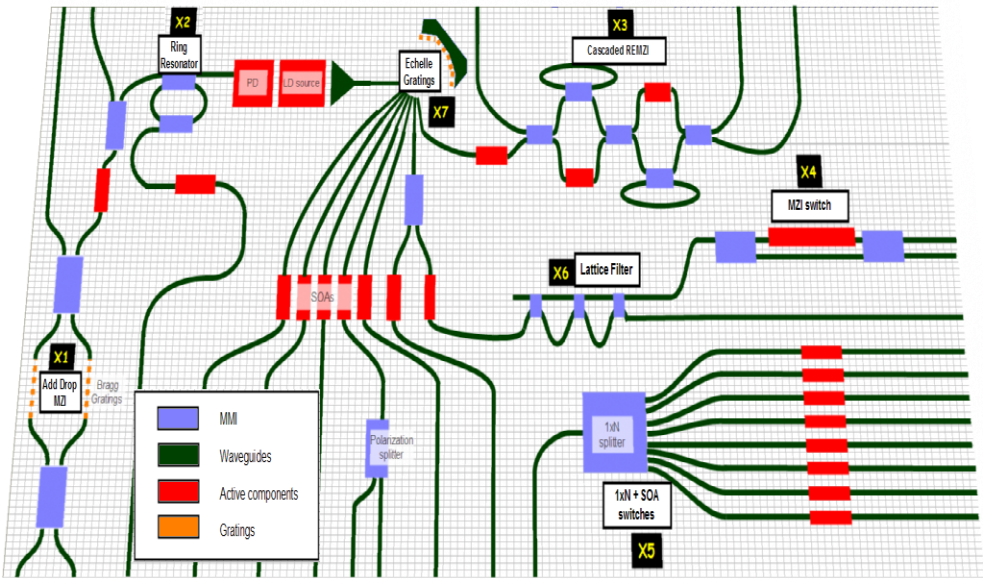

Fig. 1.5.5. Conceptual plan of an integrated circuit showing examples of how MMI can be used.

MMI devices are often used in integrated photonic circuits because its size makes it an easy component to be fabricated, and it allows input light to be split in whatsoever way is required. Examples of such applications include the ring lasers [108], polarization-insensitive MZI switches [64-68], MZI polarization splitter [109], and optical hybrids for phase diversity networks and polarization diversity receivers [46].

Another example of using MMI device in an integrated photonic circuit is the 40-Ghz mode-locked fiber-ring laser using Mach-Zehnder interferometer with integrated SOAs [110]. In order to concatenate an SOA waveguide to the MZI structure, MMI couplers are used. In an attempt to integrate ring resonators with semiconductor optical amplifiers (SOAs), using vertically stacked asymmetric twin waveguide structures, MMI couplers were also used [111]. Wavelength-selectable arrayed DFB laser with an integrated MMI coupler and SOA for WDM systems have also been demonstrated [112]. Wavelength-selectable light sources are attractive as back-up light sources.

1.6 Research Objectives and Significant Contributions

The broad objective of my PhD research is to study PIC with focus on the monolithic integration of InP-based active and passive devices using the quantum well intermixing (QWI) technique. Thus, the first part this thesis includes the study of basic device building blocks such as ridge waveguides, passive devices such as directional coupler and MMI, and active devices such as electroabsorption modulators (EAM). The second part of the thesis is focused on simple active-passive IC where prototypical examples are demonstrated, mainly involving and MMI and EAMs. The several highlights of the research are discussed below. In each case we discuss the research idea, the motivation behind it, and the significance of the achievement.

Active passive integration has long been a challenge or “bottleneck” for PIC. Traditional methods are very complex, involving many growths and processing steps which degrade the overall yield. In NTU, our collaborating group [Prof. Mei Ting] over the years has developed an ICP-based plasma-enhanced QWI technique that is comparatively simple as it is a one-step post-growth process [13]. It has been studied for various InP-based quaternary and

ternary quantum well materials, but has not been applied to or demonstrated in real integrated devices. It is a highlight of this thesis to report the achievement of the first integrated active-passive device based on the MMI + active-device configuration. In this device, QWI is used to increase the bandgap of the quantum well material to create a passive (i.e., transparent) region in the MMI device area while preserving the material quality of the active devices. We carried out a study to optimize this process such that the bandgap shift is sufficiently large in the desired (passive) region while the thermal shift (the shift due to thermal annealing alone) in the protected (active) region is relatively small. The active device in this case is designed to be an electroabsorption modulator which acts as an on-off optical switch. Coupled with the MMI 1xN splitter the MMI with electroabsorption modulators device serves as a 1:N optical switch. Alternatively, the active device can be forward biased to serve as an optical amplifier which provides gain to compensate for the splitting loss in the MMI section, so as to provide switching with negligible loss. This work is presented in Chapter 6.

Prerequisite to the design and demonstration of the MMI + EAM integrated device is the prior optimization of the constituent building block - MMI. The initial study involves the design concept of MMI and its relation with directional coupler (DC) which has a similar structure. In this study, we showed that the DC can be seen as an MMI with the center region partly removed to create the gap in the DC. When the gap depth is zero the DC is the same as the MMI. Hence, it is interesting to study the possible transformation of optical properties from one device to the other by varying the depth of this gap region. Detailed simulations show that, indeed, the modal properties evolved gradually from the coupled-mode characteristics of the DC to the multi-mode nature of the MMI. The discovery of such a relationship was first reported by us in Optics Express [113] in 2004. This is the subject of Chapter 2.

Most of the previous work on MMI had concentrated on rib-waveguide structures and tend to prefer much wider widths than necessary. In our work, we have studied the ridge-waveguides and achieved more compact solutions. These waveguides, however, tend to be more lossy hence the reduction of loss is an important requirement for both design and fabrication. The loss is mainly due to

scattering due to sidewall roughness. Further process optimization was carried out to minimize this loss. The Fabry-Perot method was adopted to characterize the loss measurement. This is discussed in Chapter 3.

The 1xN (or 1:N) MMI splitter structures which have been previously reported are often based on the rib-waveguide structure (for example ref. [114]) or other material base [107]. In order to determine the most suitable access waveguide widths along with the tailored MMIs to match, our main objective was to study and explore the insertion loss and the splitting limits of these MMIs before further integration with active devices. We successfully fabricated and measured splitters where N=2, 3, 4, 6 and 8. The wavelength envelope or bandwidth comparison of the 1x2 and 1x3 MMIs have been made along with salient analysis of these splitters.

We explored the possible applications of MMI alone as a device. The devices that have been successfully designed are the MMI coarse wavelength filters that can separate the 1.31μm and 1.55μm wavelengths for coarse wavelength demultiplexing purposes based on the beat length difference concept, and the MMI Polarization filters that are based on InP substrate that can separate transverse electric (TE) and transverse magnetic (TM) mode fields for polarization dependent devices. The successful prototype of the course WDM based on a polymer material signifies the realization of this theory to an actual device [115]. This is highlighted in Chapter 4.

Using the SOI technology, through cooperation with IMEC in Belgium, we have successfully fabricated 3dB splitting MMI with broadband capabilities with waveguides as narrow as 450nm and also demonstrated 80:20 splitting ratio capabilities on a 8.8μm long wedge shaped MMI which is possibly one of the smallest such splitter around. These are discussed in Chapter 4.

In order to develop a modulator with better modulation (a.k.a. lower driving voltage and higher power saturation) and improved coupling to fiber, we have utilized a multiple quantum well structure with dual depletion active region and large optical cavity (LOC) as one of our material structures to achieve lower driving voltage and higher saturation power. The successful

fabrication of a lumped element electroabsorption modulator is discussed in Chapter 5.

1. 7 Dissertation Outline

This dissertation mainly investigates the multimode interference device (MMI) and its role in PIC. Although MMI stands undisputed as a reliable 3dB coupler, it has many other possibilities yet to be developed. One approach is to extend the input or output of the MMI devices to another active part. In this research, I have integrated the output arms of the MMI device to EAMs thus the name of my research topic, multimode interference devices and integration with electroabsorption modulators for photonic integrated circuits.

Various approaches have been explored in order to integrate the MMI with active devices to achieve special functionality. The MMI device itself is a versatile building block that can perform many functions and its properties are reliable enough to be sustained across different sizes and material types. Thus, following this chapter, in which some PIC methods and MMI devices have been introduced, Chapter 2 describes the theoretical background for the realization of such integration which includes the salient mathematics and calculation methods.

Strongly guiding ridge straight waveguides of varying widths have been fabricated and the measurement results of these waveguides have been determined with the Fabry Perot measurement method which is included in Chapter 3. This was followed by the fabrication of 1x2, 1x3, 1x4 and 1x8 MMIs, all of which good results have been obtained. The results of these 1xN MMI splitters have been presented along with the relevant bandwidth measurements and comparisons for the 1x2 and 1x3 MMIs. The 1xN designs here are the foundation for subsequent fabrication and device demonstration of the 1x2 MMI + EAM in Chapter 6.

Chapter 4 presents the simulation results for beam propagation method (BPM) and finite difference (FD) mode solver method that have been

meticulously generated for different primary variables. The basic functionalities of MMI devices have been studied and re-examined here. The realization of a BCB based wavelength splitter prototype based on these studies is described. The various 2x2 3dB MMI designs and their suitability for achieving compact sized SOI based integration are also presented along with the prototype results.

Chapter 5 focuses on the fabrication processes that were utilized in achieving the devices that had been designed. Active waveguides were also fabricated. Techniques of integration involve a localized modification of material bandgap using the method of quantum-well intermixing (QWI). The basic EAM theory and designs are also mentioned here along with the experimental results of two types of EAMs, namely the InGaAsP/InGaAsP MQW EAM and the InGaAlAs/InGaAlAs MQW EAM.

Chapter 6 presents the experimental results of the MMI + EAM devices made. A segment by segment comprehensive comparison between two types of material structure is presented in terms of splitting ratios, optical bandwidth, extinction ratio, driving voltage, and propagation loss. A fiber-to-device-to-free-space measurement setup has been built to measure the relevant samples fabricated. The results of the integrated MMI + EAM device were also characterized.

Finally, Chapter 7 summarizes this dissertation work, highlights the important results, lists some unsolved problems and suggests future work to further improve the integrated MMI + EAM devices and their performance.

Chapter 2

Multi-Mode Interferometer (MMI) Based Devices

2.1 Introduction

In this chapter, the principle of MMI self-imaging which is the theoretical background which describes the MMI based devices is presented. MMI is a well-established basic device that has been used for many applications, mainly as an optical coupler and splitter (or combiner). Most conventional MMI have been based on weak-guiding rib waveguides. In this thesis, we focus on strongly guiding ridge waveguides in order to achieve more compact devices. At the final part of this chapter, a vigorous study of the relation between MMI couplers and the more often used directional couplers (DC) is described.

2. 2 Principle of MMI self-imaging

The operation of MMI devices is based on the self-imaging principle [1]. The self imaging of periodic objects illuminated by coherent light was first described more than 170 years ago [2]. Self-imaging is a property of multimode waveguides by which an input field profile is reproduced in single or multiple images at periodic intervals along the propagation direction of the guide [3, 4]. Self-imaging in slab waveguide, initially suggested by Bryngdahl [1], is a way to re-image any object without the need of lenses, mirrors or birefringence material. Ulrich in 1975 further described it this way [5]: Assume a coherent object in the plane x=0 of a multimode slab waveguide of uniform refractive

index and thickness (which is also known as the guide) exciting a number, *M*, of propagating modes at one frequency and at one common phase. As these modes propagate along the guide, proceeding with all different phase velocities, they soon fall out of phase and interfere in such a way that at certain length, $z=L_h$ (where h = 1, 2, 3 …), there will exist a second plane where the phases of all *M* modes coincide again. In other words, at $z=L_h$, a self-image of the object is formed. Fig.2.1.1 is an illustration of the above description.

The self-imaging property of a multimode waveguide is due to the interference of the waveguide modes [6] which are excited by the object. Therefore, when the superposition of the modal fields in the image plane is the same as the object plane (at $z=0$), the self-image is formed. At the image plane, the accumulated phase differences between any two excited modes are multiples of 2π. However, as the trend repeats itself, the phase differences are no longer exact multiples of 2π, resulting in self-images of poorer quality. In order to launch light into or recover light from a multimode waveguide, a number of access waveguides are placed at its beginning and at its end. For photonic integrated circuit applications, the input optical waveguides are usually narrower and single-mode.

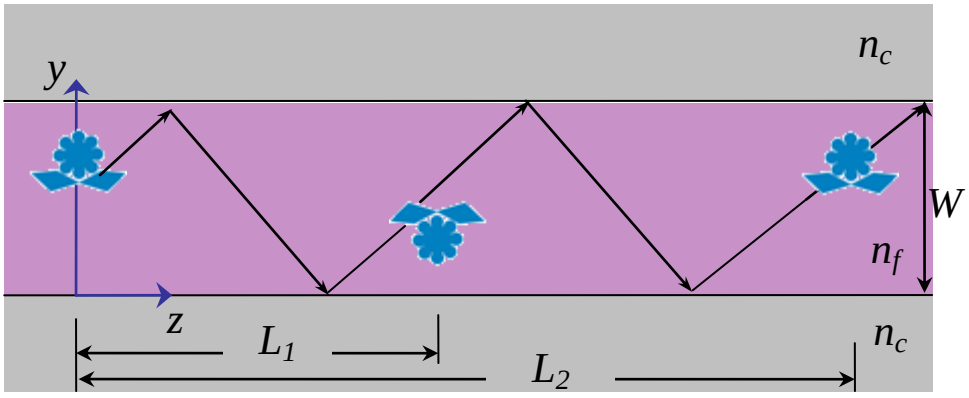

Fig.2.1.1. Schematic cross section of a planar dielectric optical guide where the *y*-axis is normal to the plane of illustration. The object is portrayed as a flower symbol for easy visualization.

A full-modal propagation analysis provides an analytical theory that describes the self-imaging phenomena in a multimode waveguide. It does not only supply the basis for numerical modeling and design, but also provides insight into the mechanism of multimode interference [3]. Other numerical

approaches make use of ray optics, hybrid methods, BPM simulations and the radiation spectrum method (RSM) [7].

The field profile at a distance z can be written as a superposition of all the guided mode field distributions as [3]:

$$\Psi(y,z)=\sum_{v=0}^{m-1}c_v\psi_v(y)\exp[\,j(\beta_0-\beta_v)z] \qquad (2.1)$$

where the phase of the fundamental mode has been taken out as a common factor.

In the effective index approximation, the MMI waveguide is characterized by an effective index n_r and the v_{th} guided modes is characterized by the propagation constant β_v and the lateral wavenumber k_{yv}, which are related to the MMI's effective index n_r by the dispersion equation $k_{yv}^2+\beta_v^2=k_0^2n_r^2$, with $k_0=2\pi/\lambda$ and $k_{yv}=(v+1)\pi/W_{ev}$; W_{ev} being the effective width of the MMI which takes into account the Goos-Hänchen lateral penetration depth of each mode field. For high contrast waveguides, the penetration depth is very small so that $W_{ev}\cong W_{MMI}$. In the paraxial approximation, $k_{yv}^2<<k_0^2n_r^2$, $\beta_v\cong k_on_r-\frac{(v+1)^2\pi\lambda_o}{4n_rW_e^2}$, and thus the propagation constant $(\beta_0-\beta_v)$ in (2.1) can be written as:

$$(\beta_0-\beta_v)\approx\frac{v(v+2)\pi}{3L_\pi} \qquad (2.2)$$

where

$$L_\pi=\frac{\pi}{(\beta_0-\beta_1)}\approx\frac{4n_rW_{ev}^2}{3\lambda_0} \qquad (2.3)$$

is the beat length of the two lowest-order modes.

Under the general interference (GI) mechanism, which is independent of the modal excitation, the input waveguides can be placed anywhere along the lateral y direction. Single images of the input field are produced at every *even* multiple of the self-image distance $\boldsymbol{L}_i = 3i\boldsymbol{L}_\pi$ (i.e. $\boldsymbol{L}_2=2(3\boldsymbol{L}_\pi)$, $\boldsymbol{L}_4=4(3\boldsymbol{L}_\pi)$, $\boldsymbol{L}_6=6(3\boldsymbol{L}_\pi)$, ...) along the direction of propagation at an identical position at the

output plane, known as the *bar* output (see Fig.2.1.1). This input field also produces single images at an antisymmetric position, known as a cross output, at every *odd* multiple of $\boldsymbol{L}_{i.}$ Substituting (2.2) into (2.1), the field at a distance $z=L$ may be written as:

$$\Psi(y,L)=\sum_{v=0}^{m-1}c_v\psi_v(y)\exp\left[j\frac{v(v+2)\pi}{3L_\pi}L\right] \tag{2.4}$$

On the other hand, to obtain multiple images, it can be seen that at half-way between the direct and mirrored image positions, i.e. at distances $L=p3L_\pi/2$ with $p=1,3,5,\ldots$, the total field at these lengths can also be translated as:

$$\begin{aligned}\Psi(y,\frac{p}{2}3L_\pi)&=\sum_{v\ even}c_v\psi_v(y)+\sum_{v\ odd}(-j)^p c_v\psi_v(y)\\&=\frac{1+(-j)^p}{2}\Psi(y,0)+\frac{1-(-j)^p}{2}\Psi(-y,0)\end{aligned} \tag{2.5}$$

with p as an odd integer

Equation (2.4) represents a pair of images of $\Psi(y,0)$, in quadrature and with amplitudes $1/\sqrt{2}$, at distances z=1/2($3L_\pi$), 3/2($3L_\pi$), … as shown in Fig. 2.1.2.

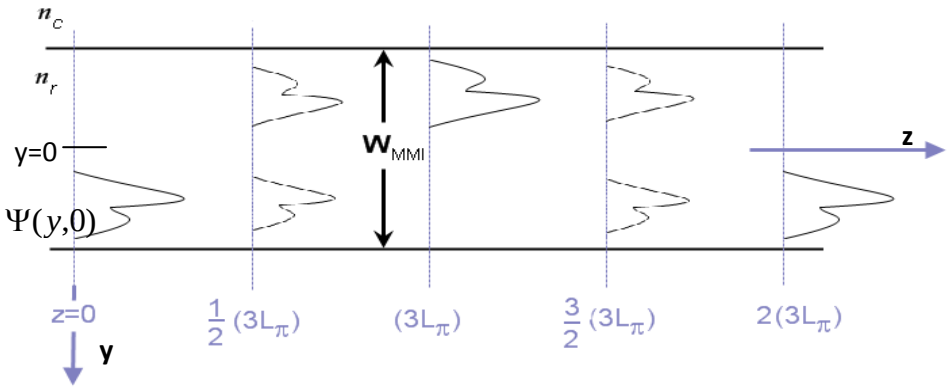

Fig. 2.1.2. Multimode waveguide showing the input field $\Psi(y,0)$, a mirrored single image at $(3L_\pi)$, a direct single image at $2(3L_\pi)$, and two-fold images at $\frac{1}{2}(3L_\pi)$ and $\frac{3}{2}(3L_\pi)$.

The three interference schemes as first introduced by Soldano, et. al [3] consisted of the general interference, restricted interference and symmetric interference. General interference does *not* place any restrictions on the modal excitations, whereas for restricted interference, the input and output locations

are placed at a lateral offset of $\pm W_{MMI}/6$, and symmetric interference is obtained if the input waveguide is placed in the center of an MMI device. The schematic diagram of the interference schemes are shown in Figure 2.1.3. Different schemes will give the desired outputs at different lengths, so the choice of schemes will depend on the number of inputs, outputs and other considerations [8]. These schemes are the different manifestations of the self-imaging principle [9].

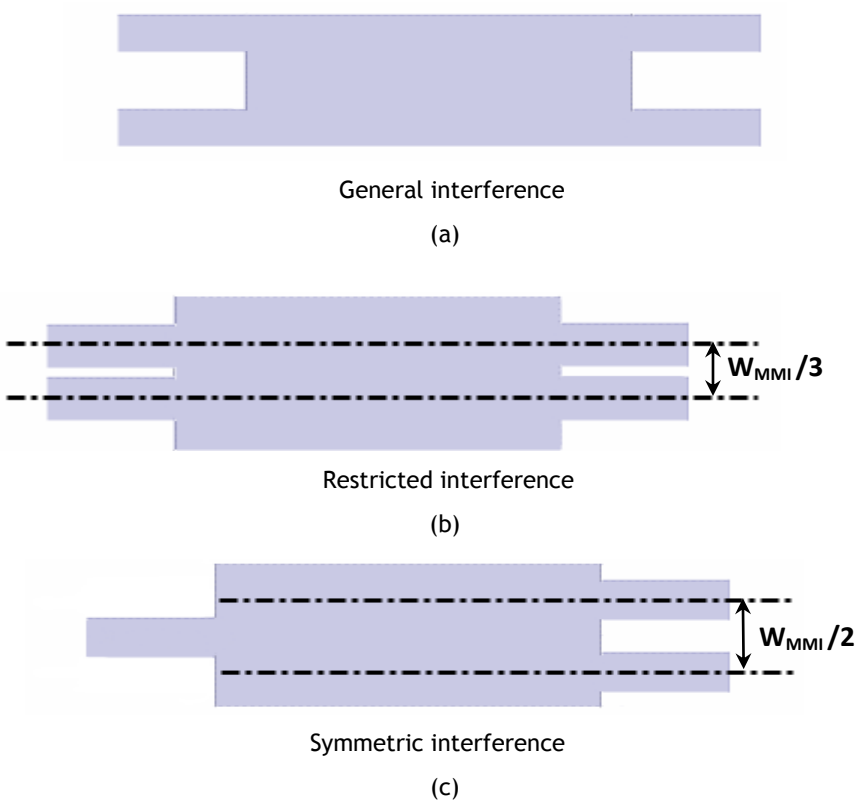

Fig. 2.1.3. Schematic diagram of the interference schemes for the 3-dB MMI-based power splitter.

Restricted and symmetric interference arises when certain modes are not excited. When certain restrictions are imposed upon the input position, with reference to the *y* direction, overlapping of the images can then be observed [4, 10]. Of all the input positions that causes overlapping-image MMIs, only when the input is at the centre or at one third of the MMI coupler does the MMI coupler yield a uniform spitting ratio. That is why these two interference mechanisms hold much more impact than other positions. Table 2.1 gives a summary of the characteristics of general, paired and symmetric interference mechanisms.

TABLE 2.1: Summary of characteristics of the general, restricted and symmetric interference mechanisms

Interference mechanism	*General*	*Restricted*	*Symmetric*
Input x Outputs	NxN	2xN	1xN
First single image distance	$(3L_\pi)$	(L_π)	$(3L_\pi)/4$
First N-fold image distance	$(3L_\pi)/N$	$(L_\pi)/N$	$(3L_\pi)/(4N)$
Excitation requirements	None	c_v=0 for v=2,5,8,...	c_v=0 for v=1,3,5,...
Input(s) location(s)	any	y=±W_e/6	y=0

The beat length $\boldsymbol{L_\pi}$ (2.3) may be rewritten as

$$L_\pi = \frac{\lambda}{2(n_0 - n_1)} \qquad (2.6)$$

where λ is the optical wavelength, n_0 is the effective index of the zero-order (fundamental) mode and n_1 is the effective index of the first-order mode. These eigen-indices can be calculated using an exact finite-difference mode-solver (e.g., Apollo APSS). One such example of the optical field shapes of these modes are shown in Figure 2.1.4. In these figures, the MMI width, W_{MMI}=4μm and finite difference (FD) simulations were ran at λ=1550nm. The effective indices simulated for the fundamental and first-order modes are 3.2475 and 3.2306 respectively for the TE mode and 3.2427 and 3.2269 for the TM mode which gives us the beat length, $\boldsymbol{L_\pi}$=45.9μm for TE mode and 49.1μm for TM mode.

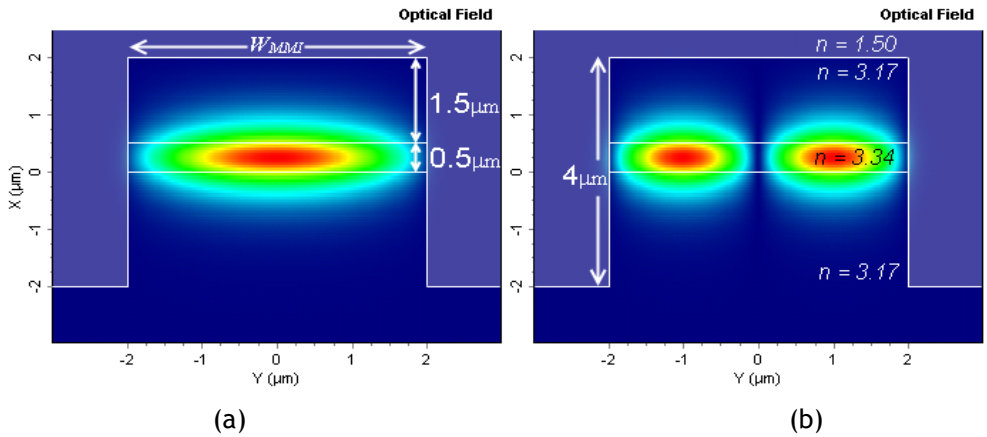

Fig. 2.1.4. Optical field of (a) n_0 and (b) n_1 where W_{MMI}=4μm, background refractive index is 1.5, cladding index of InP is 3.17 and the 0.5μm thick InGaAsP core's refractive index is approximated as 3.34. In this example, the top cladding is 1.5μm thick, etch depth is 4μm and the substrate thickness is simulated down to 3μm.

2.3 Ridge Waveguides

The design ground work of MMI consists of three steps. The first is to determine the material structure; the second, to determine a suitable waveguide (WG) structure and lastly, the type of MMI to be used. Most of our initial work was based on the InGaAsP/InP material [11] as it is one of the more suitable materials for monolithic integration of photonic devices. In the earlier papers on MMI devices, researchers used or assumed rib waveguides which were weakly confined. We concentrated, instead, on deeply etched ridge waveguides because of the strong confinement and the associated advantages that they offer. The ridge waveguide is a high index contrast waveguide. For semiconductor waveguides, the lateral index contrast is as great as 3:1. This index contrast provides the strong lateral confinement that enables the waveguide to bend with very small radii. Fig.2.2.1 shows the optical mode profile in a (a) rib waveguide and (b) a ridge waveguide. In these figures the background refractive index were assumed to be 1.5 as most devices are usually coated with SiO_2 or polymer for device preservation purposes. The top and bottom cladding (and/or substrate) are assumed to be InP with the refractive index of 3.17. The core is InGaAsP with the material index of 3.34. Ridge and rib widths have been varied between 1.5μm to 3.0μm. The figure showed the 1.5μm results. Etch depth of the rib and ridge waveguides are 1.0μm and 4.0μm respectively. The top claddings for both simulations are 1.5μm thick, followed by the core layer, which was 0.5μm thick, and the bottom cladding is >2μm. Because of the strong lateral confinement, the width of such waveguide with a given number of modes is much smaller than the rib waveguide, hence enabling the length of MMI (or other similar devices such as directional couplers) to be much smaller also than is possible in conventional designs based on rib waveguides. At the same time, however, it also makes it more difficult to fabricate single-mode waveguides. Aside from the stringent fabrication requirement, this small width (<0.8μm) could incur other problems—high propagation loss over long distances [12, 13], high fiber coupling loss, and high polarization dependence.

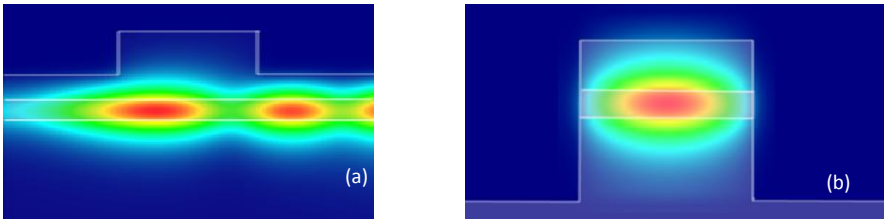

Fig. 2.2.1. (a) A Rib WG with R=100 bending radius showing field leakage whereas in (b) A Ridge WG with R=100 bending radius, the field is still confined.

However, although it is natural to use single-mode waveguide for single-mode devices, such as directional couplers, it is not essential and, in practice, not always desirable to do so. The multi-mode waveguide is effective for single-mode devices so long as the higher-order modes are not excited. Mode conversion, however, can occur whenever a waveguide bends or wherever there is any irregularity such as roughness or geometric asymmetry. To avoid this it is necessary to make the multi-mode waveguide *effectively* single-mode. One approach in attaining this is to eliminate the higher-order modes through differential leakage loss by controlling the *etching depth* of the ridge waveguide. The idea of using differential leakage loss to eliminate higher-order modes has been demonstrated for GaAs waveguides [14]. In the case of InP, the differential loss mechanism occurs because the higher-order modes, which have lower effective indices, can leak easily into the substrate when the etch depth is reduced. Therefore, for a given waveguide width, there exists an optimum etch depth determined by the acceptable loss for the fundamental mode as well as the required *differential* loss for the first-order modes [15, 16]. In short, it is possible to use a combination of widths and etch depths, to design ridge waveguides with reasonably low loss for the fundamental modes, and to design waveguide widths which are much more robust and easy to fabricate using standard photolithography.

Figure 2.2.2 shows the waveguide geometry and structure that has been designed based on these requirements. The material indices stated are based on Broberg [17] and Martin [18]. The 0.5μm thick InGaAsP layer, which is the core, has the refractive index of about 3.4. It is sandwiched between InP (n=3.17) layers. The etch depth of this structure, H is 4μm, where the InP layer above the core (the top cladding), L1 is about 1.5μm thick. The ridge structure

is covered with polymer or SiO_2 layer with refractive index of ~1.5. The ridge widths W which have been investigated, ranges from 0.3μm to 8.0μm.

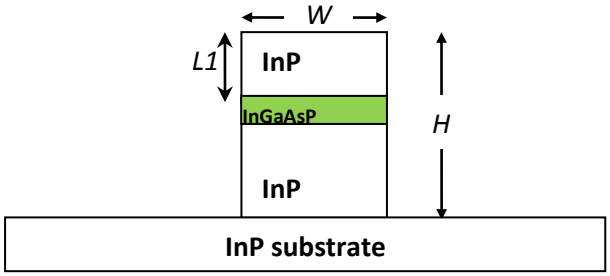

Fig. 2.2.2. Schematic diagram of ridge waveguide structure used.

2.4 Comparing MMI device with Directional Couplers

A two-mode MMI coupler, may be considered as a fused *directional coupler* (DC) where the gap between the DC waveguides has been filled. A legitimate question, then, is: When does a DC start becoming an MMI? We show, for the first time, an evolutionary lineage between the DC characteristics and the MMI characteristics as one is structurally transformed from the other [16].

The directional coupler considered consists of two parallel, symmetric waveguides separated by a gap. The coupling between the waveguides results in a periodic transfer of power between them in a way that obeys the cosine-squared law. The distance in which complete transfer occurs is defined as the *coupling length* and is given by:

$$L_c = \frac{\pi}{\beta_e - \beta_o} = \frac{\lambda_o}{2(n_e - n_o)} \qquad (2.7)$$

where n_e and n_o are the effective indices of the even and odd *supermodes*. This equation is similar to (2.3) and (2.10). The coupling length is sensitive to many parameters, the most significant of which is the gap width (or waveguide separation). If the gap width is fixed (say, at 0.5 μm), we can still control the coupling length by varying the etch depth in the region between the waveguides. To obtain a reasonably small coupling length, a shallower etch could be used here so that the evanescent coupling here resembles that of a rib waveguide, while a deeper etch on the outer edge is retained to provide strong

overall confinement, as shown in Fig.2.3.1.(b). In fact, if the etch depth is further reduced above the waveguide core layer (Fig.2.3.1.(c)), then it can be shown that the DC's characteristic transfer function will look more and more like the MMI characteristics (Fig.2.3.2.).

We investigate the change in mode coupling behavior in a directional coupler as the structure is transformed through the steps (a) to (e) depicted in Fig.2.3.1. The access waveguide width is fixed at w = 1.5 μm, and their center-to-center separation is D = 2 μm. The resulting MMI shown in (d) has the smallest possible width given by $W_{MMI} = (D + w)$. For convenience we refer to this general interference MMI as Type I, since it may be considered as the direct descendent from the directional coupler of (a). The *restricted interference* MMI can be formed by expanding the MMI width to $W_{MMI} = 3D$ [see Fig. 2.3.2.(e)]. This MMI may be considered as a derivative of Type I, so for brevity it is referred to as Type II.

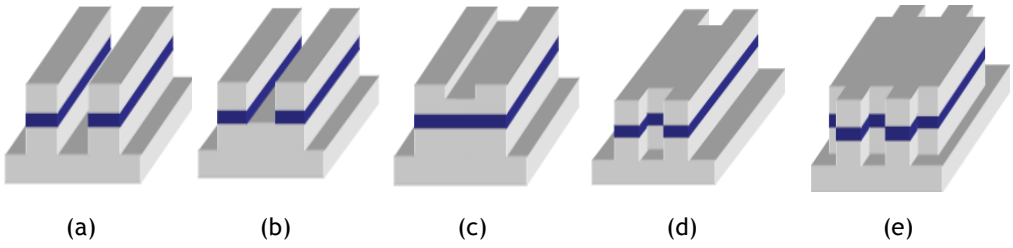

Fig. 2.3.1. DC-MMI transformation from (a) to Type I MMI (d) and Type II MMI (e).

As the gap depth is reduced, there are increasing ripples in the transfer curves for both TE and TM arising from the dielectric perturbation in the gap (Fig.2.3.1.), and there is a continuous reduction in the coupling length to about 100 μm. Eventually, as the light sees a much bigger waveguide the power distribution is no longer determined by the coupling between the supermodes, but rather shaped by the multimode interference inside the much bigger waveguide. When the etch depth is 1.1 μm (or 0.4μm above the top of the core layer), the device characteristic is already MMI-like, with the coupling length still at about 100μm. When the etch depth is 0.6μm, the 3-dB coupling length is also well defined, and the MMI characteristic is fully developed even though there is still a sizable etched gap.

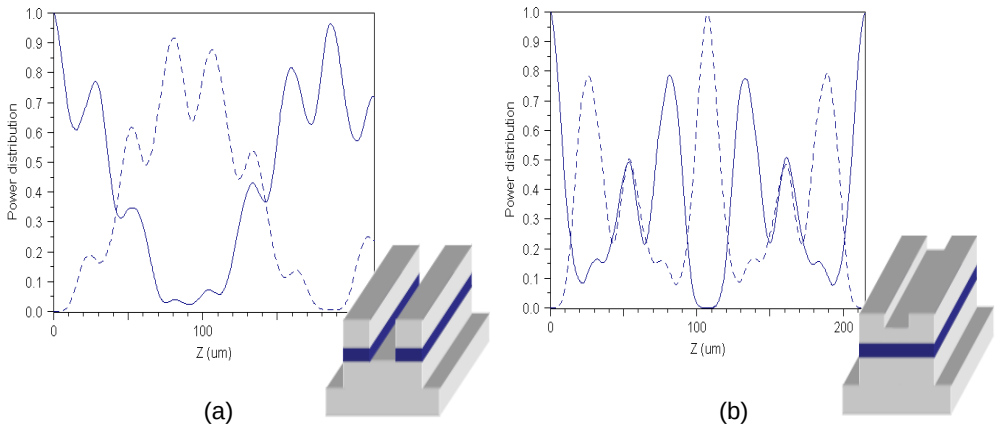

Fig.2.3.2. Power distribution of a partially etched directional coupler while (a) it is still resembling the characteristics of directional coupler and (b) when it has started to display the characteristics of an MMI coupler.

Underlying the structural transformation from a directional coupler to a 2 x 2 multimode interferometer is the modal evolution from single-mode to multi-mode waveguides. In the left half of Fig. 2.3.3 we show this modal evolution by plotting the effective modal indices as a function of the etch depth. These effective indices are obtained directly by solving the symmetric and anti-symmetric modes of the coupled structures using a finite-difference mode solver. Initially, with very deep gap, the two eigen-indices are nearly equal. When the etch depth is 0.1μm above the bottom of the core layer, the coupling increases rapidly, and the supermode indices start to separate, reaching a maximum separation when the etch depth is 0.5μm above the top of the core. These supermodes become the fundamental (m=0) and first-order (m=1) modes of the combined waveguide that forms the MMI. This MMI is based on the *general interference* (GI) mechanism, for which the input waveguides can be placed anywhere along the lateral x direction. For this MMI, cross coupling will occur at the coupling length $L_c = 3L_\pi$. From Fig.2.3.1, we have $n_0 = 3.2434$ and $n_1 = 3.2212$, giving $L_\pi \approx 35\mu m$ according to Eq. 2.10, so $L_c \approx 105\mu m$. We can see why *MMI is always more compact than the DC* from which it evolves.

On the right half of Fig.2.3.3 we show that when the MMI waveguide width is further increased, n_0 and n_1 approach each other as higher-order modes emerge, implying that L_π is increasing. When the MMI width is three times the centre-to-centre separation between the access waveguides, certain modes will not be excited and the MMI is said to be in the *restricted interference* (RI)

mode. In this case, the smallest coupling length is L_π, where L_π is now equal to 102 μm. Hence, both types of MMI have about the same coupling length L_c, even though they have quite different widths and are based on different self-imaging mechanisms.

The results of MMI lengths for Type I and Type II MMI are summarized in Table 2.2. It should be noted that the L_π for TE polarization is slightly *smaller* than that for TM. This result is consistent with BPM simulations, but is not always correctly pointed out in some papers. It is a characteristic of MMI that essentially reflects its modal evolution from a directional coupler origin. This small polarization dependence can be used as the basis for the design of a polarization splitter, which will be discussed in Chapter 4.

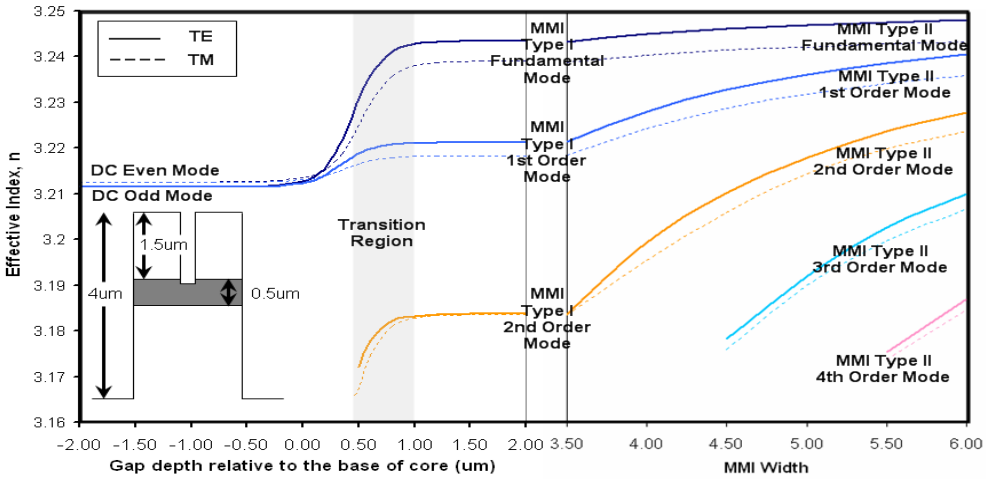

Fig. 2.3.3. The change of TE and TM effective indices with changing gap depth, showing the transition from DC to MMI (left), and with changing MMI width

TABLE 2.2: Cross Coupling & 3dB Coupling length for 2X2 MMI Devices with w=1.5μm; g=0.5μm and W_{MMI} increasing gradually from 3.5μm to 6.0μm

W_{MMI} (μm)	L_{MMI} for cross coupling (0:100)		L_{MMI} for 3dB coupling (50:50)	
	TE (μm)	TM (μm)	TE (μm)	TM (μm)
3.5 Type I	103	111	51	55
4.0	132	141	67	71
4.5	167	177	83	88
5.0	206	240	104	109
5.5	82*; 251	87* ; 264	42*; 125	44*; 132
6.0 Type II	100*; 296	104*; 310	49*; 149	52*; 156

Conclusion

In this chapter, a detailed study of MMI which encompasses its basic theory and its transformation from a directional coupler has been given. For the first time, the continuous evolution from the two mode coupling characteristic of DC to the multi-mode mixing and interference characteristic of MMI, as the DC is structurally transformed into the MMI is presented. Not only is the resulting MMI more compact than the original DC, the same compact size can be given by two different types of MMI based on the two different self-imaging mechanisms. Furthermore, we have also shown that DC can be designed to have the MMI features of compactness and polarization-insensitivity, two traits that reflect their shared lineage.

Chapter 3

MMI splitters: Measurement and Characterization

In order to understand the performance of an MMI device, a systematic device characterization is required. In this chapter, after introducing the MMI as an 1xN splitter with its most commonly applied design parameters, the straight optical waveguides' loss were determined, followed by the bending loss and MMI devices' loss. In order to measure the waveguides' optical propagation loss, the Fabry Perot measurement method was employed. Most of the measurement methods are difficult to apply because they require a very careful alignment of the samples in the optical benches, and good accuracy and repeatability is necessary. Besides, the measurements to be taken are usually greatly dependent on the reflections from the interfaces between the waveguides and the input and/or output media (often air). These effects are particularly pronounced for semiconductor waveguides, because of their high refractive indices (typically approximately 3.2). Consequently, for the InP based material system, the Fabry-Perot (FP) method is used to characterize the straight waveguides and the MMI device.

All the waveguides have been fabricated with high ridge etch which can ensure smaller MMI devices. The performance data of the 1x2, 1x3, 1x4, 1x6 and 1x8 type MMI is also delivered in this chapter.

3.1 Design of 1xN Power Splitters

A splitter is defined by the power split ratio P_b:P_c, where P_b represents the output power at the bar port, also known as the direct arm output, and P_c denotes the output power at the cross port. Generally, this ratio can be arbitrary, such as 15:85 or 30:70. Unlike a directional coupler (DC), the MMI-based coupler incurs some loss for an arbitrary split ratio other than 0:100, 100:0 and 50:50. It is, however, more robust and easier to fabricate, and thus is commonly used instead of DC to provide power coupling. For example, it has been integrated with a ring resonator to couple a small percentage of power from the bus waveguide to the resonator [1].

Such splitters are based on the general interference mechanism, where the lateral position of the input port and those of the output ports, as well as the MMI length and width, all affect the optimum splitting ratios. The cross-section of the access waveguides (AWs) for the MMI splitter along with its dimension and refractive indices are indicated in Fig. 3.1.1(b). The cross section for the MMI devices simulated also shared similar dimensions and refractive indices except for the width (i.e. W_1 is replaced with W_{MMI}). The device parameters that affect the end results are shown in Fig. 3.1.1(b). Although a few reports [2-4] have shown methods to obtain approximate lengths for these different splitting ratios, simulations that utilize the finite difference and beam propagation methods are needed to obtain the exact designs for the desired ratios. The example of 15:85 ratio 1x2 power splitter is shown in Fig. 3.1.1(c). Simulations of various MMI lengths have been combined in order to plot the power response from the output ports and illustrate how much power is lost when the MMI length changes. In this design study, the access waveguides' width (W1-W3) are all set at 1.7μm as the effective indices of TE and TM modes at this width are found to be quite close. The 15:85 ratio for both polarization cases occurred at a length of 75μm and 78μm, respectively. The 70-85μm range in the figure was selected because both polarizations lay between this range. One of the factors that need to be taken into consideration when designing these splitters is the internal power loss. The TM mode is found to experience a 2.5% loss whereas the TE mode power loss is higher at 5.9%. These power loss

values will differ for different MMI designs and placement of the output ports. In general, loss increases for smaller access waveguide widths. Although the splitting ratios repeat at periodic distances, the first image (M=1) should always be taken to minimize loss.

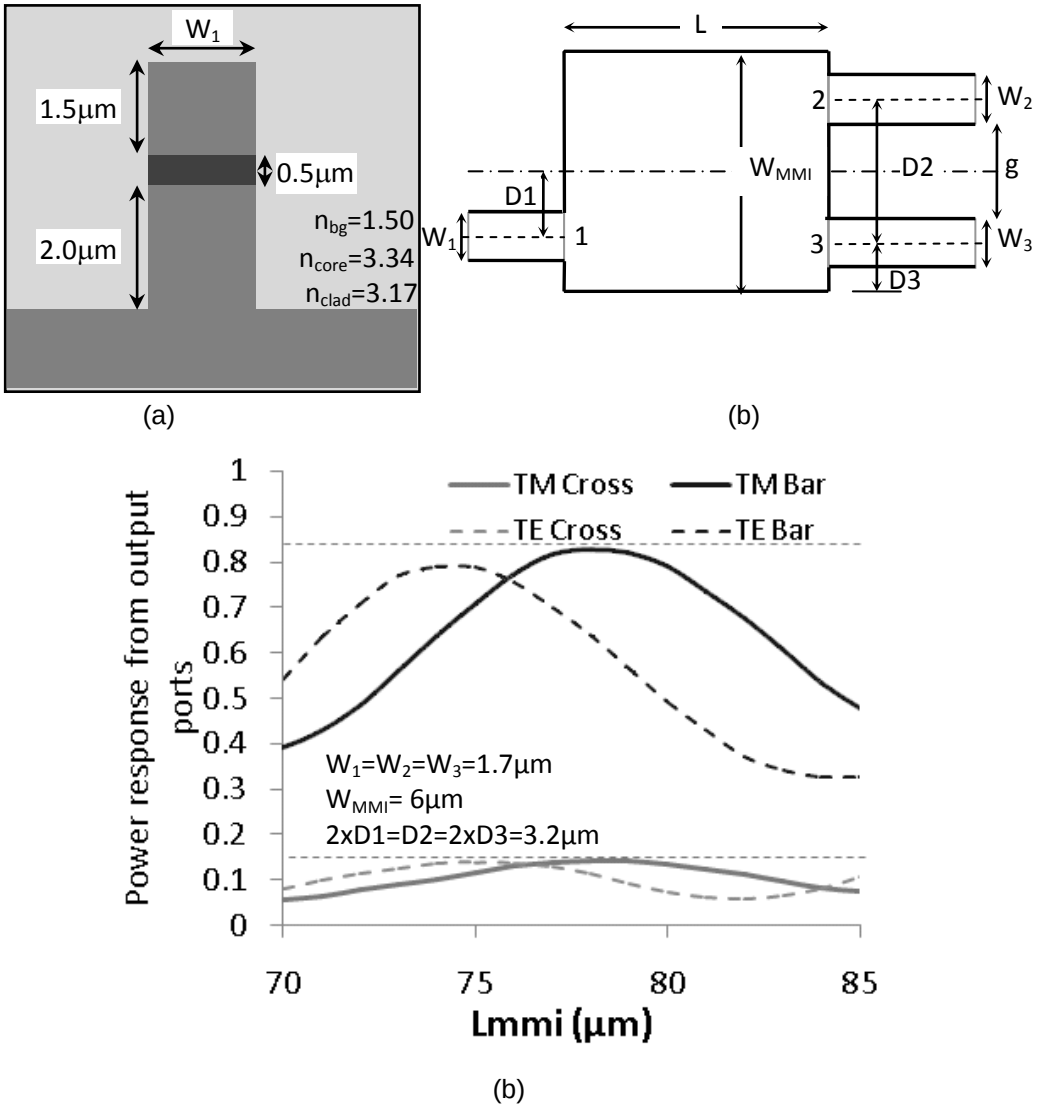

Fig.3.1.1. (a) Refractive indices and cross-section of the MMI devices' AW; (b)Device parameters that were manipulated to obtain the desired splitting ratios; (c) Simulation results for a 15:85 split ratio MMI device. The figure shows the normalized output result for MMI with different lengths.

A more widely applied splitter is the uniform 1xN splitter, where the input power is split equally among the N output ports. This is the type of splitter which all our designs are based upon. This type of splitter is based on the symmetric mechanism, where the input is launched at the centre of the MMI,

and would provide the shortest possible MMI length. The N self-images are generated at the shortest distance of $3\mathbf{L}_\pi / 4N$, where $\boldsymbol{L}_\pi$ is given by Eq. (2.6). The port or AW widths are denoted as *W* and the port pitch, *D*, is the distance between the centre of one output port to the next. The output ports are arranged in equal distance, $D=W_{MMI}/N$, from one another, and the distance from the edge of one side of the MMI to the centre of the edge output port should be half of the port pitch or $W_{MMI}/(2N)$. We have designed equal 1xN splitters where N = 2, 3, 4 and 8. Table 3.1 tabulates some of the design parameters used.

TABLE 3.1: Design parameters for 1xN splitter

N	W	D	W_{MMI}	n_0	n_1	$\mathbf{L}_\pi$	L_{MMI}	Simulated L_{MMI}
2	3	6	12	3.282597	3.280696	407.7	152.9	152
3	3	6	18	3.282949	3.282103	916.1	229.0	229
4	4	8	32	3.283142	3.282874	2891.8	542.2	543
8	4	8	64	3.283231	3.283142	8707.9	816.3	1089

The design of the different splitters involves (1) setting of the AW and MMI widths based on the number of splitting desired, (2) obtaining effective indices of fundamental and first order modes of the MMI waveguide (width) to calculate the relevant L_π (using equation (2.6)) and subsequently determining MMI length using the $3L_\pi / N$ formula. This was then followed by (4) a BPM simulation to confirm the MMI length as Fig. 3.1.2(a) and (b) showed. This step is necessary because as the MMI width increases, the estimation of $\boldsymbol{L}_\pi$ based on equation (2.6) becomes less accurate due the increased number of ports (*N*). In the cases where the designs were to be fabricated, (5) decisions on the lengths to be extended or reduced (to cater for fabrication tolerances) were made, and (6) S-bend extensions to waveguide for easier visibility during measurement were added as shown in Fig. 3.1.2(c) and (d).

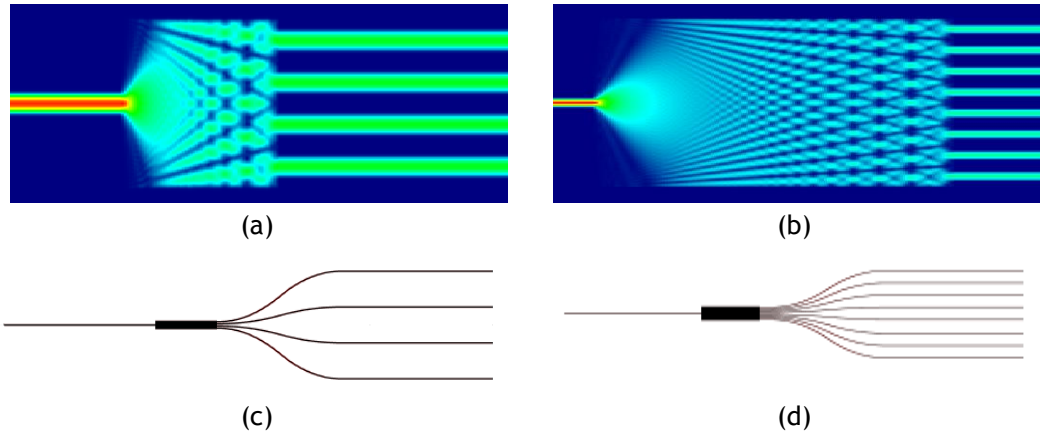

Fig.3.1.2. Simulation of designed (a) 1x4 and (b) 1x8 MMI power splitter and (a) 1x4 and (b) 1x8 MMI device with S-bend extensions used in fabrication.

A problem often faced is the existence of higher order modes if a wider access waveguide (AW) is used. If higher order modes are guided into the MMI, the MMI results would also deviate from the $3L_{\pi}/N$ length as been previously reported [5]. Although the best solution would be to utilize narrower AWs, fabrication complications like photolithography tolerances could complicate this. The higher order modes, usually the TE_{01} first order mode, can be excited at the input waveguides due to small deviations from the optimal alignment and will only be lost after an appreciable distance from the input. When AWs are not single mode, unbalanced measurements of as much as 30% at TE outputs could be occur [6].

In order to determine the best access waveguide width within our fabrication capabilities which would not degrade PIC performance, straight waveguides of various widths were fabricated, its propagation loss determined and existence of higher order modes, if any, identified. The Fabry-Perot method for characterization has been opted to calculate the propagation loss.

3.2 Fabrication of 1xN MMI splitters

The samples in this chapter were fabricated in Nanyang Technological University's (NTU's) clean room labs. The waveguides and 1xN splitters which were fabricated were based on the InP substrate. The layer structure of the waveguides is shown in Table 3.2.

TABLE 3.2: Layer structure of waveguides and MMI splitters

Layer Number	Material	Thickness (nm)	Doping	Refractive Index
3	InP	1500	P ($3x10^{16}$)	3.17
2	InGaAsP (λ=1.35μm)	400	-	3.41
1	InP	3000	N($3x10^{16}$)	3.17
	InP substrate	350000	N(~$1x10^{18}$)	3.17

These layers were grown epitaxically using metal-organic chemical vapor deposition (MOCVD). Epitaxy is defined as the deposition of some material layers on a substrate, all having similar single crystal lattice structure. The lattice constant of the layers and the substrate must be closely matched, and this is denoted as 'lattice-matched'. The core (InGaAsP) and cladding (InP) indices of the structure is also given in the similar table. In all of our III-V waveguides, the core indices were designed to be higher than that of the claddings to provide sufficient light confinement. In order to create strongly guided waveguides where the core level is etched through, the etch depth was set around the range of 3μm to 4μm. Before actual 1xN MMI splitters were fabricated, 3, 4, 5 and 8μm wide straight ridge waveguides were designed and the UV-masks made for the fabrication to be carried out in order to test the limitation of the fabrication capabilities of our fabrication machines. The UV-masks' designs were drawn using the L-Edit software before they were sent to commercial mask makers to be made. The mask design preparation included design details, simulations to confirm the design, space allotment of masks made, adding tapering and S-curves to the AWs and numbering each 1xN splitter for easier identification. The fabrication process for straight waveguide and 1xN MMI splitter were similar. Only the UV-masks used were different.

The fabrication of these III-V waveguides involved 5 major fabrication process steps, as shown in Fig. 3.2.1. These fabrication steps utilize processing procedures which are in large part similar to that of microelectronic devices would also be used in subsequent fabrication processes.

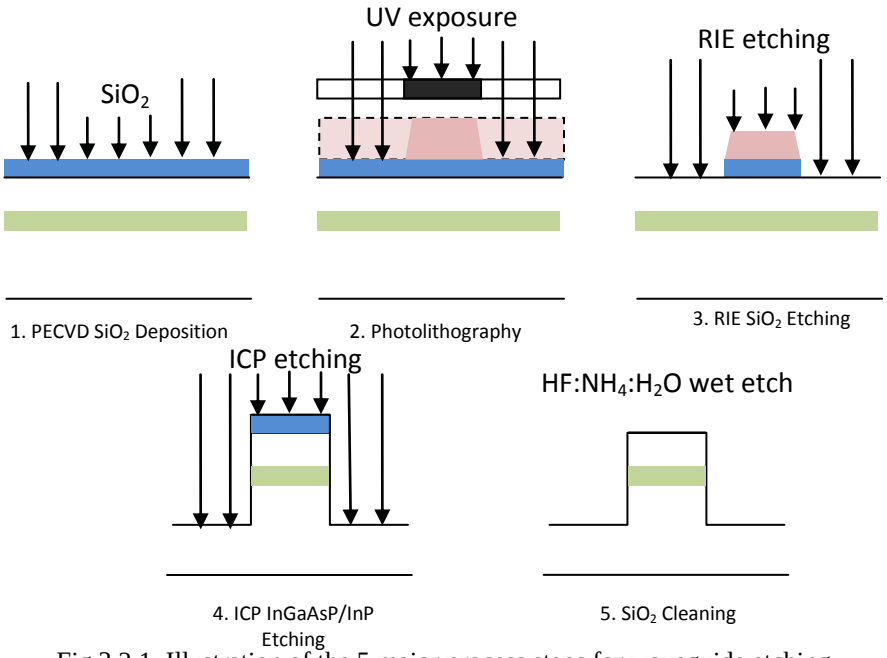

Fig.3.2.1. Illustration of the 5 major process steps for waveguide etching

In most fabrication, the dielectric thin film deposition is usually the first step. The dielectric film is preferred as the etch mask for the subsequent dry-etching process – reactive ion etching (RIE) and inductively coupled plasma (ICP) etching - due to its relatively high thermal stability and strong etch resistance as compared to other types of etch mask, such as metal and photoresist. The SiO_2 dielectric deposition for our process is achieved using the plasma-enhanced chemical vapor deposition (PECVD) machine. The PECVD machine used is the Unaxis Neutral D2000. The PECVD process deposits thin films from a gas state (vapor) to a solid state on the wafer sample. Chemical reactions occur between these reacting gases after the ignition of plasma from the gas mixture. The deposition rate at 50 degrees Celsius is approximately 140nm/min. The source gases used are silane (SiH_4) and nitrous oxide (N_2O). As silane is highly pyrophoric (ignite spontaneously), the process and safety precautions have to be followed closely. The 300nm of SiO_2 is deposited on top of the samples and patterned by photolithography and RIE, which are the second and third process steps respectively.

Photolithography is a patterning process where the device pattern on a glass photomask is transferred onto a photoresist layer above the SiO_2 film. Photoresists are sensitive to UV light, and once exposed, will become soluble in a certain solvent known as the developer. The photoresist used is the AZ-5214e

positive photoresist. For the spin coating process, we used the CEC Model 100 spincoater, set at 4krpm for 30 seconds. After spin coating this photoresist onto the samples and dry-baking it, they are exposed to the UV-rays using a Karl Suss MJB4 mask aligner. We utilized hard-contact (1.5mbar force) mode in order to ensure good patterning result from the 340nm UV light exposure. After exposing the sample for 15~20s, it is placed in the developing solution. The developing time depends on the spin coated layer thickness and UV exposure time. After developing, the patterned photoresist can now be used as the etch mask for etching the SiO_2. It is crucial to obtain the right exposure and developing time as over exposure would cause waveguide broadening and over developing would result in rough photoresist side wall and peeling of photoresist in severe cases.

In the third process, the RIE system used is Oxford Plasmalab 80 Plus. The RIE is used to etch away the exposed SiO_2. The etch rate of the SiO_2 has to be tuned in such a way that it is higher than the etch rate of the photoresist in order for the etch mask to sustain its function until the SiO_2 which needs to be removed is completely etched away. The primary etchant for the SiO_2 is tetrafluoromethane (CF_4) gas, with a small amount of oxygen (O_2) added to remove the polymer formed on the etched sidewall during the etching process. For our RIE process, the RF power used is 150W with 50mTorr of pressure. The CF_4 and O_2 volume used are 70sccm and 5sccm respectively. The SiO_2 etch rate is about 40nm/min whereas for the photoresist is about 30nm/min.

After the SiO_2 etching is done and the photoresist is removed using acetone, leaving only SiO_2 pattern on the sample surface, the fourth process step which uses the ICP machines is performed. When it comes to plasma etching (dry etching) and wet etching (etching using acid), the main concern would be the etching recipe, the etch rate, the etching time and last but not least, the crystal alignment. The latter is more important with regards to etching. Dry etching gives a more vertical or anisotropic etching compared to wet etching, which tends to be much more isotropic. However, wet etching has the advantage of producing much better (smoother) surface finish. One way to take advantage of both is to utilize dry etching first followed by a shorter wet etching. This would produce an anisotropic etch with smoother sidewalls. In our

case, we have optimized our ICP etching recipe in a way which is sufficient to make do without the wet etching finish.

In our optimized recipe, Cl_2 gas which promotes faster etching and N_2 gas which produces lesser surface damage as compared to argon due to its smaller Z number is used. More details on the optimization of this process step which have been accomplished by our group can be found in ref. [7]. In the waveguide definition process, RF and ICP power are set at 125W and 700W respectively, and the process pressure is maintained at 4mTorr. The Cl_2:N_2 ratio found to give the optimum balance between surface finish and etch rate is 10:5 sccm. The etch rate is about 2μm/min with a high selectivity against oxide of 55:1.

After the ICP etching process, the remaining SiO_2 is cleansed away using HF acid. The 1:2:3 mix ratio of HF, NH_4F and H_2O was utilized, giving us the etch rate of about 80nm/min. When a sample was fabricated very well, another SiO_2 layer is deposited to protect the waveguides which had been fabricated.

The devices on the relatively large pieces of cut wafer (~1cm^2) are then 'lapped' to thin them down to a thickness of 100-150μm so that easier cleaving could be done. The 'lapping' process is optionally a machine or manual process which involves tools which are used with the polishing machine. In the case of InP substrates which are relatively less hard than other materials, we opted for hand-polishing. The process involves cleaning and heating mounting blocks (cylindrical blocks of aluminum or metal) up to 110°C for ~15minutes so that the blocks are hot enough to melt the thermal wax (QuickStick™ 135 Mounting Wax) which is applied on top of the blocks. A piece of fabricated wafer sample is then gently placed (face down) on the wax and tap down gently. The block is then cooled until the wax is hardened. We then mix small spoonfuls of 9μm sized aluminium oxide (Al_2O_3) powder with water on a piece of thick glass surface to polish (or sand off) the exposed side of the wafer. The mounting block gives us a better and even grip on the sample. The lapping is done in small figure-of-eight movements of the arm or wrist. The block height (with sample) is measured at minute's interval to gauge the thickness of the remaining wafer. When the wafer is sufficiently thinned, and residue paste cleaned, the

mounting block is reheated until the wax is soft and fluid enough for the sample to be gently pushed away from the block using a cotton bud. The sample is then treated to an acetone bath to wash away any residue wax and dirt. After the lapping process, the thinned samples are cleaved using diamond cutter or surgical blade.

3.3 Fabry-Perot method for characterization

The propagation loss of straight waveguides can be determined either by the Fabry Perot (FP) resonance method or the sequential-cleaving (or cut-back) method. When the refractive index of a waveguide is sufficiently larger than air, the optical waveguide forms a good FP resonator, where the mirrors are formed by the cleaved waveguide end facets. When the multiple reflections at the air-waveguide interfaces are considered, the relative transmission, T of a symmetrical single-mode FP waveguide resonator, which is also known as the Etalon transmission formula, is given by

$$T = \frac{I_T}{I_o} = \frac{A_t A_t^*}{A_{in} A_{in}^*} = \frac{(1-R)^2 A}{(1-RA)^2 + 4RA\sin^2(\delta/2)} \tag{3.1}$$

where $A_t = \frac{T\sqrt{A}}{1-RAe^{i\delta}} A_{in}$ and $A_t^* = \frac{T\sqrt{A}}{1-RAe^{-i\delta}} A_{in}^*$, A_t being the transmitted field amplitude and A_{in} the incident field amplitude; $R = r^2$, where r is the reflectivity of the end facet, and R is the reflectance for the guided mode; $A = \exp(-\alpha L)$ is the amplitude transmission factor *per pass*, where α is the propagation loss coefficient and L is the length of the waveguide; finally $\delta = \frac{2\pi}{\lambda} n_{eff}(2L)$ is the round trip phase shift, where n_{eff} is the effective index. Equation (3.1) can be further simplified as

$$\frac{I_T}{I_o} = \frac{t_{\max}}{1 + F\sin^2(\delta/2)} \tag{3.2}$$

where $t_{\max} = \frac{(1-R)^2 A}{(1-RA)^2}$ and $F = \frac{4RA}{(1-RA)^2}$

The T_{max} and T_{min} in a typical interference patterns obtained using the FP technique (see Fig.3.3.1.) can then be defined as $T_{max} = t_{max}$ and $T_{min} = \frac{t_{max}}{1+F}$. The contrast of the transmission oscillations is given by

$$K \equiv \frac{T_{max} - T_{min}}{T_{max} + T_{min}} \qquad (3.3)$$

K can be rewritten as:

$$K = \frac{F}{F+2} = \frac{2RA}{1+(RA)^2} \qquad (3.4)$$

Solving for RA using equation (3.4), $(RA)^2 - \frac{2}{K}(RA) + 1 = 0$ and thus $RA = \frac{1 \pm \sqrt{1-K^2}}{K}$. To obtain the propagation loss α, $A = \exp(-\alpha L)$ is substituted into the equation above, which gives

$$\alpha L = \ln R - \ln\left(\frac{1 \pm \sqrt{1-K^2}}{K}\right) \qquad (3.5)$$

and α [in dB/mm] is then

$$\alpha[dB/mm] = \frac{4.34}{L}\left[\ln R - \ln\left(\frac{1 \pm \sqrt{1-K^2}}{K}\right)\right] \qquad (3.6)$$

where L is expressed in *mm*.

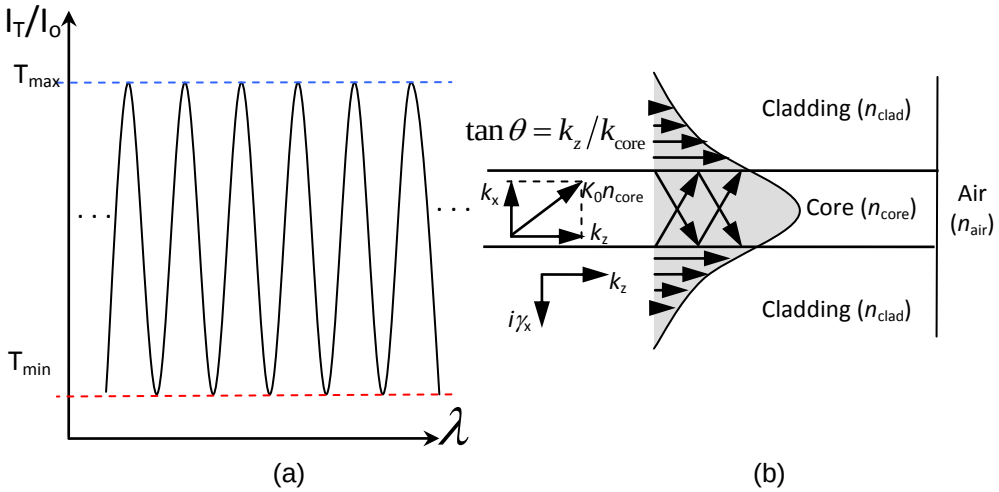

Fig.3.3.1. (a) Possible FP patterns observed in experiment and (b) Illustration of the fundamental eigenmode for a slab waveguide

The loss can be determined only if the reflection R is known, and the uncertainty depends on how R is determined. The reflection at an interface

between medium 1 and medium 2 is calculated by $R=[(k_{Z2}-k_{Z1})/(k_{Z2}+k_{Z1})]^2$, where $k_Z = k_0 \cos\theta$ is the longitudinal wave vector in a medium, and k_0 = $(2\pi/\lambda)n$. For simplicity we first consider a dielectric slab waveguide, for which the eigenmode, shown in Fig.3.2.1(b) consists of a core field propagating by total internal reflection at an angle given by $\cos\theta_{core} = n_{eff} / n_{core}$, (n_{eff} is the effective index and n_{core} is the core refractive index) and an evanescent cladding field propagating longitudinally with the same wavevector k_z (hence has the same effective index). It follows that the reflection at the waveguide-air interface will be different at the core and the cladding. At the core the reflection is angle-dependent and is given by $R_{\text{core}} = |r_{\text{core}}|^2$, where

$$r_{core} = \frac{1-\sqrt{1-(n_{core}^2-1)/n_{eff}^2}}{1+\sqrt{1-(n_{core}^2-1)/n_{eff}^2}} \qquad (3.7)$$

In the cladding, the reflection $R_{\text{clad}} = |r_{\text{clad}}|^2$ is normal incident and thus can be resolved with

$$r_{clad} = \frac{(n_{eff}-1)}{(n_{eff}+1)} \qquad (3.8)$$

If the confinement factor in the core is G, then the total reflectivity is

$$R = Gr_{core}^2 + (1-G)r_{clad}^2 \qquad (3.9)$$

The confinement factor is itself related to n_{eff} approximately by n_{eff} = $Gn_{\text{core}}+(1-G)n_{\text{clad}}$. Thus, G can be expressed as G = ($n_{\text{eff}} - n_{\text{cl}}$) / ($n_{\text{core}} - n_{\text{cl}}$). However, Eq. (3.9) would be more suitable in the case of a well confined waveguide with a thick core and strongly guiding narrower width where G~0.7. The effective index here can be obtained from finite difference (FD) numerical simulations using Apollo's APSS software. We can use this relation, as well as equations (3.8) and (3.9) to deduce R.

It is more convenient to assume that the reflection of light in a waveguide is from a waveguide-air interface as approximately given by Eq. (3.7) because this equation is valid for normal incidence and is a good approximation for weakly guiding waveguides having large mode areas compared to the optical wavelength.

3.4 Measuring InGaAsP/InP straight optical waveguides

The loss measurements were performed on 3, 4, 5 and 8μm wide straight waveguides and the FP resonance patterns were recorded for each waveguides from three samples of varying lengths. The measurement and characterization of the waveguides were undertaken in one of the Photonics Labs with a fiber-to-device-to-free space setup.

An illustration of the waveguide setup is shown in Fig. 3.4.1. A Santec tunable laser with wavelength between 1530-1610nm with fiber output was coupled into the cleaved facet of a waveguide. An infrared polarizer was used to control the input state of polarization (TE) and (TM) before the laser light was launched into the waveguide. For earlier parts of the characterization, cleaved fibers were used and much light was lost due to unwanted coupling into the substrate. Using cleaved input fibers, coupling into samples was low and visibilities of modes were poor for waveguides with widths smaller than 5μm. Once the cleaved fiber was replaced by a tapered fiber, better coupling of light into the waveguides have been obtained.

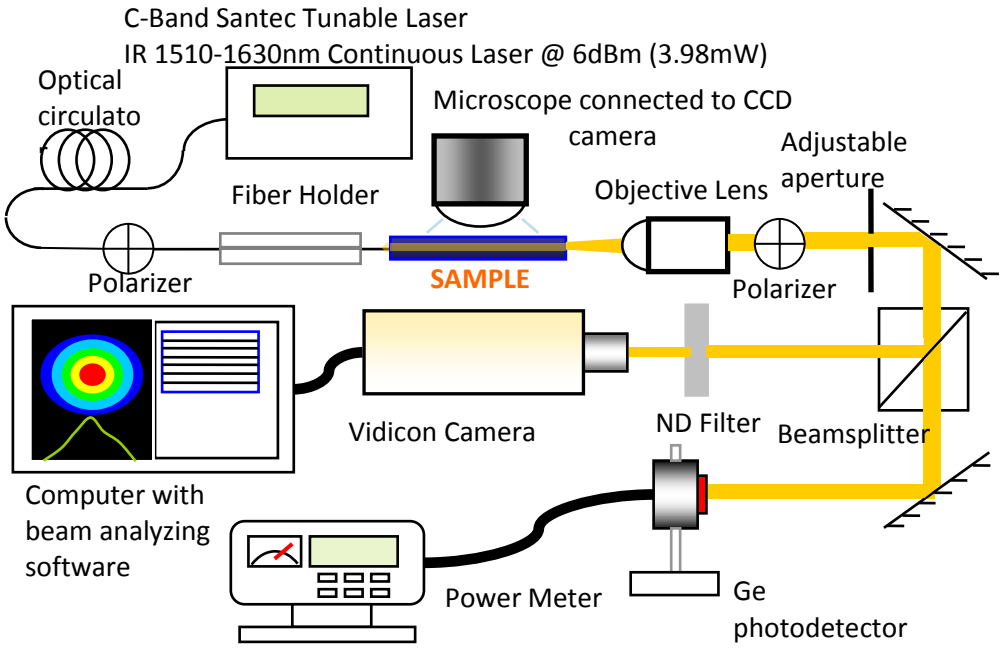

Fig.3.4.1. Waveguide measurement setup

The guided optical field pattern at the cleaved output facet was displayed on the Coherent Beamview Analyzer software by use of an objective lens and a Coherent Micron viewer Model 7290A Vidicon Camera placed about 155cm away from the objective lens. The Ge photodetector connected to a Newport Model 1930C Power Meter also detects the power output from the waveguide via a beam splitter placed between the objective lens and vidicon camera. An adjustable aperture was placed before the beam splitter to eliminate scattered light. The Ge photodetector was used to measure output intensity. The observed near-field pattern indicated whether a single-mode was observed and whether there were other higher order modes present.

The fiber-to-device-to-free-space setup used for the conducted measurements was inherently lossy due to the many components in the setup. There was a 5dB loss after the light passes through the optical circulator and connectors, another 0.8dB lost when it passes through a fiber→free-space→fiber polarizer and ~5dB loss from the polarizer's connector to the tapered fiber's output. The objective lens and polarizer which collects the light that exits the waveguides also experiences ~1dB of loss. Finally, the beamsplitter halves the output and absorbs some light as well, thus averaging a total of 19±1.0dB loss for the entire setup for the range of 0.03mW up to 15mW (input power).

In Fig.3.4.2 the brightest and dimmest TE polarization modes obtained while the FP resonance is being collected is shown. These images were captured using the infrared camera. An advantage of a fiber-to-device-to-free-space was that it provided a better picture of the data being collected. With the more common fiber-to-device-to-fiber configuration, it would not have been be possible to visually view the modes or filter out stray lights that would have affected the measurement of the actual light that was propagating through the waveguide.

The output was collected as a function of the input wavelength (sweeping/scanning the laser from 1547nm to 1553nm) using a LabView software which has been created to interact and collect data from the Newport Model 1930C Power Meter which is connected to the Ge photodetector. Fig.

3.4.2 also shows that the first order TE modes do appear for waveguide of 8μm width. Therefore, during measurement, the slightest change of fiber angle (misalignment) and position would excite this mode instead. The effect on FP transmission is easily identified with the appearance of an additional shorter peak in the overall intensity results collected. Although based on the BPM simulations, higher order modes are evident at 3μm waveguides; no apparent higher modes were visible when the waveguides were measured. We believe that these narrower waveguides' higher order modes are lost quickly due to a few loss mechanisms. The main factor would be that the narrower waveguides would be more sensitive to the rough side walls of the narrow waveguides. The high index contrast between the material and the background also causes the sidewall effect to be more significant, and especially so for higher order modes. The substrate leakage loss is also be higher for narrower waveguides. The sensitivity of the infra-red camera also plays a role. The more radiative higher order modes would be too weak for the camera to detect.

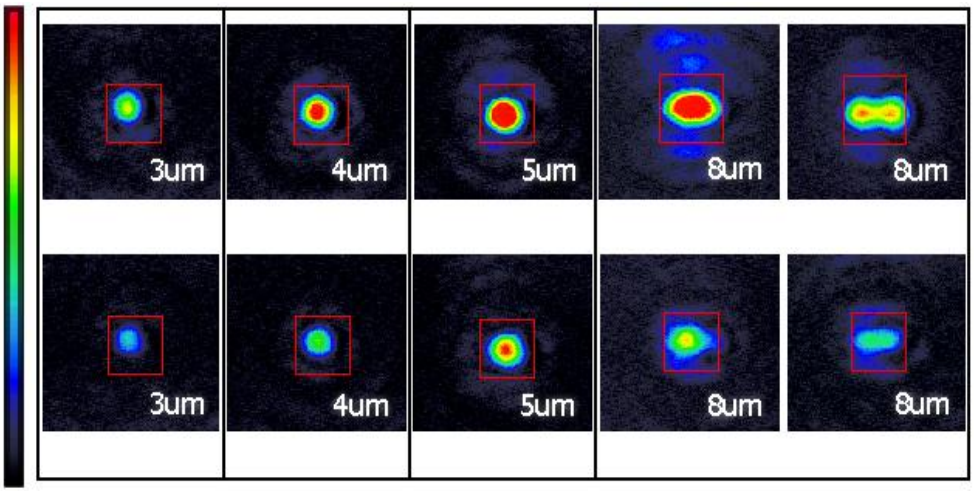

Fig.3.4.2. Images of modes captured using the vidicon camera. Top row shows captures of modes at brighter resonance and lower row shows captures of modes at dimmer resonance. For 8μm, higher order modes were easily excited and captured.

Representative interference patterns for the waveguides are shown in Fig. 3.4.3. Complications which had been encountered included jerky or jagged results caused by the use of unsuitable wavelength step size (different tunable laser wavelength sweep speed while maintaining constant data acquisition speed) and unstable lenses. The transmission patterns were collected only after the problems had been resolved.

Fig. 3.4.3 plots the measured transmission against wavelength for the four waveguides with the length, *L*, of 0.73mm. The input light is 1mW with TE and TM polarization. The fiber-to-device-to-free-space optical insertion loss (excluding the measurement setup's inherent loss) is 10±1.0dB. Smaller insertion loss could be obtained by more accurate cleaving and AR coating at the facets. Based on the effective index, n_{eff} simulated from Apollo Software for the 0.3μm thick InGaAsP core cladded with InP 3μm deep etch, the *R* can be extracted from Eq. (3.8). Due to the thin core thickness (400nm), a poor confinement factor in the core (G~0.19-0.25) was obtained and this resulted in a larger mode area which covers a wider cladding surface ratio in relative to the core, which is the reason why Eq. (3.8) would be more suited for propagation loss estimation.

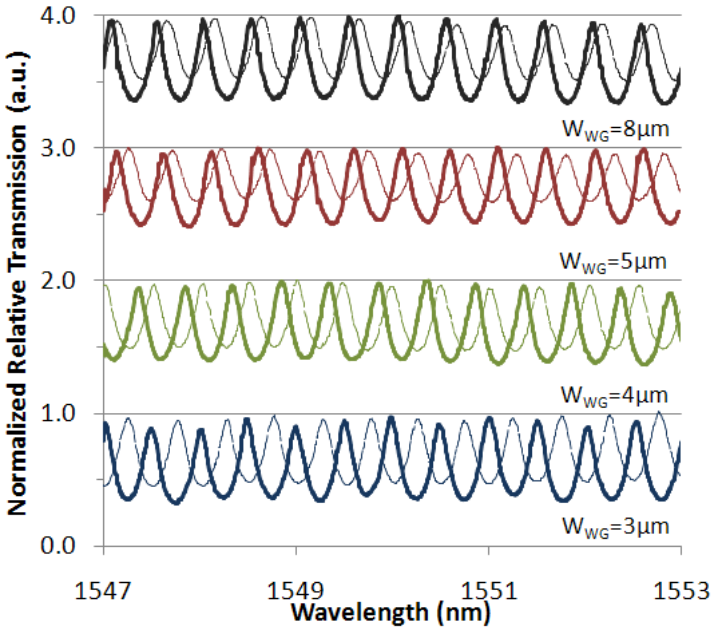

Fig. 3.4.3. Normalized transmission power for the FP resonance with waveguide widths of 3, 4, 5 and 8μm and length, L=0.66mm, as a function of wavelength. The bold lines are for TE polarization and the thin detached lines are for TM polarization

The lowest measured propagation loss α, for 8μm is at ~ 0.6dB/mm for TE polarization and 2.4dB/mm for TM polarization as calculated from the FP resonance and equations in Section 3.3. The propagation losses of the other 3 waveguide widths have been plotted in Fig. 3.4.4. The measurements clearly indicated that TM polarization suffered more loss than TE polarization. This owes to the fact that the material structure was based on a thin core. The TE

mode, which is confined at both ends with air (refractive index = 1.0) and with a minimum core width of 3µm, is less lossy than the TM mode, which is perpendicular to the core width and parallel to the cleaved facet. The effective indices of the TE mode waveguides are always higher than that of the TM mode, for all four waveguide widths used. Higher effective indices translate to better confined modes. This is one of the main reasons why TE polarization is less lossy compared to the TM polarization. The TM mode is confined with InP material with the refractive index of ~3.17. This index value is much closer to that of the core refractive index (~3.41) and with the InGaAsP core merely 0.4µm thick is therefore relatively poorly confined by the core and more easily dissipates through the InP cladding. Therefore, as it propagates along a waveguide of indefinite length, its propensity to have higher loss than the TE mode due to substrate leakage is also expected.

As for the increasing loss as the waveguide widths reduced, this is also often expected as the sidewall effect due to the high index contrast and the sidewall roughness will become more significant for narrower waveguides. Furthermore, the substrate leakage loss will be higher for narrower waveguide. Based on the layer structure shown in Table 3.2, the waveguide loss is also expected to be high due to the free-carrier loss since the cladding layers are heavily doped. Although these results are not the best reported, they indicate that the fabricated ridge waveguides behaves consistently with the overall trend found in the literature.

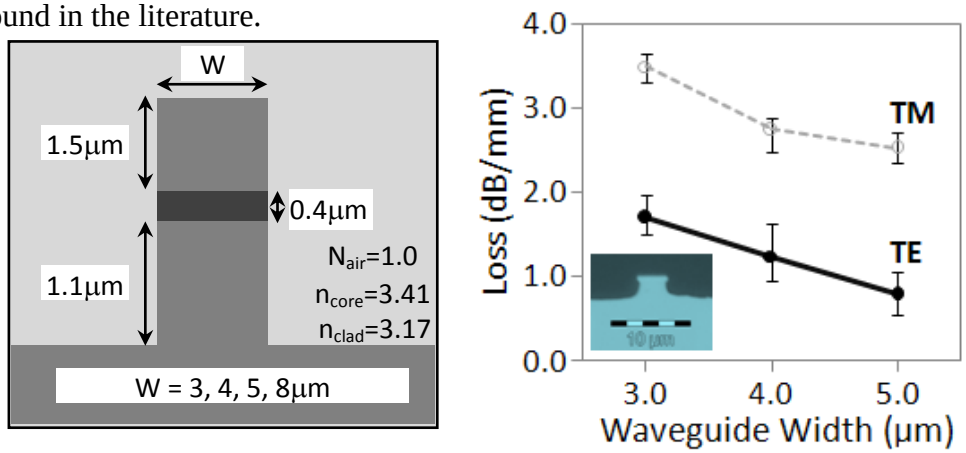

(a) (b)

Fig.3.4.4. (a) Refractive indices and cross-section of the straight waveguides; (b) Propagation loss, α result for 3, 4 and 5µm wide waveguides. TE polarization is represented with filled marker and bold line while TM polarization propagation loss is marked with unfilled marker and connected with a detached line. Inset shows a microscope capture of the cleaved facet of a 4µm wide waveguide.

Although fiber coupling to wider waveguides is much easier, waveguides of 8μm width tend to retain its higher order modes for a long distance and this could affect our 1xN MMI devices. Therefore, based on the results on Fig. 3.3.4, designs of 1xN MMIs using AWs widths of 3 and 4μm have been chosen. Even though theoretically these too are multi-mode waveguides, in practice the higher modes were not excited and did not increase the total propagation loss.

3.5 Characterization of 1xN MMI splitters

With the AWs set as either 3μm or 4μm, four types of 1xN MMIs, namely the 1x2, 1x3, 1x4 and 1x8 MMIs were designed and fabricated. The MMI dimensions followed those tabulated in Table 3.1 with additional ±10μm variations for fabrication tolerance. Splitters can be characterized by a few parameters. One of these would be its insertion loss. The insertion loss is the sum of its splitting and excess loss. Splitting loss is defined as $-10\log\frac{1}{N}$ where N is the number of splits. Excess loss is defined as $-10\log\frac{P_{In}}{P_{Out}}$ where P_{In} is the input power and P_{Out} is the summation of all the output power.

3.5.1 1x2 MMI

The 1x2 MMI (also known as 3dB MMI splitter) had the combined length of 1580μm. This length is made up of 5 segments: an input AW (L_{in}), the length of the MMI itself (L_{MMI}), a 5μm straight AW output from the MMI (L_{out}) before the 600μm long S-shaped transition AWs (L_{bend}) and straight AWs (L_{end}) before the dicing segment. The illustration of the device is shown in Fig. 3.4.1(a). The input, output and end segments are all straight waveguides with the width of 3μm and their propagation loss has been found in the previous section to be ~1.25dB/mm for TE polarization. These are grouped as one

portion. The S-shaped curves are 600µm long with a 25µm wide bend offset and this makes up the second portion of the device. Although bending waveguides are often associated with higher loss, the inherent properties of strongly guiding ridge waveguides allow for much smaller radius bends with negligible loss difference. The calculated radius of the S-shaped bends, based on the curve length (which is a few hundred times longer than the width offset) is approximately r~3606µm, which is relatively large, thus ensuring negligible difference from a straight waveguide. Therefore, the propagation loss of the S-shaped portion can also be assumed to be the same as the first portion (~1.25dB/mm). The total actual length of the S-bend portion (where θ=2.3859˚) would be $2\times\frac{\theta}{360^\circ}\times 2\pi r = 600.69\mu m$ which is nearly similar to L_{bend} (600µm). The 152±10µm long MMI which splits the power into two makes up the third portion of this device.

The simulation result shown in Fig. 3.4.1(b) is obtained from the Apollo Software's BPM simulation where the output of A and B against varying wavelength is so identical, they overlapped each other through the range of 1510-1630nm so that only one line appears to be visible. $T_{(C)}$ -$T_{(A),(B)}$ (dB) is the insertion loss from Outputs A and B obtained by deducting the output from (A) or (B) in dBm with that of (C).

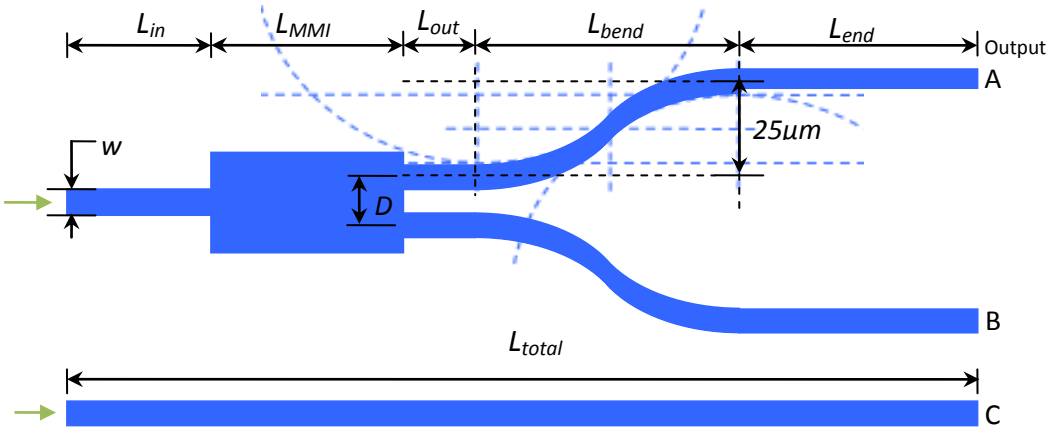

(a)

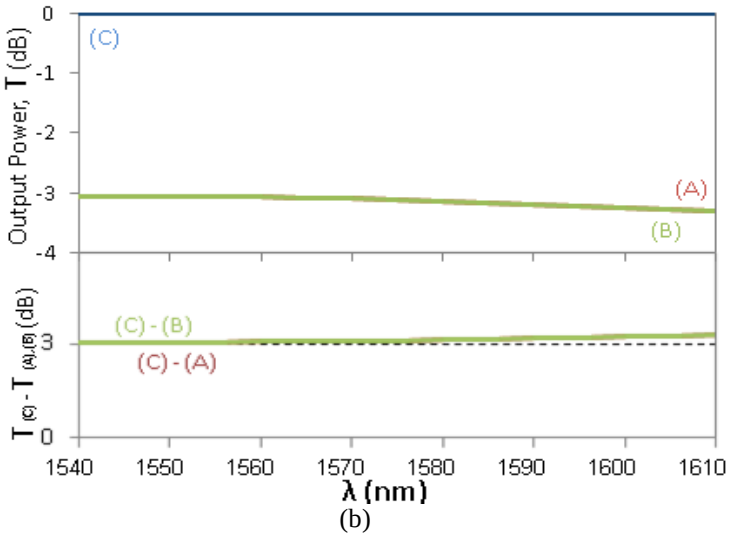

(b)

Fig.3.5.1. (a) Illustrations of a 1x2 MMI with S-shaped transition bends and a straight waveguide. Cross and Bar output of the 1x2 MMI is denoted as Output A and B respectively and the output from the straight waveguide is named Output C; (b) Simulation result of the expected output from A, B, C and T(C)-T(A),(B)

Fig. 3.5.2(a) shows the measured output power from the Outputs A, B and C of Fig. 3.4.1. The output power is plotted in dB (i.e., normalized to the incident power from the laser). Output C represents the output of the straight WG whereas A and B represent the outputs of the left and right arms of the 1x2 MMI device. Fig. 3.4.2(b) is the excess loss plot of the device obtained by taking the difference between that of the straight WG and each arm of the 1x2 splitter. In short, Output C is assumed to be the P_{In}. The power is measured for a range of 70nm from 1540nm to 1610nm. The measured results showed that ~3dB splitting occurred for a wavelength range of about 35nm where the excess loss is less than 1 dB. Inset shows an infrared capture of the output from both arms at ~1580nm. The tolerance for excess loss (i.e., variations from one output to another) which we have set is ±0.5dB.

The overlapping 3dB bandwidth is narrower than what simulations (ideal case) gave - the output from (A) and (B) deviates from one another at wavelengths away from the 1555-1600nm range. This deviation may have been caused by several factors, one of which would be that the photodetector, objective lens and polarizers in the measurement setup have a limited wavelength range, resulting in an ‘envelope’ of their own. These envelopes were then isolated by measuring the output from the fiber to the photodetector

sans the waveguide and further normalizing the result. The unimproved outcome reveals that the limitation in bandwidth is most likely caused by the higher absorption of power by the waveguide material at wavelength beyond its range which simulations have not accounted for. Measurement results at wavelengths further away from this range is also less reliable due to coupling loss, which is why at larger/smaller wavelengths, we found that the summation of output power of both arms (A+B) could exceed that of the straight waveguide (C).

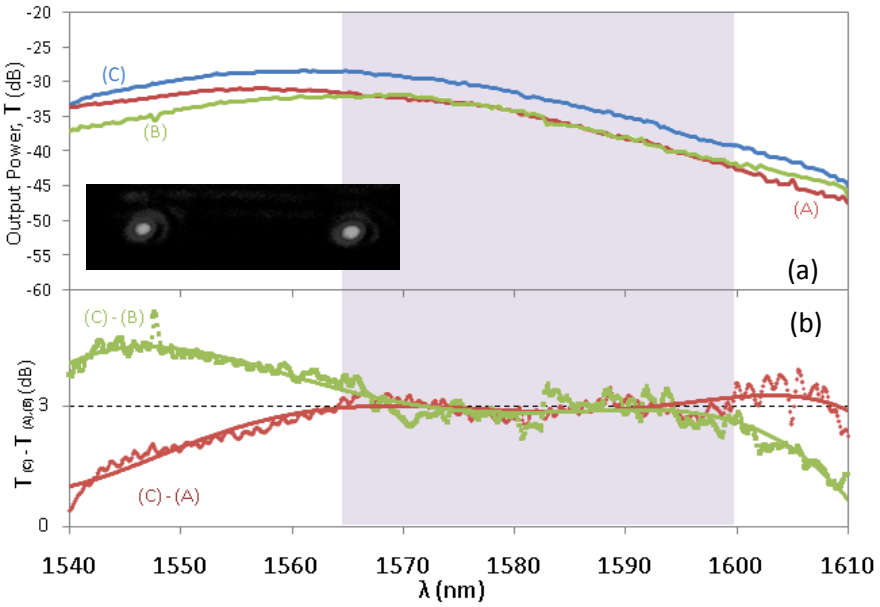

Fig.3.5.2. (a) The measured output power of Output arms A, B and C (not normalized), (b) Insertion loss, or normalized output arm results of A (left arm) and B (right arm). Inset is the output mode results capture using vidicon camera.

3.5.2 1x3 MMI

The 1x3 MMI had a combined total length of ~1570μm, which was quite similar to the 1x2 MMI previously tested, due to the similarity in the S-curve dimensions used. The output power of the 1x3 MMI device were obtained from the three output arms at the wavelength of 1560nm by coupling in an input power of -12dBm. Fig.3.4.3 shows the (a) fabricated device and (b) infrared capture of the modes collected. The S-shaped bend adopted here had a bend offset of 50μm to maintain a uniform output separation. Simulation results as shown in Fig. 3.4.3(c) indicated that MMI with odd numbers of output arms

would inherently result in relatively slightly higher output from the centre arm for the most part. The L and R output are similar and overlap each other.

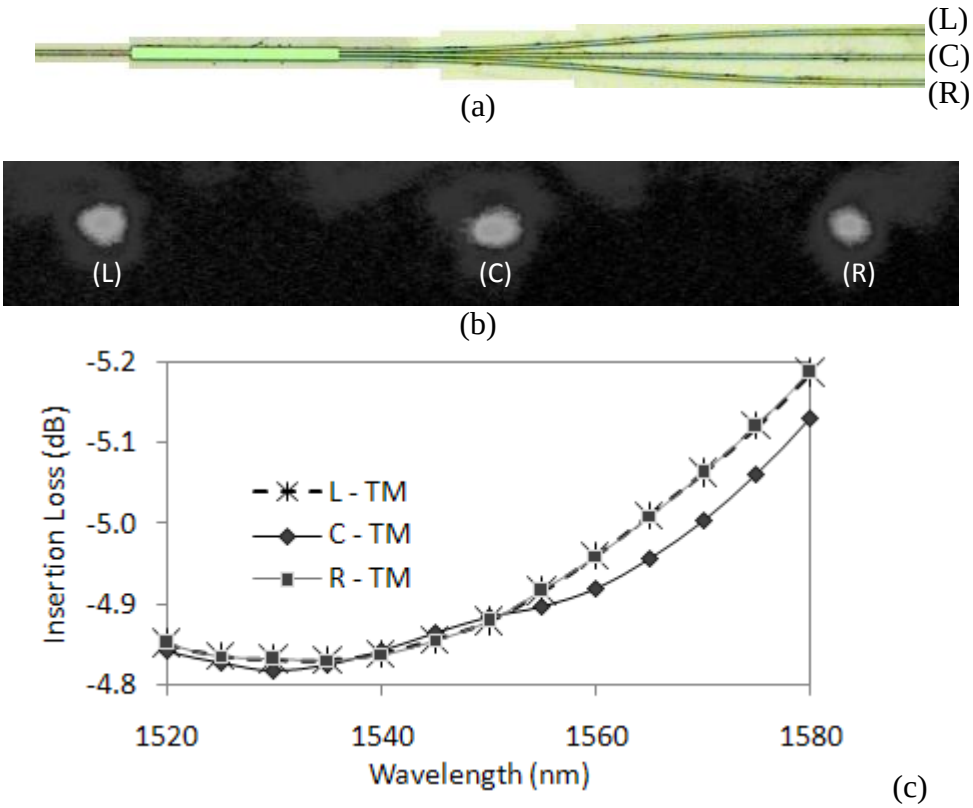

Fig.3.5.3. (a) Fabricated 1x3 MMI device with AW=3μm and WMMI=18μm; (b) Image capture of the three outputs from the three respective arms seen from the cleaved end; (c) Simulations results of the insertion loss for the 3 output arms. L, C and R denote left, centre and right output arms respectively.

Table 3.3 lists the output power of each arm collected from the power meter. In all the devices tested, the intensity of the centre output (C) arm was relatively higher than those of the left (L) and right (R) arms. The non-uniformity was also possibly contributed by a small percentage of light from the input part of the arm that was captured along and also the lack of any offset bending, hence giving lower loss at the centre arm. This is also why in designing 1xN MMIs, generally even number of N is preferred.

TABLE 3.3: Output power of a 1x3 MMI Splitter

Arm/Output	Output Power (dBm)
Left (L)	-30.09
Centre (C)	-29.74
Right (R)	-30.05

The bandwidth of the 1x3 device is shown in Fig. 3.4.4. Equal 1/3 splitting (~4.77dB) can be found in all three waveguides within a narrower band of 8nm wavelength (1585-1593nm), which is less than half of that for the 1x2 MMI. The tolerance for excess loss (i.e., variations from one output to another) which is set at 1.0dB in view of possible measurement errors has been shaded in Fig. 3.4.4(b) for better distinction.

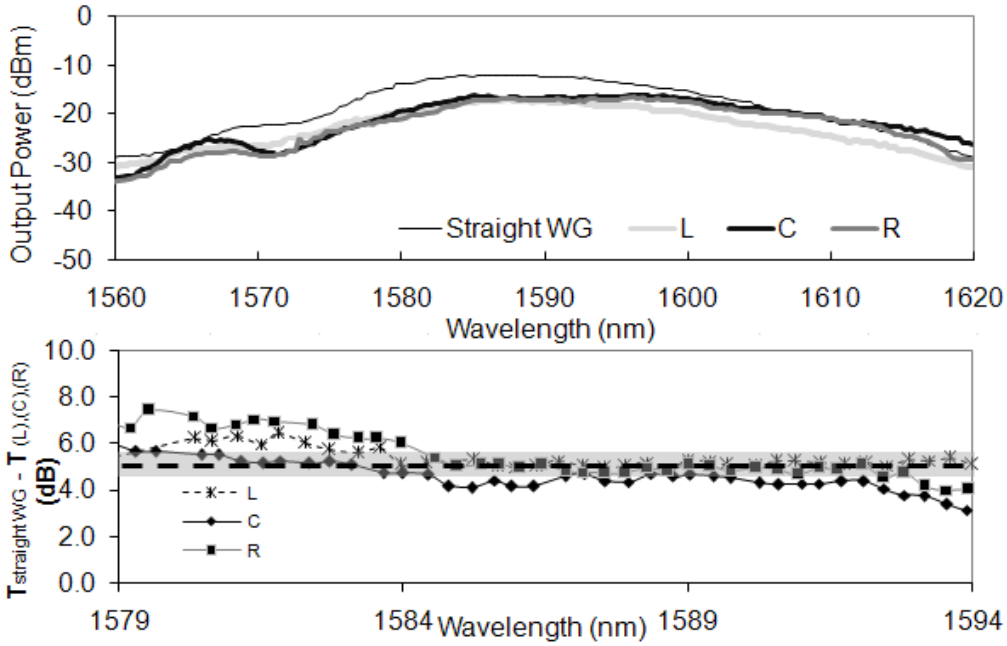

Fig. 3.5.4 (a) The measured output power of a straight waveguide, Output arms L, C and R (not normalized), (b) Insertion loss, or normalized output arm results of L(left arm), C(centre arm) and R (right arm) obtained by obtaining the difference between the output from the straight waveguide and the different output arms.

Although the simulations in Fig. 3.4.3(c) showed that the centre arm tends to exhibit a different wavelength envelop curve from the left and right arms, the L and R arms still retained a similar curve unlike our experimental results. Our experiments showed that although less discernable due to a slightly shifted centre, the L and R results between the range of 1570-1610nm also displayed a wavelength envelop which is a mirror image of each other, which is one of the reasons why the overlapping 1/3 splitting is narrower compared to the 1x2 MMI. However, although the different wavelength envelope plays a part in reducing this range, there is also another factor at play.

The width of the wavelength envelope or bandwidth is related to the AW width in relation to the MMI width. As the ratio of MMI width to the AW width

(W_{MMI}/W_{AW}) increases, the bandwidth of the output in each arm decreases. Therefore, in 1xN MMI splitters, as N increases and MMI widths increase as well while the AW widths remain the same, the wavelength range will become narrower [8] (i.e. bandpass filter). This MMI behavior is also what makes it suitable for wavelength splitting [9].

3.5.3 1x4 and 1x8 MMIs

The cleaved 1x4 MMI including AWs is 2223μm long whereas the 1x8 MMIs was cleaved as short as 2273μm. 4μm wide AWs were utilized in order to improve coupling, relax fabrication tolerance and reduce loss. Fig. 3.5.5 shows the fabricated InGaAsP/InP devices. The use of bigger AWs necessitated longer MMIs. All the output AWs have S-shaped bend transitions in order to separate the modes away from each other. As the number of output arms of the MMI increased, the MMI lengths and the waveguide S-shaped bend offsets also increased. In practice, fabrication slip-ups for e.g. rough side-wall etching, accidental scratching or dirtying of device, bad cleaving or poor sample handling would more greatly affect these devices. These problems contributed to lower yield of good samples.

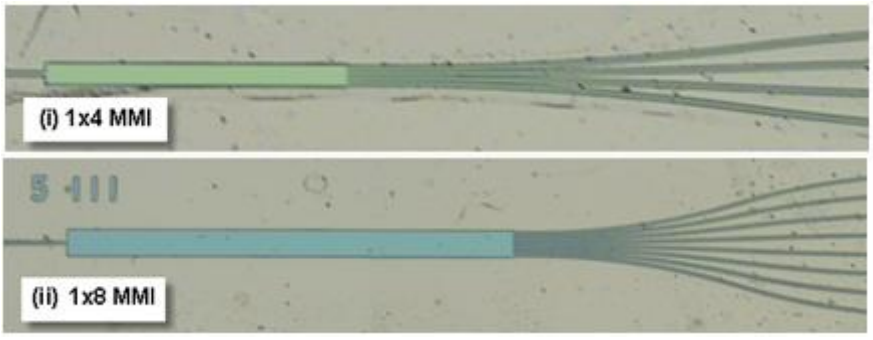

Fig. 3.5.5 (i) and (ii) are the microscope captures of the 1x4 and 1x8 MMIs fabricated for this experimental purpose

If the MMI were to be folded at the centre horizontally along the centre of the 1x4 MMI, arms 2 and 3 would overlap one another, similar to arms 1 and 4. The arms that are the direct opposites of each other tend to share more similar bandwidth envelopes. Although simulations tend to indicate that

bandwidths of all outputs are similar, experimentally, output waveguides in the centre portions (waveguides 2 and 3) have relatively broader bandwidth compared to waveguides nearer to the edge (waveguides 1 and 4). The faster reduction rate in intensity of Output 1 compared to Output 2 at wavelengths beyond 1570nm could be caused by the larger S-Shaped bends at the outer waveguides [10]. The response of two of these waveguides are plotted it in Fig. 3.5.6 to demonstrate this point. The inset shows the simulation results of the two arms.

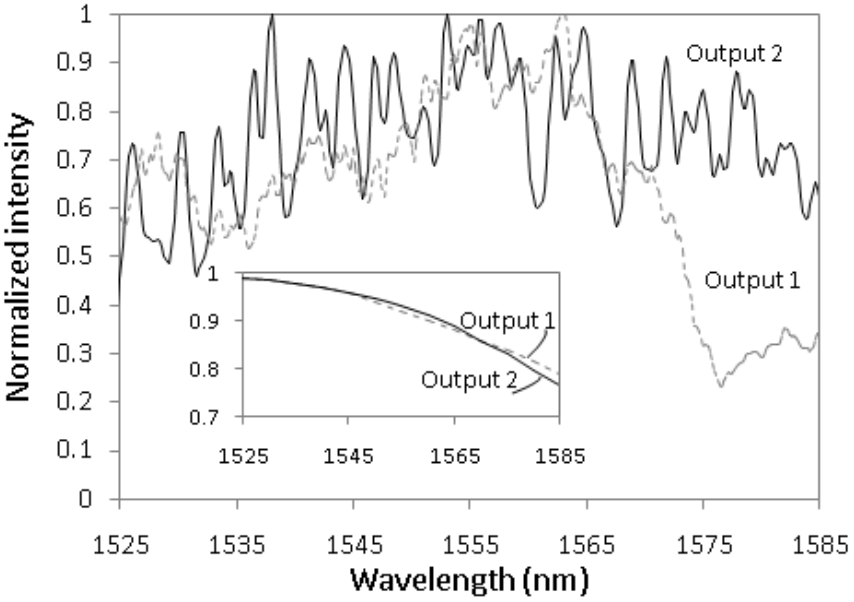

Fig. 3.5.6 Experimental and theoretical (inset) results of output waveguides 1 and 2 of a 1x4 MMI power splitter

Fig. 3.5.7(a) is a plot of the output from the 1x4 MMI. The average values of each arm for the range of 1540-1590nm had been marked and the error bars displayed the max and min values in that range. For the case of the 1x8 MMI, the wavelength range taken was between 1530nm and 1550nm. Although the yield for the 1x8 MMIs was much lower, uniformity was found as shown in Fig. 3.5.7(b).

As N increases, it was more difficult to obtain good splitting. The problem here could be the higher order transmission or leaky modes in the AW [11]. These higher order modes, although not visible in the straight waveguide measurements, could have been generated at the junctions of the components having different geometries, in this case, between the straight input AW and the

large MMI or between the straight and curved waveguide. When fundamental and slight first-order modes are injected into the input at the same time, the propagating light tends to wind up and down along the waveguide due to the difference in the propagation constants between the fundamental and first-order modes. This beating of the modes destabilizes the field input to the MMI splitter which in turn exhibits asymmetric and unpredictable splitting ratio [11]. This higher order mode causes fluctuation in the output transmission, ghost images and degradation in the transmission spectrum; all of which would hamper output results. We believe that is the reason why in our case we encountered more power imbalance in our power splitters for the wider AW (4μm) used for the 1x4 and 1x8 MMIs.

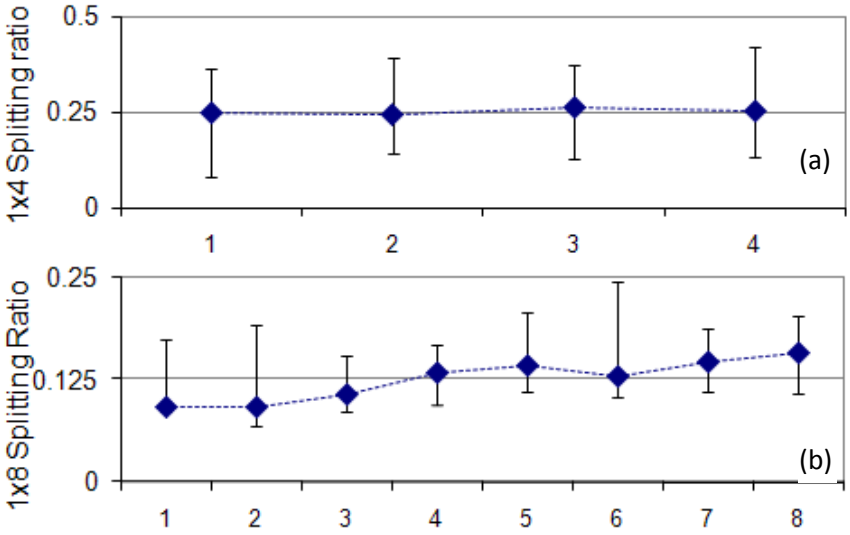

Fig.3.5.7. Splitting ratios and error bars for each output arms in the fabricated (a) 1x4 and (b) 1x8 MMIs.

Conclusion

At the first section of this chapter, a detailed description of the Fabry Perot method and measurement setup and instruments used to measure these devices were given. The propagation loss for single mode InP-based deep-ridge waveguides has been investigated through simulation and experiment. The lowest waveguide propagation loss obtained was for the InP based 8μm strongly guided ridge waveguide at 0.6dB/mm. The propagation loss for the waveguides would be increased with smoother side walls.

The 1xN way beam splitters based on the self-imaging effect in centre fed MMI devices had been demonstrated in the second half of this chapter. Measurement for a large number of fabricated devices have shown that a beam splitting uniformity of ±5% is reliably achieved for values of N=2, 3, 4 and 8. The relationship between reduced bandwidth with increasing W_{MMI}/W_{AW} through increasing 1xN (from 1x2 to 1x3 MMI) was also analyzed. These devices' characterizations served as guidelines in producing better PICs.

Chapter 4

Functional MMI splitters: Designs and prototypes

Compact MMI can make many other compact devices, such as power, polarization, or wavelength splitters, that can be useful building blocks for dense photonic integrated circuits. A compact power splitter, for example, can be used as a coupler between a bus waveguide and a compact ring resonator, in ring-based filters. The design of these devices is discussed in this chapter. A few of the designs were fabricated and tested. The experimental data are presented and compared with theory.

4.1 Type I and Type II MMI splitter

Using the Type I and Type II MMI 3dB MMI splitters which were described in Chapter 2, a few functional devices were designed and fabricated for further purposes. As a brief recap, Fig. 4.1.1 is an illustration of the BPM simulations of both types of MMI undertaken using RSoft BPM software.

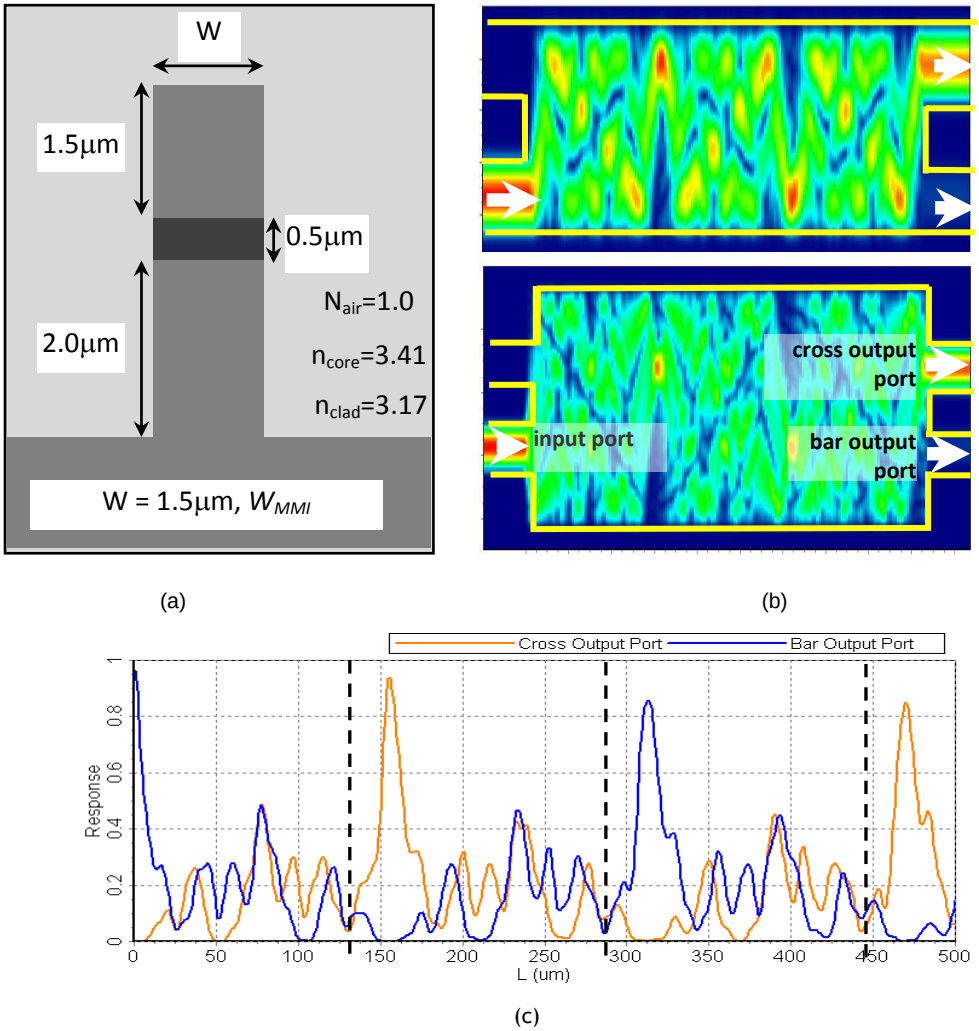

Fig.4.1.1. (a) Refractive indices and cross-section of the MMI devices and AWs; (b) Field distribution of a 2x2 Type I (top) and Type II (bottom) MMI device where W_{MMI}=4.0µm and 7.7µm respectively. The access waveguides are 1.5µm wide with 1µm gap in between them. (c) Response vs. Length for a 2x2 Type II MMI device. The dotted lines mark the positions of the output for MMI splitters that are designed as 3-dB couplers.

4.1.1 Sensitivity and crosstalk

One of the known advantages of MMI over directional couplers or Y branches as splitters is their relative robustness against variations in geometric parameters as well as external factors such as wavelength, polarization, and temperature. Their sensitivity to variations in MMI length, MMI width, operating wavelength and polarization will be analyzed here. The MMI device's sensitivity to polarization and wavelength can be engineered to devise useful devices such as the polarization splitter and polarization-independent wavelength splitter.

The sensitivity is expressed in terms of excess loss caused by deviations from the optimum values of the relevant parameters. Excess loss is defined as

$$\text{Excess loss (dB)} = -10 \log\left(\frac{P_b + P_c}{P_{opt}}\right) \qquad (4.1)$$

where P_{opt} is the maximum total output power (P_b + P_c) under optimum condition. Fig. 4.1.2 shows the excess loss against the MMI length for both the W_{MMI}=3.5μm (Type I) and W_{MMI}=6.0μm (Type II) designs for 3dB splitters. Their respective lengths are L_{MMI}=54.5μm and 51.5μm. With both graphs stacked together, it can be seen that the curve for the Type II design is slightly narrower, implying that Type II is more sensitive to variations in length.

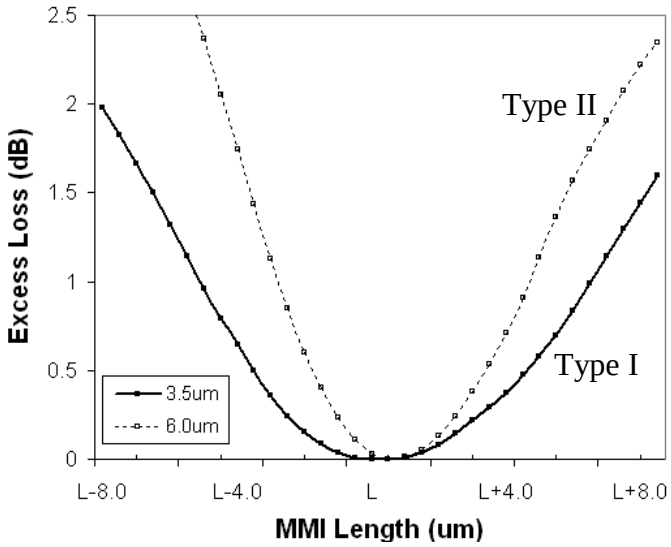

Fig.4.1.2. Excess loss vs. MMI 3dB splitter length for Type I MMI (3.5μm) and Type II MMI (6.0μm). Both designs have input/output gap separations of 0.5μm.

For a cross coupler, an important performance parameter is the crosstalk, which is defined as:

$$crosstalk\ (dB) = 10\log_{10}\left(\frac{P_b}{P_c}\right) \qquad (4.2)$$

where P_b and P_c are the power in the bar and the cross states. For both MMI and DC, there will be some difference in L_c between TE and TM, and hence for any given length, the crosstalks for TE and TM will be different.

The result shows that the MMI's crosstalk is quite sensitive to length where polarization-independent operations are concerned. The sensitivity of crosstalk to length is important as it may set a stringent limit on the usable range of device length, L_{MMI}, that can satisfy a given crosstalk requirement. For polarization-independent operation L_{MMI} should be set at the point where the crosstalk curves for TE and TM polarizations intersect at the first cross-coupling (0:100) length. In the case of the Type I (II) MMI the curves intersect at L_{MMI} = 108.5μm (102.5μm). At this point the MMI's crosstalk is significantly degraded from its minima at L_π because of the sensitivity to length as seen in Fig. 4.1.3. If the required crosstalk for both TE and TM is to be less than -25 dB, for example, then the device length must fall within only ± 1 μm of the polarization-independent point. To avoid this stringent requirement, it is desirable to minimize the L_π difference between TE and TM. The figures also showed that the crosstalk for Type II MMI is more sensitive to length variations than Type I MMI.

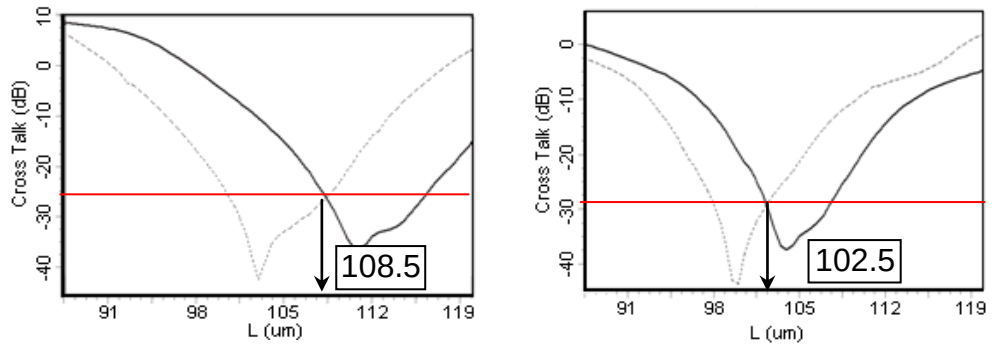

(a) (b)

Fig.4.1.3. The variation of crosstalk (for both TE and TM) for (a) Type I and (b) Type II MMI with input/output gap separation of 0.5μm. Waveguide widths are 1.5μm. Dotted lines represent the TE mode while solid lines represent TM mode.

The performance of a device is also characterized by its sensitivity to wavelength change. In Fig. 4.1.4, the comparison of the effect of wavelength change on the response or in this case, the excess loss is presented for both the Type I and Type II cases at the previously simulated MMI lengths of L_{MMI}=108.5μm and 102.5μm respectively. The broad optical bandwidths observed indicate that both devices are quite insensitive to wavelengths. However when both these cases are compared, Type II MMI is slightly less tolerant to wavelength change (sharper curve). This is because the MMI bandwidth is loosely inversely proportionate to its port width over MMI width ratio. The bigger this ratio is, the narrower the bandwidth would become. This information is used when selecting the type of MMI for the devices in the following section.

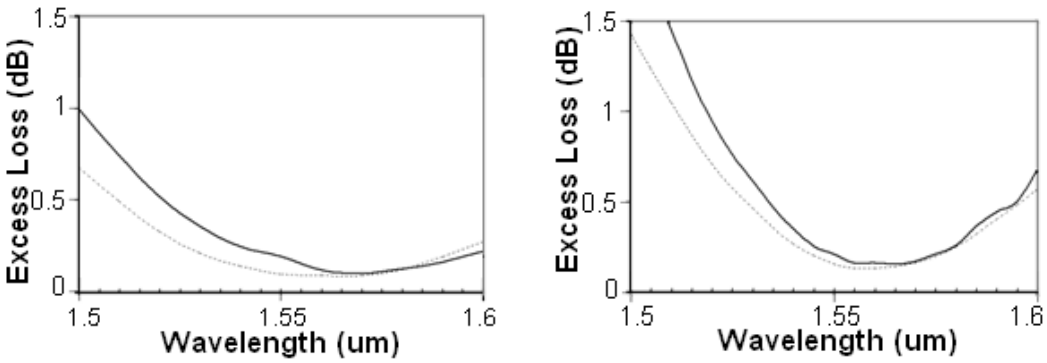

Fig.4.1.4. Excess loss vs. wavelength for (a) Type I and (b) Type II MMI. Both have input/output gap separation of 0.5μm.

In the subsequent sub-section, applications of MMI as wavelength and polarization splitters based on the (weak) dependence of the coupling length on wavelength and polarization are explored.

4.1.2 Design of Type I Polarization Splitter & Type II Wavelength Splitter

(A) Polarization splitter

One of the fundamental issues of photonic integrated circuits (PIC) is the polarization dependence. Because of the structure and geometry of the waveguides used for devices, the devices are generally polarization dependent, meaning that their performance depends on the polarization of the input light. These devices will have limited application in fibre-optic communication

systems in which the polarization states of input optical signals to the photonic devices may change randomly as a function of time. If the devices cannot be designed to be polarization independent, then polarization has to be managed. *Polarization diversity* is one way to utilize polarization-dependent devices for both polarizations, one device for each polarization. In this case, a polarization splitter is an important component. It splits the input light, which may have random polarization, to two beams - TE and TM.

MMI and directional couplers can be used to split the TE and TM modes. Type I MMI was found to be more sensitive to the polarization change and thus have been used to design the polarization splitter. The material and waveguide structure used for the simulation of the polarization splitter is similar to what was illustrated in Fig. 4.1.1(a) whereas the basic design is quite similar to Ref. [1]. The difference in the material used between our work and that given in Ref. [1] resulted in different MMI and AW sizes and subsequently different device lengths. In utilizing Type I MMI, the width of the MMI can be further reduced compared to the general interference mechanism that had been attempted. The design principle makes use of the beat-length difference in self-imaging and when two different polarizations are input into the waveguide, the beam can be split into a bar or cross state. For the two polarization splitting mechanism, since the TM coupling length is generally larger than the TE coupling length, the two polarizations can be separated if the interaction length of the multimode interference device satisfies the condition:

$$l = M \times l_c(TM) = (M+1) \times l_c(TE) \tag{4.3}$$

where M is an integer. Using Eq. 2.7, Eq. (4.3) can be expanded as follows:

$$M \frac{\lambda}{n_0(TM) - n_1(TM)} = (M+1) \frac{\lambda}{n_0(TE) - n_1(TE)}$$
$$or \qquad \frac{M}{M+1} = \frac{n_0(TM) - n_1(TM)}{n_0(TE) - n_1(TE)} \tag{4.4}$$

As the polarization dependence of an MMI is quite weak, the integer M is expectedly large. We designed a polarizer using an MMI which is 4μm wide. The AW width is set as 1.5μm and the port distance, D is set as 2.5μm. The

layer structure of the waveguides is as stated in Table 3.2 of Chapter 3. The effective indices used are tabulated in Table 4.1.

TABLE 4.1: Effective indices and calculated MMI lengths for polarization splitting

Effective index of TE		Effective index of TM	
n_0	n_1	n_0	n_1
3.241367223	3.224263302	3.236010691	3.219970702
L	135.933743	L	144.950224
M+1	16	M	15
(M+1) x L	2174.93989	M x L	2174.25336

The calculated length (~2174.5μm) is slightly shorter than the simulated length (2180 μm). In Fig. 4.1.5(a) the particular example is illustrated- an MMI with *M*=15, for which at the simulated length of 2180 μm, the TE mode is output at the cross port and the TM mode at the bar port, for a wavelength of λ = 1550nm. Part (b) of the figure shows the extinction ratio against the wavelength around 1550nm. Similar to crosstalk, extinction ratio is an important figure of merit, defined by the amount of unwanted polarization mixed with the desired polarization in the same output port. It can be seen that the acceptable extinction ratio limits the wavelength range for which the polarization splitter will work. For example, if minimum acceptable extinction ratio is 20 dB, then the range of wavelength for which this requirement is satisfied is only about 10nm. This is defined as the *optical bandwidth* in which the polarization splitter can operate satisfactorily.

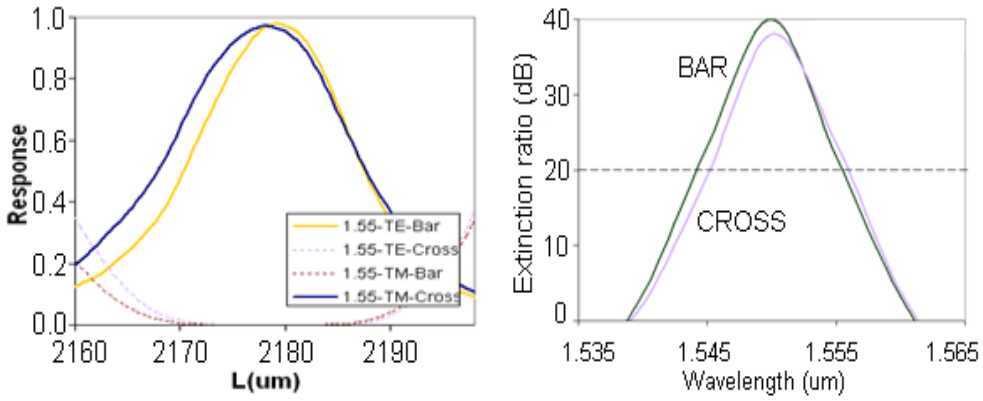

(a) (b)

Fig.4.1.5. (a) A 1550nm polarization splitter at L=2178μm for a Type I MMI (b) Extinction Ratio around the 1550nm wavelength

(B) The coarse wavelength splitter or demultiplexer

In the case of wavelength splitter or demultiplexer, we have selected to base it on a different material in order to realize it experimentally [5]. The polymer material has been opted as this alternate base. Polymeric materials are particularly attractive in integrated optics because of their ability to be processed rapidly, cost-effectively, and with high yields [6]. Classes of polymers used in integrated optics include acrylates, polyimides, polycarbonates, and olefin (e.g., cyclobutene). BenzoCyclobutene (BCB 4024–40), a product of DowTM, is a photodefinable polymer and is commonly used for board-level interconnects. Because of its low cost and low loss characteristics [7], it is a suitable candidate for optical device applications.

The cross section of the BCB waveguide in illustrated in Fig. 4.1.6(a). The widths of the designed AWs were 10μm wide. Previous investigation has indicated that Type II MMIs is more susceptible to wavelength difference as shown in Fig. 4.1.4 indicated. This means that the Type II MMI will give a shorter splitting length. The MMI width employed was W_{MMI}= 23μm and the port pitch, D of the access waveguides were set at 7.7μm. Again, because of the relatively weak dependence of MMI on wavelength, its application as a wavelength splitter is expected to be feasible only two wavelengths that are spaced far apart, e.g., 1310nm and 1550nm. Such a wavelength splitter is called a coarse wavelength splitter or coarse wavelength division (de)multiplexer (CWDM). As a reciprocal device, it can also be used as a wavelength combiner (or multiplexer). Such CWDM devices are important for some fiber-to-the-home (passive optical network) applications. The design of wavelength splitter or combiner is based on the same principle for polarization splitter and applies the same equations, (4.3) and (4.4), only in this case, the variation of the beat length is caused by the different wavelengths instead of the different polarizations. In this design, the two wavelengths are designated as λ_1 and λ_2, where $\lambda_2 > \lambda_1$.

Eq. (4.4) can be expressed as follows:

$$M\frac{\lambda_1}{n_0(\lambda_1)-n_1(\lambda_1)} = (M+1)\frac{\lambda_2}{n_0(\lambda_2)-n_1(\lambda_2)} \qquad (4.5)$$

$$or \qquad \frac{M}{M+1} \approx \frac{\lambda_2}{\lambda_1}$$

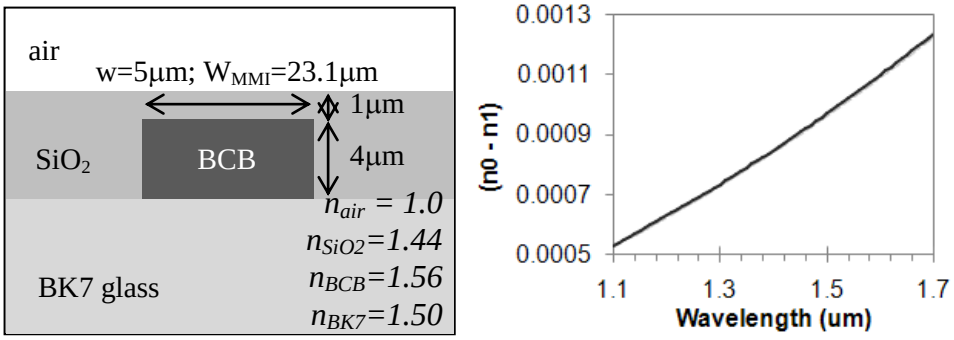

(a) (b)

Fig.4.1.6. (a) Refractive indices and cross-section of the BCB based material waveguides; (b) Effective index difference (n_0-n_1) vs. wavelength

Once the refractive index value is obtained, the coupling length for each case can be calculated and the right splitting length, determined as shown in Table 4.2.

TABLE 4.2: Effective indices and calculated MMI lengths for wavelength splitting at W=23.1μm

Effective index at λ=1.31μm		Effective index at λ=1.55μm	
n_0	n_1	n_0	n_1
1.53813	1.53729	1.53531	1.53433
$L_{1.31\mu m}$	922.6	$L_{1.55\mu m}$	790.8
M	6	M+1	7
(M+1) x L	5535.6	M x L	5535.6

The ratio found in this case based on (4.5) is approximately 6/7 (i.e., M=6) for λ_1=1.55μm and λ_2=1.31μm, since the effective index difference n_0-n_1 is only a weak function of wavelength (Fig. 4.1.6(b)). This design is different from previously reported MMI related wavelength designs in that it does not make use of any MZI structures. Its difference from Ref. [2-4] was in the material used. From the calculations based on (3.5) and the simulations ran for the MMI width, the most suitable MMI length was found to be 5534μm, as shown in Fig. 4.1.7.

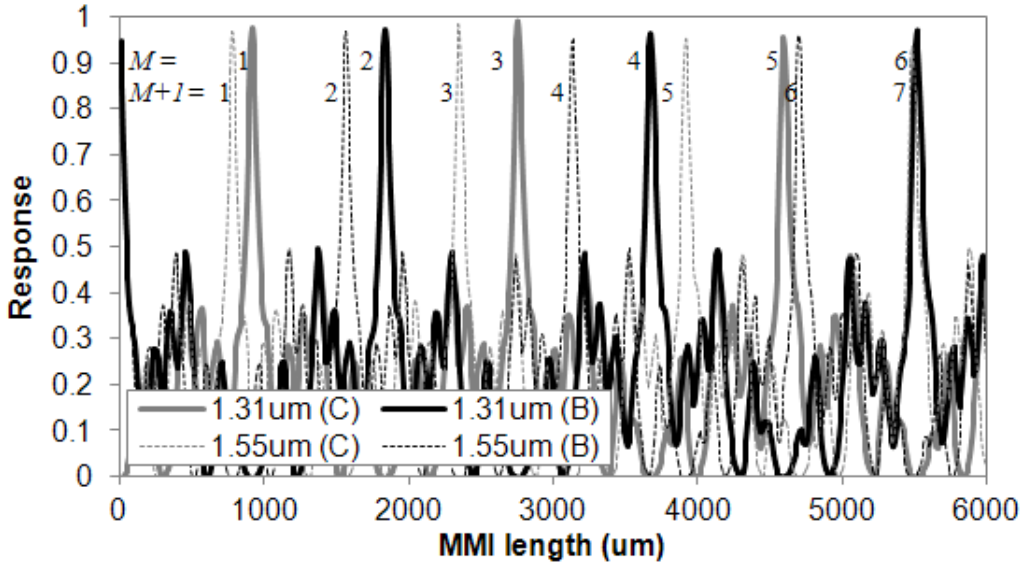

Fig.4.1.7. Simulations results of the periodicity of normalized TE mode power output response for a 23μm wide Type II MMI wavelength filter versus MMI device length, L in μm.

Similar results are obtained for the TM mode, and unlike for III-V material, the lengths simulated for the TM mode are almost the same as that of the TE mode due to the more symmetrical channel structure employed. Therefore, only the TE mode characteristics are discussed and utilized. An important parameter for wavelength splitter is the contrast. Fig. 4.1.8 shows the sensitivity of the contrast to the MMI length. The contrast here is defined as the ratio between the power in the desired wavelength and the power in the unwanted wavelength at a given output port.

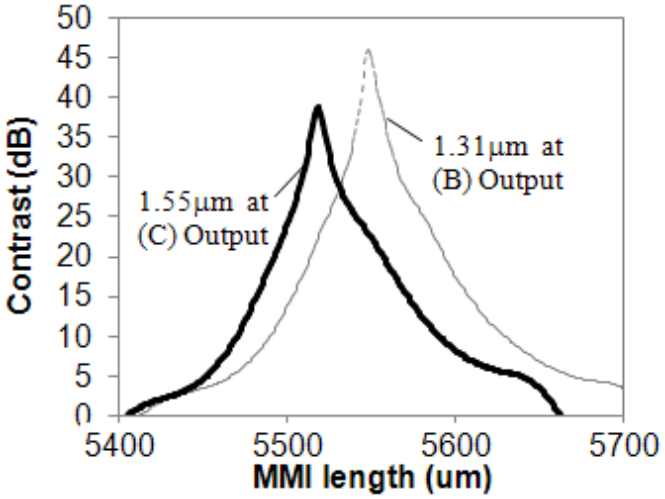

Fig.4.1.8. Contrast at opposing output arms as noted in the graph for the wavelength splitter design vs. MMI length around the designed length at the designed MMI length of L=5534μm

Fig.4.1.9 shows the simulated power output and the contrast as a function of the different sets of wavelengths at the length of 5534μm. The simulations indicated that the contrast of above 20dB with a bandwidth exceeding 20nm is obtainable around both wavelengths which confirmed the optical filtering capability of the MMI designed.

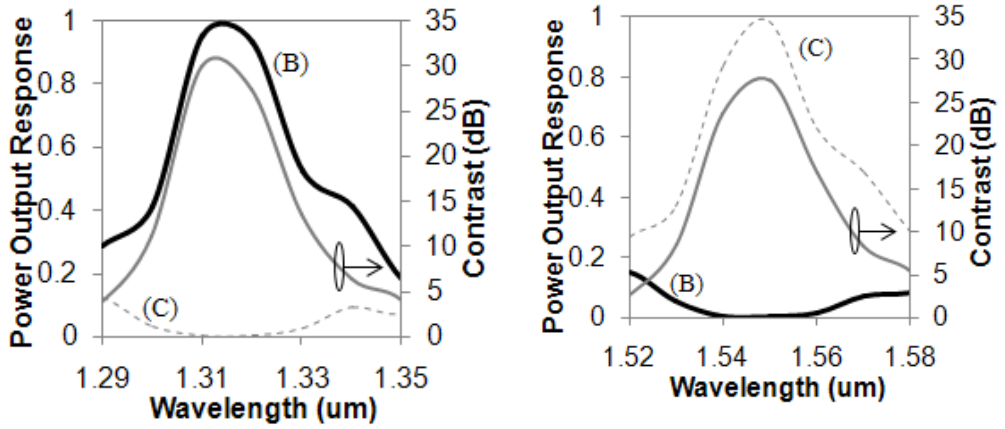

(a) (b)

Fig.4.1.9. Simulated power output response at the Bar (B) and Cross (C) output arms and its contrasts against wavelength for the (a)1.310μm & (b)1.550μm range.

4.1.3 Experimental Verification

Based on the design principle in section 4.1.2, the experimental verification was implemented on the introduced BCB material base [5]. With the AW of 5μm and the Type II MMI width used (W_1 = 23μm), the output access waveguide spacing is only 7.7μm. To increase the spacing one could interpose S-curve waveguides as introduced in Chapter 3. However, in this design an MMI cross coupler operating in each output waveguide was used to offset the outputs by about 13μm, thereby increasing the separation to W_3 = 34μm. These MMI couplers operate in the GI mode and have a width of W_2 = 15μm. The schematic layout of the complete filter is shown in Fig. 4.1.10.

The process for the fabrication of MMI filter using BCB 4024–40 is similar to a thin film multi-chip module process. The coating speed of 3000 rpm was chosen to realize a 4μm thick BCB which acts as the single-mode square structure core. To maintain good adhesion with the BK7 substrate layer, AP3000 adhesion promoter was spin coated on the substrates before polymer

coating. After the polymer was spin coated, the film was heated on a hotplate for a specific time (40seconds) and temperature (70°C) to drive out the residual solvent. The time and temperature depend on the film thickness such as to prevent film wrinkle.

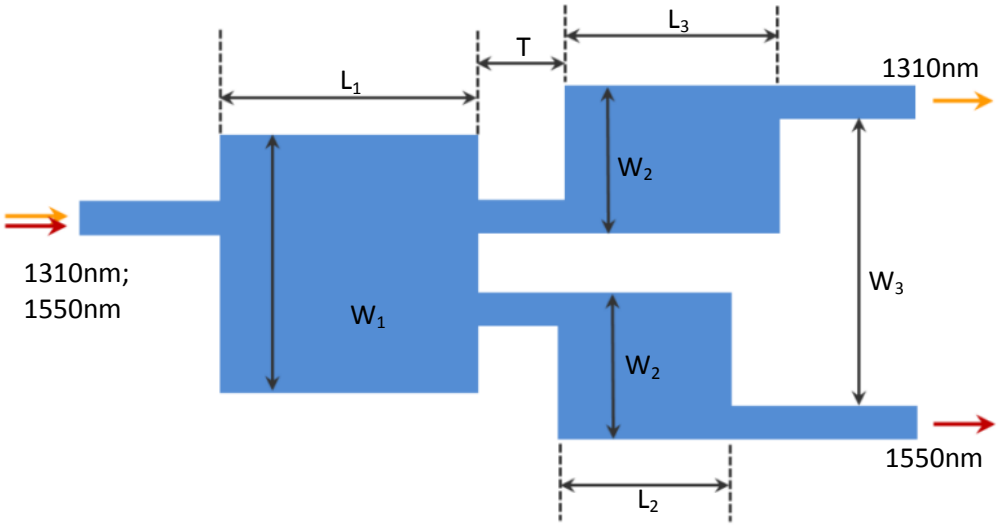

Fig.4.1.10. Schematic illustration of the BCB based optical wavelength filter with L1=5534μm, L2=1076μm, L3=1239μm, T=200μm, W1=23μm, W2=15μm and W3=34μm. The 1550nm wavelength exits from the cross coupler whereas the 1310nm wavelength passes through the bar coupler

This is followed by the photolithography step which is the process of transferring the two-dimensional patterns on the photomask to the polymer film. As the BCB 4024–40 is a negative acting polymer, a dark field mask was utilized. A mask aligner having I-line UV exposure at 365 nm wavelength was used to crosslink the exposed polymer region. The mask aligner power density was set to 3 mW/cm^2 and the exposure time was 20 sec. After exposure, a pre-develop bake was carried out to increase the etching resistance and film adhesion to the substrate. The pre-develop bake temperatures were 10°C lower than the pre-exposure bake. The chemical etching or developing process of BCB 4024–40 polymer requires the puddle development process. In this process, a DS2100 developer solvent was dispensed onto the sample surface. After 30 sec of puddle time, sample was then rinsed for 10 sec and spun at high speed to remove the developer solvent. To further dry the film and stabilize the side wall, the sample was baked on a hot plate immediately after developing. Finally, the sample was cured in a box oven at 250°C to remove the residual

solvents and harden the polymer. At the end of the process only the masked areas remain which form the devices. Note that neither photoresist nor RIE or plasma etching is necessary. The drawback of this chemical etching method is reduced quality of sidewall resolution of the waveguide [7]. BCB 4024–40 polymer is photodefinable with similar properties to a negative photoresist, hence the material can be exposed directly to define the waveguide and the process does not require any plasma or reactive ion etching, enabling simple devices to be fabricated easily. The average refractive index obtained from our measurement is 1.5556 for transverse electric (TE) polarization and the average value of slab loss is measured to be 1.01 dB/cm.

For the characterization of the fabricated filter, a single-mode fiber is used to couple 1550-nm laser source with TE polarization into the polished end facet of the access waveguide. The output is measured using a Germanium (Ge) photodetector and the near field profile is imaged onto an infrared camera integrated with beam analyzer software. The images of the output beam for both wavelengths are shown in Fig. 4.1.11. It shows that the wavelengths were filtered at respective branches as intended, which indicate the functionality of the proposed wavelength filter.

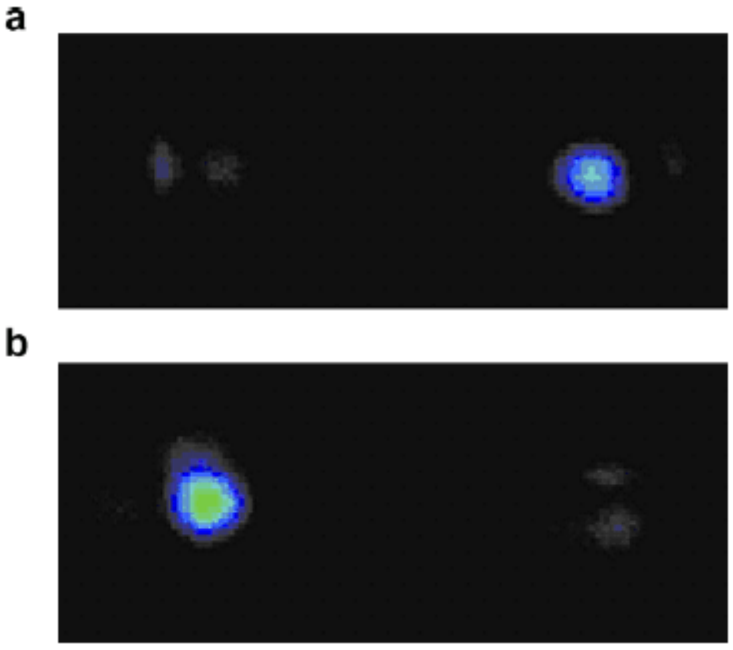

Fig. 4.1.11. Near field profile of the demultiplexer output for (a) 1310 nm and (b) 1550 nm

To characterize for its performance, two parameters are employed which are defined as follows [8]:

$$Extinction \quad Ratio \quad = 10 \log \frac{P_r}{P_w} \qquad (4.7)$$

$$Insertion \quad Loss \quad = -10 \log \frac{P_r}{P_i} \qquad (4.8)$$

where P_r and P_w denote the light intensities in the right and wrong output port of the filter while P_i denotes the light intensity at the input port. The extinction ratio was measured to be -14.4 and 20.6dB for 1310 and 1550 nm, respectively. The measured insertion loss is around 3.2–3.5 dB for both filtering operations.

In conclusion, we have successfully demonstrated an MMI-based wavelength filter for the 1310 and 1550 nm operation on ridge waveguides fabricated in a photodefinable BCB 4024–40 polymer. The structure consists of two cascaded MMI sections, employing general and PI mechanism and fabricated on BK7 glass using only chemical etching and standard photolithography with thin film of SiO2 as cover.

4.2 Ultra compact SOI Tapered MMI

Recently researchers have begun to attribute more weight to multimode interference couplers (MMIC) for ring resonators [9-13] thanks to their more relaxed fabrication tolerances. In the past, these MMIs are designed more for InGaAsP/InP based devices and their dimensions tend to be larger than that of the SOI based racetrack ring resonators. However, the interest in using MMI couplers in SOI racetracks have caught on and the latest compact MMI used for SOI is as small as $3x9\mu m^2$ [9]. At present SOI process is suitably well established, ensuring high-yield and low-cost fabrication of superior passive optical devices. Due to the high core-cladding refractive index contrast, the design known as the silicon photonic wire waveguide can be adopted to enable more symmetric mode in Si channel than that in the more frequently used rib-SOI designs. The photonic wire design allows scaling down of devices and made it possible to realize near-circular ring-resonators with MMICs. Such ultra-compact resonators, with the size limit of resonator cavity pushed down to

enhance nonlinear optical interactions, may find their wide application in future ultra-broadband DWDM applications and dense photonic integration.

It has been known that Mach-Zehnder interferometric (MZI) devices using 3dB MMI couplers have unnecessarily larger footprints due to the MMI length. For example, in the work of ring coupled MZI devices [14, 15], the MZI section of the device is often much longer as compared to the ring size. Therefore, in order to *minimize* valuable real estate on PICs and to *maximize* high density integration for increased optical functions per optical chip a deeper study of compacting MMICs is valuable.

Aside from MZIs, the miniaturization of micro-ring resonators (MRRs) requires the WG cross-sectional dimensions to be reduced to the *submicron* scale (width and height < 1μm) and the bend radii to be shrink into the *ultrasmall* regime (bend radii below 10μm). Ring resonators based on directional couplers (DCs) are commonly used but the coupling ratio of DC is more sensitive to wavelength variation and a small change in the gap size of DC would cause unwanted and often, unpredictable wavelength shift (tens of nm) which would greatly affect the devices, especially where cascaded ring configurations are concerned. Therefore, the objective here is to study miniaturized MMICs in detailed so that it may serve as a guideline for future racetrack configurations with MMICs. Although MMICs in MRRs have been fabricated in recent years, there has yet been effort in investigating these MMICs which have been miniaturized. A key consideration in designing compact MMICs is to ensure the excess loss is as small as possible while maintaining a good 3dB splitting ratio over a wide bandwidth. The excess loss is due mainly to sidewall roughness. To scale down MMICs, researchers would often resort to designs with tapered geometric features [16-20] namely, the tapered access waveguides and the tapered MMI section. Tapering however, greatly affects the influence of sidewall roughness to the device loss. Therefore, there has to be a balance between both choices. Here, we have also investigated the miniaturization of non-tapered MMICs. 2-D Numerical simulation based on finite-difference method, beam propagation method (BPM), and finite-difference time-domain (FDTD) method have been utilized to confirm the

lengths of the MMIC and in simulating the waveguide losses of all the individual components.

4.2.1 Device Structure and Design

The MMIC designs are demonstrated in silicon-on-insulator (SOI) technology, where the waveguide core is silicon and the cladding is SiO_2. The SOI platform gives a high freedom for designing compact devices [21-23]. Using this platform, single mode propagation is ensured up to 580nm waveguide width for telecommunication wavelength range [24], and the waveguide can be bent down to 5μm radius with negligible bending losses[25]. With the high refractive index contrast between silicon (n=3.45) and its oxide cladding (n=1.45), waveguides of the width as small as 100-500nm can be made for operation at the telecommunication wavelength of 1550nm [21, 22]. In this technology, the silicon core width is 450nm wide and 220nm thick, with a buffer oxide (BOX) thickness of 1μm as shown in Fig.4.2.1(a) for supporting single quasi-TE mode propagation with negligible substrate leakage loss as shown in Fig.4.2.1(b). However, it is difficult to avoid TM mode leakage into the substrate, especially in our designs where tapers are incorporated [26]. An oxide layer as thick as 4μm is necessary for maintaining the TM mode polarization component in the 200nm-thick silicon core layer, whereas such a small core thickness is required for single mode operation of the TE polarization component. Fig. 4.2.1(c) indicates distinctly that TM modes also tend to be lossier as compared to the TE mode. Limited by the available oxide thickness in commercial SOI wafers, MMICs are thus designed only for TE operation in this work.

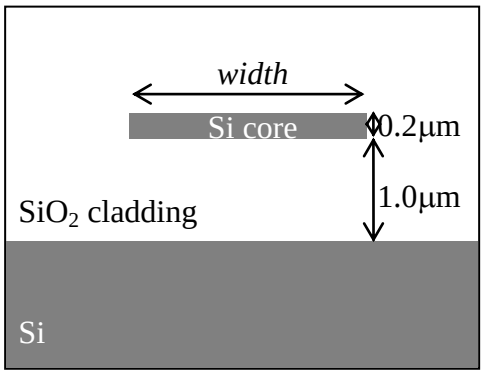

(a)

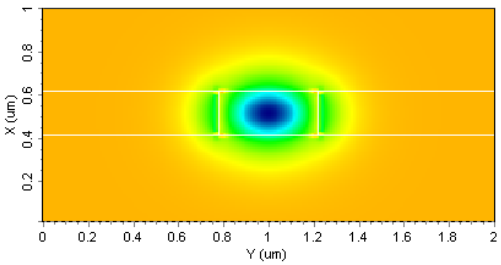

(b)

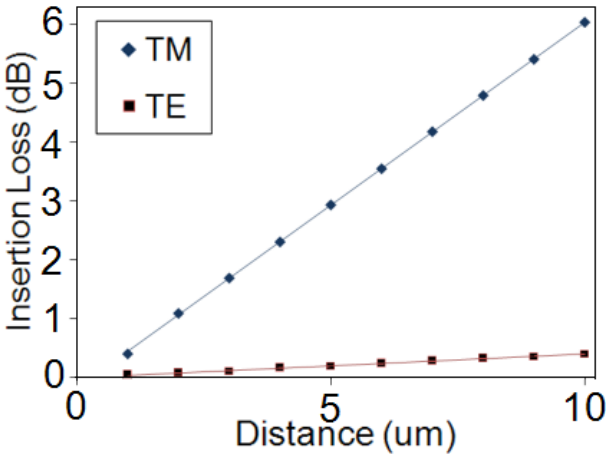

(c)

Fig.4.2.1. (a)SOI structure of the analysis waveguide where width would vary depending on whether it is the AW, the MMIC or the tapered portion of the device; (b) Simulation result showing the TE optical mode field of the SOI structure; (c) Insertion Loss vs. distance for the access waveguide width of 450nm for TE and TM

The full-vectorial simulation method which is also known as polarization coupling (PC) numerical method was employed in determining the effective indices because the more common semi-vectorial method is less accurate for very narrow waveguides. Fig. 4.2.2(a) indicates that as the width of the waveguides increases, the results obtained from these two methods begin to converge, i.e. the semi-vectorial method becomes acceptable. Since at 450nm, this has yet to occur, the PC method, albeit more time consuming, is necessary.

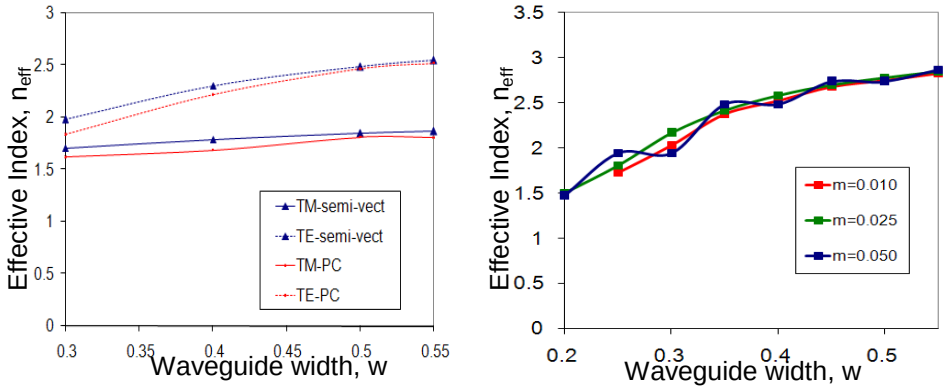

(a) (b)

Fig.4.2.2. Comparison of effective indices for different waveguide widths (0.3~ 0.55μm), (a) obtained using two different numerical methods (i.e. full vectorical (aka polarization coupling (PC) and semi-vectorial methods) and (b) using different mesh sizes (m=0.01, 0.025, 0.050) for the PC numerical method.

Mesh size which is usually sufficient in obtaining the necessary simulation results may not be sufficient when dealing with smaller scaled devices. Although the best solution to this is simply to reduce the mesh sizes to the smallest values possible, this is not viable as the computation power needed is increased many folds when the mesh size is halved and this taxes the machine unnecessarily. The simulations indicated that in the case of SOIs with similar structures as that of Fig. 4.2.1, when the mesh size, *m*, is 10nm, the simulation is sufficient to give accurate results. The simulation results of insertion loss vs. varying gap for 10μm and 5μm long parallel waveguides are plotted in Fig. 4.2.2(b). The rule of thumb often applied in determining the mesh size is to make sure the m is smaller than $\lambda/(10n)$ where *n* here is the core refractive index.

Having set the material, AW dimension and simulation method, the MMIC geometry reduction is first designed by obtaining the optimum or minimum gap distance between the AWs. In order to determine the most suitable separation distance between the AWs for the SOI material base, 2D-BPM simulations of two waveguides placed at different separation distances, very much like a directional coupler was undertaken. Since the distance where such waveguide travel in parallel is quite short in a conventional MMI + Racetrack Resonator (see Fig. 4.2.4(a)), the simulation length was limited to 10μm. The insertion loss of 10μm and 5μm long waveguide with varying gaps up to 0.8μm is plotted in Fig. 4.2.3. The insertion loss is $20\log |S_{ij}|$ where $|S_{ij}|$ is the ratio of the amplitude of the output light to the amplitude of the input light. The inset of Fig. 4.2.3 shows the case where the separation is 0.45μm (or *w*), where coupling has taken place due to the closeness of the AWs; an occurrence to be avoided. The minimum gap between the access waveguides has been found to be 600nm for a relatively short distance (<10μm) of access waveguide (AW). This gap size is easily achieved with deep UV lithography [22].

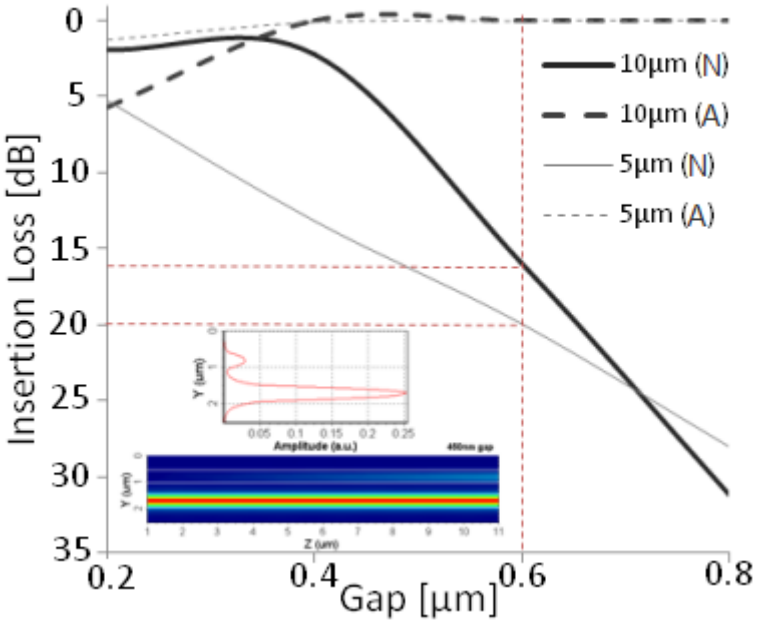

Fig. 4.2.3. Simulation of insertion loss vs. varying gap for 10µm and 5µm long parallel waveguides. (A) denotes the actual waveguide while (N) denotes the waveguide next to it. Inset shows the result of a 0.45µm gap simulation.

Once this minimum gap value is determined, the next design process explores the various approaches to reduced MMIC size while a few vital parameters were observed. The design of compact MMIC was undertaken with the following objectives in mind: (1) shorter device total length; (2) less than 1dB excess loss in the device; (3) splitting ratio within ±5% of the device splitting ratio and, (4) larger bandwidth in the device output. The illustrations of the proposed MMICs are given in Fig. 4.2.4(a). The three types of MMIC designs to be considered here are illustrated in the figure as the MMIC with tapered access waveguides *(top)*, Tapered MMIC *(middle)* and Un-tapered MMIC *(bottom)*. The discussion regarding each of the proposed MMICs are in the following sub-section. These sections can then be inserted whole in racetrack resonator devices such as Fig. 4.2.4(c).

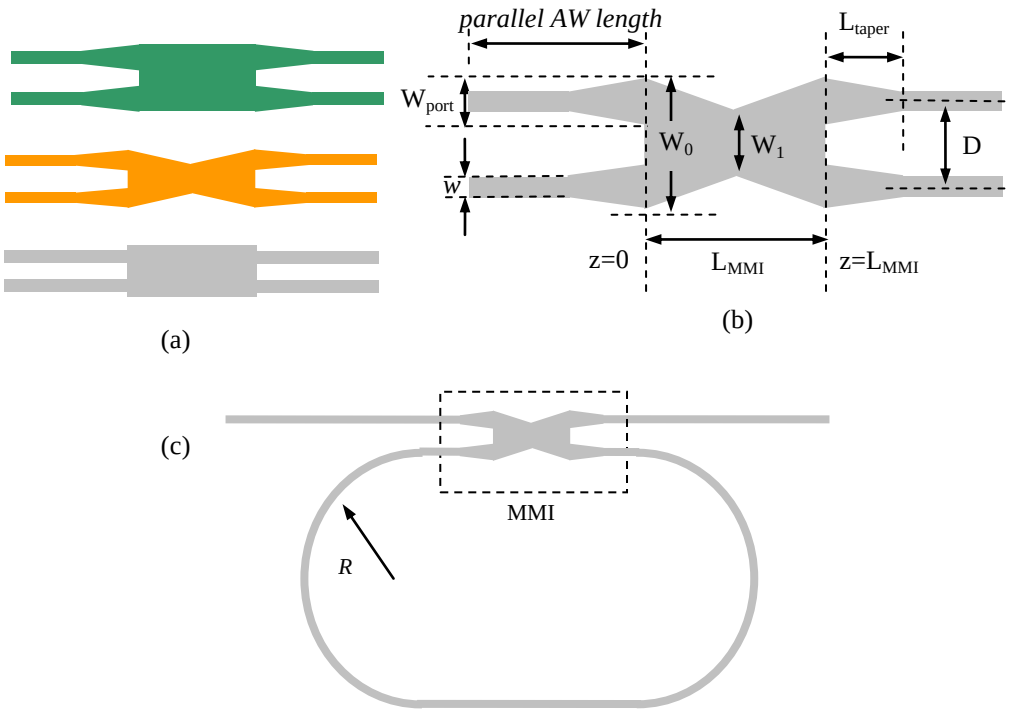

Fig.4.2.4. (a) Three types of MMICs from the top, (i) MMIC with tapered AW (ii) Tapered MMIC and AW (iii) Un-tapered MMIC; (b) schematic drawing of Bow Type I MMIC with tapered AWs and (c) its application for racetrack resonator

(A) MMIC with tapered access waveguides

The input and output waveguides of the MMIC device are commonly known as access waveguides (AWs). The AWs are tapered when entering and exiting the MMIC device as shown in Fig. 4.2.4(a) - broadening on the side that contacted the MMI side - mainly to reduce insertion loss. This is because the AWs are all as narrow as 0.45μm; a common waveguide width in SOI resonators [9]. The tapered AWs also enables waveguides which are separated sufficiently apart to avoid unneeded coupling to have a bigger mode size as it enters the bigger MMI. The length of the taper has to be taken into consideration when designing, since, in a ring or race track resonator, when an MMI is used as a coupler, the total length of the coupler (which affects the racetrack length) would include the taper length and any other straight waveguide before the bending can take place (see Fig. 4.2.4(b)). The tapering up to the MMICs which we have designed is up to 1.0μm wide and 5 to 10μm long. These type of MMIC is the most commonly used as the design is straight

forward and with the AWs all the way to the edge of the MMI, it gives the largest gap between the AWs while maintaining the smallest possible MMI width. The straight forward design, which we have denoted as Type I MMIC with tapered AW also gives the advantage of wider bandwidth. The bandwidth of an MMI is loosely related to its W_{MMI} /w ratio as indicated in Fig. 4.1.4 when simulated Type I and Type II MMI bandwidth were compared. Therefore, in short, The Type I MMI with tapered AW allows most of the design requirements to be fulfilled except for its relatively long length. With the added tapering and the wider MMI width due to this tapering, the MMI length could easily be two or three times longer than it could potentially be. In order to achieve this potential, researchers would often resort to tapering the MMIC itself and this is discussed in the following sub-section.

(B) Tapering MMIC

In tapering the MMICs, we concentrated on a symmetrical and linear type of tapering which resembles a bow tie hence the name Bow Type I. Fig. 4.2.4(b) shows the Bow Type I with tapered AWs and all parameters which are involved in the designs have been noted. The MMI widths of Type I and Type II MMI (restricted interference MMI device) [27] can be written as D+w and 3D respectively where D is the centre-to-centre distance between the access waveguides, also known as the port pitch and w is the width of the access waveguide. Based on equation (2.3), the ratio of these MMICs can then be written as [28]:

$$\frac{L_{TypeI}}{L_{TypeII}} = \frac{(D+w)^2}{3D^2} \qquad (4.9)$$

The width of the tapered MMIC at distance z (along the propagation direction) from z=0 for Bow Type I MMIC is

$$W(z) = W_1 + (W_0 - W_1)\left(1 - \frac{2z}{L_{mmi}}\right) \qquad (4.10)$$

where W_0 and W_1 are the widest and narrowest width of the MMIC, respectively, and L_{MMI} is the MMI length. For a conventional MMI device, the 3dB coupling

appears at the device length of L_{MMI} =3L_c/2 where L_c is approximately given by (2.3). But for the tapered MMIC, it is given by [20]

$$L_{c^*} = \frac{4n_{eff}(W_0 \cdot W_1)}{3\lambda} \tag{4.11}$$

Thus, $L_{c^*} = L_c W_1 / W_0$. Usually when tapering is concerned, the normalized width variation $d\Omega$ is employed. $d\Omega$ can be expressed as[17, 18, 20]:

$$d\Omega = \frac{(W_0 - W_1)}{W_0} \tag{4.12}$$

In bigger sized MMICs, an often used method of tapering is the parabolically tapered device. In such devices, L_{c^*} is defined [19] as $L_{c^*} = L_c / \chi$ where 1/χ is the length reduction brought on by the net relative phase change over the taper region. 1/χ can reasonably be approximated as 1/χ≈1-1.25×$d\Omega$ when 0≤ $d\Omega$ ≥0.4 [19]. Linear tapering will cause the splitting ratio to deviate more substantially as $d\Omega$ increases because of the phase changes sustained at the midplane of the device [20]. However, since $d\Omega$ tends to be smaller than 0.2, these deviations are found to be negligible. As such, we have opted for linear tapering to reduce our MMI lengths. The simulations confirmed a reduction of ~10% in length without affecting performance and severe loss. Fig. 4.2.5(a) is an FDTD simulation of a 3μm wide Bow Type I MMIC with a D=2.0μm port pitch where the 3dB coupling length is ~23.0μm. Fig. 4.2.5(b) shows the simulation results of a Bow Type II case where W_{MMI}=6.0μm, $d\Omega$ =0.167 which is the same as the Bow Type I MMIC and all other parameters remain the same as the Bow Type I MMIC for comparative reasons as tabulated in Table 4.3. All the numerical values are in μm. The splitting length for the Bow Type II is slightly longer than the Bow Type I and no 3dB is apparent for the Type II across the wavelength bandwidth.

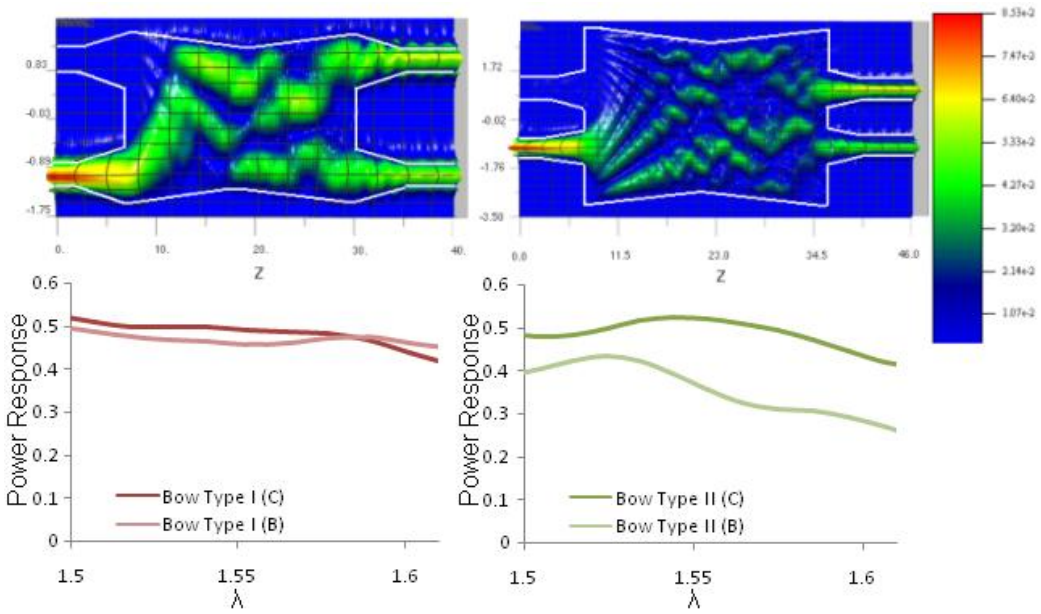

(a) (b)

Fig.4.2.5. Simulation of (a) Bow TypeI MMIC and (c) Bow Type II MMIC using Optiwave FDTD. The top part is the field simulation of the software and the bottom part is the plotted output amplitude against wavelength. The design parameters for these devices are indicated in Table 4.3.

TABLE 4.3: Design values for 2x2 3dB Bow Type I and II MMICs

Bow Type I with tapered AWs				
W_o	W_1	D	W_{port}	L_{MMI}
3.0	2.5	2.0	1.0	27.0
Bow Type II with tapered AWs				
W_o	W_1	D	W_{port}	L_{MMI}
6.0	5.0	2.0	1.0	29.0

(C) Un-tapered MMIC with offset AWs

The problem for un-tapered compact MMIC lies in its narrow width, where only limited number of modes would fit in. When structures are smaller than 1μm, there is a major concern on the precision of power splitting in such devices. The BPM simulations often show that the MMICs in smaller size starts displaying a combination of basic directional coupling and self-imaging due to the reduced number of modes inside the MMI body. A conventional MMIC usually must have more than 3 modes to work properly. Where compact structures are concerned, these devices tend to exert characteristics which are similar to that of directional coupler as well, a phenomenon which is the inverse of what occurs when the height of the gap between a directional coupler is

varied as previously discussed in Chapter 2. We try to avoid excessive directional coupler characteristic because directional couplers have more selective wavelength selection and this encumbers broadband efforts.

In order for a restricted interference MMI (or Type II MMI) to be shorter in length than a Type I MMI ($L_{TypeII} < L_{TypeI}$), the separation gap between the access waveguides (edge to edge or (D-w)) will have to be less than 0.37w. In compact MMI cases with untapered AWs, the AW gap distances need to be at least w or wider. Simulations to determine appropriate gap distances had been discussed earlier in this section. Since the pre-determined gap was ≥0.60μm or ≥1.33w, Type II MMI was found to be unsuitable in compact MMI cases. Although Type I MMI would offer the shortest possible MMI lengths, the simulation results showed that the 3dB coupling failed to be realized. Fig. 4.2.6 shows that instead of equal splitting, the cross coupler arm has significant loss. The L_π calculation based on simulated effective indices for the 1.35μm wide MMI is 4.35-3.64μm for the wavelength range of 1480-1550nm. Based on this value, the estimated MMI length ($3/2L_\pi$) for a Type I 3dB coupling should be around 6.5-7.0μm. The simulation results however, indicated that at these lengths, the 3dB splitting is distorted. Similarly, the self-imaging which should appear at $3L_\pi$ has also been distorted due to the smaller dimensions. Instead of a full coupling to the cross access waveguide, a portion of light is lost.

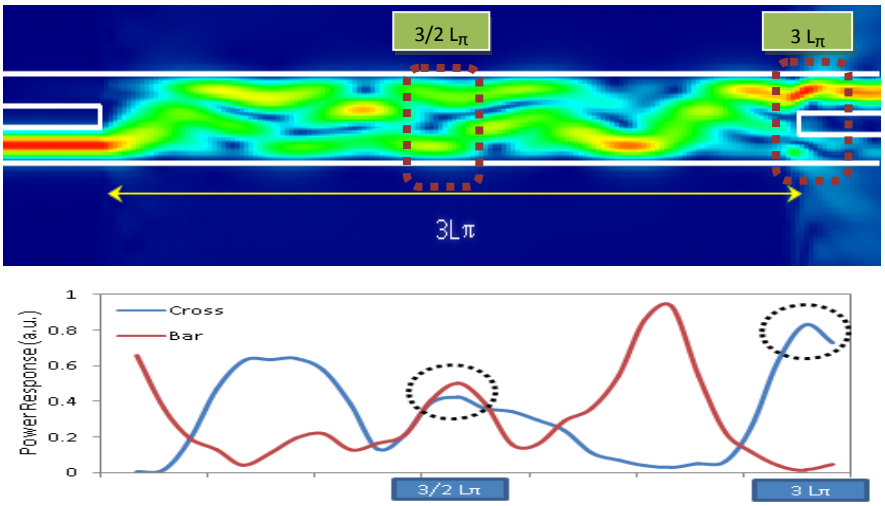

Fig.4.2.6. Simulation of a Type I MMI for the length of $3L_\pi$

The problem here lies not with the limitation of the numerical softwares used. Instead, the size of the MMIC is what affects this change. One reason

why the 3dB splitting did not occur at the estimated length would be that the W_{eff} in equation (2.3) which refers to the effective width of MMI in this case is much wider than the physical width of the MMIC. But this does not explain why the 3dB splitting is no longer equal. The main reason for this would be that an MMI width with insufficient modes interference to take place would also start to exhibit directional coupler characteristics. This in turn would cause the output power response pattern to be distorted. A solution to both these problems would be to widen the MMI width. However, sufficient changes to the MMI width to avoid such problems would result in lengthening of the device, and this would ultimately defeat the aim of reducing the MMI dimensions. Instead, we found that if the MMI width is fixed but the AWs were kept slightly away from the MMI sidewalls (see Fig. 4.2.4(a) *(bottom)*) the distortion of the optical field at $3/2L_{\pi}$ becomes less pronounced. We named these MMIs with a slight offset of AWs from the edges as Type I* MMIC. Although some imbalances still seem to exist, the simulation results of Type I* MMIC showed marked improvement over those of Type I. Due to the narrow widths of the AWs, the waveguide modes tend to spill out of the channel as the simulation results indicated in Fig. 4.2.1(b). In other words, the effective width of the access waveguides is larger than 0.45μm. Therefore, if the AWs were placed right at the edge, then, when one side suddenly expanded while the other side remains the same, the sudden asymmetrical change will cause an imbalance. This compounded with the diffraction from the MMI side walls would lead to a change in the self-imaging pattern. Although this change goes in tandem with MMI waveguides, in this case the MMI width with reference to the mode size is much smaller, thus magnifying the effect of the diffraction caused by the modes at the MMI sidewalls. With the offset, this imbalance is less pronounced. To demonstrate this, the simulation for these two devices- the Type I MMIC and Type I* MMIC – with the fixed MMI width of 1.90μm is shown in Fig. 4.2.7. The simulation results confirmed that when the input waveguides were placed 0.2μm away from the edge of the MMI, the 3dB coupling is more clearly exhibited. The FDTD simulations in Fig. 4.2.7(a) also indicated that at positions where compact Type I* have 3dB splitting, Type I MMICs have an additional loss caused some additional interference remnants.

The splitting ratio in Fig. 4.2.7(b) is calculated by dividing the output in each output arm with the input intensity. They do not add up to 1.0 in cases where there are losses. In the cases where Type I* MMIC is simulated, they consistently have equal splitting ratios although as the width reduces (<1.65μm) the smaller offsets losses its effectiveness in maintaining the 3dB splitting.

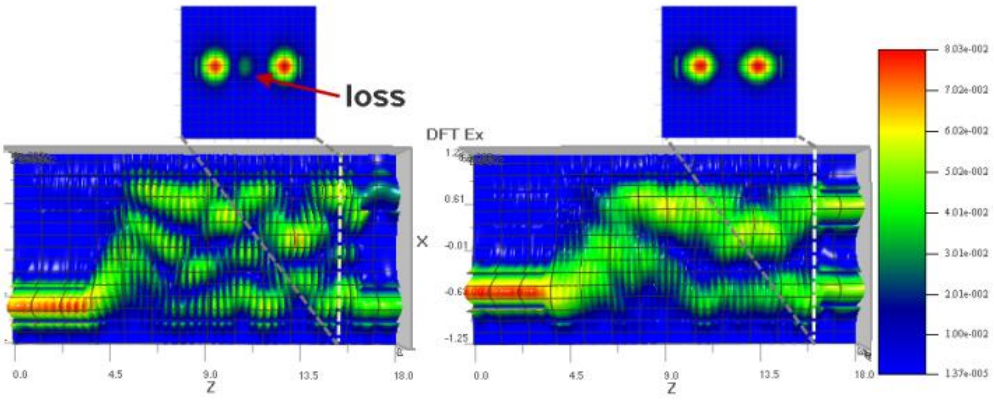

(a)

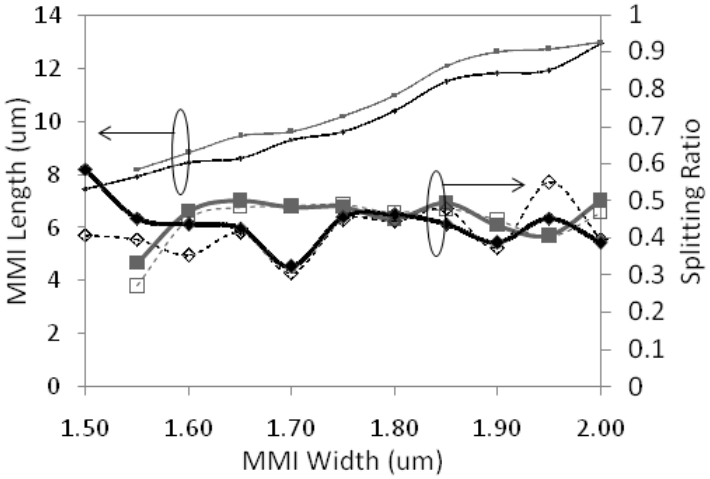

(b)

Fig. 4.2.7. (a)The left simulation illustrates a Type I MMI and the right simulation is a Type I* MMI. Both MMIs are 1.90μm wide. The Type I* MMI has a port pitch of 1.05μm. (b) Simulated Type I and Type I* MMI for MMI width 1.50 to 2.00μm wide shows different MMI lengths and splitting ratios for both cases. Black color plot denotes Type I MMI and Gray color plot denotes Type I* MMI. Bold lines are for the bar coupler and detached lines are for the cross coupler.

For the case of Type I MMIC, at lengths where equal power splitting was present, the losses were clearly too high (splitting ratio <0.3 for both arms). Therefore, in the Fig. 4.2.7(b) graph, the results plotted were at lengths where although splitting ratios are less equal, losses are less. The graph also shows that although Type I MMIC has a slightly shorter length (~0.3-10% shorter) compared to Type I* MMIC, its overall unpredictable splitting behavior and

additional loss renders it less suitable for reduced size MMI device. The smallest simulations we have attempted is a 1.45μm wide MMI with a port pitch of 0.9μm. The simulations indicated that a Type I* MMIC in such dimensions could be as short as 6.0μm for 3dB coupling to be realized. Although we have yet to realize such dimensions, in the next sub-section, the designs of slightly bigger dimensions had been verified experimentally.

4.2.2 Experimental Verification

For the SOI based material, the wafers used have been fabricated using the advanced CMOS research environment of the LETI (France) with cooperation from Interuniversity Microelectronics Center (IMEC) in Belgium [22, 23]. The devices consist of photonic wire waveguides with 200-nm thick silicon layer grown on 1-μm thick SiO_2 buffer layer on 200-mm Si wafers. Photonic wire (PW) waveguides are strongly confined in both the x and y transverse dimensions due to high index contrasts.

The MMI were characterized using transmission measurements. For ease of optical in-coupling and out-coupling, grating couplers etched in 10-μm broad ridge waveguides are integrated with the access waveguides of the MMI devices [29]. Standard single mode fibers were positioned above the substrate at a 10˚ angle off vertical axis and couples just one fiber polarization into the waveguide TE mode [21]. The coupling efficiency is about 30% and has a Gaussian spectral profile with a bandwidth of about 30nm. The couplers are adiabatically tapered to the single mode photonic wire (~0.45μm wide) waveguides going into the MMI. The photonic wire waveguides fabricated have propagation losses as low as 0.24dB/mm [27]. The devices are excited with a broadband source with a wavelength ranging from 1.42μm to 1.61μm. The output power is then passed through a 90:10 splitter, where 10% of the power goes to a fiber power meter that helps to indicate alignment accuracy whereas the remaining power goes into an optical spectrum analyzer (OSA) for

normalization with the input spectrum. Fig. 4.2.8(a) shows the fabricated grating couplers with tapers connecting them with the MMIs (Fig. 4.2.8(b)-(d)).

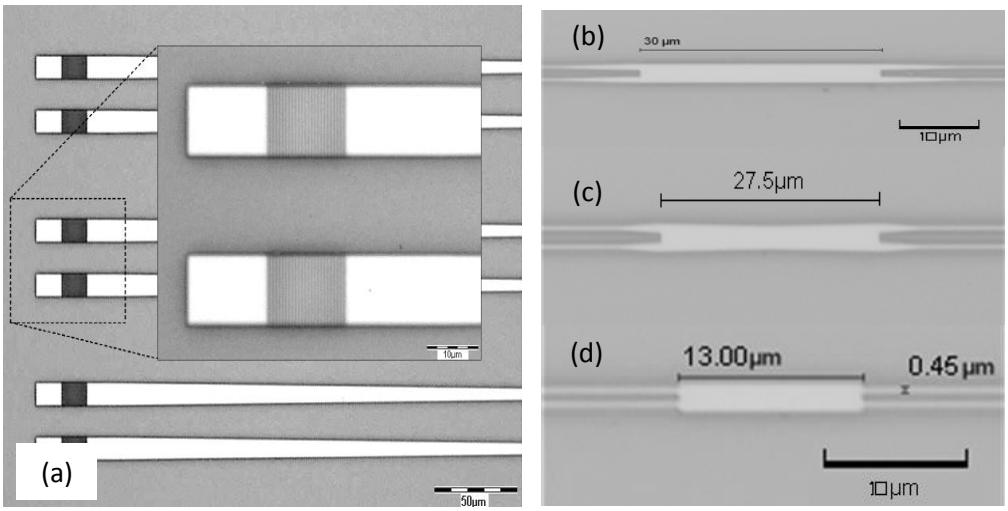

Fig.4.2.8. (a) Fabricated grating; (b) Type I MMIC with tapered AW; (c) Tapered MMIC and AW (d) Un-tapered MMIC

In order to determine whether a device is working as a 3dB splitter, the often used parameter is the value of its insertion loss (=*-10log(Pr/Pin)*) as defined in (4.7) where *Pr* in this case would be the optical intensity collected either at the cross or bar arm of the AW via OSA. The *Pin* here was obtained by collecting the output power of a single straight waveguide with adiabatic tapers and grating at each end which have been fabricated alongside the MMI devices. When the insertion losses for both arms are at 3dB, this means that the device is able to achieve 3dB splitting or 50:50 splitting without any device loss.

The first set of device fabricated was a set of Type I MMIC with the width of 3µm and tapered AWs. The tapered lengths are L_{taper}=10µm resulting in a total device length of 46 to 54µm. Table 4.4 tabulates the parameters of the devices under test (DUTs). The experimental results were put in the same graph as the simulated insertion loss generated using the Apollo 2D-BPM software. From fine comparison between the experiment and simulation results in Fig. 4.2.9(a), it was found that the simulation results attributed higher insertion loss to length variation as compared to actual experiment results. The figure indicated that the experiment results (bold lines) are lower than the simulated results (detached thin lines). This implied that the compact MMIC is less sensitive to length variation than was initially assumed and is another positive

indication that it is less susceptible to loss caused by device length related fabrication errors.

The excess loss (defined in chapter 3 as $-10\log\frac{P_{In}}{P_{Out}}$) for the device TI-3 for the wavelength range of 60nm as shown in Fig. 4.2.9(b) is below the 0.6dB average. The splitting ratio, obtained by dividing the output optical power from each arm with the summation of both arms (P_{out}), are also depicted in the figure. 2D FDTD simulations results based on the Optiwave simulation software have been included as insets for comparison purposes. The device consistently displayed linear 50:50 splitting for the 60nm wide wavelength range with power balance uniformity of ±5%, which signifies their suitability for broadband use. Although these MMIC devices with tapered access waveguide outputs yielded good results, even with further reduction in width and length, the overall lengths for these devices are much too long for compacting purposes.

TABLE 4.4: Device parameter variations for Type I MMIC (TI –1 to 5)

Device	Wport	D	W_0	L_{MMI}	L_{taper}	Wall offset	Total Overall Length
TI - 1	1	2	3	26	10	0	46
TI - 2	1	2	3	27	10	0	47
TI - 3	1	2	3	30	10	0	50
TI - 4	1	2	3	33	10	0	53
TI - 5	1	2	3	34	10	0	54

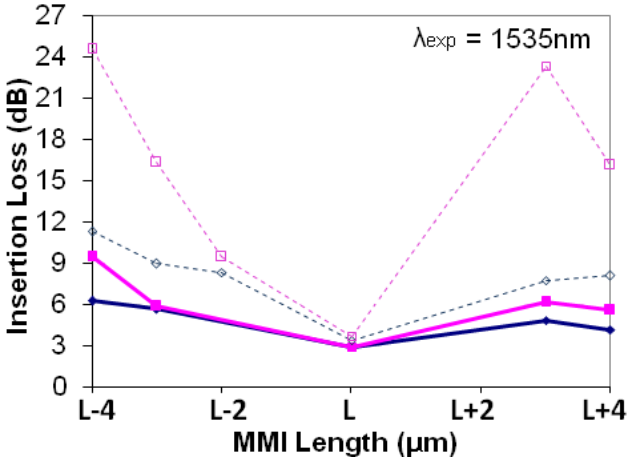

(a)

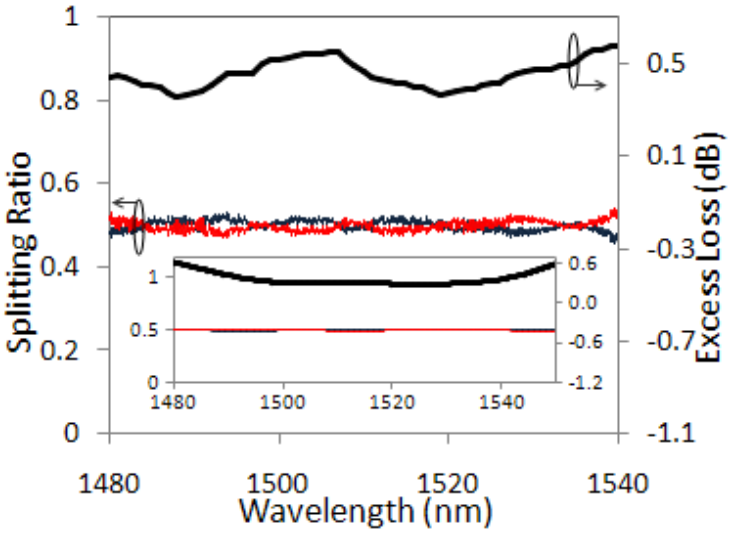

(b)

Fig.4.2.9. (a) Type I MMIC with tapered access waveguides where diamond shaped markers denote the bar output and square markers the cross outputs. The bold lines are experimental results and the dashed lines are simulation results. The experimental L=28μm and simulation L=32μm; (b) Excess loss and splitting ratio plot of the TI-3 MMIC DUT (Inset: Accompanying FDTD simulation results)

In the second set of 3dB devices, Bow Type I MMIC with the dimensions of W_0=3 and W_1=2.5 with 5μm long tapered AWs and varying lengths were fabricated. The total length of these devise were ~50% shorter than that of the previous set. The dimensions for the DUTs are indicated in Table 4.5 below. Comparison of simulations and actual experimental results indicated that for the Bow Type I case, the actual device proofed to be lossier than simulation values (Fig. 4.2.10(a)). Excess loss was markedly higher than that of the Type I MMI with tapered AWs and exceeded 2.5dB after 40nm of wavelength as shown in Fig. 4.2.10(b). This could be attributed to MMI's sensitivity towards sidewall roughness where MMI tapering is involved. The splitting ratio started to diverge from 50:50 after about 40nm of wavelength bandwidth. The experimental results from this fabricated device is an indication that tapering MMIs ($d\Omega$ =0.167) may not be a suitable choice for size reduction purposes.

TABLE 4.5: Device parameter variations for fabricated Bow Type I MMIC device

Device	W_{port}	D	W_0	W_1	L_{taper}	L_{MMI}
Bow - 1	1	2	3	2.5	5	23.0
Bow - 2	1	2	3	2.5	5	26.5
Bow - 3	1	2	3	2.5	5	27.0
Bow - 4	1	2	3	2.5	5	27.5
Bow - 5	1	2	3	2.5	5	28.0

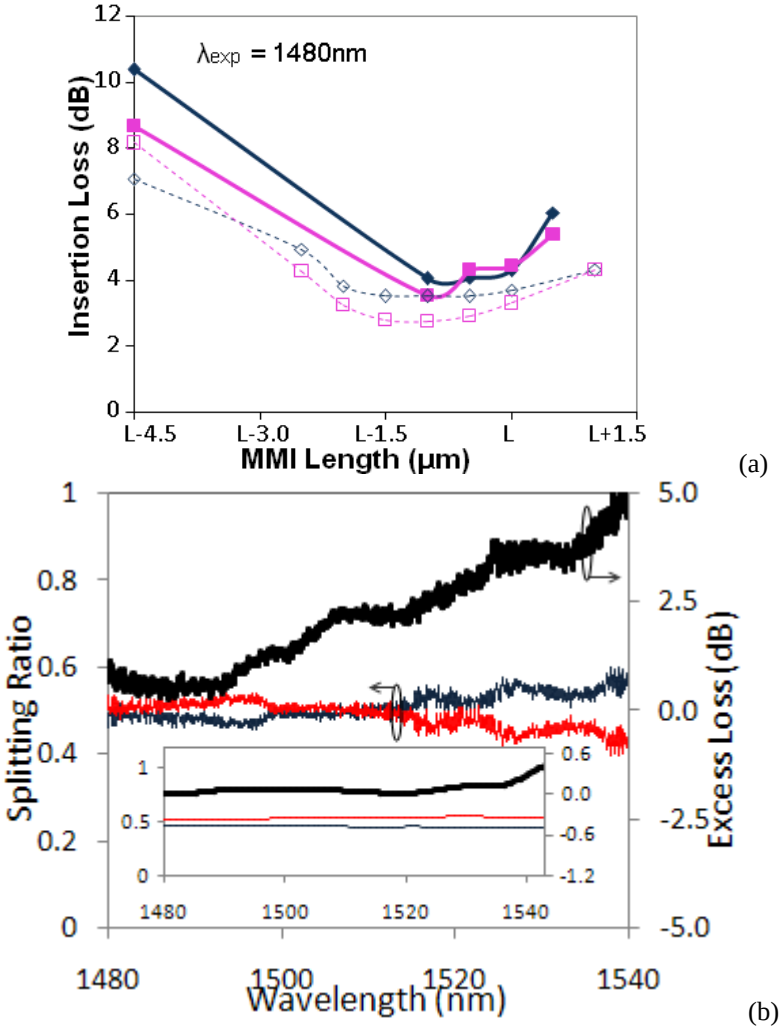

Fig.4.2.10. (a) 3μm wide Bow Type I MMIC which tapers to 2.5μm width at the centre. The L indicated is 27.5μm for experiment and 29.5μm in simulations. Diamond (square) shaped markers denote bar (cross) outputs. The bold lines are experimental results and the dashed lines are simulation results; (b) Excess loss and splitting ratio plot of the experimental results for Bow Type I MMIC (Inset: Accompanying FDTD simulation results)

In the third batch of fabricated devices, Type I* MMICs the lengths of 13 to 17μm were fabricated. Table 4.6 lists the parameter variations associated with these devices. Although the BPM simulation results indicated that 50:50 splitting ratio would occur with an additional 1dB of insertion loss in both arms, the experimental results as shown in Fig. 4.2.12(a) gave a 3dB splitting which was better than expected. Fig. 4.2.11(b) shows that the excess loss remained well below 1dB, indicating it as a less lossy device than the Bow Type MMIC.

TABLE 4.6: Type I* 3dB MMIC coupler fabricated for testing (T1*-1 to 5)

Device #	w	L_{MMI}	Wall offset	D	W_{MMI}
TI* - 1	0.45	13	0.325	0.9	2
TI* - 2	0.45	14	0.325	0.9	2
TI* - 3	0.45	15	0.325	0.9	2
TI* - 4	0.45	16	0.325	0.9	2
TI* - 5	0.45	17	0.325	0.9	2

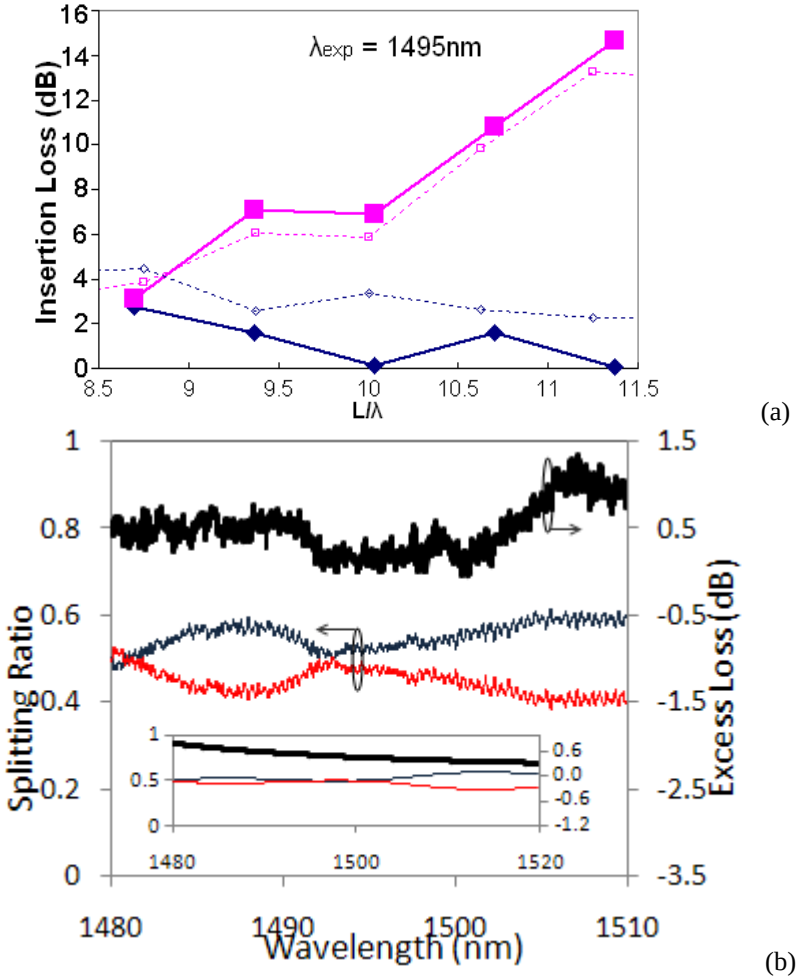

Fig.4.2.11 (a) Experimental data and simulated result at the wavelength of $\lambda_{simulation}$=1600nm and $\lambda_{experiment}$=1495nm. Diamond (square) shaped markers denote bar (cross) outputs. The bold (dashed) lines are experimental (simulation) results. (b) Excess loss and splitting ratio plot of the experimental results for TI* - 1 MMIC (Inset: Accompanying FDTD simulation results)

The results verified that the fabricated Type I* MMICs worked well with minimal loss at the mere length L_{MMI}=13μm without the need for any kind of tapering albeit for shorter (~30nm) wavelength bandwidth. In conclusion, the rectangular shaped Type I* MMIC was found to have lower insertion loss as compared to the Bow Type I MMIC. This was due to the fact that the MMI is more severely affected by the roughness of the tapering sidewalls. In the Bow Type I MMIC cases, the simulations also seemed to indicate less accuracy in

determining splitting ratio and excess loss when FDTD method is employed. The insertion loss is less affected by the device size than device shape. The shortened length of the device also helps reduce the propagation loss of the multimode device. Based on the experimental results for MMIs with lengths shorter than 30μm, there are some length differences between simulation and experimental results of about 1-4μm which can be attributed to the systematic error of the 2D numerical simulations. Having fabricate MMI with tapered AWs and with/without tapered MMIs with relatively good splitting ratios, we then verified that SOI MMI as small as 13μm is possible without fritters like tapers. We believe that smaller Type I* MMI devices are possible, and insertion loss is often lower than simulations have depicted. In the following section, a 80:20 splitting MMI device is demonstrated.

4.2.3 80:20 Wedge Splitter

When it comes to arbitrary ratio power splitters, the use of a standard rectangular geometrical design MMIC would only offer a few discrete values (50:50, 100:0, 85:15, 72:28) of the splitting ratios [30, 31], which was why a few other methods have been utilized down the years, among them, the butterfly MMI [20] and the angled MMI [32]. The basic working principles of these various design is that by introducing tapering into the MMI model, the symmetrical tapering is equivalent to introducing a phase-shifter which is very much like an MZI but with the phase shifter waveguides in between the couplers exchanged with the broader and tapered MMI portion.

Instead of adhering to these designs, which aimed to alter the power splitting ratios for a range of *any* splitting ratio between that of 50:50 splitting to 100:0 splitting, we concentrated instead on observing the shifting of the output away from the 50:50 through the manipulation of the wedge variation, $d\Omega$. Studies on how higher $d\Omega$ would affect the splitting ratio was carried out by Levy, et al. back in the late 90s [18]. The studies indicated that a linearly tapered design would deviate from its 50:50 splitting ratio as $d\Omega$ increased, and at the cost of transmission loss. We extended this study to concentrate on a smaller $d\Omega$ variation so that the transmission (excess) loss would be within

acceptable limits, and instead of the Bow Type I like design employed, we chose instead to apply a wedge design.

A Wedge splitter is similar to a Bow Type MMI in that both types of MMI have tapering. However, for the wedge design, instead of tapering at the centre, the tapering is at the end of the MMI, which results in an MMI which is shaped like a wedge, hence the name. We opted for this asymmetrical design for a few reasons, the main reason being, given the length of the shorten MMIC, a Bow Type design (which we have had experience measuring) would result in an excess loss which is higher than what simulation predicted as shown in Fig. 4.2.10, whereas a wedge would give a similar $d\Omega$ at a lower sidewall taper gradient. Fig. 4.2.12 shows the dimensions of a wedge splitter with tapered AWs.

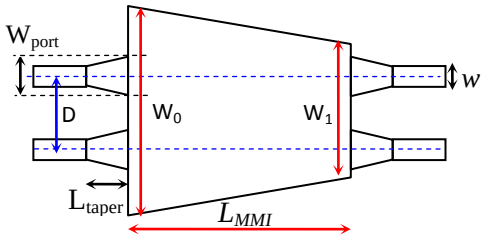

Fig. 4.2.12 Schematic illustration of a Wedge Splitter where design parameters have been noted

The wedge width can be defined as:

$$W(z) = W_1 + (W_0 - W_1)\left(1 - \frac{z}{L_{mmi}}\right) \qquad (4.13)$$

2D-FDTD simulations based on the similar material base and layer structure were undertaken. As per the 3dB MMIC designs, the first part of the design was to determine a fixed minimum gap distance. In this wedge design, we used a narrower gap separation (0.45μm) which is the width of the AWs and set the port distance, D as 0.9μm. The W_{port} and L_{taper} are 0.8μm and 5.0μm respectively whereas w remained as 0.45μm. While the wider end of the wedge is fixed at W_0 = 3.0μm, which is 0.3μm wider than width of a Type II MMI device, FDTD simulations of varying $d\Omega$ are run to observe the splitting ratio trend and excess loss results as shown in Fig. 4.2.13(a). The minimum W_1 is

($D+W_{port}$) which are equivalent to a maximum $d\Omega$ of 0.433. The plotted simulation results are for the fixed wavelength of 1500nm in order to reduce too many changing variables. The excess losses increased with increasing $d\Omega$, but remained less than 1 dB until $d\Omega$ > 0.333 which is comparable lossier than the results of the parabolically tapered MMI proposed by other research [18] . Based on the results obtained, we selected a $d\Omega$ for our design ($d\Omega$ = 0.2) which would offer a transmission of 90% or above which translates to an excess loss of <0.45dB. The splitting ratio we obtained indicated that as $d\Omega$ gradually increased to the dimensions' limits, the splitting ratio could reach a maximum of close to 95:5.

While the splitting ratio of the Wedge splitter is gradually being altered, the length of the device also becomes substantially shorter as $d\Omega$ is increased, due to the reduction in the average width of the device. This length varies approximately linearly with $d\Omega$ as shown in Fig. 4.2.13(b). Using a linearly tapered device with $d\Omega$ = 0.433 yields almost a factor of two decrease from the length of the straight device with $d\Omega$ = 0. For comparison, Fig. 4.2.13(b) also shows the comparable Type II MMI device with W_0 = W_1 = 2.7μm (solid square along y-axis). The 80:20 Wedge splitter device design at $d\Omega$ = 0.2, and W_1 = 2.4μm with simulated 0.44 dB of loss (8.8μm) is ~17% shorter than the 50:50 standard rectangular geometrical MMIC device.

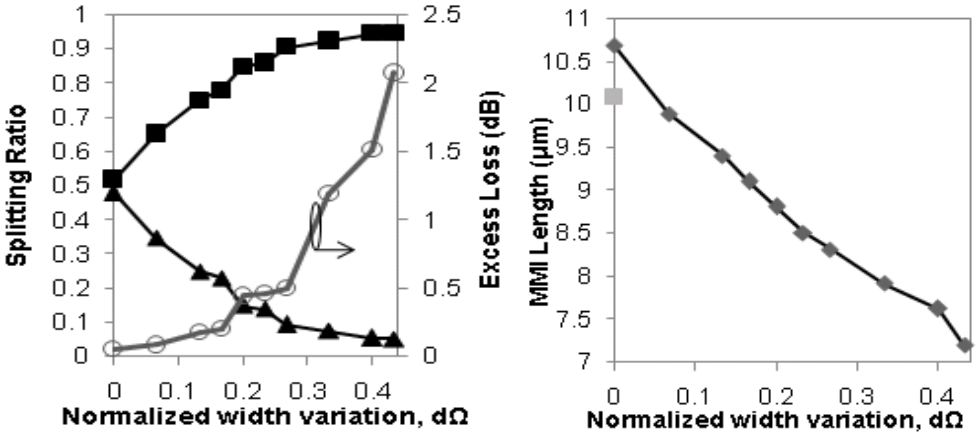

(a) (b)

Fig. 4.2.13 (a) Simulations of splitting ratios versus normalized width variations $d\Omega$, for the Wedge splitter device. The solid triangles and squares represent the cross and bar outputs, respectively. The un-tapered device is obtained at $d\Omega$ = 0. The open circles show the device's total power output. (b) Device length versus the normalized width variation for the Wedge splitter device (diamond). The solid square is the comparable un-tapered, Type II MMI device with W_0 = W_1 = 3.0μm.

We then validated the Wedge splitter design by measuring an actual device. The fabricated wedge has the dimensions of W_0=3.0 and W_1=2.4 ($d\Omega$ = 0) with length, L_{MMI} of 8.4 to 9.2µm. For comparative reasons, simulation of the splitter's splitting ratio and excess loss has been plotted in Fig. 4.2.14(a). The inset is the optical field simulation results of the device. Comparing the simulation results to the actual experimental results in Fig. 4.2.14(b), one would find that the simulated splitting ratio is closer to 85:15 and that the splitting ratio is less affected by change in wavelength. The lower part of the graph in Fig. 4.2.14(b) shows the splitting ratio of the fabricated splitter. The difference in the splitting ratio could be chalked up to refractive index differences between that of the actual device and simulated device. Often, simulations at different lengths are run in order to find the most fitting curve. Although the splitting ratio steadily changed over the 60nm wavelength span, the gradual change is not too severe to impede device performance. The excess loss for the wedge type MMI 80:20 (Cross: Bar) splitter as plotted in the same figure, can be as low as 0.88dB, an indication that such a small device is able to perform as a reliable splitter.

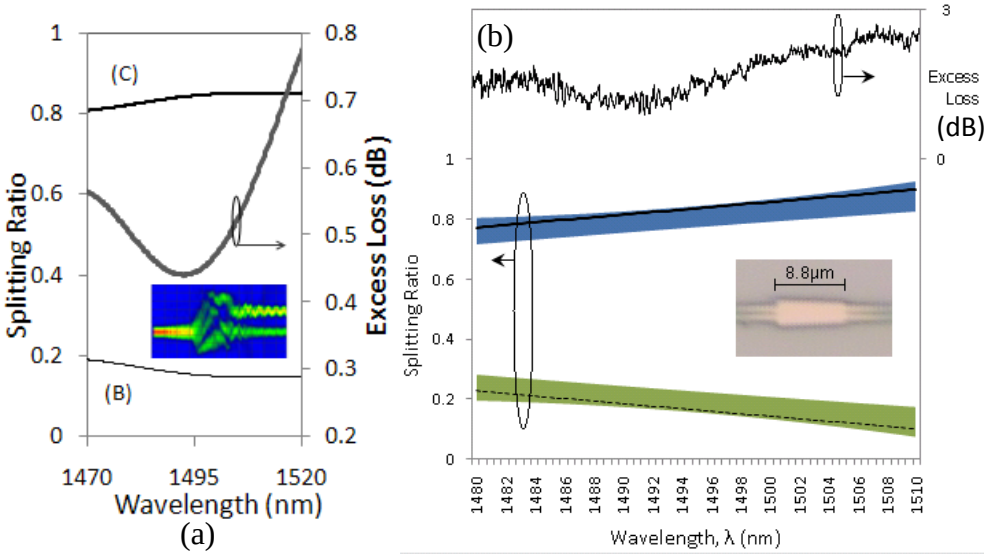

Fig.4.2.14. (a) Simulation and (b) experimental results for an 8.8µm long 80:20 (Cross: Bar) MMI splitter. For (a), the bold (C) and thin (B) lines represent the cross and bar results simulated for the device along with the simulated excess loss in dB. For (b), the bold and detached lines represent the cross and bar result line fit result obtained from the 8.8µm long device. Shaded area denotes measured shift in ratio when MMI length is varied from 8.4 to 9.2µm. Excess loss is plotted above the splitting ratio. Inset picture is a microscope capture of the device.

Conclusion

MMI devices as standalone passive components which are able to perform splitting with very compact sizes have been demonstrated in this chapter. The two examples here were the wavelength splitters based on BCB material and compact 3dB splitters for ring-resonators and MZIs based on SOI material.

With these devices, it has been shown that it is possible to achieve splitting results for two different types of materials and dimensions. For the case of compact MMIs, we have demonstrated on SOI, fabricated using DUV lithography, MMI devices as standalone passive components are able to perform splitting even with very compact sizes. A considerable reduction in size is obtained using high-contrast photonic wires with strong confinement and therefore sharp bends and high group index. Instead of the conventional tapered MMI with tapered AWs or Type I MMI, we have employed an MMI design, with the dimensions of $2x13\mu m^2$ (width x length), which instead can retain the compactness of edge port coupling without erring in the 3dB splitting ratio that the miniaturization of such conventional design usually entails. We have also demonstrated an 8.8μm short 80:20 wedge splitter which is possibly the smallest of such device to date.

Chapter 5

Electroabsorption Modulator

In this dissertation, the integration of MMI with electroabsorption modulator (EAM) involves the MMI which is the passive device and the EAM which is an active device. The electroabsorption modulator (EAM) is based on a multi-quantum well (MQW) material. It is one of the most compact and efficient optical modulators that have been developed over the past thirty years. The EAM waveguide modulator is a field-effect device and consists of a *p*-*i*-*n* semiconductor structure in a waveguide configuration, as shown in Fig. 5.1.1. The reverse biased electric field is applied across the intrinsic (*i*) layer between two electrodes formed on the p- and n-doped layers. It may also be forward biased in which case it may serve as an optical amplifier under suitable condition.

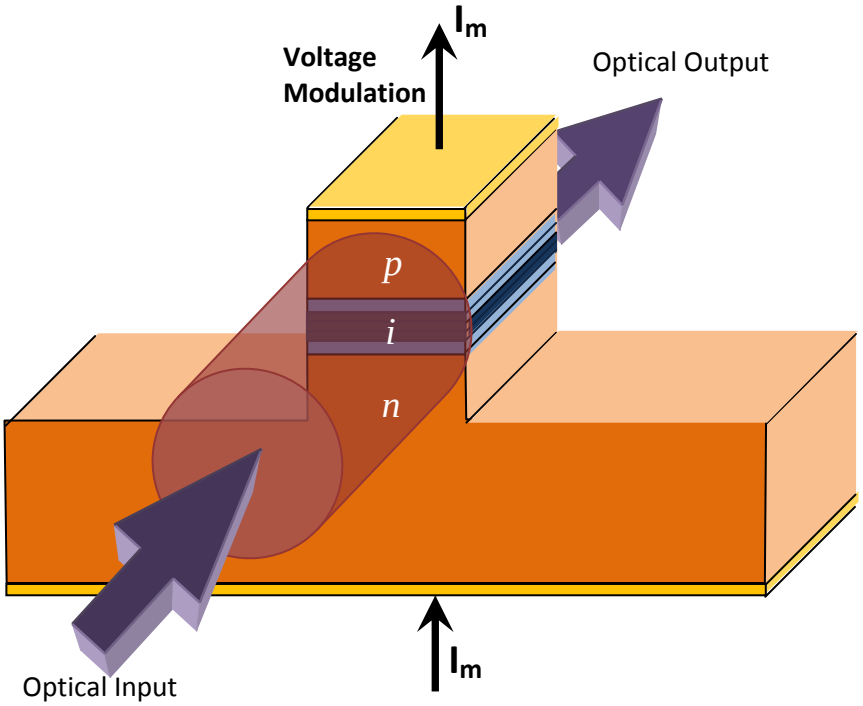

Fig.5.1.1. Illustration of EAM structure and operation

The intrinsic layer, which is also the core of the waveguide, has a higher optical refractive index and smaller energy bandgap than the p-type and n-type

doped layers which sandwich it. When light from an input fiber is coupled into the waveguide, the intrinsic layer holds the largest optical power intensity. This ensures a good overlap between the optical and electric field. The lateral optical confinement is usually achieved by etched waveguide mesa. The bandgap of the undoped absorption layer is slightly larger than the photon energy of the modulated light, the difference being known as the detuning energy. Without external electric field, the absorption layer has little absorption to the light; but when a bias voltage is applied, an external electric field will be present, the absorption edge will shift to lower energy, and the absorption coefficient will increase rapidly. This is the "electroabsorption effect". Our EAM waveguides are made up of multiple quantum wells (MQW), thus, the dominant electroabsorption effect is the quantum confined Stark effect or QCSE. Due to this effect, the optical power transmitted from the EAM will change in response to the reverse bias voltage applied to the *p*-*i*-*n* junction; which is the basis of the optical modulation in the device. The photo absorption creates electrons and holes which are swept away from the absorption region by the electric field forming the external photocurrent.

The QCSE is illustrated in Fig. 5.1.2. Electrons and holes generated in and around the quantum wells are strongly confined within the well in well-defined energy levels, and orbit each other forming *excitons*. The strong overlap between their wavefunctions gives rise to strong excitonic absorption resonance. There are two types of holes: the transition between the lowest heavy-hole and light-hole energy levels in the valence band and the lowest electron level in the conduction band gives rise to two lowest transition energies corresponding to the first heavy-hole and light-hole excitonic peaks, respectively, in the absorption spectrum. The absorption transitions are governed by certain selection rules which depend on the photon polarization. The TE polarization is coupled more strongly to the heavy hole while the TM polarization couples only to the light hole, thus the two polarizations give rise to different absorption spectra. The shape of these absorption peaks, and the corresponding transition energies, can be controlled by varying the well width and the well potential depth (i.e., the relative well and barrier bandgaps). The potential depth depends on the material compositions while the well width can be controlled by epitaxial

growth. Finally, the excitonic peak amplitudes and the transition energies are highly sensitive to electric fields, and thus can be controlled externally. This is the basis of the QCSE EAM.

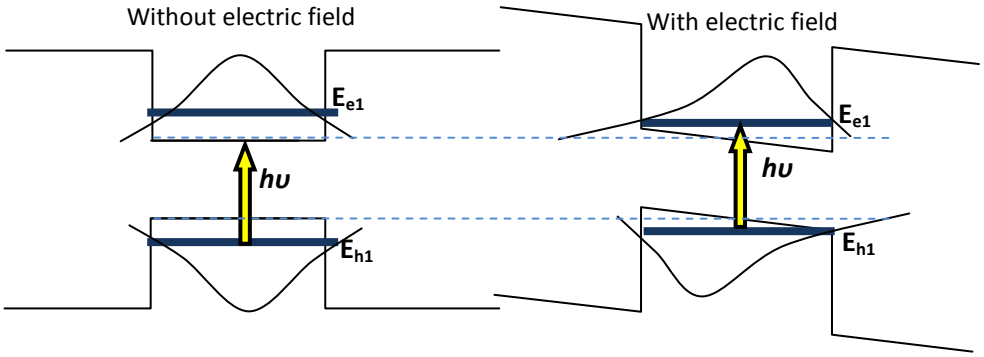

(a) (b)

Fig.5.1.2. Band diagram for a single quantum-well to show quantum-confined Stark effect

The modulation effect of an EAM for a light beam is optimized for a specific wavelength and a specific polarization. When there is no electric field present, the photon energy of the modulated light is lesser than the lowest relevant (i.e., heavy-hole or light-hole) absorption peak by a small detuning energy of about 30-50 meV. The optimum detuning energy will depend on the sharpness of the absorption resonance which, in turn, depends on the well width. In the presence of electric field, the energy band becomes tilted, changing the electron and hole confinement energies and their wave-functions (see Fig. 5.1.2(b)). The transition energy is reduced, thus increasing the photo-assisted transition rate or absorption while reducing the resonant peak amplitude due to the smaller overlap integral [1].

Although the electroabsorption mechanism is highly efficient and the resulting device highly compact (and integratable with other devices such as lasers), the EAM (especially that based on QCSE) has certain drawbacks compared with other types of modulators such as Mach-Zehnder interferometer based electro-optic modulators (MZM). EAMs are much more sensitive to wavelength and thus have small optical bandwidth, higher temperature dependence, relatively unstable transfer curve and non-zero chirp. Chirp refers to the change in refractive index that accompanies the change in absorption, resulting in a broadening of the optical signal bandwidth. These are the prices

paid for the efficiency of the intrinsic mechanism used in EAM, which is contingent on the proximity of the operating wavelength to the resonant absorption edge of the semiconductor material.

5.1 Lumped element EAM

In order to design a serviceable EAM which is simple and effective, the EAM modulation efficiency parameters have to be understood. These parameters are rooted in the EAM transfer curve which has been illustrated in Fig. 5.1.3. The modulator transfer curve is defined as the optical transmission factor as a function of the modulator voltage, which can be written as:

$$T(V) = t_{ff} e^{-\gamma \Delta\alpha(V) L} \tag{5.1}$$

where γ is the optical confinement factor defined as the ratio of the optical power in the absorption layer to the total optical power in the waveguide; $\alpha(V)$ denotes the absorption change due to the non-zero voltage, V applied to the EAM; L is the waveguide length and t_{ff} denotes the EAM insertion loss, which is the fiber-to-fiber loss for the EAM at zero voltage. t_{ff} can be broken up as:

$$t_{ff} = C^2 e^{-\alpha_0 L} \tag{5.2}$$

where C is the optical loss factor at both facets of the waveguide. Optical loss factor includes the mode coupling loss between that of the EAM waveguide and the optical fiber and the reflection loss. α_0 is the optical attenuation coefficient in the waveguide at zero bias voltage. The attenuation is caused by certain loss mechanisms such as the scattering loss at the waveguide sidewalls and at the layer interfaces, the free carrier absorption loss in the doped layers and the photo absorption loss in the intrinsic layer.

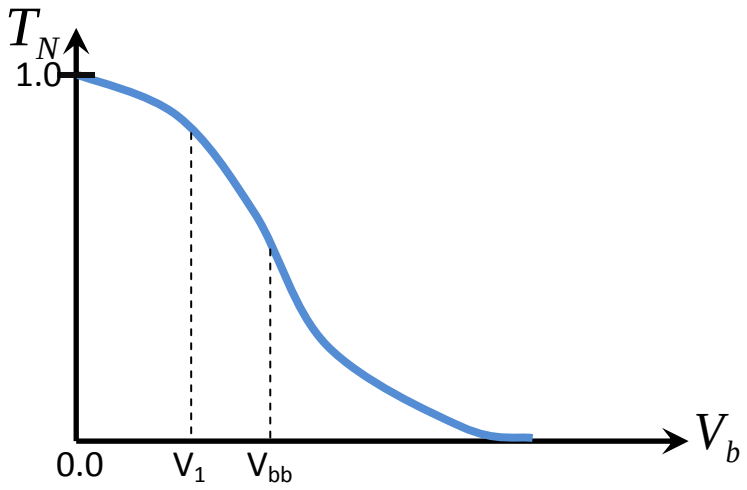

Fig.5.1.3. An illustration of an EAM transfer curve

Since the EAM transfer curve is often normalized at zero modulator voltage (zero bias voltage), $T_N(V) = e^{-\gamma \Delta\alpha(V)L}$ can be denoted as the normalized transfer curve. During modulation, the total modulator voltage consists of DC bias voltage V_b and radio-frequency (RF) modulation voltage ν_m. Under small signal (ν_m) approximation, the modulator transmission factor is then

$$T(V) = t_{ff}\left[T_N(V_b) + T_N^{'}(V_b)\nu_m\right] \qquad (5.3)$$

where $T_N^{'}$ is the derivative of the normalized transfer curve. When an optical power P_{in} is incident upon the modulator input facet, we can assume that the power coupled into the output fiber to be $P_{out} = P_{in}T(V)$. Assuming fiber loss is negligible, the modulated optical power due to the RF voltage would be:

$$P_{Mod} = P_{in}t_{ff}T_N^{'}(V_b)\nu_m \qquad (5.4)$$

If the parameters related to EAM low-frequency design were grouped together, the EAM modulation efficiency can then be defined as:

$$r_m^2 = (P_{in}t_{ff}T_N^{'})^2 \qquad (5.5)$$

where r_m^2 is also equal to $\left(\frac{P_{Mod}}{\nu_m}\right)^2$, which can be derived from the modulator transfer curve and has the unit of $(W/V)^2$. A larger r_m^2 value would indicate a

well designed EAM. $T_N^{'}$ is a bias voltage dependant derivative, known as the slope efficiency. An EAM bias voltage is selected in such a way as to maximize $|T_N^{'}|$. The graph in Fig. 5.1.3 illustrates that this point occurs at V_{bb}, the best bias point with the highest slope gradient. r_m^2 is expanded here to analyze the design parameters more closely [2]:

$$r_m^2 = (P_{in} C^2 e^{-\alpha_0 L} \gamma \Delta\alpha'(V_{bb}) L e^{-\gamma \Delta\alpha(V_{bb}) L})^2 \qquad (5.6)$$

The three ' L 's in the equation above indicates the importance of modulator length L in designing an EAM. In the case of the first exponential in the equation, $e^{-\alpha_0 L}$ is actually the optical propagation loss at zero bias. This value therefore depends on how well the waveguide is fabricated, and what is the material and structure design of the waveguide in question. A favorable α_0 would allow for a longer L. Therefore, although the second L in the equation indicates that a longer L is favorable, and why it is often desirable to have a longer modulator length to increase modulation efficiency, there is an upper limit to this as optical propagation loss has to be taken into account.

If the last exponential term in (5.6), which is actually $T_N(V_{bb})$, is considered, longer L would lead to smaller best bias voltage, V_{bb} and subsequently, smaller $\Delta\alpha(V_{bb})$ because both the L and $\Delta\alpha(V_{bb})$ terms are inversely proportional, letting the $T_N(V_{bb})$ value to fall between 0.5-0.7 in practice. Therefore L here plays little role in affecting $T_N(V_{bb})$.

The $\Delta\alpha'$ in this equation represents the slope of the absorption coefficient change with respect to the applied bias. Although $\Delta\alpha'(V_{bb})$ and $\Delta\alpha(V_{bb})$ are more affected by the doping profile and the material energy band diagram (absorption layer bandgap) than other factors, however, since smaller V_{bb} results in smaller $\Delta\alpha'(V_{bb})$, and V_{bb} is inversely related to L, there is also some dependence of $\Delta\alpha'(V_{bb})$ on L.

L also greatly affects the modulation bandwidth and modulation speed. Larger L results in higher capacitance which would in turn limit the

modulation speed, both of which are unfavorable in a modulation device. In order to understand these effects better and to analyze the microwave properties of the EAM, the common practice is to model the EAM as an equivalent circuit model.

EA modulators are devices typically <400μm long. The phase variation of modulation voltage along the EAM waveguide can be ignored since the microwave wavelength at modulation frequencies below 20GHz (~2mm) is many times longer than the EAM length. Hence, EAM waveguides can be considered as a *lumped element* in the whole microwave circuit.

Fig. 5.1.4 shows the equivalent RF circuit model [3] of an EA modulator where V_s is the RF source voltage. Here the inductance elements (L_{w1} and L_{w2}) from the probes or wire bonding are also included. In practice, a parallel 50 Ω load (R_s) is usually used to reduce microwave reflection back to the driver. R_L (~50Ω) is the load resistance (or shunt resistance) and is sometimes added to help broaden the bandwidth but it will also reduce modulation frequency response at low frequency.

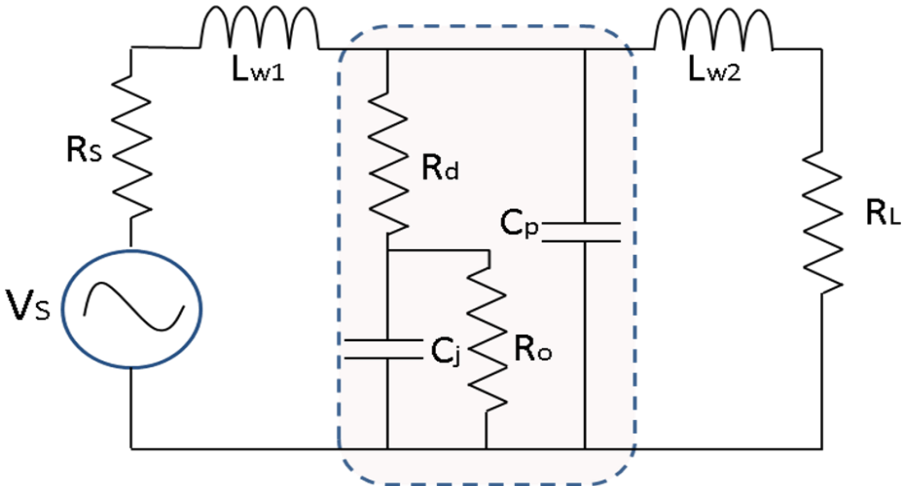

Fig.5.1.4. Equivalent circuit model of an EA waveguide modulator

The bared chip modulator itself can be modeled as a junction capacitance (C_j) paralleled to the photocurrent resistance (R_o) and both in series with a differential resistance (R_d). These are then parallel with the contact pad capacitance (C_p). C_p is also known as the parasitic capacitance and is mainly

due to the p-pad which is typically ~30fF. In our case, since our probe pad for the n-contact is 70μm by 70μm, using the equation $C = A\frac{\varepsilon_o \varepsilon_r}{d}$, where A is the pad area, ε_0= 8.8542×10^{-12}, d~2.4×10^{-6} and our dielectric monomer (Cyclobutene 3022-35 Advanced Electronic Raisins) has the dielectric constant ε_r ~ 2.5, we calculated our C_p to be approximately 36.9fF. Therefore, for devices with C_j>>37fF, C_p can be ignored. R_d, also known as device series resistance includes the ohmic resistance at the electrodes and the bulk resistance in the doped semiconductor layers. R_o can be used to model the RF impedance of the photocurrent path ($R_o = (dI_0/dV_J)^{-1}$) where I_0 is the EAM DC photocurrent and V_J is the junction DC voltage. R_o also incorporates the junction leakage resistance that is usually larger than 1MΩ. The three physical parameters (ignoring C_p) can be separately calculated or measured using conventional methods. C_j can be measured by a C-V measurement; R_d can be determined by measuring the slope of forward I-V curve at large current and R_o from the slope of reverse I-V curve with optical input to the EAM.

In this EAM configuration, the microwave signal is applied from the center of the optical waveguide via the p-pad; therefore, the microwave signal will experience strong reflections from two ends of the waveguide. As a result of this, the device performs as a lumped element and the intrinsic speed of the device is limited by the total $R_{eff}C_j$ time constant. R_{eff} here represents the resistance of R_o in parallel with R_S and R_d ($R_o = R_o \parallel (R_S + R_d)$). With low optical power (such as 1mW), R_o is very large, and R_{eff} is simplified to $R_S + R_d$. C_j on the other hand is related to the modulator's surface area, thus the need for narrower width and shorter modulator length. In this case the "electric bandwidth" or "3-dBe bandwidth" is:

$$f_{3dB} = \frac{1}{2\pi R_{eff} C_j} \qquad (5.7)$$

whereas the 3-dB optical bandwidth which is defined as the frequency range in which the modulated output optical power is reduced to half value is equivalent to 6-dB electric bandwidth which is about double that of the 3-dBe bandwidth.

The speed of the device is also limited by the total parasitics, which is why L cannot be too long but an L which is too short would also make the packaging and handling of the device difficult and potentially increase the drive voltage and reduce the saturation power. Consequently, the L was set to be between the ranges of 150μm to 300μm, which is the optimum length for waveguides of 3μm width.

Although the MQW composition, thickness and strain would also affect modulators, details of such studies [4, 5] were not taken here. It is worth taking note however that modulators generally adopt a deep ridge design. The modulator waveguide is deep or shallow ridge depending on whether they are etched through the active layer or not. In a deep ridge modulator, the extinction ratio is larger because the modes in the waveguides are better confined leading to a larger γ value. The width of the ridge also influences the performance. The larger the width, the larger the electrode capacitance would be.

5.2 Material Structure: Dual Depletion Region and Large optical cavity EAM

N-doped InP is chosen as the substrate material for the wafer growth so that the N-pad can be fabricated on the backside of the sample. In selecting the material structure for the EAM, we also took into consideration to avoid power saturation of the EAM which is mainly caused by the pile-up of the photo-generated holes in the wells. The pile-up of these holes occurs when the optical power which is guided into the EAM is too high. In order to improve the power handling ability of an EAM, the focus should be on facilitating the escape of these holes. A method used by the UCSD group [1, 2] involved the adoption of intrastep quantum well (IQW) active layers that have resulted in the achievement of high saturation power of around 100mW. The introduction of IQW structure effectively delays the red shift of the QCSE at high electric field because the block of step barriers for holes under low electric field allow for holes to move down the steps easily thus avoiding pile-ups. Therefore, under higher electric field that helps sweep out the holes, absorption can still take

place. Unfortunately, although this structure is effective in improving saturation power, it needs to be operated under high electric field, which is something we want to try and avoid.

Another more direct and common method to improve saturation power is to facilitate the escape of holes out of wells by lowering the barrier height, that is, to adopt the quantum well structures with small valence band offset to reduce the block effect of barrier for sweeping out of holes. The schematic illustration is shown as follows in Fig.5.2.1.

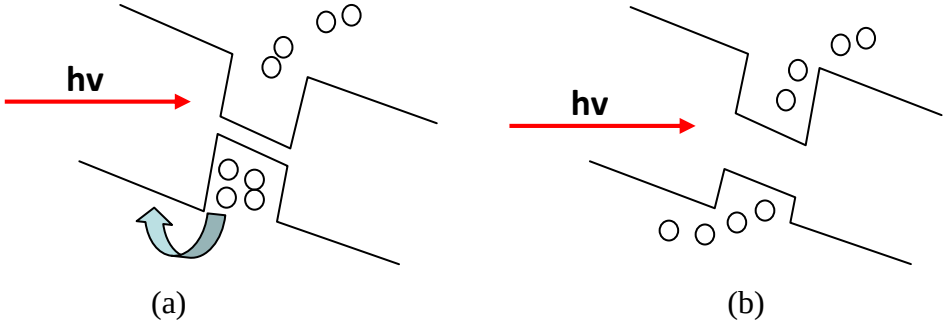

Fig. 5.2.1 Illustration of (a) a QW with high barrier height and (b) an alternate QW design with smaller valence band (lower barrier height)

The material InGaAlAs is chosen over the more common InGaAsP because the ratio of conduction band offset (ΔEc) to valence band offset (ΔEv) for the InGaAlAs is 70:30, while the ratio of the latter is 40:60. The InGaAlAs material is more favourable to hole escape from the wells and hence reduced absorption saturation. Larger ΔEc benefits for better confinement of electrons in wells to get large extinction ratio under low driving, while smaller ΔEv is good for high power operation. However, it is important to take note that ΔEv which is too small will result in a loss of confinement of carriers and finally small extinction ratio of the device. Therefore, there is a sensitive balance required in the design of this parameter. According to previously reported findings, ΔEv value at around 80meV could be balanced for high power handling capacity and large extinction ratio requirements. Therefore, the structure has been designed to make this value between 85—100meV. Besides lowering barrier height, there had also been reports that thinner barrier layers can reduce the escape time

of holes because of the reduced tunneling time. A thin barrier layer with the thickness of 5nm for the material was selected in compliance to this.

The material structure of our InGaAlAs MQW-EAM is shown in Fig. 5.2.2. The structure consists of p-i-n-i-n structure with two undoped core (high-index) layers, where the first is made of active InGaAlAs/InGaAlAs MQW and is separated by a 10-nm thin n+ doped InP layer from the second core layer, which is made of passive bulk InGaAlAs with a larger material bandgap energy than the absorption wavelength, This configuration is known as the dual depletion region (DDR) core structure [6]. This structure was selected in order to realize lower driving voltage for our modulator. Although many methods were employed to realize low driving voltage [2-5], the most direct way is to adopt a thin undoped intrinsic active region in order to obtain a large electric field under low bias with the relation of $F=V/d$ where d is the total thickness of the active region. However, the introduction of an intrinsic region will directly increase the capacitance and subsequently limit the bandwidth. Therefore, the contradiction between bandwidth and low driving voltage is a big problem. In order to solve this problem, most reports adopted very short absorption region length and narrow waveguide to reduce capacitance. But the too short waveguides result in small extinction ratio and handling difficulty, which is why we opted for the DDR core structure design. In the DDR structure, only the MQW layer acts as the absorption layer while the bulk layer material does not absorb the incident light. This is because the highly doped charged layer between the two undoped layers can concentrate all or most of the electric field in the MQW layer. When the material structure is designed in this manner, the total thickness of the depletion region is (d1+d2) as shown in Fig. 5.2.3(a), which implies that the equivalent capacitance is no longer that of one lump capacitor but actually two capacitors in series ($\frac{1}{C_{eq}} = \frac{1}{C_1} + \frac{1}{C_2}$). The DDR structure, therefore, effectively reduces the overall capacitance without significantly reducing the electric field in the MQW region. By adjusting the relative values of d1 and d2, we can achieve better and more flexible tradeoff between bandwidth and drive voltage. Therefore, even though the total thickness of the active region is now greatly increased, thus obtaining a large

electrical field, the capacitance problem is better contained. With this structure, we could then achieve the high electric field in the MQW region under low bias voltage. In addition, with thicker overall active region, the device can be designed longer, which is desirable for large extinction ratio and low voltage, but not too long, or it will increase the absorption loss.

P^+ InGaAs layer	Doping >$1x10^{19}cm^{-3}$	200nm thick
P InP layer	$1x10^{18}cm^{-3}$	1.8µm
U 1.15 InGaAlAs	$In_{0.5274}Al_{0.2047}Ga_{0.2679}As$	50nm
9x U InGaAlAs QW /10x U Q1.15 InGaAlAs Barrier	$In_{0.458}Al_{0.015}Ga_{0.527}As$/ $In_{0.5274}Al_{0.2047}Ga_{0.2679}As$ (λ_{PL}≈1480-1500nm)	13/ 5nm
N^+ InP layer	$5x10^{18}cm^{-3}$	10nm
U Q1.15 InGaAlAs	$In_{0.5274}Al_{0.2047}Ga_{0.2679}As$	400nm
N Q1.15 InGaAlAs	$1x10^{18}cm^{-3}$	600nm
N InP substrate	**S-Doped 2-8 $x10^{18}cm^{-3}$**	

Fig. 5.2.2. Material layers for EAM device. All layers are lattice-matched to InP. Q1.15 means quarternary InGaAlAs with bandgap wavelength of 1.15µm, corresponding to bandgap energy of 1.08eV.

In order to confirm that the electric field distribution of the DDR structural EAM is truly concentrated on the active QW region alone, a DDR model with GaAs/AlGaAs multi-quantum wells was built and simulated using an open source software *SimWindows32*, a one-dimension free software which can also be used for simulating electronic devices. The MQWs' undoped layer was 162nm thick while the other undoped layer (undoped bulk) is 400nm thick. The doping concentration of the 10nm thick high n-doped layer between the two undoped layers was designed as 5e+18. The simulated distribution of electric field on the DDR along with the program code used for running the simulation is in Appendix A. From the simulations we can see that most of the electric field is concentrated in the multi-quantum wells active layer, and only a very small part was shared by the additional undoped layer which confirms that

the DDR structure would distribute the electric field in the assumed manner. The optical confinement and mode shape was determined by simulations using the parameters as shown in Fig. 5.2.3(b). The refractive indices used for the simulation are 3.6 for the InGaAs contact layer, 3.17 for the InP layers and 3.41 for the InGaAlAs layers. The average index value calculated and applied for the MQW layers was 3.6.

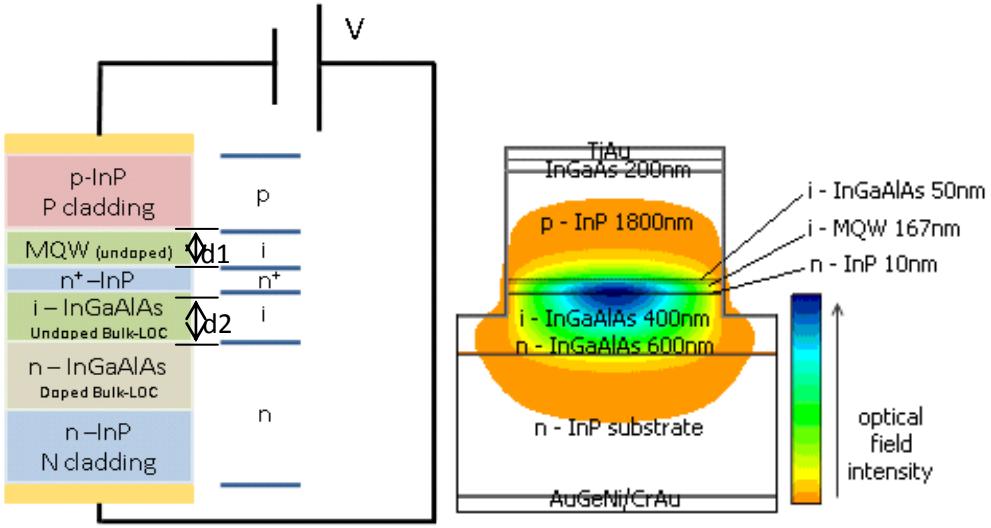

(a) (b)

Fig. 5.2.3. (a) Illustrations of DDR active layer structure of EAM core designed to balance between low driving voltage and high speed and the equivalent circuit. (b) Simulation result of a deep-ridge LOC waveguide structure with the width of 3μm.

In our design, we fixed the MQW thickness to 167nm, consisting of 9 layers of 13nm thick $In_{0.458}Al_{0.015}Ga_{0.527}As$ quantum wells lattice-matched to 10 layers of $In_{0.5274}Al_{0.2047}Ga_{0.2679}As$ barriers which are 5nm thick and 0.5% compressively strained. The choice of a relatively large well thickness of 13nm is based on the consideration of energy level shifts which depend on the well width (L) according to the equation

$$\Delta E \propto (m^*.e^2.F^2L^4)/2 \qquad (5.8)$$

where ΔE is the energy level shift, m^* is the effective mass, e is the electron charge, and F is the electric field intensity. The larger energy shift does not necessarily mean large absorption change, but the focus is low drive voltage, so the point is to achieve a given energy shift at a much lower E field. We have

introduced a tensile strain of -0.5% to the wells to attain a photo-luminescence (PL) peak wavelength (λ_{PL}) of 1500nm.

For the waveguide design we adopted a large optical cavity (LOC) structure [7-10] to improve the optical profile of the EAM and the coupling efficiency of fiber to waveguide. The LOC designs are often incorporated into EAM designs to increase saturation power. The LOC structure adopts a thick lower waveguide layer under the QW active layer, and in our case, this can be combined with the additional undoped layer of the DDR structure.

The mode profile of this structure will also be more rounded for better fiber matching and increased coupling efficiency. The LOC structure consists of a 1μm thick lower waveguide core layer under the QW active layer. The lower core is made up of an additional 0.6μm of lightly n-doped InGaAlAs layer below the 0.4-μm undoped bulk layer of the DDR structure. Although the smaller overlapping between the large mode size with thin active quantum wells lead to a smaller confinement factor (γ) in the active quantum wells area, which one may instantly associate with lesser modulation efficiency, the DDR structure's (which is also combined with the LOC structure) efficiency is also dictated by other parameters as given in equation (5.6). The DDR-LOC structure greatly enhances the coupling efficiency C^2 which gives it significantly higher modulation efficiency here. The LOC structure has also been experimentally verified [7-8] to be able to modulate efficiently, which is why the DDR-LOC structure was used here.

In our case, the total thickness is also limited by the difficulty to grow thick lattice-matched quarternary layer. The simulated mode profile of our 3μm wide waveguide design using *Apollo APSS* software is shown in Fig. 5.2.3(b). The simulated theoretical confinement factor is 0.115. A lower confinement factor would also indicate that the lower optical waveguide is lossier. This is desirable because it would mean that the small portion of light absorbed in the active region will increase the optical handling ability of EAM. Nevertheless, the smaller confinement factor may result in small extinction ratio. Therefore, a balance need to be struck where sufficient light is confined to the MQW region whereas the mode is increased suitably to fit the fiber mode shape and not too much light remain at the lower waveguide region to affect the EAM efficiency.

5.3 Device Fabrication

In order to fabricate the device, we grew an additional 300nm thick SiO_2 layer above the material structure shown in Fig. 5.2.2. With our photolithography capabilities, we patterned this SiO_2 into a mask through RIE etching and subsequently etched the sample to an etch depth of 2.6μm with ICP under the SiO_2 mask. The SiO_2 layer was then removed through HF wet-etching. After the definition of the waveguides, we then moved on to define the EAM p-electrode windows, which is also the process which outlines our EAM design. This fabrication process is also regarded as the major challenge in fabricating the EAM component as it involves crucial alignment of the electrode mask over the narrow waveguides and an additional process step called planarization and etch back process.

The planarization step involves spin coating bisbenzocyclobutene (BCB) monomers, which would act as an additional passivation step and help flatten out the sample surface and the etch-back step which will reduce this BCB layer until the waveguide layer is exposed again. This step is introduced in order to avoid the alternative method which is defining photoresist pattern over ~3μm waveguide ridge height difference; a method which is more prone to misalignment and poor yield. The metallic p-pad is usually designed as a square or rectangular shape and is needed for probing or wire bonding. The pad should be as small as possible as it will contribute parasitic capacitance to the EAM device, which is harmful to the modulation bandwidth.

With the introduction of BCB monomers underneath the p-pads, we have helped reduce this problem, as BCB has a low dielectric constant. The BCB which covered the waveguide sidewalls also served to passivate the surrounding area so that the p-pad need not be too small. For a <20-GHz bandwidth device, ~500nm thick gold deposition is sufficient as thicker gold does not help to reduce resistance due to microwave skin effect. As for our n-pad, the bottom surface of our device serves as the n-contact. In order to improve the p-i-n contact, the sample is thinned by lapping before the metallization process. A good *p-i-n* contact comes from better doping level of the contact. A thicker *n*-layer may cause higher contact resistance, which is why

it is often thinned down. This is because when a layer is too thick, like in our case where it is the thickness of the substrate (~350μm) before lapping, we cannot be sure that the whole of the thick layer is highly doped. In cases where it isn't, some of the bias voltage that passes through it may drop in the low doped area, and this would result in a lower *real* voltage on the *p-i-n*. This in turn would cause the threshold voltage of the *p-i-n* to be higher (e.g. above 0.7V). Through lapping, we can reduce the sample thickness from its initial ~350μm to about 100μm. This thinning process also facilitates the dicing and cleaving of the samples for subsequent testing.

The facet view of a cleaved sample and top view of the sample prior to cleaving is shown in Fig. 5.3.1. These images were captured using an Olympus microscope. The cleaved samples' lengths ranged from 150μm to 350μm according to the width of the p-contact strips along the waveguides. We kept the processing steps for our EAM to a minimal in order to cut down processing time and to loosen the fabrication tolerance in anticipation of numerous additional steps we would need to incorporate in the final integration with the MMI device.

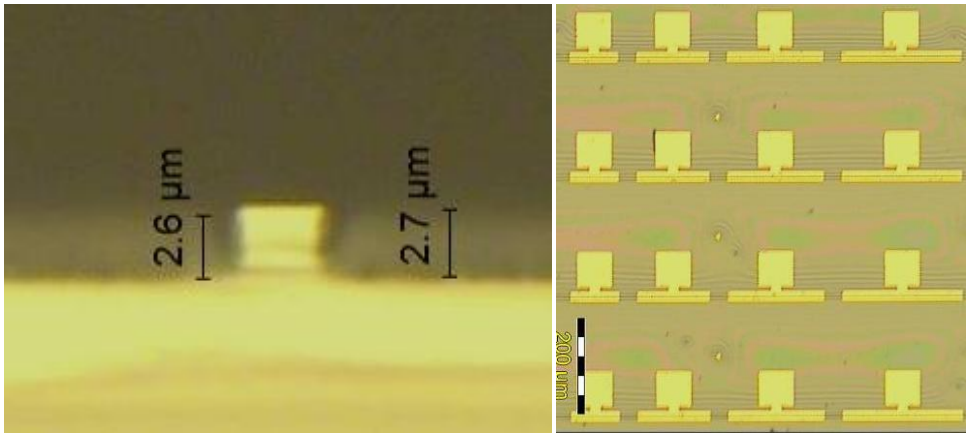

(a) (b)

Fig. 5.3.1 (a) Facet and (b) top view of the chip array for InGaAlAs sample prior to cleaving

5.4 Device Characterization

Since InGaAsP is the preferred and more well established choice of material in III-V optoelectronics, we compare our InAlGaAs-based device

performance with an InGaAsP/InGaAsP MQW–based EAM with similar design that we have also fabricated, as well as with another previously reported result which is also invariably based on InGaAsP material[8]. The InGaAsP/InGaAsP MQW DDR-LOC EAM's material structure is similar to the InAlGaAs/InGaAlAs MQW DDR-LOC EAM in all aspects including the MQW wall (13nm) and barrier (5nm) thickness. The bandgap energy of the MQWs for the InGaAsP/InGaAsP MQW DDR-LOC EAM are 0.7949eV (well) and 1.127eV (barrier). The third device used as comparison has a 252nm thick 14-period InGaAsP/ InGaAsP/ InGaAsP intrastep quantum well (IQW) active core sample with a large optical cavity (LOC) that closely resembles our present design. The thicknesses of barrier, step barrier and well for this third design were determined as 5nm, 6nm and 7nm and the material are $In_{1-x}Ga_xAs_yP_{1-y}$ with bandgap energy of 1.127eV, 0.8857eV and 0.774eV respectively. The samples described here would be denoted as Samples A, B and C for easier identification. The device length for Samples B and C are both 150μm and for the Sample A is 300μm.All the samples have a ridge width of 3μm. The cross-sections of the samples are illustrated in Fig. 5.4.1 for better visualization. All the measurement data obtained were taken without anti-reflection coating on the facets.

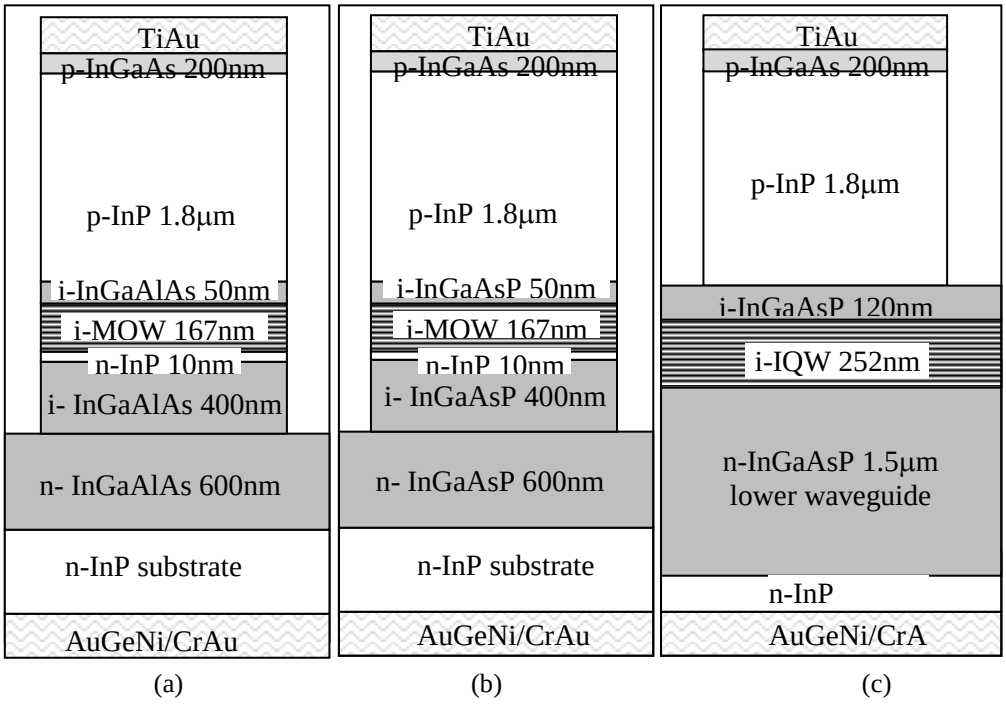

Fig. 5.4.1. Cross sections of (a) Sample A: InGaAlAs MQW DDR-LOC; (b) Sample B: InGaAsP MQW DDR-LOC and (c) Sample C: IQW LOC EAM waveguide

The device performance characterization is limited to DC optical measurements. The samples were pasted unto copper surmounts with indium foil, and each surmount is then clamped unto a copper block connected to a semiconductor parameter analyzer. A tapered fiber was used to couple light into the waveguide and an objective lens with 10x magnification was used to image the output mode from a tunable laser unto a vidicon camera and photo-detector via a beam splitter. After aligning the fiber and sample until the best coupling had been achieved, a probe is attached to the p-pad to introduce the bias voltage. Only one electrical probe is needed for applying the DC voltage to obtain the photocurrent. The semiconductor parameter analyzer is able to measure the I-V response of the sample and help us plot the photocurrent curves. We then attached the probe (p-type) and clamp (n-type) terminals to a DC power supply to measure the extinction ratio by plotting the fiber-to-device-to-free-space optical transmission versus reverse bias voltage. This is repeated for varying wavelengths in both polarizations. The optical transmission is defined as

$$\text{Optical Transmission} = 10 \log (P_{modulator}/P_{fiber}) \quad [\text{dB}] \qquad (5.9)$$

where $P_{modulator}$ is the power detected by the free space photodetector after passing through the modulator and P_{fiber} is the power from the fiber which was detected by the photodetector.

Fig. 5.4.2 shows the fiber-to-device-to-free-space optical transmission versus reverse bias voltage for several wavelengths in both the TE and TM polarization states for Samples A, B and C. Firstly, in Sample A, from the modulator DC transfer curves we have plotted; we deduced that the best absorption wavelength is between 1560nm and 1570nm. For these wavelengths, an acceptable extinction ratio of 10 to 15dB can be achieved under 1 volt of reverse bias, with that for TE generally higher than for TM. The insertion loss which is defined as the negative of optical power transmission at 0V was about 14dB for the 1570nm.

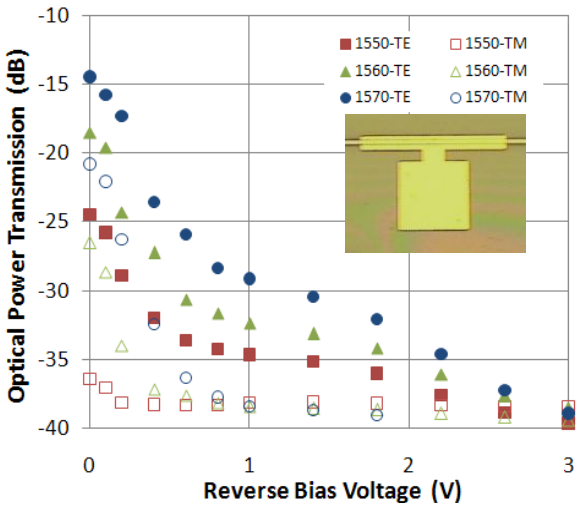

(a)

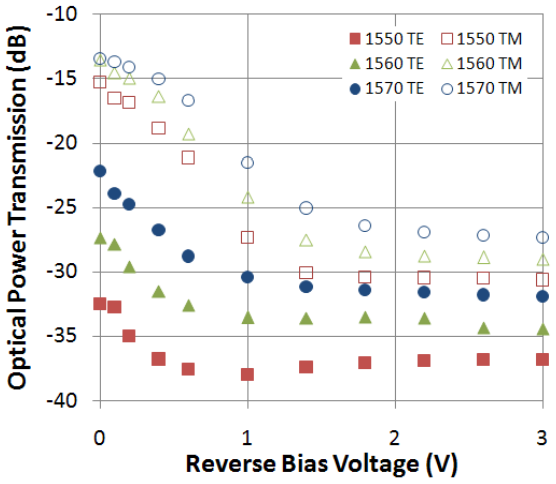

(b)

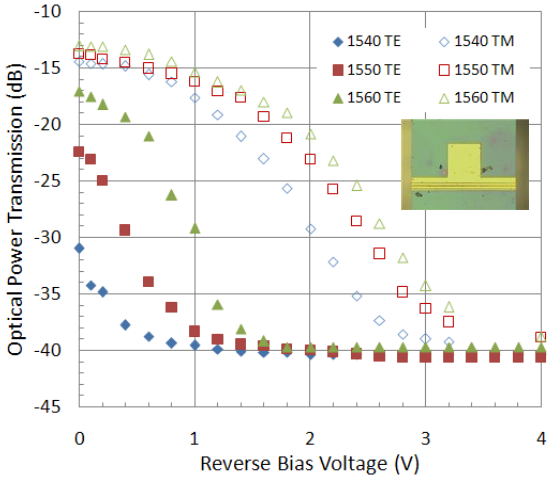

(c)

Fig.5.4.2. Fiber-to-device-to-free-space transmission versus reverse bias voltage for several wavelengths for both TE and TM polarization states. Facets are without anti-reflection coating. The inset picture is a microscope capture of the modulators. The material type of each structure is (a) InGaAlAs/InGaAlAs MQW (b) InGaAsP/InGaAsP MQW and (c) InGaAsP/InGaAsP/InGaAsP IQW

The extinction ratios we obtained for Sample B showed better performances for the TM polarization and is optimized to function better at the wavelength of 1550nm due to the difference in its bandgap energy as compared to Sample A. For both these devices, drive voltage for extinction ratio of 10-dB for both TE and TM polarizations were lowered to -2V or less. Sample A exhibited better extinction ratio slope as compared to Sample B. The insertion loss for Sample C was 13dB for the TM polarization at the wavelength of 1560nm. The insertion loss increased as wavelength decreased due to the tail of MQW absorption.

With TE polarization, the drive voltage for 10-dB extinction ratio was 0.5V at 1550nm and it was 1.3V for a 20-dB extinction ratio at 1560nm. The device showed large polarization dependence. However, this issue is often resolved with the manipulation of the MQW structures [11, 12]. The drive voltage for 20-dB extinction ratio was 2.4V for TM polarization at the laser wavelength of 1540nm.

The EAM devices' insertion loss is greatly influenced by the absorption of the light by the QW material. The higher the amount of absorption of the light at a particular wavelength, and at a particular polarization, the higher the insertion loss would be. The absorption can be thought of as the sum of the absorption due to heavy-hole (HH) and light-hole (LH) transitions. Due to the nature of the EA effect, the HH transition mostly contributes to the absorption in TE polarization light whereas the LH transition is the only contribution to the absorption in the TM polarization light. Therefore, the insertion loss of any material structure may vary, depending on how highly strained the well and barriers may be. This is also why, although Sample B and C share the same material base (InGaAsP), the absorption of its TE and TM polarized light could differ. Although it is possible the render an EAM polarization independent and therefore its insertion loss and wavelength dependence through careful manipulation (tensile or compressed straining) of the wells, we did not cover this in the course of our work.

Each modulator design here has different bandgap and polarization. Therefore, the corresponding input has to be chosen properly to realize its best

performance. For the case modulator in this experimental verification, the most suitable wavelength would be the 1540nm TM polarization. There is a balance needed to be maintained between the extinction ratio and bias voltage. Often, a larger extinction ratio with lower insertion loss is a preferred choice. All the modulators which we have measured and shown here have low driving voltage suitable for modulation purposes. They also demonstrated good I-V response as shown in Fig. 5.4.3(a).

With both TE and TM polarized 1560nm wavelength light, the modulator DC transfer curves and photocurrent curves are plotted in Fig. 5.4.3(b) with input power of 3mW. The photocurrent does not change significantly with the different polarization but the maximum slope efficiency of $1.06V^{-1}$ is measured at -0.2V bias for the TE polarization. For the TM polarization, the bias point for maximum slope efficiency shifted 0.2V and the maximum slope efficiency is degraded by ~46%. This similarly manifests some sort of polarization dependency. In order to compare the DC characteristics of the different devices, the maximum slope efficiency for the samples' respective biases was calculated and the results are presented in Table 5.1.

TABLE 5.1: Measurement results for DC modulation properties of EAM

Parameter	Sample A		Sample B		Sample C	
	TE	TM	TE	TM	TE	TM
Insertion Loss (at zero bias) [dB]	14.5	20.8	32.5	15.3	13.1	17.1
Maximum slope efficiency (MSE) [V^{-1}]	2.25	4.71	2.36	0.94	1.06	0.49
Best Bias Point, V_{bb} [V]	-0.1	-0.1	-0.2	-0.2	-0.2	-0.4

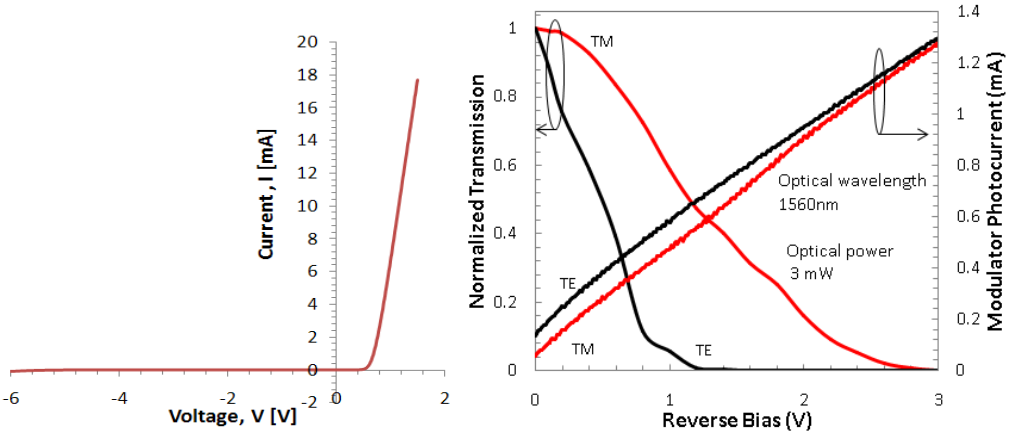

(a) (b)

Fig.5.4.3. (a) I-V curve for Sample C; (b) Modulator DC transfer curve and modulator current versus reverse bias for a 300μm long Sample C measured with both TE and TM polarization

An impedance analyzer Agilent 4294A was used to measure the capacitance of devices A and B under different reverse bias voltage (Fig. 5.4.4). Since R_d measured from Fig. 5.4.3(a) is ~0.216mΩ, $R_S + R_d$ in this case is 50.000216Ω which can be simplified as 50Ω. (Note: the R_d for all three samples is similarly low). Therefore, the 3-dB optical bandwidth at -2.0 bias voltage is $1/(\pi R_{eff} C_p)$ =1.5GHz for Sample A and 3.18GHz for Sample B.

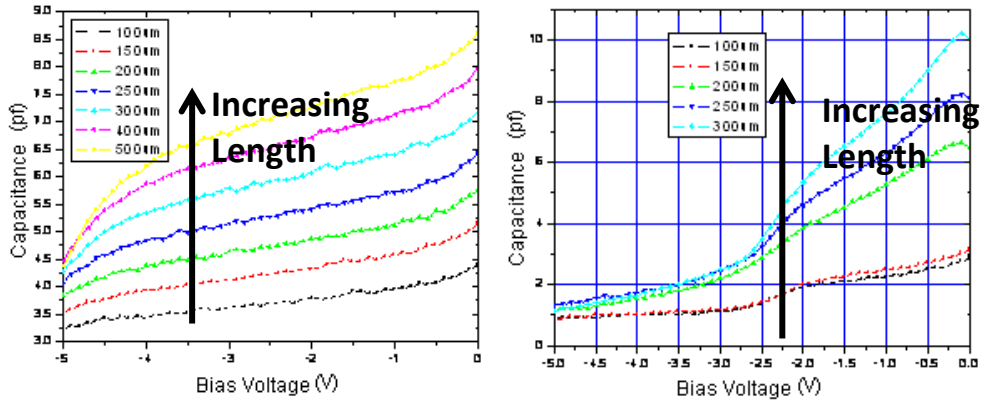

(a) (b)

Fig.5.4.4. C-V for Samples (a) A and (b) B for varying modulator lengths

A basic Radio-frequency (RF) measurement was used to confirm the calculated values expected from Sample A based on the capacitance measurement. In order to be able to feed RF signal into the device, we had to add a few post processing components to the sample. The sample was firstly

mounted onto a hi-beam so that it is suitable raised to allow fiber to be drawn closer to both its input and output cleaved surface. Since the sample was designed in such a way that the p-contact and n-contact are on different planes (top and bottom of the device respectively), whereas the regular RF probes are made up of a three-prong probe which can be used only on a single plane, we then wire bonded the n-contact pad to a G-S-G pad which is soldered on the same hi-beam as the sample and used the G-S-G pad as the probe base for the RF probes. Fig. 5.4.5 is a microscope capture of the successfully mounted 300μm long Sample A.

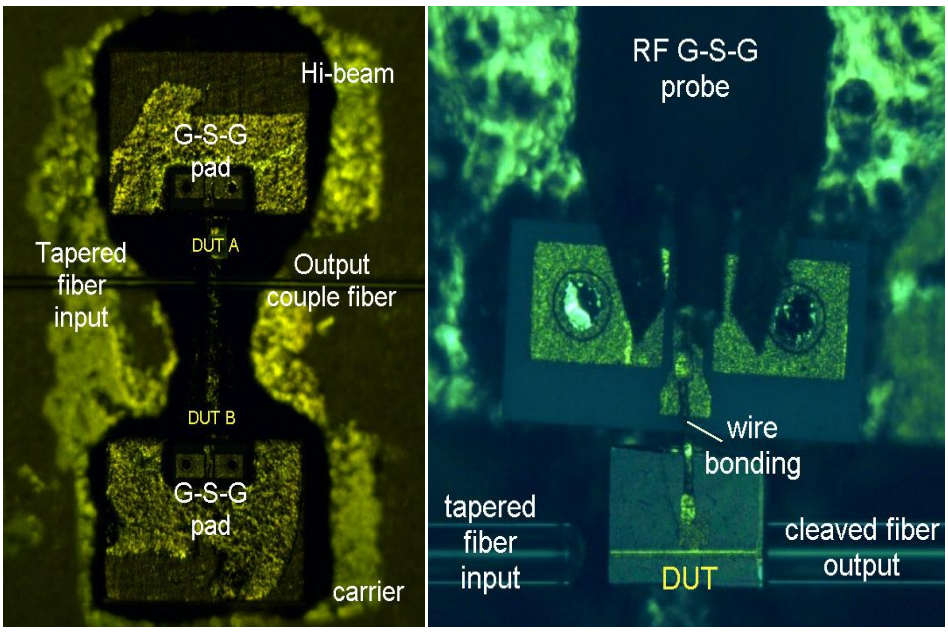

Fig. 5.4.5 Microscope capture of (a) Sample A (DUT A) which is soldered onto the hi-beam with a G-S-G pad; (b) Wire bonded Sample A (DUT) with the RF probe resting on the G-S-G pad, and with input and output fiber aligned to the input and output of the device.

The device is then measured with the equipments as illustrated in Fig. 5.4.6. The lowest insertion loss obtained at zero bias was 13dB while fiber-to-fiber coupling loss was ~9dB. Due to the rather high loss, caused by the cleaved surface without AR coating, an optical amplifier was needed to boost the optical input power.

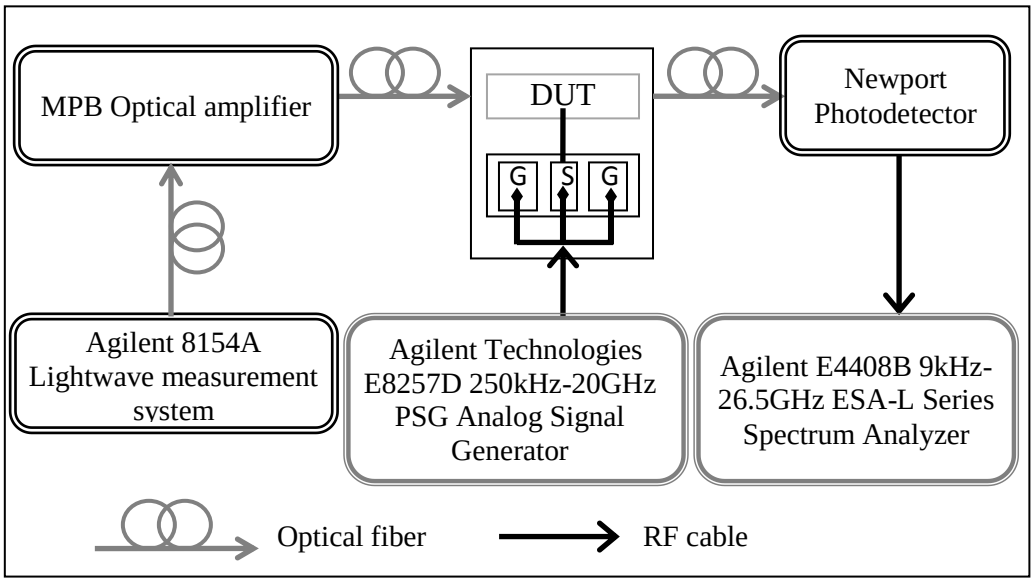

Figure 5.4.6 Schematic diagram of RF measurement setup for measuring EAM

Fig. 5.4.7 is the normalized response of the measured RF signal obtained from the spectrum analyzer. At the wavelength of 1552nm, the 3-dB bandwidth measured indicated that the modulator is able to modulate up to 2GHz, which is close to the calculated bandwidth. The actual bandwidth is slightly higher that the measured capacitance due to poorer device contact with the measurement stage used for the capacitance measurement.

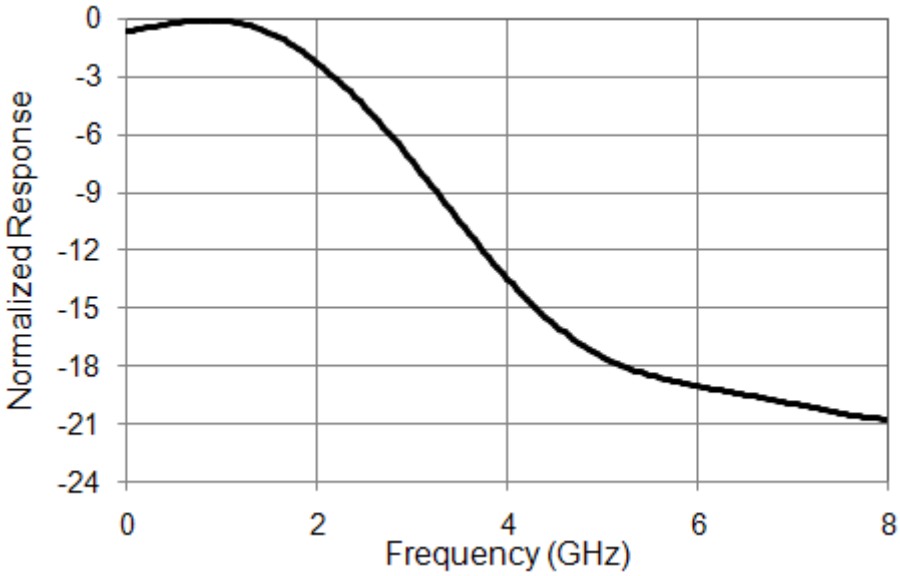

Fig. 5.4.7. Normalized response curve of measured RF signal obtained from a 300μm long device at 1552nm

Conclusion

In this chapter, the design and fabrication of lumped element electroabsorption modulators with MOCVD grown InGaAlAs/InGaAlAs and InGaAsP/InGaAsP MQWs were discussed. Low driving voltage DC modulation has been achieved with the introduction of DDR and LOC structures for both types of MQWs. For a 3μm wide, 150μm long device, drive voltages of < 1.0V have been obtained for extinction ratios of 10 dB. The MQW-EA modulator with integrated access waveguides for optical input and output has the advantages of easy fabrication and packaging, while maintaining a small device capacitance, sufficient to achieve high-speed modulation. Insertion loss is as low as modulators which are not integrated with waveguides or other structures.

Based on the capacitance values obtained, no significant bandwidth improvement was observed from these lumped EAMs. The modulation bandwidth can be further increased by shortening the modulation-region length but this would affect the extinction ratio and increase the driving voltage for modulation.

We were not concerned with the polarization dependence in the design. However, this problem can be resolved by optimizing magnitudes of the tensile strain of the well and manipulation of well thickness. We have found our measurements to be in good agreement with our basic assumption and were therefore prepared for the next step which was the realization of an MMI + modulator(s) device.

Chapter 6

Integration of an MMI Splitter with Electroabsorption Modulators

This chapter presents the experimental implementation of an MMI which is integrated with an electroabsorption modulator (EAM), based upon the work discussed in previous chapters. The integration of an MMI and an EA modulator to form a 1x2 optical signal switch or controller, and which involves various fabrication process and measurement methods are demonstrated. The active and passive devices have quite different properties. The active device tends to be much smaller compared with the passive device. Secondly, the active device must have different material property from the passive device in order to perform its unique function distinct from that of the passive device. In this case of MMI-EAM the MMI serves simply as a 1xN power splitter while the EAM is an electrically driven device that modulates the MMI output using the quantum confined Stark effect inherent in a MQW structure. The integrated device will then serve as a 1xN modulator or switch. The EAM has a p-i-n diode structure and is reverse-biased.

For optimum performance the bandgap of the EAM would only be slightly larger than that of the light energy, while to minimize propagation loss the passive device must be transparent to the input light and hence have bandgap energy much greater than the light energy. This incompatibility of bandgap requirements poses a major challenge for active-passive integration, especially if more than one type of active devices is involved. Many methods have been developed to resolve this problem. One group of methods is to grow two different compositions of the same MQW material in different regions of the device layer. This includes selective area growths and regrowths, a difficult process that is not scalable with the number of distinct active devices. To overcome this difficulty, another group of post-growth techniques that are more

robust has been developed based on the quantum-well intermixing (QWI) process, essentially a process to increase the QW bandgap energy in the passive device area as much as possible while minimizing the shift in bandgap energy in the active region. This method is more scalable as the process can be extended to multiple regions using selective masking. Although we have experimented with two particular variants of this technique; the plasma-enhanced inductive coupled plasma (ICP) QWI developed in NTU [1] and the impurity-free vacancy diffusion (IFVD) [2, 3], only the IFVD processed devices will be presented here.

The fabrication process is divided into 3 parts; (1) the QWI process to define the passive and active regions, followed by the fabrication of the (2) passive and (3) active devices, respectively. The intermixing process has been optimized using one of the MQW structures and the material structure and process details will be discussed in Section 6.1. The MMI and EAM step-by-step fabrication process in order to realize the MMI+X device is then described in Section 6.2. The objective of fabricating and demonstrating this 2-device integrated module is to demonstrate the feasibility of using QWI to realize active-passive device integration with modest performance and reasonably novel functionality.

The availability of a good technique to confirm that the fabricated devices exhibit characteristics as designed is crucial in pin-pointing weaknesses or strengths in designs. As the device in question is made up of different components, each part of the device have to be tested, measured and characterized in different ways. The segmented pieces help us to compare the propagation losses of waveguides which have been intermixed, characterize the MMI devices' loss, the EAM's functionality, and the integrated device's overall performance. All the different segments in this device have been characterized based on a fiber-to-device-to-free-space configuration as described in Chapter 3.

6.1 Quantum Well Intermixing

The material structure of the waveguides which will be used in the photonic integration consists of quantum wells. In order to achieve modulation

operation at a certain wavelength (for e.g. 1550nm), the quantum well has to be designed to have an absorption edge wavelength just slightly shorter than the working wavelength. Therefore, at the working wavelengths of the active device (modulators in this case) the wafers which have not been intermixed are termed as the "active" materials. To make "passive" devices in such a material, intermixing process is performed on the areas where passive devices are to be integrated, causing the bandgap in this area to increase, further lowering residual absorption and thereby making the passive devices transparent to light. The intermixing mechanism is based on the fact that MQWs is an inherently metastable system due to the large concentration gradient of atomic species across the QW/barrier interface. At temperatures above 750˚C, significant diffusion of atomic species will occur resulting in an interdiffusion or intermixing of the QW and barrier materials, and a rounding of the initially square QW bandgap profile and subsequently, an increase in the bandgap energy (i.e., a "blue shift" of the emission wavelength) as shown in Fig. 6.1.1(a). The bandgap energy data obtained here is derived by incorporating a bowing term to the linear Vegard's law employing known binary compound parameters. The calculation method and material parameter functions employed are detailed in Appendix B of this thesis. The bandgap structure generated in Fig. 6.1.1(a) was generated using a Matlab simulation program written by ref. [4]. When the bandgap energy is increased, the refractive index value may also be reduced but the much lower absorption of photons brought on by the bandgap expansion will sufficiently lower the optical light absorption of the waveguides as a whole and to provide optical confinement with lower propagation loss. This intermixing process can be greatly enhanced by the presence of impurities or defects in the vicinity of the interfaces of the QW, allowing intermixing to occur at temperatures that are substantially lower than that normally required. Ion implantation provides controlled levels of defect in regions of the wafer that need to be modified. For the plasma enhanced quantum well intermixing (PE-QWI), the higher the plasma density or the longer the plasma exposure time, the more defects are generated. Although the damage depths will remain constant, the exposure time cannot be excessive as the sputtering rate due to the argon plasma on the material is quite severe (~200nm/min) and will damage the

surface of the devices rendering it unsuitable for subsequent device fabrications. The defect density will also saturate after certain exposure time.

For the intermixing of quaternary materials like InGaAsP/InGaAsP, the interdiffusion in both group III (InGa) and group V (AsP) sublattices are characterized by their respective diffusion lengths, L_{III} and L_V. The material bandgaps of different L_{III}-L_V combinations can be mapped out for a better visualization of the extent of diffusion each group experienced in order to obtain the optimum blue shift. In Fig. 6.1.1(b), the calculated material bandgap (Eg(eV)) which changed as the III-V diffusions were varied were mapped out in a contour graph. The material structure used for this particular simulation is a 5xQW layer with a bandgap wavelength of 1.58μm sandwiched among InGaAsP barriers of λg=1.24μm which are lattice matched to InP. At L_{III}=L_V=0 where no intermixing took place, the material bandgap calculated for the structure is about 0.768eV. The numerical example to illustrate the procedure for calculating the bandgap and intermixed properties in summarized in Appendix B.

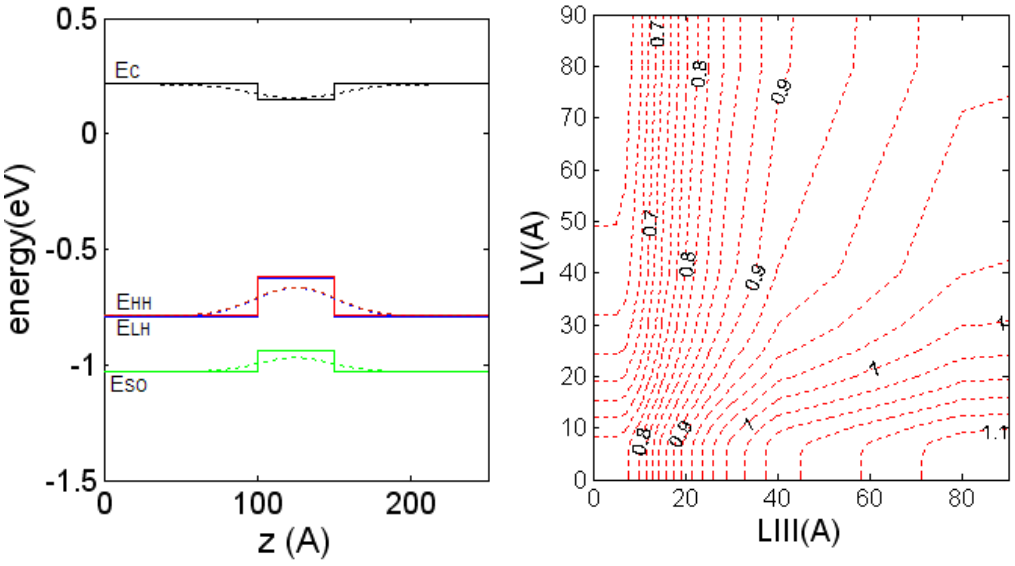

(a) (b)

Fig.6.1.1. (a) Band profile of a single 5nm thick InGaAsP quantum well with 10nm thick InGaAsP barriers before (solid lines) and after intermixing (dotted lines) for the conduction band (E_C), heavy hole valence band (E_{HH}), light hole valence band (E_{LH}) and split off band (E_{SO}); (b) Bandgap contour of 5xQW material structure as the diffusion lengths for both groups are varied.

6.1.1. The sample structure

The QWI process presumes a quantum well material structure. We attempted the MMI + EAM device on two types of MQW material structures. The first of these is the InGaAs-InGaAsP type lattice matched MQW design which will be described below while the second is the InGaAlAs-InGaAlAs type MQW with large optical cavity (LOC) (Sample A) previously detailed in Chapter 5. Both materials are based on InP substrate.

The lattice-matched InGaAs-InGaAsP QW samples used in the integration process were grown by metal-organic vapor phase epitaxy on (100) oriented n^+-type S-doped InP substrate with an etch-pit density below 1000cm^{-2}. The structure consists of five periods of 6nm $In_{0.53}Ga_{0.47}As$ strained QWs with four 10nm InGaAsP barriers with bandgap of 1eV. The active region is sandwiched by a step-graded index waveguide core consisting of InGaAsP confining layers. The thickness of these confining layers is 60 and 60nm above the MQWs and 60 and 60nm below the MQWs. The structure was completed by an upper cladding InP layer of two doping density: Zn doping of $5\cdot10^{17}$ cm^{-3} (0.4μm) and $2\cdot10^{18}$ cm^{-3} (1.0μm).The contact layer is a simple 50nm InGaAsP (Zn-doped of $1\cdot10^{19}$ cm^{-3}). In general, the larger the difference between the QWs and the barriers' bandgap, the larger the expected blue shift brought on by a set of intermixing recipe. The blue shift will also be increased if the QW width is thinner, but if it is much narrower than 3.0nm, the blue shifting will be affected as the quantized electronic levels in such wells are close to the "top" and must remain within the wells no matter how shallow they become due to the rules governing quantization. The strain present on the various layers will also affect the magnitude of the shift. The layer structure is shown in Fig. 6.1.2.

The material layer structure used for the MMI+EAM as shown in Fig. 6.1.2 is based on a commonly used InGaAs/InGaAsP MQW material structure for laser diode waveguides where the MQW (active region) is sandwiched with step-graded index (GRIN) waveguide core consisting of InGaAsP to enhance optical confinement. An average bulk core thickness is about 0.4-0.5μm as the previous simulations in Chapters 2 to 4 have adopted. The MQW layer (78nm) alone is too thin to support a single optical mode, which is why the GRIN structure is employed.

InP Sacrifice layer	Doping $2x10^{18}cm^{-3}$	500nm thick
P^+ InGaAs layer	$1.8x10^{19}cm^{-3}$	150nm
P InP layer	$1x10^{18}cm^{-3}$	200nm
P InP layer	$7.3x10^{17}cm^{-3}$	1.0µm
P InP layer	$1x10^{18}cm^{-3}$	200nm
U 1.15 InGaAsP	$In_{0.82}Ga_{0.18}As_{0.383}P_{0.617}$	60nm
U 1.24 InGaAsP	$In_{0.76}Ga_{0.24}As_{0.5106}P_{0.4894}$	60nm
5x U InGaAs QW /4x U Q1.24 InGaAsP Barrier	$In_{0.53}Ga_{0.47}As$/ $In_{0.53}Ga_{0.24}As_{0.5106}P_{0.4894}$ (λ_{PL}≈1580-1600nm)	6/ 12nm
1x U InGaAs QW	$In_{0.53}Ga_{0.47}As$	6nm
U 1.24 InGaAsP	$In_{0.76}Ga_{0.24}As_{0.5106}P_{0.4894}$	60nm
U 1.15 InGaAsP	$In_{0.82}Ga_{0.18}As_{0.383}P_{0.617}$	60nm
N InP buffer/substrate	**S-Doped 2.5 $x10^{18}cm^{-3}$**	

Fig.6.1.2. Layer structure of the epitaxial wafer used in the fabrication for integrated device

Fig. 6.1.3 is an illustration of the cross-section of an 8µm wide waveguide with the material structure and accompanying refractive indices of the different layers. Although there are more accurate refractive indices (e.g. refractive indices based on linear perturbation theory) which could be applied, the work involved here does not require such high accuracy. The optical simulation shown in Fig. 6.1.3(c) assumed the MQW thickness to be 80nm (instead of 84nm) to reduce number of mesh needed for simulation. The MQW layers are assumed to be a single bulk layer with the refractive index of 3.5031. This value is the average index value calculated by multiplying the refractive index of Q1.24 InGaAsP (3.357943) with the number of QW barrier layers (x4), refractive index of the QW InGaAs (3.6) with the number of layers (x6) and dividing the summed value with total number of layers (10). The 500nm thick sacrificial layer (InP) for intermixing purposes is removed after the intermixing process is completed and therefore not part of the optical

simulation. The InGaAs cap layer (150nm) is similarly not included in the simulation.

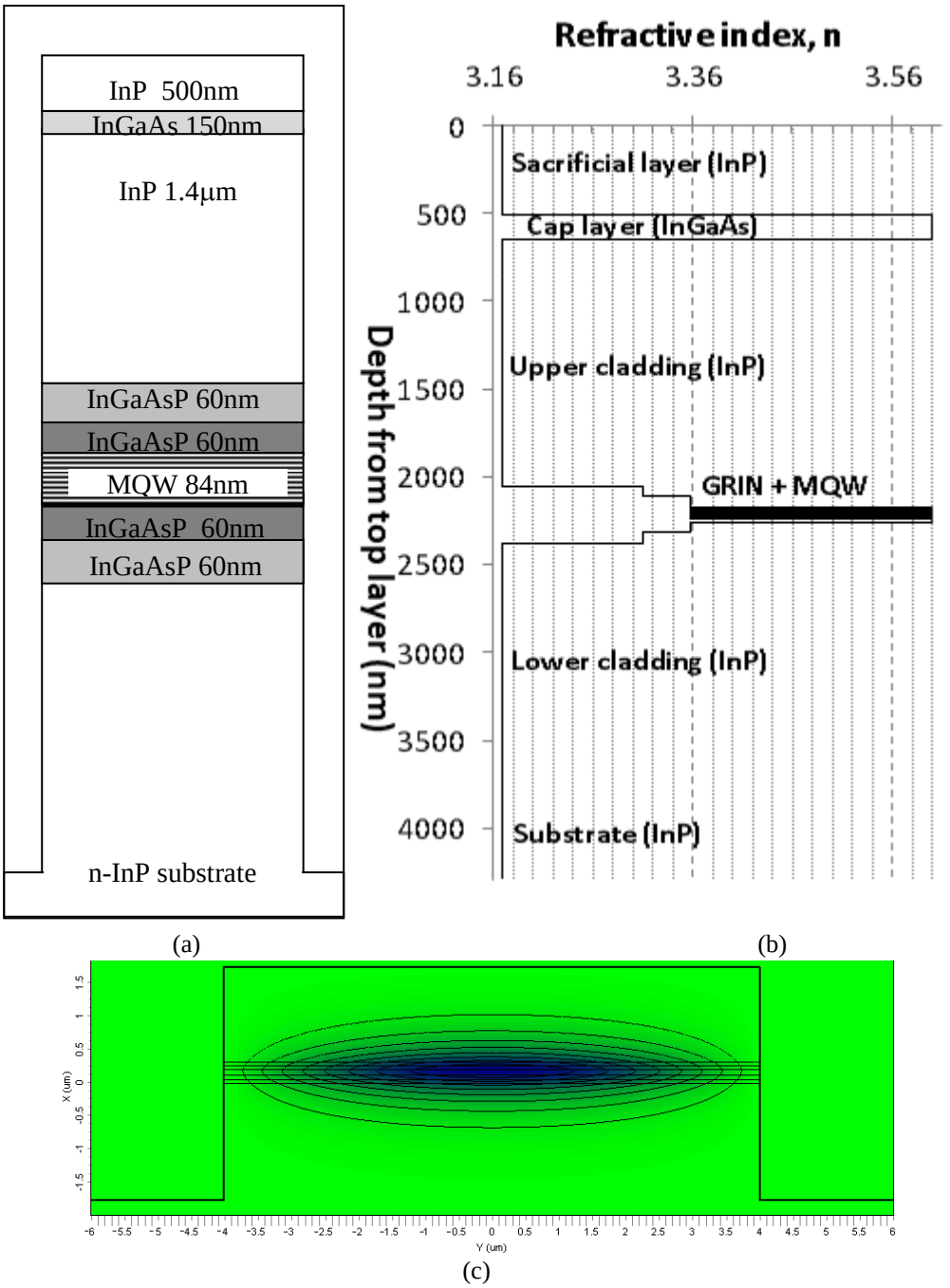

Fig. 6.1.3: (a) Material layer structure cross-section illustration (not to scale); (b) Refractive index vs. waveguide layers (depth from the top layer); (c) FD simulation of optical waveguide at working wavelength of 1.55μm.

Henceforth, the InGa**AsP**/ InGa**AsP** MQW structure material will be reclassified as the ***AsP Sample*** whereas the InGa**AlAs**/ InGa**AlAs** MQW material structure is shortened as the ***AlAs Sample*** for easier identification.

Throughout this chapter, the devices' results from both types of material will be compared together. The *AsP Sample* material was used because this material had always been a preferred intermixing material [1, 4-6], designed to perform optimally at the wavelength of 1550nm after intermixing. However, an actual device which is made up of the passive waveguide and active modulator has yet to be thoroughly researched. The *AlAs Sample* material on the other hand yields a higher performance EAM due to its lower voltage drive as described in Chapter 5. This type of material, which has been sandwiched with additional InGaAsP material results in an LOC, provides better coupling to fiber at the input and better propagation mode confinement but its intermixing characteristics have not been thoroughly explored.

6.1.2. The PE-QWI process

To protect the active area where we do not want the intermixing to take place, 200nm thick SiO_2 masks are used as cover (see Fig. 4.1.1.). The SiO_2 is deposited using the plasma enhanced chemical vapour deposition (PECVD) process. After depositing the SiO_2, the area where QWI is to be performed is defined using a photolithography process followed by an RIE etching process. For this device, the width of the active strip of area not intermixed is set as 500μm.

Photolithography is a patterning process where the device pattern on a glass photomask is transferred onto a photoresist layer above the SiO_2 film. Photoresists are sensitive to UV light, and once exposed, will become soluble in a certain solvent known as the developer. The photoresist used is the AZ-5214e positive photoresist. After spin coating this photoresist onto the samples and dry-baking it, they are exposed to the UV-rays using a Karl Suss MJB4 mask aligner. We utilized hard-contact (1.5mbar force) mode in order to ensure good patterning result from the 340nm UV light exposure. After exposing the sample for 15~20s, it is placed in the developing solution. The developing time depends on the spin coated layer thickness and UV exposure time. After developing, the patterned photoresist can now be used as the etch mask for etching the SiO_2.

Fig. 6.1.4 shows the microscopic view of the photoresist which covers the SiO_2 and which separates the active from the passive region.

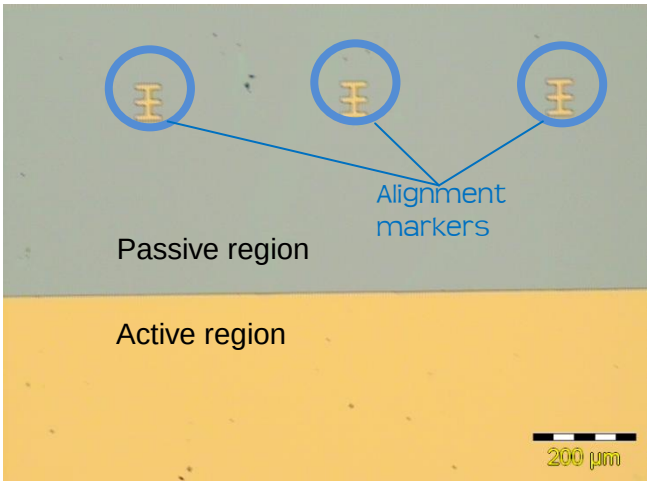

Fig.6.1.4 5x magnification view of photoresist (bottom part) covering SiO_2 which separates the active from the passive region for PE-QWI process

For the etching process, the RIE system used is Oxford Plasmalab 80 Plus. The RIE is used to etch away the exposed SiO_2. The etch rate of the SiO_2 has to be tuned in such a way that it is higher than the etch rate of the photoresist in order for the etch mask to sustain its function until the SiO_2 which needs to be removed is completely etched away. The primary etchant for the SiO_2 is tetrafluoromethane (CF_4) gas, with a small amount of oxygen (O_2) added to remove the polymer formed on the etched sidewall during the etching process. For our RIE process, the RF power used is 150W with 50mTorr of pressure. The CF_4 and O_2 volume used are 70sccm and 5sccm respectively. In our process, the SiO_2 etch rate is about 40nm/min whereas for the photoresist is about 30nm/min.

After the SiO_2 etching is done, the photoresist is removed using acetone. Now that the SiO_2 mask is in place, the PE-QWI process can be done. The plasma source generator ICP 180 used in the experiments was a Plasmalab System 100, which was built by Oxford Instruments. The system uses inductive coil to generate high-density “remote” plasma with no direct contact between the plasma and the substrate. The 13.56-MHz radio frequency (RF) and ICP power supply can provide the independent control on ion bombardment energy and ion current density with the operating powers up to 500 and 3000W, respectively. The chamber pressure is maintained at $5 \cdot 10^{-5}$ tor. The ICP chamber

is equipped with a water circulator to maintain the table temperature at 60˚C. The thermocouple, which is attached to the ICP chamber's wall, allows for the small temperature variations to be monitored. The ICP system is equipped with the He-back side cooled electrode with quartz as a wafer susceptor.

The argon plasma process was done on the samples for 1 min with the RF power and ICP power set at 400W and 500W, respectively. After the plasma process, the rapid thermal annealing (RTA) that promotes the near-surface defects' (brought on by the plasma exposure) propagation toward the MQW region is performed at 750˚C under flowing N_2 ambient for 120s. We used the Jipelec Jetstar 100 RTA system for the process. InP proximity caps were used on both sides to create group III over-pressure on the samples and prevent P (group III) out-diffusion during the annealing process. The temperature and RTA process time will determine the blue-shift which the sample experiences.

6.1.3. The IFVD QWI process

The IFVD technique involves the deposition of a dielectric cap layer, which is a 300nm thick SiO_2 in our case, onto the MQW substrate. This process step is exactly the same as that of the PE-QWI process. It is then patterned by photolithography and RIE. The photomask contains the necessary pattern that covers the passive region, where intermixing is required (i.e., the MMI and the waveguide areas) while exposing the active region (i.e., the EA switch region) where the bandgap is to remain as it is. In the RIE etching process step, the exposed SiO_2 is etched whereas the areas protected by the photoresist are not. Therefore, we would get a SiO_2 covering areas where intermixing is to take place while leaving the active region exposed. In the subsequent annealing step, the thermal expansion difference between the InGaAs layer and the SiO_2 film results in a strain effect. The thermal expansion coefficient of InGaAs is about ten times that of SiO_2 leaving the InGaAs surface layer under compressive strain. Under this condition, the out-diffusion of group III atoms into the SiO_2 film leaves vacancies behind, a favorable condition which minimizes strain in the system and inter-diffusion between the vacancies and atoms is promoted. All the recipes used are the same as those presented for the PE-QWI process

earlier. The samples were annealed at 750˚C for 120s in the RTP to induce the intermixing.

Once the intermixing is done, an acid bath of HF for about 3~4 minutes (until surface of wafer stop showing color or reaction change) is used to clean the remaining SiO_2 off. This applied to both the PE-QWI and IFVD process.

In order to determine the efficiency of the intermixing done, we performed a photoluminescence (PL) measurement on the intermixed and un-intermixed (as-grown) wafers in a measurement setup detailed in ref. [7]. The PL spectra from edge emission allow us to obtain more details of the electronic energy structure [7, 8]. The PL measurement of the QWI and as grown samples performed on both the *AsP Sample* and *AlAs Sample* are plotted in Fig. 6.1.5. The shifting of the peak of the spectra towards smaller wavelength is synonym to a blueshift. The blueshifts for the PE-QWI *AsP Sample* are about 100nm and 40nm for the pasive and active regions respectively giving rise to a differential blueshift of 100nm. For the *AlAs Sample*, the demonstrated differential blueshift was lesser at ~56nm for the IFVD intermixing. The blueshifts in both samples indicates that for the passive regions, a bigger bandgap have been induced in the waveguide material, which translates to minimized absorption loss. This lower blueshift in the case of the *AsP Sample* would therefore result in a bigger propagation loss at lower wavelengths. In order to reduce the propagation loss, a higher operating wavelength which would make the waveguides ‘transparent’ in the passive region is preferable. However, this would have to be balanced with the active region’s working bandwidth in order to obtain the best operating wavelength for the integrated circuit.

Using a set of Matlab software coding written specifically for investigating interpolation of quaternary III-V alloys parameters with surface bowing estimations [9] and QW states calculation using 8-band k·p method with finite difference [10], the interdiffusion between group III and group V components (in angstrom) for the case of the InGaAs/InGaAsP MQW was estimated from Fig. 6.1.5(c) to be 10:12 angstrom whereas the interdiffusion of the x and y values in InGaAlAs/InGaAlAs MQW is approximately 18:17 angstrom based on Fig. 6.1.5(d). These estimations were based on a single QW layer for the heavy-hole (HH) case (TE polarization).

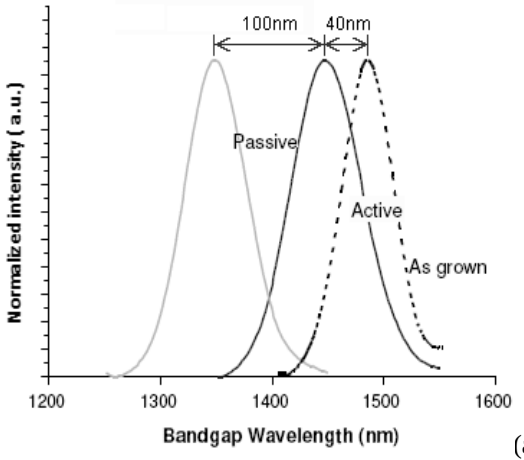

(a)

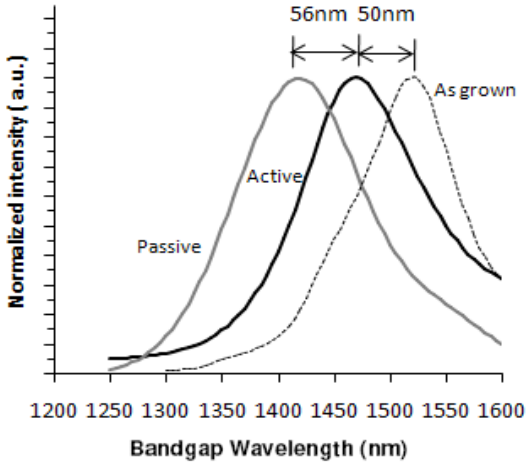

(b)

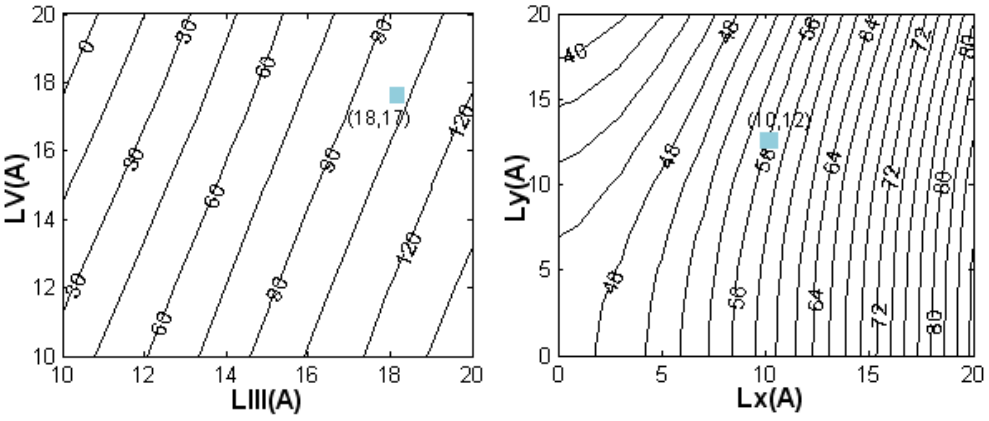

(c) (d)

Fig. 6.1.5. PL spectrum at room temperature of a (a) 5 quantum wells waveguide sample (Sample AsP) after the PE QWI with ICP for 60s and RTA at 750°C for 120s and a (b) 9 quantum well waveguide sample (Sample AlAs) after the IFVD with RTA at 750°C for 120s. The PL spectra from edge emission is obtained at room temperature ambient. The simulated wavelength shift contour based on interdiffusion of the (c) group III-V for the InGaAs/InGaAsP MQW and (d) components x-y in the In(x)Al(y)Ga(1-x-y)As MQW where the squares indicate the wavelength shift obtained from experiment

6.2 Fabrication of the active and passive components

6.2.1. Electrical Isolation Trenches

Once the IFVD-QWI process is completed for the necessary area, the next step of the integration would be the defining the electrical isolation trenches. The purpose for the electrical isolation is to create a break, or isolation, between the active and passive regions so that electrical leakage is minimized. Without the isolation, the passive region will also be active when an electric field or current is applied to the active region, since the passive region has the same p-i-n structure. Some isolation, however, might have been achieved during QWI as the passive region was exposed to plasma and so the top contact layer could have been sputtered away during QWI.

To improve the isolation, the waveguide side walls can be insulated with polyimide or other materials and small trenches can be etched between the two regions. We designed our trenches to be ~10μm wide and ~1μm deep. The trenches are deep enough just to remove the p-doped upper layer, but cannot be too deep as this may affect the light propagation along the waveguide core underneath. Fig. 6.2.1 shows the SEM photographs of the isolation trenches separating both regions.

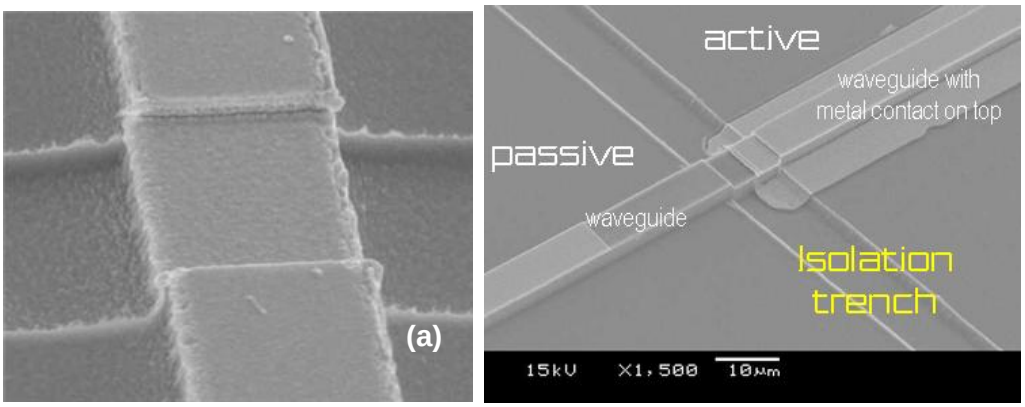

Fig.6.2.1. SEMs showing (a) a closeup of the crucial intersection between regions along a waveguide and (b) the isolation trench that separates the active and passive regions after p-electrode metal deposition on the active waveguide

To achieve the trench, 300nm of SiO_2 is once again deposited on the intermixed sample using PECVD. This is followed by photolithography and RIE SiO_2 etching where SiO_2 acts as an etch mask for the ICP dry etching process. The ICP power is set at 400W and the RF power at 100W. The process pressure is set at 32mTorr and the CH_4:H_2:O_2 flow rates are set at 30:10:1sccm. This optimized process recipe gives us the etch rate of ~250nm per minute. Although this process can be done either before or after the waveguide definition step, we often prefer to define the isolation trenches before the waveguides are etched because the trenches are shallower with respect to the waveguide etch depths, and thus, by performing this process first, the pattern definition in the next process would be less affected and the critical places where the waveguides and the trenches intersect, would be better defined (see Fig. 6.2.1(b)).

6.2.2. Fabrication of strongly guided 1xN MMI splitters

In order to allow for more tolerance in fabrication, the waveguide width for the device is set as 8µm. For the 1x2 MMI, the MMI width W_{MMI} designed is 32µm and the L_{MMI} is set as 1150µm. In order to create strongly guided waveguides, where the core level is etched through, the etch depth is set as 3µm. To achieve this, the 5 major fabrication process steps previously described in

Chapter 3 were followed. A 300nm thick layer of SiO_2 is deposited on top of the samples and patterned by photolithography and RIE.

These processes are almost similar to the ones used to define the active and passive area during PE-QWI and also for the isolation trenches. However, because the waveguide widths are much narrower, more critical alignment and care are needed in handling the samples. For instance, in order to ensure better adhesion of the photoresist, a layer of hexamethyldisilazane (HMDS) is added onto the SiO_2 before the photolithography process as HMDS promotes better adhesion of the photoresist to the SiO_2 surface. The HMDS vapour is applied via a HMDS oven heated up to the temperature of 150ºC. HMDS vapour is then pumped into the heated oven at 500torr for 300seconds. For the photolithography process, we used the CEC Model 100 spincoater, set at 4krpm for 30 seconds to spin coat the photoresist before proceeding with the mask aligning, UV exposure and developing. The alignment markers from the previous process are utilized to align the waveguides in the right positions. It is crucial to obtain the right exposure and developing time as over exposure would cause waveguide broadening and over developing would result in rough photoresist side wall and peeling of photoresist in severe cases. After the SiO_2 etching is completed, the photoresist is removed using acetone, leaving only SiO_2 pattern on the sample surface.

With the SiO_2 acting as the etch mask, the ICP process now acts as a dry etching process. In the waveguide definition process, RF and ICP power are set at 125W and 700W respectively, and the process pressure is maintained at 4mTorr. The Cl_2:N_2 ratio found to give the optimum balance between surface finish and etch rate is about 2μm/min [11]. During the isolation trench process however, Cl_2 gas is not used as high etching rate is not necessary for the shallow trenches. After the ICP etching process, the remaining SiO_2 is cleansed away using HF acid. The 1:2:3 mix ratio of HF, NH_4F and H_2O was utilized, giving us the etch rate of about 80nm/min.

6.2.3. Fabrication of the EAM

After having defined the passive and active regions by QWI, the isolation trenches and completed the waveguides which crosses the trenches and pass through the active area, the EAM active portion was fabricated. The final few fabrication steps are similar to what have been used to fabricate the standalone EAM waveguides previously mentioned in Chapter 5.

The next process step begins with the planarization of the sample. This involves spin coating a thin layer of BCB 3022-37 onto the fabricated sample and thinning down the layer until the waveguides are exposed. This planarization step is then followed by the p-pad metallization step which also defines the modulator. The metallization were accomplished using the E-beam Evaporator. After defining the pad coverage with photolithography, the samples were attached to the E-beam evaporator for the layers of metal to be evaporated onto the samples. 50nm of Ti was evaporated onto the device followed by a 200nm thick gold film. This was followed by the lift-off process, where an acetone bath was used to remove the excess gold by washing away the photoresist where the excess gold has been evaporated upon. As for the n-pad, the bottom surface of our device had been designed to serve as the n-electrode. The n-contact is made up of Ni/Ge/Au/Ni/Au in the thickness of 5/25/100/20/50nm. In order to improve the p-i-n contact, the sample was thinned by lapping before the metallization process. Through lapping, we reduce the sample thickness from its initial ~350μm to about 100μm. This thinning process also facilitates the dicing and cleaving of the samples for subsequent testing. After the samples had been diced, they were attached unto copper plats or surmounts with heated indium. The fabrication steps for the entire integration process have been illustrated in the process flow chart in Fig. 6.2.2.

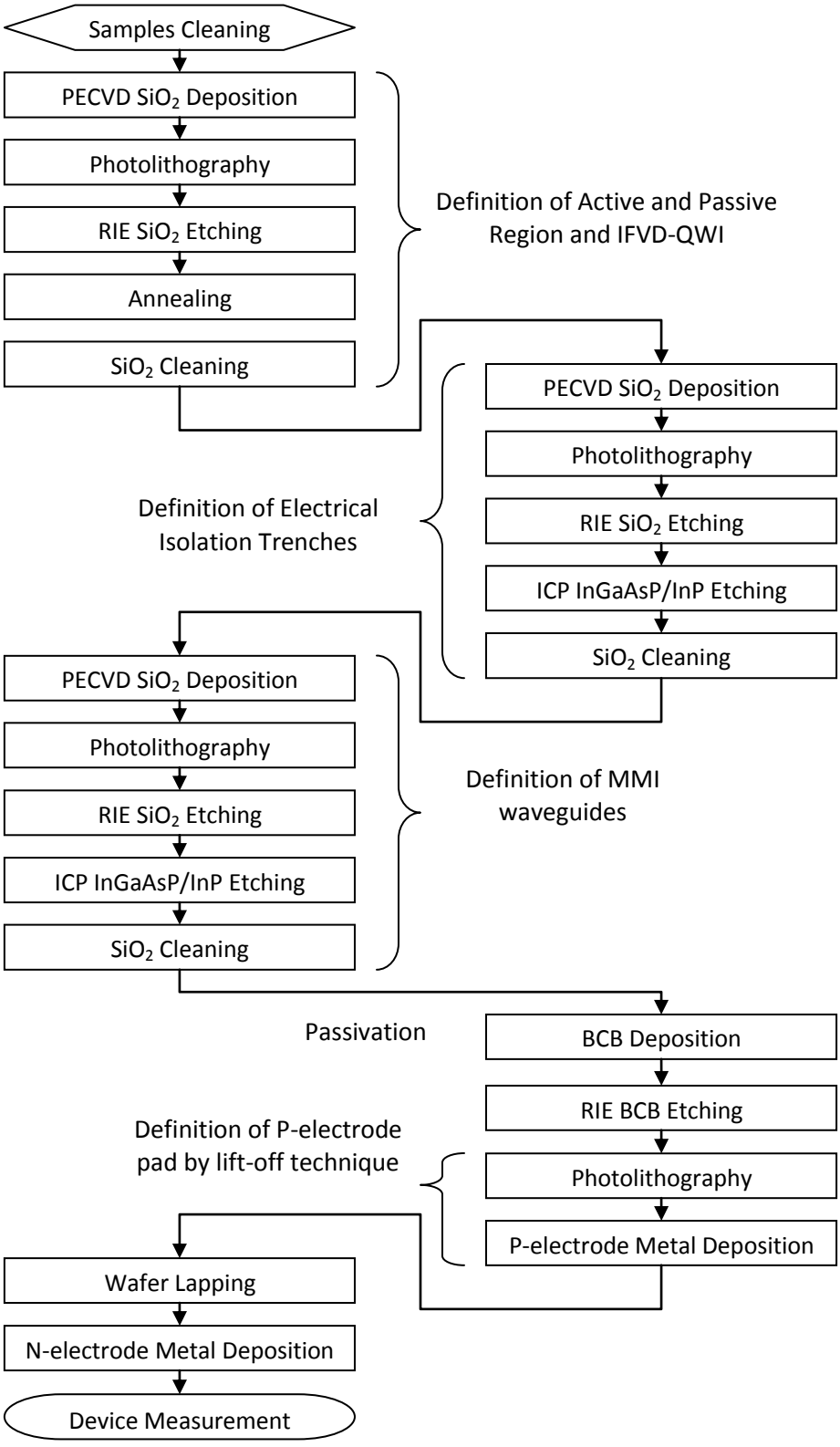

Fig.6.2.2. Process flow steps for the MMI + X device fabrication

6.3 Segment properties of the MMI + EAM device

Although the MMI + EAM is a device on its own, intermixing has rendered different level of changes on both parts of the device. Therefore, before analyzing the fabricated device as a whole, the device was segmented and individually measured to understand the component lost and other relevant measurement parameters. The device was divided into four segments as shown in Fig. 6.3.1. Segments #1 and #2 represent the passive and active waveguides respectively. Comparison between the two segments helps us determine how well the QWI has rendered most of the device 'passive'. Segment #3 is the 1x2 MMI with AWs of 8μm width and MMI with the width of 32μm and the length of 1100μm and Segment #4 is the 500μm long active region EAM with 300x300μm^2 wide p-pads.

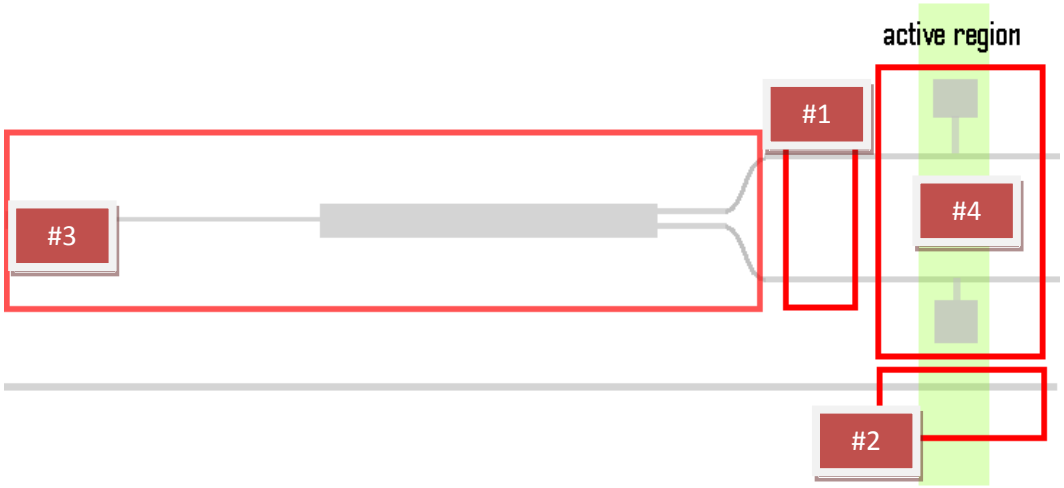

Fig. 6.3.1. Segmentation of the MMI + EAM device for separate studies.

6.3.1 Segments #1 & #2: Intermixed and active straight waveguides

The wavelength propagation range of both the intermixed (Segments #1) AsP and *AlAs Sample*s were measured as shown in Fig. 6.3.2 and the 3.2mm long *AsP Sample* generally had an even distribution which centered around the 1550nm region for both polarizations. For the 2.0mm long *AlAs Sample*, the visible range of the TE polarization which can be viewed with the vidicon infra-red camera was from 1570nm onwards whereas for the TM polarization, visibility begun at 1585nm. Although both polarizations for the *AlAs Sample* had a more stable and linear wavelength propagation at wavelengths >1620nm, it was beyond the working range intended.

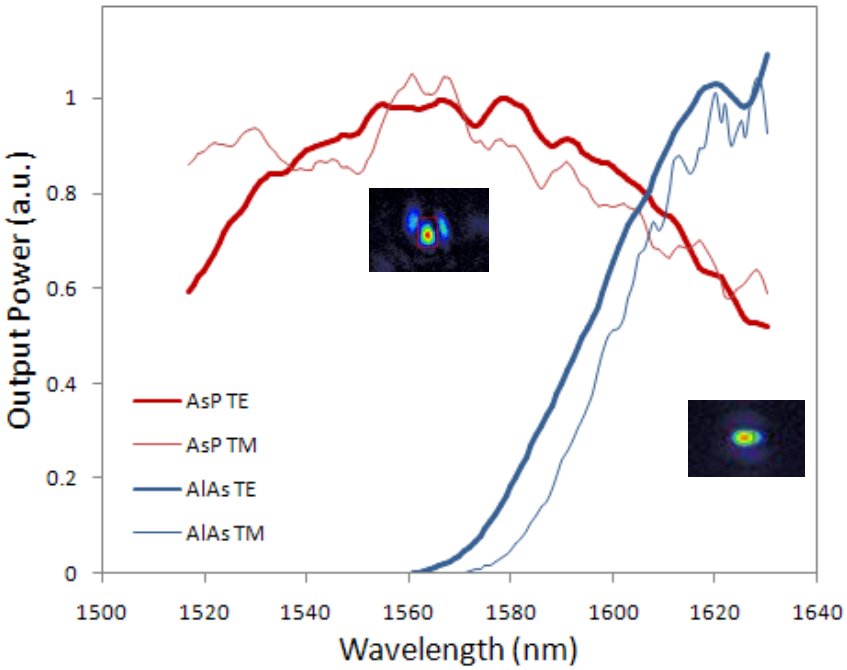

Fig. 6.3.2. Normalized output power of the straight waveguide spectrum for AsP and *AlAs Sample*s for TE and TM polarizations. Insets shows the optical output viewed from the vidicon camera.

Fig. 6.3.3(a) shows the optical transmission spectrum of the similar *AlAs Sample* (TE polarization) as above with finer resolution. A finer scan across the wavelength enabled us to determine the contrast, K of the output, and subsequently, the propagation loss constant, α as described in Chapter 3. The calculated results are presented in Fig. 6.3.5. The optical output views indicated that waveguides which are etched deeper often give better confined outputs, an

affirmation that strongly guided ridge waveguides are a better choice of structure over shallow etched waveguides regardless of concerns over rough sidewalls and perpendicular etching. From the F-P measurement undertaken for the *AsP Sample*, the loss of the intermixed straight waveguide was approximated to be ~0.87dB/mm-2.13dB/mm (TE) and ~3.2dB/mm-4.2dB/mm (TM) for our 3.2mm long sample. The TE polarization's propagation loss is close to the loss previously reported for similarly intermixed device (1.0 – 1.3dB/mm) [6]. The wavelength of the propagation range is centered on 1550nm as designed. The propagation loss of the *AsP Sample* is comparatively lower than that of the *AlAs Sample* which was about 6.5dB/mm for both polarizations.

Fig. 6.3.3(b) shows a Vidicon Camera capture of a 1.78mm long *AsP Sample* which is made up of a 500μm long active device and a 1.28mm long intermixed waveguide. The output obtained is bright and clear although the input power is only 0.5mW and an ordinary fiber (instead of a tapered fiber) was butt coupled to the input facet.

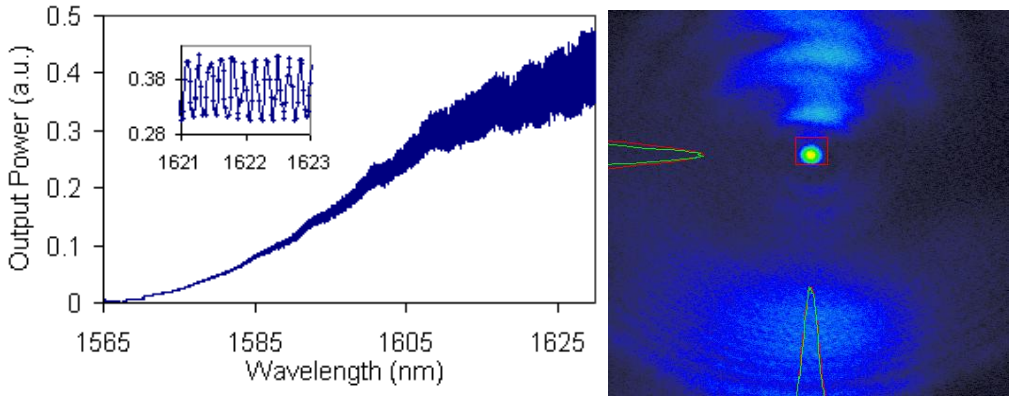

(a) (b)

Fig. 6.3.3. (a) Measured transmission of a TE polarized light through an 8μm wide 2mm long *AlAs Sample* waveguide. The loss includes propagation loss and insertion loss. The inset shows an enlarged portion of the measurement. (b) Measured output mode profile from a 1.78mm long *AsP Sample* made up of active and passive waveguide observed using a Coherent MicronViewer Vidicon Camera Model 7290A at 1550nm

In the second segment (Segment #2) the propagation loss of the 'active' portion of the device was measured. Although the 500μm long active portion makes up only a short length of the entire device, the effect of rapid thermal annealing process during the intermixing process may have altered the material.

Temperature annealing may cause disorder at the heterointerfaces and reduce the quantum confinement effect of the quantum wells. The active portion which is also the equivalent length of the active device is much longer than the EAMs that were fabricated and tested in Chapter 5 (~300μm) because the main concern here was with achieving lower reverse bias voltage modulation (as opposed to lower capacitance). This extended length could impede the optical propagation loss of the integrated device and therefore should be as low as possible. Fig. 6.3.4(a) shows the normalized transmission spectrum of an active *AsP Sample* which is about 0.5mm long. The device's propagation loss for the range of 1540nm-1560nm for TE polarization was ~5.2dB/mm-7.5dB/mm and for TM polarization, ~10.2dB/mm-13.7dB/mm which was about the same level as that reported for EAM waveguides which ranged from 15dB/mm to 20dB/mm [12]. The propagation loss gradually increased as the wavelength deviated from the 20nm range for both polarizations. For the case of the *AlAs Sample* waveguides, the propagation loss calculated from the FP spectrum as shown in Fig. 6.3.4(b) was ~16.5 (25.0) dB/mm for TE(TM) polarization at the wavelength of 1575nm.

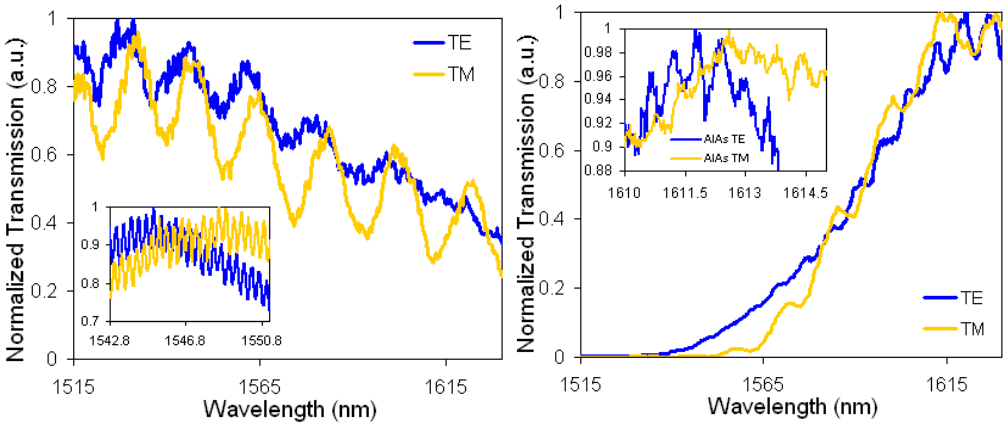

(a) (b)

Fig.6.3.4. Measured transmission of an active (a) 0.8mm long *AsP Sample* and (b) 0.5mm long *AlAs Sample* for the wavelength range 1514-1630nm. Inset shows a finer scan of a shorter wavelength range which is used for FP propagation loss measurement

Fig. 6.3.5 summarizes the propagation loss for the respective working range of both material structures for both polarizations for both the intermixed and annealed waveguides. Although the output intensity of both devices was almost similar, calculations indicated that the *AsP Sample* overall had lower loss compared to the *AlAs Sample*. This could be due to the poor cleaved

surface for the case of the *AlAs Sample*s tested. The measured loss for the *AsP Sample* was quite consistent with the propagation loss of InGaAsP/InP sample which was measured and demonstrated in Chapter 3. This goes to show that the QWI had been a successful process which has helped reduce the absorption of light from the material. However, although the *AsP Sample* experienced less propagation loss, its optical mode field was less confined and its narrower cavity compared to that of the *AlAs Sample* resulted in higher coupling loss between the fiber and the waveguide. The *AlAs Sample* on the other hand, with its bigger cavity and better confinement, tended to excite higher modes easily since the waveguides were as large as 8μm. However, when accurate alignment was achieved, the higher order modes were no longer visible.

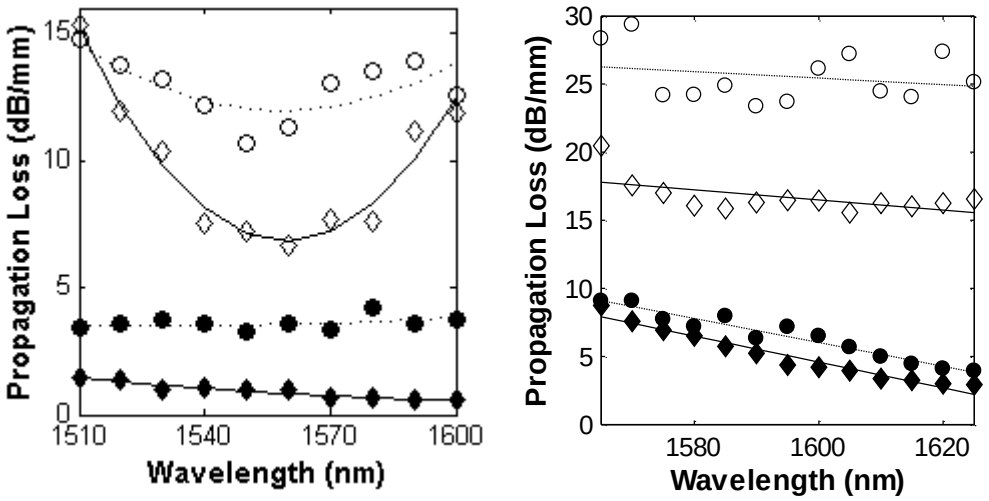

(a) (b)

Fig. 6.3.5. The propagation loss derived from the output power spectrum for both passive (shaded) and active waveguides (unshaded) for TE (diamond) and TM (circle) polarization for the 8μm wide (a)*AsP Sample* and (b)*AlAs Sample* waveguides

The devices which had been exposed to humidity and oxidation could have degenerated their condition. We realized that the major yield killer in our fabrication when segmenting these devices was the cleaving process. This is because as the device's waveguide width is scaled down it increases the sensitivity of the device towards the tinniest bit of damage on the cleaved facet. These facet defects increases the difficulty of locating the actual modes and also retard the mode quality. Subsequently, it also affects the F-P results which were collected because the F-P results are also dependent on the mirror like facet surface of a good cleave (or dicing) - an ideal condition in obtaining accurate F-

Ps. Thus, we often found discrepancies in our propagation loss results. Nevertheless, the high loss of the waveguides found here may also be due to the gold above the waveguides. The mode shapes in these waveguides are also less well defined because of the similar reason.

6.3.2. Segment #3: 1x2 MMI

The 1x2 MMI splitter serves to split the input light from the laser source into two. The fabricated MMIs' dimensions are based on simulation results from the APSS Apollo software's for the *AsP Sample*'s material and structure. Since the *AsP Sample* and *AlAs Sample*s' material refractive indices are quite similar, the MMI dimensions are maintained for the latter. With the AWs set as 8μm, the MMI device is 32μm wide and 1100μm long, Fig. 6.3.6 illustrates how the designed 1x2 MMI would work. The S-shaped offset bend is 400μm long and 50μm wide.

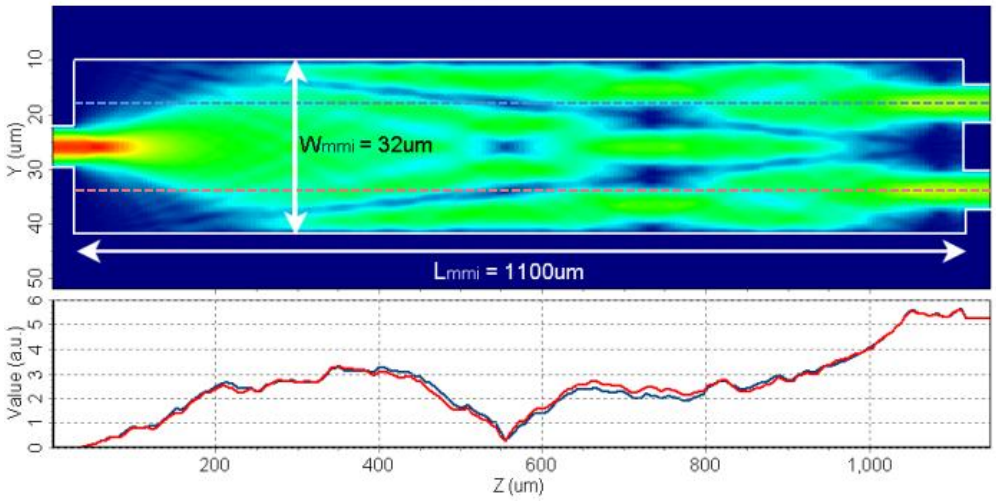

Fig. 6.3.6. 2D-BPM simulation of a 1x2 MMI device. The top half shows the field distribution of light in the device while the bottom part shows the output amplitude from both arms at different lengths of the device.

The diced MMI segments along with the AWs and S-bends for the AsP and *AlAs Sample*s are 2.42mm and 2.0mm respectively. The different lengths gave rise to different output power collected but do not affect the characterization of the MMI performance in other ways.

Fig. 6.3.7 shows the MMI results collected for the (a) *AsP Sample* and (b) *AlAs Sample* across two bands of wavelengths (1515-1630nm and 1565-1630nm). For the *AsP Sample*, 50:50 splitting is apparent around the range of the 1550nm which is the range the MMI was designed for. However, at wavelengths further away, the splitting ratio gradually changes. The 3dB splitting is maintained for ~20nm for both polarizations. The wavelength band shown for the *AlAs Sample* is much shorter because of its weak output power at lower wavelengths. At 1550nm, the output from the *AsP Sample*'s MMI adds up to 4.165μW which is 95% of the 4.366μW obtained from a straight waveguide of equal length, which gives an excess loss of about 0.205dB.

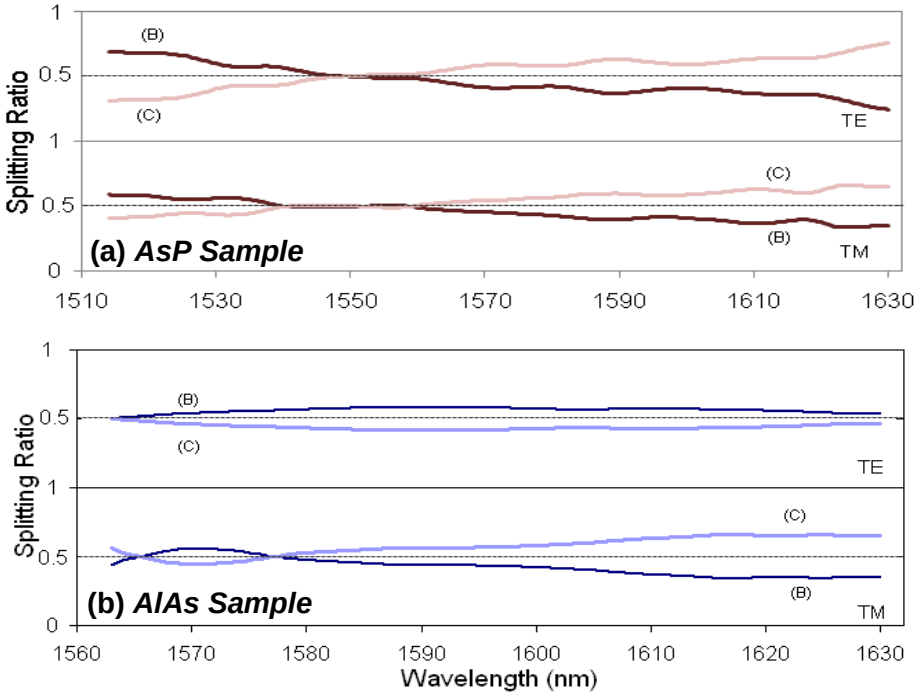

Fig. 6.3.7. Splitting ratio for both TE and TM polarization for the (a) *AsP Sample* and (b) *AlAs Sample*

The *AlAs Sample*'s material structure was highly absorptive at lower wavelength as seen in the measurement results of Segment #1 in Fig. 6.3.2. The intermixing process performed appeared to be less effective for this device at lower wavelengths as compared to the *AsP Sample*. Because of its high loss at lower wavelength, the MMI was only able to perform at wavelengths higher than 1580nm. Therefore, although the splitting ratio was much closer to the desired 50:50 split at the lower wavelengths, the higher wavelength

range >1575nm was a more preferable working range with the splitting ratio closer to 55:45 for TE and 65:35 for TM polarizations.

This difference in output power splitting ratio was probably brought on by the different materials employed. The MMI mask was designed for the *AsP Sample* for 50:50 splitting ratio at 1550nm. The *AlAs Sample* with the core refractive index of approximately ~3.6 is much higher than that of the *AsP Sample*. Therefore, the MMI length of the *AlAs Sample* would need to be slightly longer according to equation (2.3). Therefore, the splitting ratio of this device at a slightly shorter length would not be as equal as the *AlAs Sample*.

6.3.3 Segment #4: EAM

Measurements have been carried out to verify the modulators' extinction ratio and the reverse voltage bias necessary to achieve the acquired ratio. All the EAMs which have been integrated with MMI devices were 500μm long and 8μm wide. Fig. 6.3.8 is a collage of pictures regarding the measurement of both types of devices. The *AsP Sample*'s material bandgap design (PL emission peak) is centered on the wavelength of ~1500nm with a differential blue-shift of 100nm after QWI (as shown in Fig. 6.1.5). The structure therefore should work as an EAM device at a wavelength farther away from this active material bandgap at ~1550nm, about 20nm to the right of the peak range. The devices were measured with an input power of 10mW. At TE polarization, the modes were easily found at higher wavelengths (above 1550nm), an indication of lower absorption by the device at that working wavelength. As for the *AlAs Sample* (TE polarization), its peak PL emission was at the wavelength of 1540nm before intermixing and a differential bandgap blue shift of ~56 nm was achieved between the passive and the active regions against ~50 nm thermal shift in the active region. Its working wavelength will therefore be relatively higher at >1560nm.

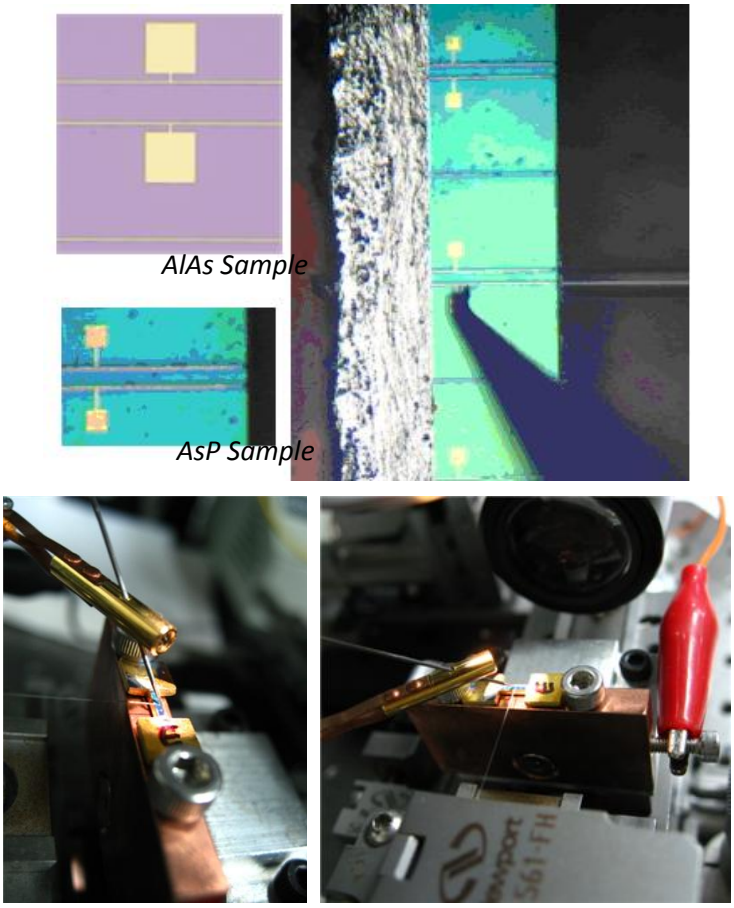

Fig. 6.3.8. The pictures in clockwise shows the *AsP* and *AlAs Sample*s viewed from above the stage with a 50x magnification; the 3rd picture shows a cleaved fiber butt coupled to one end of the device while a probe rests on the p-type gold pad. The device rests on a 'H' copper plate which is screwed tight to a copper stage base which acts as the ground. The figures show a fiber input and free space output with bias voltage applied using probes and copper base. The last picture shows a close up view of the probe, fiber and device from the side.

Since the working principle of the EAM switches is based on the electroabsorption effect, the absorption spectra of the device would also assist in determining the devices' optimum working wavelength. Instead of the absorption spectra, we can deduce the absorption through the photocurrent spectra [13] which can be obtained from I-V curve measurements. The I-V curve measurements undertaken for the devices was measured using the Hewlett Packard 4155A Semiconductor Parameter Analyzer and showed good p-i-n contact and correlation between modulator's photocurrent and varying input wavelength as shown in Fig. 6.3.9. The photocurrent increase at lower wavelengths translates to lower photocurrent resistance, R_0 and reduced RC time constant in equation (5.7). The photocurrent spectra (inset) of the device indicated that the higher the absorption of the material, the higher the

photocurrent generated. At shorter operating wavelength, the photocurrent generated (a.k.a. absorption difference) under different bias voltages were relatively higher. As the operating wavelength shifted farther from the active material bandgap, the device performance would theoretically improve. The *AlAs Sample* (figure not shown) similarly demonstrated good I-V curves; an indication of good passivation process, etch back and metal deposition, albeit at longer wavelengths.

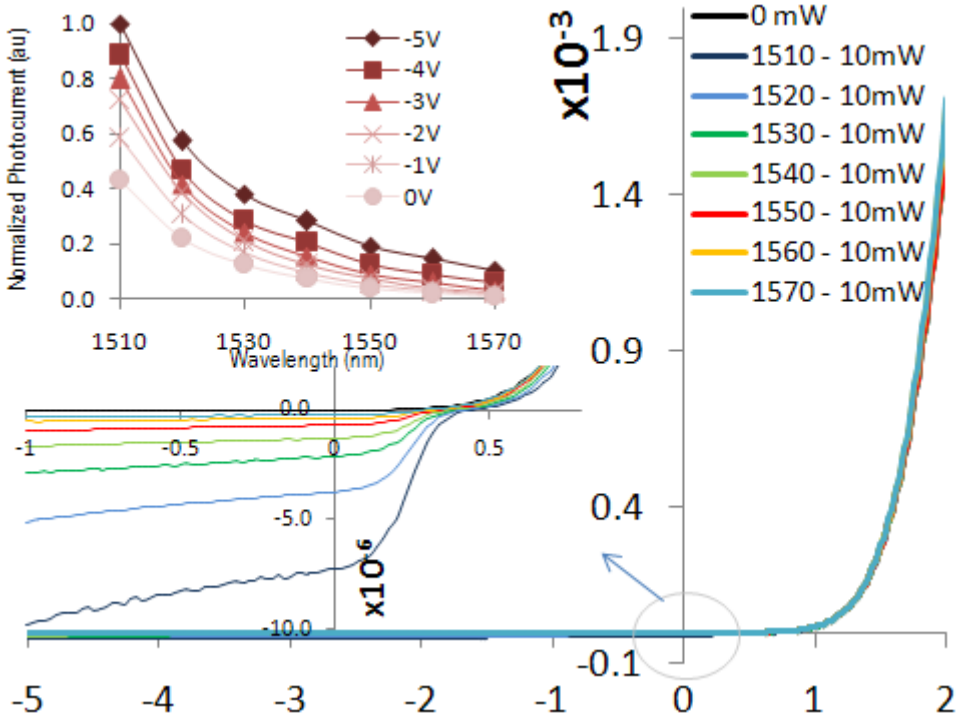

Fig.6.3.9. IV-curves of an *AsP Sample* straight modulator obtained for zero input voltage (without light coupling) and a 10mW light coupling of various input wavelengths (from 1510nm to 1570nm). The subsets are the zoomed in view of the circled area show increasing photocurrent in shorter wavelength (bottom) and the normalized photocurrent of the modulator (top).

Fig. 6.3.9(a) shows the plotted graph of the output TE and TM power from the *AsP Sample*'s modulator waveguide versus reverse bias voltage for three wavelengths – 1540nm, 1550nm and 1560nm with input optical power at 10mW. For the TE polarization, both the 1540nm and 1550nm measurements showed and extinction ratio of only about 5dB whereas at wavelength of 1560nm, although 10dB extinction ratio was achieved, the reverse bias needed to achieve this was as high as 15V. Similarly, for all the TM measurements, although 10dB extinction ratios were achieved across the wavelengths, they were all at the cost of high reverse bias voltages. The non-uniform curves for

different wavelengths were caused by the high bias voltage applied, which affected the modulation efficiency of the device.

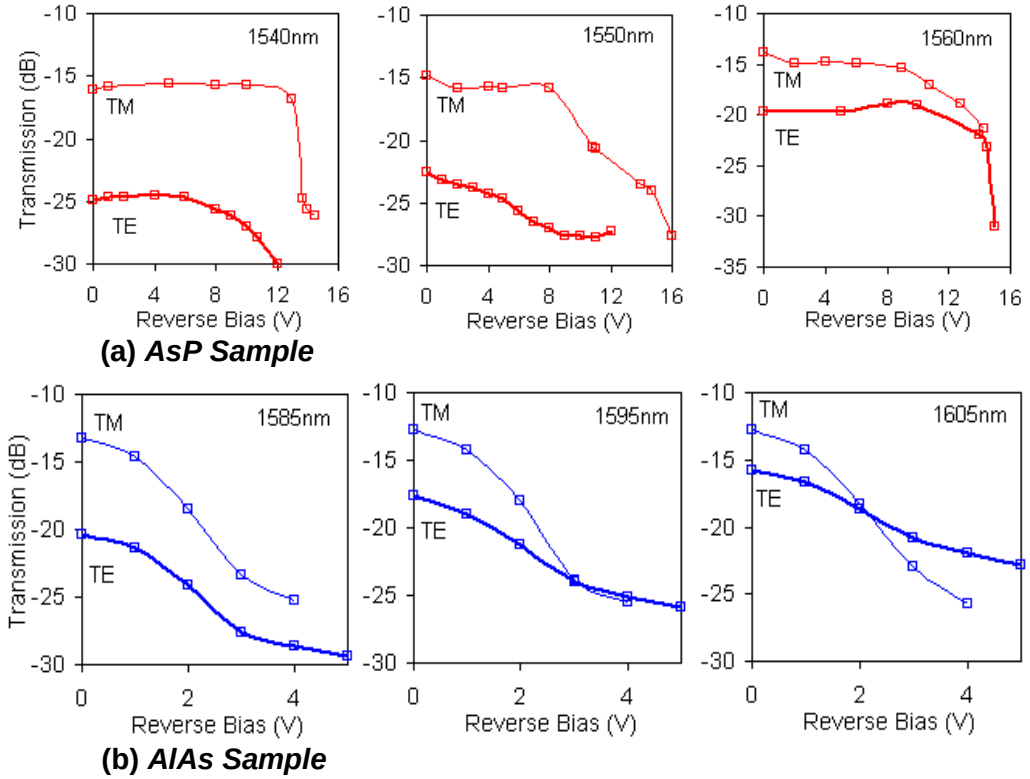

Fig.6.3.10. Transmission vs. reverse bias voltage measured for the (a) *AsP Sample* at the wavelengths 1540, 1550 and 1560nm and for the (b) *AlAs Sample* at the wavelengths 1585, 1595 and 1605nm for both polarizations

The modulation results of the *AlAs Sample* as shown in Fig. 6.3.10(b) were much improved compared to the *AsP Sample*s. Extinction ratio of >10dB was obtained for the TM polarization consistently at reverse bias voltage of 4V for the wavelengths of 1585, 1595 and 1605nm. The TE polarization on the other hand only had extinction ratio of up to 9dB for the 1585nm wavelength, and the extinction ratio gradually decreased to only about 7dB in the 1605nm case. This is because for this device, the TE polarization modulates better at lower wavelengths whereas for the TM polarization at this range of wavelength, it is less sensitive to wavelength variation and is able to work optimally.

The working modulators in both types of materials confirmed that the QWI intermixing on the other parts of the device have not affected the active properties of the protected region. Although the *AsP Sample* yielded waveguides with good propagation loss and splitting ratio, the *AlAs Sample* was able to function as a better modulator due to its structural design which is more

suited for EAMs. Fig. 6.3.11 demonstrates the TE polarization reverse bias voltage effect on AsP and *AlAs Sample*s at 1540nm and 1585nm respectively.

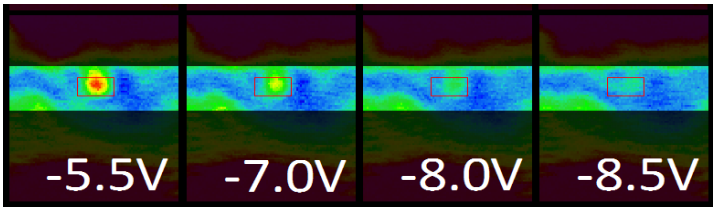

(a)

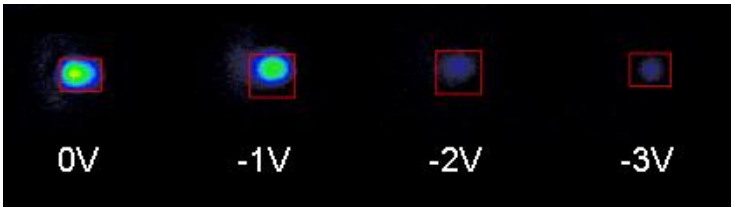

(b)

Fig.6.3.11. Bias voltage effect viewed from the Coherent MicronViewer Vidicon Camera Model 7290A for (a) *AsP* and (b) *AlAs Sample*

When forward bias voltage is applied on the devices, the less deeply etched devices are able to function as a semiconductor optical amplifier (SOA). Fig. 6.3.12 demonstrates this effect when a voltage of 2V is applied on one of the devices. The spectrum range, propagation loss (Segments #1 and #2) and component performance (Segments #3 and #4) study of each segment allowed for better understanding of the best fit for the overall MMI + EAM 1x2 switching device in the following section.

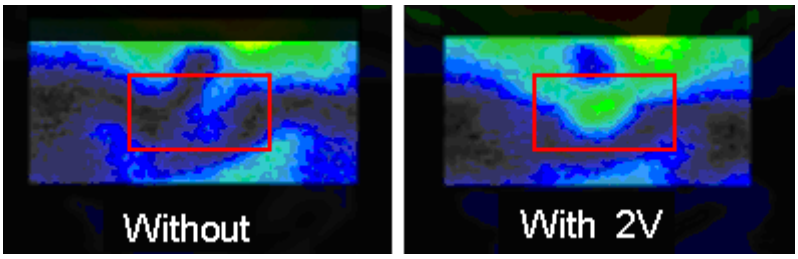

Fig.6.3.12. SOA effect at 1600nm obtained from vidicon camera without and with the application of 2V of DC voltage.

6.4 Characterization of MMI + EAMs

The characteristics of the fabricated MMI + EAM device, shown in Fig. 6.4.1, is determined by its I-V response, the output mode of the device and its response towards reverse bias and wavelength variation.

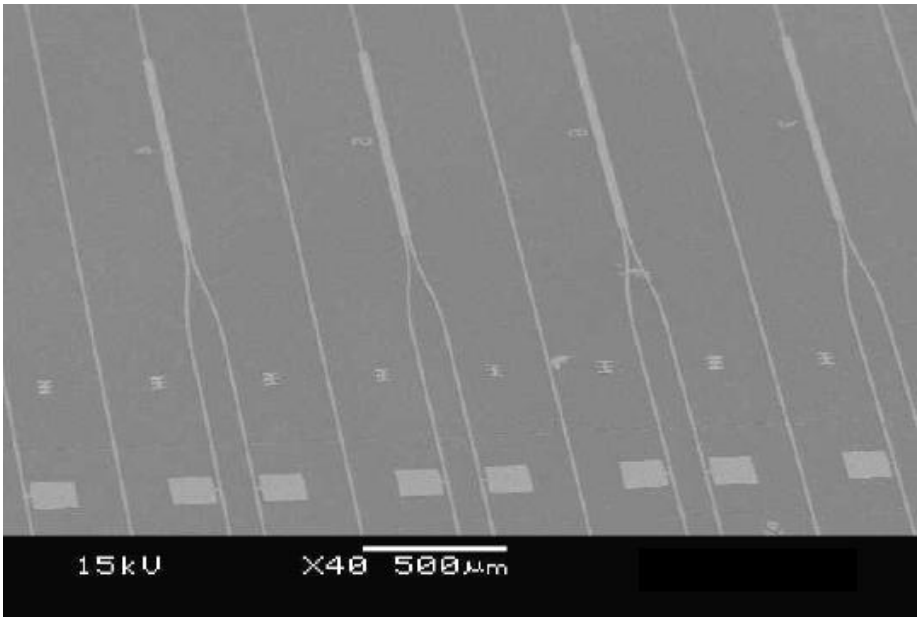

Fig.6.4.1. SEM of the completed MMI + EAM devices

The measurement was performed with a setup similar to that which was illustrated in Fig.6.3.7. The I-V response of both the *AsP Sample* and the *AlAs Sample*s were measured by biasing each of the active portions of the AW arm via its p-electrode metal pad. The photocurrent was measured with and without input light which was coupled to the input AW of the MMI via a tapered fiber. Fig. 6.4.2 plots the measured I-V or current against reverse bias voltage for both the *AsP Sample* and *AlAs Sample* devices with 500µm long active length and a summation of ~2000µm long passive device at both ends of the active portion depending on the dicing position. By observing the I-V response the fiber can be accurately positioned. Aside from getting a bright round clearly defined mode, when the fiber is rightly coupled, the I-V response would also indicate the highest photocurrent change. Due to the size and high propagation loss of the devices, an optical fiber amplifier (OFA) was used to amplify the input tunable laser (max output power of laser ~ 12dBm). The OFA used was a Benchtop Optical Fiber Amplifier GA12000 Series from Connet which can amplify input light between the wavelength ranges of 1529nm to 1562nm up to 23dBm. Therefore, at the wavelength of 1575nm (slightly beyond the maximum range), which is the wavelength used to measure the AlAs TE polarization, the maximum output the amplifier could reach was merely 14.5dBm. Although there is lower insertion loss at higher wavelength ranges of 1580nm to 1630nm

for the *AlAs Sample*s, only 12dBm of maximum input laser power was achievable.

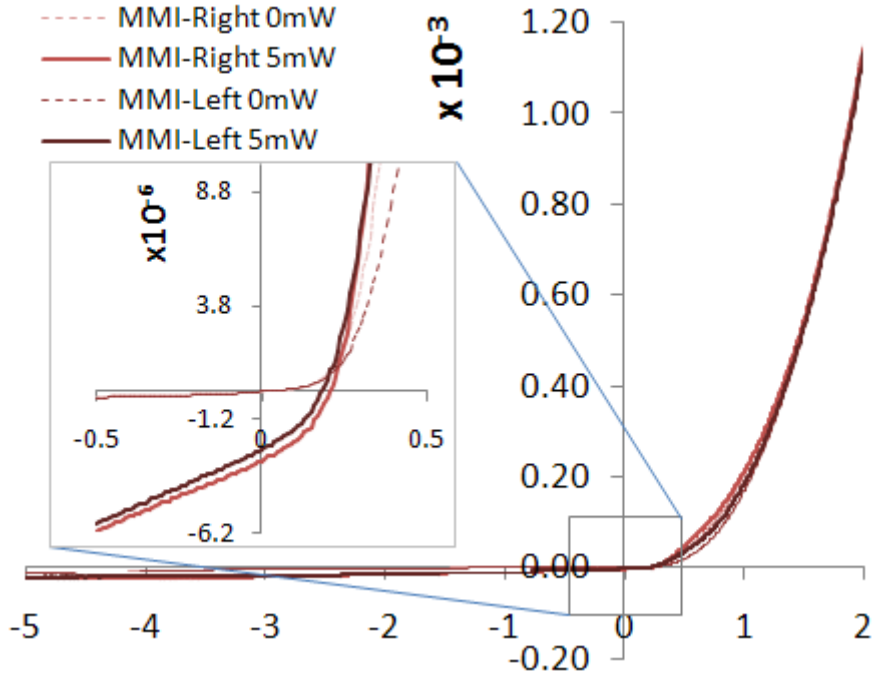

(a)

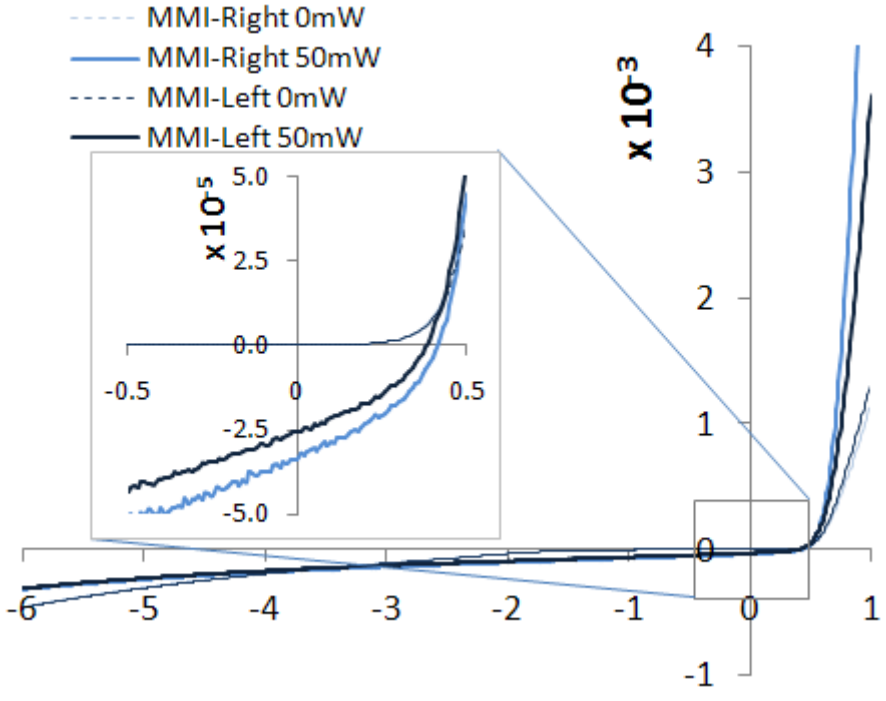

(b)

Fig.6.4.2. IV-curve of an (a)*AsP Sample* and (b)*AlAs Sample* MMI + EAM's left and right arm. The insets are the enlarged portion showing that photocurrent exists when light is coupled into the MMI device

The measured photocurrent against wavelength for both arms of the MMI + EAM for the *AsP Sample* for 0V, 0.5V and 1.0V reverse bias voltage

was plotted in Fig. 6.4.3. High input power (up to 23dBm) was necessary in order to locate the weak output mode due to the high insertion loss. The graphs can be used as indication of the absorption spectra of the device. From the figure, it can be seen that at higher wavelength, the absorption of the material (a.k.a. photocurrent produced) reduces, which is expected as the operating wavelength is getting father from the active material bandgap. The figures are also indicative of the possible working wavelength of the MMI + EAM device as we require the absorption to be low at 0V reverse bias voltage (>1540nm) but the working wavelength should be as near to the active material bandgap as possible. Actual measurement indicated the best operating wavelength to be 1550nm for the *AsP Sample* which is close to the indicated wavelength.

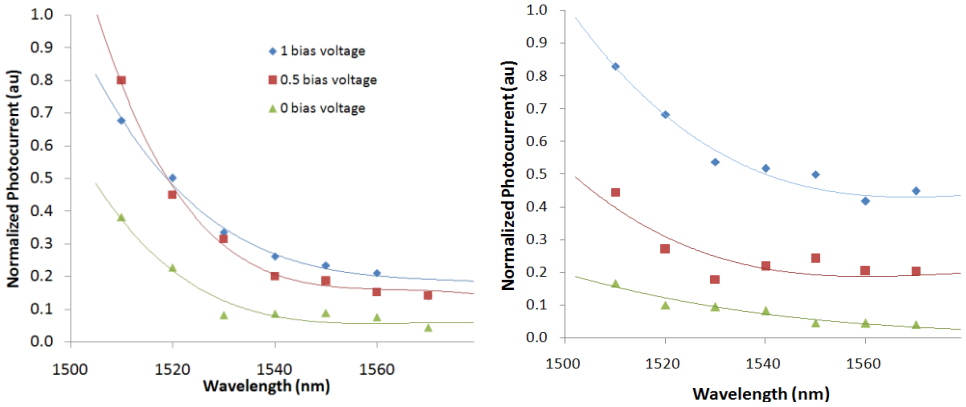

(a) (b)

Fig.6.4.3. Normalized photocurrent vs. wavelength for the (a) left and (b) right arms of an MMI+EAMs

The fiber-to-free-space loss (excluding device) measured was ~19dB (discussed in Chapter 3). At zero bias, the losses (excluding that of the free-space loss) for each arm in both types of devices is shown in Table 6.1. Smaller insertion loss can be obtained by better cleaving and through AR coating of the facets of the device. The maximum slope efficiency of the normalized transfer curve at their respective best bias points, V_{bb} are also tabulated in Table 6.1. Only the TE polarization results were measured and presented in the table due to the high propagation loss of the TM polarization (see Fig. 6.3.4). The best extinction ratio measured for the *AsP Sample* was 6.5 dB at a reverse bias of 13 V, which is relatively too high for a switch. The poor extinction was partly caused by the thin core layer which consisted of only five quantum wells and

which offered a smaller confinement factor. Stray light that leaked into the detector may have also lowered the extinction ratio measured. A possible reason for the stray light is scattering from the isolation trench between the passive and active sections of the device (the trench might have been etched too deep).

In Fig. 6.4.3, the normalized transmission and modulator's photocurrent against reverse bias for the TE polarization of the *AlAs Sample* at the wavelength of 1575nm for both left (C) and right (B) arms was plotted out. The extinction ratio (ER) obtained at 4V reverse bias was about 10dB. The ER was obtained for a 2-V voltage swing (from −2.0 to −4.0 V). Although the extinction ratio was comparable to that of the diced individual modulators (Segment #3), the normalized transmission curve obtained was less smooth because the higher input power coupled into the device may have caused saturation in the bandgaps of the MQWs which in turn impeded the absorption ability of the switch. The much longer device also needed much better aligning and tilting to obtain a device which is parallel to the fiber, with perpendicular facets. A little misalignment or poor cleaving would excite higher order modes in the waveguides which are quite broad (8μm). These higher modes tended to modulate less efficiently.

TABLE 6.1 Measurement results for optical properties of MMI + EAM

Parameter	*AsP Sample*		*AlAs Sample*	
	Left arm (C)	Right arm (B)	Left arm (C)	Right arm (B)
Insertion Loss (at zero bias) [dB]	21.7	18.6	24.0	24.1
Maximum slope efficiency (MSE)	0.43	0.50	0.11	0.36
Best Bias Point, Vbb [V]	-8.8	-11	-2.2	-2.6
Working wavelength, λ [nm]	1550	1550	1575	1575

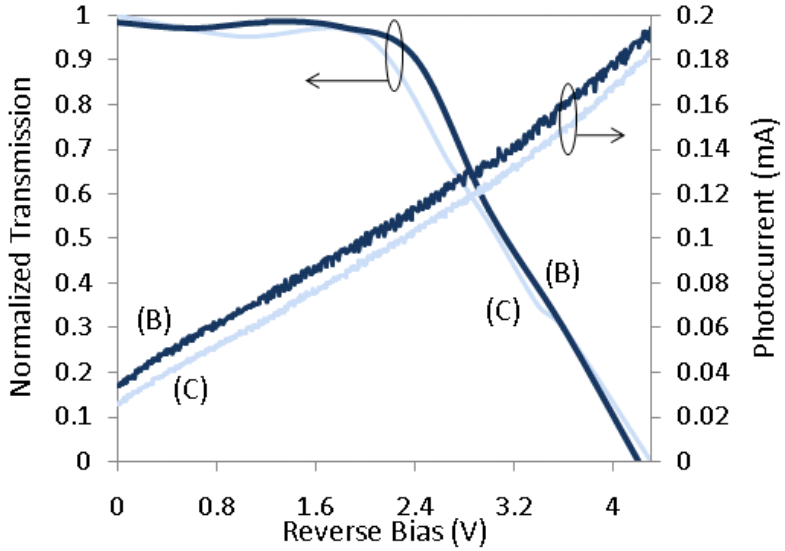

Fig.6.4.4. Normalized transmission and modulator photocurrent vs. wavelength for the left and right arms of an *AlAs Sample* MMI+EAM at 1575nm with input power of 14.5dBm (TE polarization)

Another parameter which is of interest is the absorption change $\Delta\alpha$ because it can be used to gauge how severely the residual absorption loss of the device may affect the device as a whole. The absorption change $\Delta\alpha$ can be deduce from the ER (in dB) according to $ER=4.34\gamma\Delta\alpha L$ derived from the modulator transfer curve equation (5.1). At the bias of 4.0V, the ER for the 500-μm long device was 10dB, implying that $\gamma\Delta\alpha = 46\ cm^{-1}$. The theoretical confinement factor simulated γ is 0.115 which approximates $\Delta\alpha \sim 297\ cm^{-1}$ which is much higher than the optical absorption constant of the device. This large value validates the assumption that propagation loss can be neglected in the section where the modulation takes place.

6.4.1 Discussion

The foremost problem faced was the insertion loss, coupling and the finding of the output mode (fiber-to-device-to-free-space). Because of the large insertion loss (>20dB at the bias point), the output optical signal is rather weak, which causes power penalty even after EDFA amplification. The waveguide modes at the overall much long length (2mm) are also often much harder to be located. This problem was more evident when measuring the *AsP Sample*. Due

to its narrow core (~5QWs and 6 barriers), the light was often poorly confined and stray light was often detected. Therefore, when searching for the mode, the spread-out mode can be mistaken as just part of the interference patterns often obtained when aligning fiber to device (see Fig. 6.3.4).

The second major problem faced when measuring the MMI + EAM devices was the overheating and burning of the metal contacts and waveguides when higher reverse bias voltage was applied. Coupled with the high input power (up to 23dB when measuring *AsP Sample*s), most devices under test were degraded after a few measurements.

Another problem was the imbalance of output intensity from both MMI arms for the *AlAs Sample*. Often, we would get a strong output from only one arm. The poor 3dB coupling of the MMI is related to two major factors. One being the MMI was designed to work best around the wavelength of 1550±15nm. At wavelengths further away from this, we had to contend with higher insertion loss. Secondly, the excitation of higher order modes due to misalignments would cause an imbalance of output power in both arms even at wavelengths within the design range.

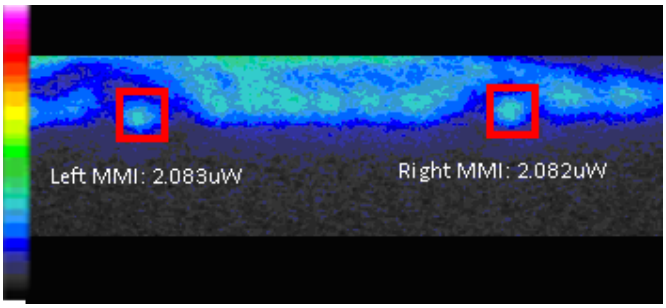

Fig.6.4.5. Mode for both left (C) and right (B) arms of MMI for a poorly aligned *AsP Sample*. Stray light is visible around the weakly guided modes.

Conclusion

A 1x2 optical switch based on two material bases with different material structure designs has been realized here. The device is made up of a 1x2 MMI beam splitting device integrated to two electroabsorption modulation devices through postgrowth bandgap energy tailoring of the material structures. The two material structures used are the InGaAs/InGaAsP MQW (*AsP Sample*) and the InGaAlAs MQW material structure with an enlarged core (*AlAs Sample*). The *AlAs Sample* modulators have shown significant attenuation with bias voltage swing of 2V (from -2V to -4V), suggesting the capability of signal modulation. The propagation loss reduction of the waveguides from active to passive (intermixed) component highlights the importance of QWI in realizing photonic integrated circuits. Further improvements on performance depend on increasing the technical capability of QWI for larger differential shift and smaller thermal shift, with which the material structure can be designed to optimize electroabsorption modulation at the desired wavelength.

Chapter 7

Conclusions and Suggestions for Future Work

This dissertation explores one of the various approaches toward achieving photonic integration circuits which comprises of both passive and active device. Major contributions of this dissertation include the theoretical and experimental works on the following 1) Understanding of the passive device multimode interference device (MMI) and its transformation from passive device directional coupler; 2) Wavelength splitter for 1310nm and 1550nm based on benzocyclobutene material; 3) Compact MMI based on SOI material 4) Optimizing EAM for optimum performance; 5) Demonstrating a 1x2 MMI with EAMs.

7.1 Conclusions of the Dissertation

Traditionally, integration of active devices to a passive photonic circuit on boards is accomplished by assembly methods that include the assembly of discrete components like lenses, amplifiers, attenuators, modulators and lasers. However, in photonic integrated circuits (PIC), all these discrete components can be fabricated onto a single chip thus reducing size and cost.

The theoretical comparative study between directional couplers and MMIs based on strongly guided ridge InGaAsP/InP waveguides had been explored.

Basic MMI structures based on three different materials have been demonstrated. 1xN MMIs based on the InGaAsP/InP structure has shown the efficiency of strongly guided ridge waveguides based on the InP material. A ~0.75cm long MMI based on the BCB material have successfully demonstrated wide range wavelength splitting capability for the range of 1310 and 1550nm. Compact MMI based on the SOI material with access waveguides (AW) the width of 450nm and MMIs as short as 14μm had shown 3dB splitting capabilities for the brand bandwidth of 40nm. A 6μm short Wedge shaped MMI has also demonstrated 80:20 splitting ratios with excess loss as low as 0.6dB.

Among the various developed optical modulators for fiber communication systems, EAM is the smallest and most efficient device. The ease for EAM to integrate with other optical electronic components also makes it more attractive. Therefore, when opting for an active device to be integrated into an MMI as part of the aim of integrating an MMI to active devices, we have settled on a dual depletion region (DDR) large optical cavity (LOC) InGaAlAs/InGaAlAs MQW EAM.

A segment by segment study of a fabricated MMI + EAM device had been examined. The measured 4mm long whole device with a 500μm long active waveguide had an extinction ratio of 10dB at a driving voltage of 4V. The realization of the modulation performance in the device was attributed to a QWI process which helped to reduce absorption loss and material structure which reduced coupling loss. The integrated passive device, 1x2 MMI is capable of splitting an input light in two before the modulation in both/either arms.

Ultimately this dissertation has demonstrated how small ideas can be used to realize new devices for broader applications. The devices reported here are largely made with an initial objective of realizing the photonic integrated circuits (PIC). Most reported PIC works are of DFB lasers with modulators or modulators with extended intermixed waveguides at both ends to expand its size for easier packaging. However, a PIC which involves a large area of intermixed component in relative to a small portion of un-intermixed material had yet been attempted. The feasibility of such large scale intermixing, and the

effect it has upon the un-intermixed portion is not tested upon. The work here has hinted upon the possible damage such larger scale intermixing could impose upon the active devices, and could, eventually pave a better guided path towards achieving better performing integrated circuits.

The major challenge faced in this work is in the realization of the actual photonics integrated device in itself, for though the theoretical concept of the device is sound and relatively straightforward, the device, which is the combination of both active and passive components demanded the understanding and fabrication know how of two rather different components. For example, although the isolation trenches introduced was able to minimize electrical leakage, the depth of the trench was critical to avoid affecting the light propagation along the waveguide core beneath. The p-contact pad metallization process was also a small challenge because although the area of the pad and short waveguide it covered was small, the metallization process required the entire sample surface to be covered, and the lift-off is often not absolutely successfully, thus damaging large arrays of samples. The intermixing process which has been extensively researched upon is focused primarily in achieving optimum bandgap shifts or investigating the QW conditions with less concern over surface conditions which is easily damaged with extensive ion bombardments or annealing conditions. The repeatability of the intermixing achieved is also often subjected to the condition of the fabrication machine used. Finally, the measurement of the actual device is often successful only if the whole device is undamaged and required careful alignments and clean smooth reflective cleaved facets. The tending to these little details which needed both theoretical and technical understanding of optical and material properties, electrical properties, and fabrication and measurement skills which were largely acquired along the course of this work is regarded the major challenge.

7.2 Suggestions for Future Work

Despite the effort that has been put in the thesis, however, there are some works which could be further investigated and improved. The following

lists several areas of future work which are closely related to the aim of this dissertation.

1. Reducing the size of the SOI MMI

For the case of compact MMIs, given more fabrication opportunities, much better size reduction is possible. Studies into MMIs with different splitting ratios would also be of interest in the MMI and ring resonator circuits.

2. Analyzing the microwave properties of lumped-element EAMs

In the EAM designs, although we have demonstrated a low driving voltage EAM which combines the InGaAlAs MQW with DDR and LOC, the electrical bandwidth performance of the EAM can be further improved by reducing the capacitance. This would need additional fabrication steps like under-cut etching which would require more fabrication optimization.

In order to analyze the microwave properties of the EAMs, a proper AC system where a network analyzer and a platform where the electrical and optical ports can be integrated to the analyzer is essential.

3. Bandgap engineering the InGaAlAs MQW

The current InGaAlAs MQW is not designed for optimum performance at the wavelength of 1550nm or polarization independence. With improved strain control of the MQW layers, we would be able to lower the best wavelength working range and face fewer problems in measuring the integrated final product (MMI + EAM) as we have highlighted in Chapter 6.

4. Introducing anti-reflection coating to the EAM devices

The lowest optical insertion loss we currently obtain is ~12.7dB without anti-reflection coating. With this additional coating process in our fabrication, the device will sustain lower coupling or insertion loss. Although the introduction of LOC has greatly improved the coupling issue, more

improvements can be done to reduce the overall loss. This step should not be taken lightly as coupling loss is usually the major concern in measurement.

The concern with anti-reflection coating lies in the fabrication process. The coating has to be applied on both sides of the facets, and this requires a rather complicated jig to get the samples laying upright when it is inserted into the coating chamber. Since our EAM devices can be as small as 150μm, the jigs would have to have slots which are narrow and thin enough to accomplish this. Another major concern would be the damage that the chip would sustain during the loading and unloading from the jig as well as contamination of the top and bottom surface which would affect the contact of probe to the p- and n-electrodes.

5. Improving design and fabrication process of MMI + EAM

An MMI + EAM of a smaller size is achievable if a narrower access waveguide (AW) width was selected (~3μm). A tapered AW before the device can help reduce coupling loss that the narrower waveguides would sustain. With narrower AWs, the MMI length and width can be reduced a few folds. This would result in a much smaller compact device and greatly reduce the propagation loss the device would sustain.

The fabrication process in this dissertation could also be improved. Smoother waveguides with perpendicular side walls could be achieved with better engineering of the ICP and wet-etching process. The QWI process which is optimized for thinner InGaAsP MQW material structure would also need to be optimized for the InGaAlAs MQW with a much larger bulk core below the MQW.

References

Chapter 1

[1] R. Leckie, "Semiconductor Equipment and Materials: Funding the Future," SEMI, 2005.
[2] L. B. Soldano and E. C. M. Pennings, "Optical multi-mode interference devices based on self-imaging: principles and applications," *Lightwave Technology, Journal of*, vol. 13, pp. 615-627, 1995.
[3] S. D. McDougall, B. C. Qiu, G. Ternent, D. A. Yanson, V. Loyo-Maldonado, O. P. Kowalski, and J. H. Marsh, "Monolithic integration of InGaAs/InAlGaAs-based semiconductor optical amplifiers and 10 Gb/s broadband electro-absorption modulators using quantum well intermixing technology," in *Indium Phosphide and Related Materials, 2004. 16th IPRM. 2004 International Conference on*, 2004, pp. 403-406.
[4] H. V. Demir, J. F. Zheng, V. A. Sabnis, O. Fidaner, J. Hanberg, J. S. Harris, and D. A. B. Miller, "Self-aligning planarization and passivation for integration applications in III-V semiconductor devices," *IEEE Transactions on Semiconductor Manufacturing*, vol. 18, pp. 182-189, Feb 2005.
[5] V. A. Sabnis, H. V. Demir, O. Fidaner, J. F. Zheng, J. S. Harris, D. A. B. Miller, N. Li, T. C. Wu, H. T. Chen, and Y. M. Houng, "Intimate monolithic integration of chip-scale photonic circuits," *IEEE Journal of Selected Topics in Quantum Electronics*, vol. 11, pp. 1255-1265, Nov-Dec 2005.
[6] M. Okayasu, M. Okayasu, M. Akashi, and M. Aoki, "A 1550-nm 40-Gbit/s electro-absorption DFB laser diode module for transponders with very short reach (< 2 km) applications," in *Lasers and Electro-Optics Society, 2004. LEOS 2004. The 17th Annual Meeting of the IEEE*, 2004, pp. 513-514 Vol.2.
[7] Y. B. Cheng, J. Q. Pan, S. Liang, W. Feng, Z. Y. Liao, F. Zhou, B. J. Wang, L. J. Zhao, H. L. Zhu, and W. Wang, "Butt-coupled MOVPE growth for high-performance electro-absorption modulator integrated with a DFB laser," *Journal of Crystal Growth*, vol. 308, pp. 297-301, Oct 2007.
[8] G. Roelkens, J. Van Campenhout, J. Brouckaert, D. Van Thourhout, R. Baets, P. R. Romeo, P. Regreny, A. Kazmierczak, C. Seassal, X. Letartre, G. Hollinger, J. M. Fedeli, L. Di Cioccio, and C. Lagahe-Blanchard, "III-V/Si photonics by die to wafer bonding," *Materials Today*, vol. 10, pp. 36-43, Jul-Aug 2007.
[9] J. Brouckaert, G. Roelkens, D. Van Thourhout, and R. Baets, "Thin-film III-V photodetectors integrated on silicon-on-insulator photonic ICs," *Journal of Lightwave Technology*, vol. 25, pp. 1053-1060, Apr 2007.
[10] R. Osgood, "Integrated optics - Slice of perfection," *Nature Photonics*, vol. 1, pp. 365-366, Jul 2007.
[11] H. S. Djie, T. Mei, J. Arokiaraj, C. Sookdhis, S. F. Yu, L. K. Ang, and X. H. Tang, "Experimental and theoretical analysis of argon plasma-enhanced quantum-well intermixing," *IEEE Journal of Quantum Electronics*, vol. 40, pp. 166-174, Feb 2004.
[12] J. H. Marsh, "Laser induced quantum well intermixing for optoelectronic devices," in *Lasers and Electro-Optics Society Annual Meeting, 1996. LEOS 96., IEEE*, 1996, pp. 380-381 vol.2.
[13] T. Mei, H. S. Djie, C. Sookdhis, and J. Arokiaraj, "Low-loss waveguide fabrication using inductively coupled argon plasma enhanced quantum well intermixing in InP quantum well sample," in *Optoelectronic and Microelectronic Materials and Devices, 2002 Conference on*, 2002, pp. 311-314.

[14] H. S. Djie, C. Sookdhis, I. Mei, and J. Arokiaraj, "Photonic integration using inductively coupled argon plasma enhanced quantum well intermixing," *Electronics Letters*, vol. 38, pp. 1672-1673, Dec 2002.
[15] T. Mei, H. S. Djie, J. Aroklaraj, and C. Sookdhis, "Understanding the inductively coupled argon plasma-enhanced quantum well intermixing," *Journal of Crystal Growth*, vol. 268, pp. 384-388, Aug 2004.
[16] J. H. Marsh, "Quantum-Well Intermixing," *Semiconductor Science and Technology*, vol. 8, pp. 1136-1155, Jun 1993.
[17] A. McKee, C. J. McLean, G. Lullo, A. C. Bryce, R. M. De La Rue, J. H. Marsh, and C. C. Button, "Monolithic integration in InGaAs-InGaAsP multiple-quantum-well structures using laser intermixing," *Quantum Electronics, IEEE Journal of*, vol. 33, pp. 45-55, 1997.
[18] S. E. Miller, "Integrated optics: An introduction," *Bell System Technical Journal*, vol. 48, pp. 2059-69, 1969.
[19] J. W. Raring, L. A. Johansson, E. J. Skogen, M. N. Sysak, H. N. Poulsen, S. P. DenBaars, and L. A. Coldren, "40-Gb/s widely tunable low-drive-voltage electroabsorption-modulated transmitters," *Journal of Lightwave Technology*, vol. 25, pp. 239-248, Jan 2007.
[20] S. Charbonneau, E. S. Koteles, P. J. Poole, J. J. He, G. C. Aers, J. Haysom, M. Buchanan, Y. Feng, A. Delage, F. Yang, M. Davies, R. D. Goldberg, P. G. Piva, and I. V. Mitchell, "Photonic integrated circuits fabricated using ion implantation," *IEEE Journal of Selected Topics in Quantum Electronics*, vol. 4, pp. 772-793, Jul-Aug 1998.
[21] J. P. Reithmaier and A. Forchel, "Focused ion-beam implantation induced thermal quantum-well intermixing for monolithic optoelectronic device integration," *IEEE Journal of Selected Topics in Quantum Electronics*, vol. 4, pp. 595-605, Jul-Aug 1998.
[22] B. C. Qiu, G. Ternent, V. L. Maldonado, S. D. McDougall, and J. H. Marsh, "Component design and fabrication of a monolithically integrated polarisation insensitive 2/spl times/2 optical packet switch in InP," in *Lasers and Electro-Optics Society, 2002. LEOS 2002. The 15th Annual Meeting of the IEEE*, 2002, pp. 41-42 vol.1.
[23] C. D. Xu, T. Mei, M. K. Chin, J. R. Dong, and S. J. Chua, "Built-in electric field enhancement/retardation on intermixing," *Applied Physics Letters*, vol. 91, Oct 2007.
[24] D. Hofstetter, B. Maisenholder, and H. P. Zappe, "Quantum-well intermixing for fabrication of lasers and photonic integrated circuits," *IEEE Journal of Selected Topics in Quantum Electronics*, vol. 4, pp. 794-802, Jul-Aug 1998.
[25] O. Boon Siew, K. McIlvaney, M. W. Street, A. S. Helmy, S. G. Ayling, A. C. Bryce, J. H. Marsh, and J. S. Roberts, "Selective quantum-well intermixing in GaAs-AlGaAs structures using impurity-free vacancy diffusion," *IEEE Journal of Quantum Electronics*, vol. 33, pp. 1784-93, 1997.
[26] H.-S. Kim, J. W. Park, D. K. Oh, K. R. Oh, S. J. Kim, and I.-H. Choi, "Quantum well intermixing of In1-xGaxAs/InP and In1-xGaxAs/In1-xGaxA s1-yPy multiple-quantum-well structures by using the impurity-free vacancy diffusion technique," *Semiconductor Science and Technology*, vol. 15, pp. 1005-1009, 2000.
[27] L. Fu, P. Lever, H. H. Tan, C. Jagadish, P. Reece, and M. Gal, "Suppression of interdiffusion in InGaAs/GaAs quantum dots using dielectric layer of titanium dioxide," *Applied Physics Letters*, vol. 82, pp. 2613-15, 2003.
[28] E. R. H. Fuchs, E. J. Bruce, R. J. Ram, and R. E. Kirchain, "Process-based cost modeling of photonics manufacture: the cost competitiveness of monolithic integration of a 1550-nm DFB laser and an electroabsorptive modulator on an InP platform," *Lightwave Technology, Journal of*, vol. 24, pp. 3175-3186, 2006.
[29] Q. Zhao, J. Q. Pan, J. Zhang, B. X. Li, F. Zhou, B. J. Wang, L. F. Wang, J. Bian, L. J. Zhao, and W. Wang, "Monolithic integration of electroabsorption modulator

and DFB laser for 10-Gb/s transmission," *Optics Communications*, vol. 260, pp. 666-669, Apr 15 2006.
[30] V. M. Menon, V. M. Menon, X. Fengnian, and S. R. Forrest, "Photonic integration using asymmetric twin-waveguide (ATG) technology: part II-devices
Photonic integration using asymmetric twin-waveguide (ATG) technology: part II-devices," *Selected Topics in Quantum Electronics, IEEE Journal of*, vol. 11, pp. 30-42, 2005.
[31] T. Ido, H. Sano, S. Tanaka, D. J. Moss, and H. Inoue, "Performance of strained InGaAs/InAlAs multiple-quantum-well electroabsorption modulators," *Journal of Lightwave Technology*, vol. 14, pp. 2324-2331, Oct 1996.
[32] N. C. Frateschi, J. Zhang, R. Jambunathan, W. J. Choi, C. Ebert, and A. E. Bond, "Uncooled performance of 10-Gb/s laser modules with InGaAlAs-InP and InGaAsP-InP MQW electroabsorption Modulators integrated with semiconductor amplifiers," *Photonics Technology Letters, IEEE*, vol. 17, pp. 1378-1380, 2005.
[33] G. lengyel, K. W. Jelley, and R. W. H. Engelmann, "A semi-empirical model for electroabsorption in GaAs/AlGaAs multiple quantum well modulator structures," *Quantum Electronics, IEEE Journal of*, vol. 26, pp. 296-304, 1990.
[34] H.-S. Cho and P. R. Prucnal, "Effect of parameter variations on the performance of GaAs/AlGaAs multiple-quantum-well electroabsorption modulators," *Quantum Electronics, IEEE Journal of*, vol. 25, pp. 1682-1690, 1989.
[35] T. Yamanaka, K. Tsuzuki, N. Kikuchi, E. Yamada, Y. Shibata, H. Fukano, H. Nakajima, Y. Akage, and H. Yasaka, "High-performance InP-based optical modulators," in *Optical Fiber Communication Conference, 2006 and the 2006 National Fiber Optic Engineers Conference*, 2006, p. 3 pp.
[36] H. Fukano, H. Fukano, T. Yamanaka, M. Tamura, and Y. A. K. Y. Kondo, "Very-low-driving-voltage electroabsorption modulators operating at 40 Gb/s," *Lightwave Technology, Journal of*, vol. 24, pp. 2219-2224, 2006.
[37] M. Tamura, T. Yamanaka, H. Fukano, Y. Akage, Y. Kondo, and T. Saitoh, "High-speed electroabsorption modulators buried with ruthenium-doped SI-InP," *Photonics Technology Letters, IEEE*, vol. 16, pp. 2613-2615, 2004.
[38] A. M. Sonnet, M. A. Khayer, and A. Haque, "Analysis of compressively strained GaInAsP-InP quantum-wire electro-absorption modulators," *IEEE Journal of Quantum Electronics*, vol. 43, pp. 1198-1203, Nov-Dec 2007.
[39] B. Liu, J. Shim, Y.-J. Chiu, A. Keating, J. Piprek, and J. E. Bowers, "Analog characterization of low-voltage MQW traveling-wave electroabsorption modulators," *Lightwave Technology, Journal of*, vol. 21, pp. 3011-3019, 2003.
[40] B. K. Saravanan, T. Wenger, C. Hanke, P. Gerlach, M. Peschke, and R. Macaluso, "Wide temperature operation of 40-Gb/s 1550-nm electroabsorption modulated lasers," *IEEE Photonics Technology Letters*, vol. 18, pp. 862-864, Mar-Apr 2006.
[41] W. J. Choi, A. E. Bond, J. Kim, R. M. Zhang, R. Jambunathan, H. Foulk, S. O'Brien, J. Van Norman, D. Vandegrift, C. Wanamaker, J. Shakespeare, and H. Cao, "Low insertion loss and low dispersion penalty InGaAsP quantum-well high-speed electroabsorption modulator for 40-Gb/s very-short-reach, long-reach, and long-haul applications," *Journal of Lightwave Technology*, vol. 20, pp. 2052-2056, Dec 2002.
[42] B. Mason, A. Ougazzaden, C. W. Lentz, K. G. Glogovsky, C. L. Reynolds, G. J. Przybylek, R. E. Leibenguth, T. L. Kercher, J. W. Boardman, M. T. Rader, J. M. Geary, F. S. Walters, L. J. Peticolas, J. M. Freund, S. N. G. Chu, A. Sirenko, R. J. Jurchenko, M. S. Hybertsen, L. J. P. Ketelsen, and G. Raybon, "40-Gb/s tandem electroabsorption modulator," *IEEE Photonics Technology Letters*, vol. 14, pp. 27-29, Jan 2002.
[43] Y.-J. Chiu, T.-H. Wu, W.-C. Cheng, F. J. Lin, and J. E. Bowers, "Enhanced performance in traveling-wave electroabsorption Modulators based on undercut-etching the active-region," *Photonics Technology Letters, IEEE*, vol. 17, pp. 2065-2067, 2005.

[44] A. Ferreras, F. Rodriguez, E. Gomez-Salas, J. L. de Miguel, and F. Hernandez-Gil, "Useful formulas for multimode interference power splitter/combiner design," *Photonics Technology Letters, IEEE,* vol. 5, pp. 1224-1227, 1993.
[45] B. M. A. Rahman, M. Rajarajan, T. Wongcharoen, and K. T. V. Grattan, "Accurate analysis of multimode interference devices," *Photonics Technology Letters, IEEE,* vol. 8, pp. 809-811, 1996.
[46] M. Bachmann, P. A. Besse, and H. Melchior, "Overlapping-Image Multimode Interference Couplers with a Reduced Number of Self-Images for Uniform and Nonuniform Power Splitting," *Applied Optics,* vol. 34, pp. 6898-6910, Oct 20 1995.
[47] P. A. Besse, M. Bachmann, H. Melchior, L. B. Soldano, and M. K. Smit, "Optical Bandwidth and Fabrication Tolerances of Multimode Interference Couplers," *Journal of Lightwave Technology,* vol. 12, pp. 1004-1009, Jun 1994.
[48] L. H. Spiekman, Y. S. Oei, E. G. Metaal, F. H. Green, I. Moerman, and M. K. Smit, "Extremely small multimode interference couplers and ultrashort bends on InP by deep etching," *Photonics Technology Letters, IEEE,* vol. 6, pp. 1008-1010, 1994.
[49] P. A. Besse, E. Gini, M. Bachmann, and H. Melchior, "New 2X2 and 1X3 multimode interference couplers with free selection of power splitting ratios," *Lightwave Technology, Journal of,* vol. 14, pp. 2286-2293, 1996.
[50] D. S. Levy, P. Kyung Hyun, R. Scarmozzino, R. M. Osgood, Jr., C. Dries, P. Studenkov, and S. Forrest, "Fabrication of ultracompact 3-dB 2×2 MMI power splitters," *Photonics Technology Letters, IEEE,* vol. 11, pp. 1009-1011, 1999.
[51] Y. Ma, S. Park, L. W. Wang, and S. T. Ho, "Ultracompact multimode interference 3-dB coupler with strong lateral confinement by deep dry etching," *IEEE Photonics Technology Letters,* vol. 12, pp. 492-494, MAY 2000.
[52] D. G. Rabus and M. Hamacher, "MMI-coupled ring resonators in GaInAsP-InP," *IEEE Photonics Technology Letters,* vol. 13, pp. 812-814, Aug 2001.
[53] J. Leuthold and C. H. Joyner, "Multimode interference couplers with tunable power splitting ratios," *Journal of Lightwave Technology,* vol. 19, pp. 700-707, MAY 2001.
[54] K. S. Hyun, "Four channel Mach-Zehnder demultiplexer using multimode interferometers in InP/InGaAsP," *Optical and Quantum Electronics,* vol. 35, pp. 791-799, Jun 2003.
[55] Q. Lai, M. Bachmann, W. Hunziker, P. A. Besse, and H. Melchior, "Arbitrary ratio power splitters using angled silica on silicon multimode interference couplers," *Electronics Letters,* vol. 32, pp. 1576-1577, 1996.
[56] J. Yu, X. Wang, J. Liu, Q. Yan, J. Xia, Z. Fan, Z. Wang, and S. Chen, "MMI optical couplers and switches with SOI technology," in *Proceedings of the Sixth Chinese Optoelectronics Symposium, 12-14 Sept. 2003,* Hong Kong, China, 2003, pp. 251-4.
[57] D. X. Xu, A. Densmore, P. Waldron, J. Lapointe, E. Post, A. Delage, S. Janz, P. Cheben, J. H. Schmid, and B. Lamontagne, "High bandwidth SOI photonic wire ring resonators using MMI couplers," *Optics Express,* vol. 15, pp. 3149-3155, Mar 2007.
[58] X. Q. Jiang, X. Li, H. F. Zhou, J. Y. Yang, M. H. Wang, Y. Y. Wu, and S. Ishikawa, "Compact variable optical attenuator based on multimode interference coupler," *IEEE Photonics Technology Letters,* vol. 17, pp. 2361-2363, Nov 2005.
[59] L. Zhu, Y. Y. Huang, and A. Yariv, "Integration of a multimode interference coupler with a corrugated sidewall Bragg grating in planar polymer waveguides," *IEEE Photonics Technology Letters,* vol. 18, pp. 740-742, Mar-Apr 2006.
[60] C. H. Choi, M. W. Lee, J. H. Sung, B. S. Kim, and B. H. O, "Fabrication of MMI optical power splitter by UV embossing with PDMS mold," *Microelectronic Engineering,* vol. 84, pp. 1231-1234, May-Aug 2007.
[61] S.-W. Seo, S.-Y. Cho, and N. M. Jokerst, "Integrated thin film InGaAsP laser and 1×4 polymer multimode interference splitter on silicon," *Opt. Lett.,* vol. 32, pp. 548-550, 2007.

[62] C. Themistos and B. M. A. Rahman, "Design issues of a multimode interference-based 3-dB splitter," *Applied Optics*, vol. 41, pp. 7037-7044, Nov 20 2002.
[63] J. Leuthold, J. Eckner, E. Gamper, P. A. Besse, and H. Melchior, "Multimode interference couplers for the conversion and combining of zero- and first-order modes," *Lightwave Technology, Journal of*, vol. 16, pp. 1228-1239, 1998.
[64] L. O. Lierstuen and A. Sudbo, "8-channel wavelength division multiplexer based on multimode interference couplers," *Photonics Technology Letters, IEEE*, vol. 7, pp. 1034-1036, 1995.
[65] C. P. Larsen, S. Larsson, E. Almstrom, H. Carlden, B. Stoltz, O. Oberg, and J.-E. Falk, "Experimental evaluation of novel, tunable MMI-MZI demultiplexer in InP," in *Optical Communication, 1998. 24th European Conference on*, 1998, pp. 121-122 vol.1.
[66] M. P. Earnshaw, J. B. D. Soole, M. Cappuzzo, L. Gomez, E. Laskowski, and A. Paunescu, "8/spl times/8 optical switch matrix using generalized Mach-Zehnder interferometers," *Photonics Technology Letters, IEEE*, vol. 15, pp. 810-812, 2003.
[67] M. R. Paiam and R. I. MacDonald, "Design of phased-array wavelength division multiplexers using multimode interference couplers," *Applied Optics*, vol. 36, pp. 5097-5108, July 1997 1997.
[68] M. R. Paiam and R. I. MacDonald, "A 12-channel phased-array wavelength multiplexer with multimode interference couplers," *Photonics Technology Letters, IEEE*, vol. 10, pp. 241-243, 1998.
[69] B. J. Li, S. J. Chua, C. W. Leitz, and E. A. Fitzgerald, "1x2 optical waveguide filters based on multimode interference for 1.3-and 1.55-mu m operation," *Optical Engineering*, vol. 41, pp. 723-727, Mar 2002.
[70] K. C. Lin and W. Y. Lee, "Guided-wave 1.3/1.55 mu m wavelength division multiplexer based on multimode interference," *Electronics Letters*, vol. 32, pp. 1259-1261, Jul 4 1996.
[71] M. R. Paiam, C. F. Janz, R. I. Macdonald, and J. N. Broughton, "Compact Planar 980/1550-Nm Wavelength Multi/Demultiplexer Based on Multimode Interference," *IEEE Photonics Technology Letters*, vol. 7, pp. 1180-1182, Oct 1995.
[72] H. H. El-Refaei and D. A. M. Khalil, "Design of strip-loaded weak-guiding multimode interference structure for an optical router," *IEEE Journal of Quantum Electronics*, vol. 34, pp. 2286-2290, Dec 1998.
[73] D. M. Mackie, T. J. Tayag, and T. E. Batchman, "Polarization separation/combination based on self-imaging," *Optical Engineering*, vol. 40, pp. 2265-2272, Oct 2001.
[74] J. M. Hong, H. H. Ryu, S. R. Park, J. W. Jeong, S. G. Lee, E. H. Lee, S. G. Park, D. Woo, S. Kim, and B. H. O, "Design and fabrication of a significantly shortened multimode interference coupler for polarization splitter application," *IEEE Photonics Technology Letters*, vol. 15, pp. 72-74, Jan 2003.
[75] D. A. M. Khalil, "Advances in optical filters," in *Second Workshop on Teaching Photonics at Egyptian Engineering Faculties and Institutes, 24 Oct. 2000*, Giza, Egypt, 2000, pp. 1-27 BN - 0 7803 6256 X.
[76] Y. P. Li and C. H. Henry, "Silica-based optical integrated circuits," *IEE Proceedings-Optoelectronics*, vol. 143, pp. 263-80, 1996/10/ 1996.
[77] G. Lenz, B. J. Eggleton, C. K. Madsen, and R. E. Slusher, "Optical delay lines based on optical filters," *IEEE Journal of Quantum Electronics*, vol. 37, pp. 525-532, 2001.
[78] B. Broberg, B. S. Lindgren, M. G. Oberg, and H. Jiang, "A Novel Integrated-Optics Wavelength Filter in Ingaasp-Inp," *Journal of Lightwave Technology*, vol. 4, pp. 196-203, Feb 1986.
[79] R. C. Alferness, "Guided-Wave Devices for Optical Communication," *IEEE Journal of Quantum Electronics*, vol. 17, pp. 946-959, 1981.

[80] M. R. T. Pearson, P. E. Jessop, D. M. Bruce, S. Wallace, P. Mascher, and J. Ojha, "Fabrication of SiGe optical waveguides using VLSI processing techniques," *Lightwave Technology, Journal of*, vol. 19, pp. 363-370, 2001.
[81] C. Wu, C. Rolland, F. Shepherd, C. Larocque, N. Puetz, K. D. Chik, and J. M. Xu, "Ingaasp/Inp Vertical Directional Coupler Filter with Optimally Designed Wavelength Tunability," *IEEE Photonics Technology Letters*, vol. 5, pp. 457-459, Apr 1993.
[82] J.-P. Weber, B. Stoltz, M. Dasler, and B. Koek, "Four-channel tunable optical notch filter using InGaAsP/InP reflection gratings," *IEEE Photonics Technology Letters*, vol. 6, pp. 77-9, 1994/01/ 1994.
[83] T. Hattori, T. Shibata, S. Onodera, and T. Kaino, "Thermo-optically tunable wavelength filter with permanent refractive index grating into azo-polymer waveguide," *Japanese Journal of Applied Physics, Part 1: Regular Papers and Short Notes and Review Papers*, vol. 43, pp. 1492-1495, 2004.
[84] Y. Sasaki, "Recent progress in research on optical fiber grating couplers," in *2003 International Conference on Transparent Optical Networks - ICTON 2003, 29 June-3 July 2003*, Warsaw, Poland, 2003, pp. 70-3 BN - 0 7803 7816 4.
[85] S. T. Chu, W. Pan, S. Sato, B. E. Little, T. Kaneko, and Y. Kokubun, "ARROW-Type vertical coupler filter: Design and fabrication," *Journal of Lightwave Technology*, vol. 17, pp. 652-658, Apr 1999.
[86] S. Safavi-Naeini, S. K. Chaudhuri, and A. Goss, "Design and analysis of novel multimode optical filters in dielectric waveguide," *Lightwave Technology, Journal of*, vol. 11, pp. 1970-1977, 1993.
[87] J. K. S. Poon, J. Schetter, and A. Yariv, "Wavelength-selective reflector based on a circular array of coupled microring resonators," *IEEE Photonics Technology Letters*, vol. 16, pp. 1331-1333, May 2004.
[88] O. Schwelb, "Transmission, group delay, and dispersion in single-ring optical resonators and add/drop filters - A tutorial overview," *Journal of Lightwave Technology*, vol. 22, pp. 1380-1394, May 2004.
[89] Y. Hibino, "High contrast waveguide devices," in *OFC 2001. Optical Fiber Communication Conference and Exhibition. Technical Digest, 17-22 March 2001*, Anaheim, CA, USA, 2001, pp. 1-1 BN - 1 55752 655 9.
[90] Y. Hibino, "Recent advances in high-density and large-scale AWG multi/demultiplexers with higher index-contrast silica-based PLCs," *IEEE Journal of Selected Topics in Quantum Electronics*, vol. 8, pp. 1090-101, 2002/11/ 2002.
[91] S. Kamei, M. Ishii, I. Kitagawa, M. Itoh, and Y. Hibino, "64-channel ultra-low crosstalk arrayed-waveguide grating multi/demultiplexer module using cascade connection technique," *Electronics Letters*, vol. 39, pp. 81-2, 2003/01/09 2003.
[92] N. Keil, H. H. Yao, C. Zawadzki, J. Bauer, M. Bauer, C. Dreyer, and J. Schneider, "Athermal all-polymer arrayed-waveguide grating multiplexer," *Electronics Letters*, vol. 37, pp. 579-580, 2001.
[93] K. Okamoto, "Bringing telecom networks up to speed," *IEEE Circuits and Devices Magazine*, vol. 14, pp. 26-34, 1998.
[94] H. J. R. Dutton, *Understanding Optical Communications*: Prentice Hall PTR, 1998.
[95] W. H. Wang, Y. Z. Tang, Y. X. Wang, H. C. Qu, Y. M. Wu, T. Li, J. Y. Yang, Y. L. Wang, and M. Liu, "Etched-diffraction-grating-based planar waveguide demultiplexer on silicon-on-insulator," *Optical and Quantum Electronics*, vol. 36, pp. 559-566, May 2004.
[96] S. Janz, M. Pearson, B. Lamontagne, L. Erickson, A. Delage, P. Cheben, D.-X. Xu, M. Gao, A. Balakrishnan, J. Miller, and S. Charbonneau, "Planar waveguide echelle gratings: An embeddable diffractive element for photonic integrated circuits," in *Optical Fiber Communication Conference and Exhibit, Mar 17-22 2002*, Anaheim, CA, United States, 2002, pp. 69-70.

[97] S. Janz, A. Balakrishnan, S. Charbonneau, P. Cheben, M. Cloutier, A. Delage, K. Dossou, L. Erickson, M. Gao, P. A. Krug, B. Lamontagne, M. Packirisamy, M. Pearson, and D. X. Xu, "Planar waveguide echelle gratings in silica-on-silicon," *IEEE Photonics Technology Letters*, vol. 16, pp. 503-505, Feb 2004.

[98] M. Fallahi, K. A. McGreer, A. Delage, R. Normandin, I. M. Templeton, R. Barber, F. Chatenoud, and G. Champion, "Demonstration of grating demultiplexer in GaAs/AlGaAs suitable for integration," *Electronics Letters*, vol. 28, pp. 2217-18, 1992/11/19 1992.

[99] J.-J. He, B. Lamontagne, A. Delage, L. Erickson, M. Davies, and E. S. Koteles, "Monolithic integrated wavelength demultiplexer based on a waveguide Rowland circle grating in InGaAsP/lnP," *Journal of Lightwave Technology*, vol. 16, pp. 631-8, 1998/04/ 1998.

[100] L. Erickson, B. Lamontagne, J. J. He, A. Delage, M. Davies, and E. Koteles, "Using a retro-reflecting echelle grating to improve WDM demux efficiency," in *Proceedings of the 1997 LEOS Summer Topical Meeting, Aug 11-15 1997*, Montreal, Can, 1997, pp. 82-83.

[101] J.-J. He, "Phase-dithered waveguide grating with flat passband and sharp transitions," *IEEE Journal of Selected Topics in Quantum Electronics*, vol. 8, pp. 1186-93, 2002/11/ 2002.

[102] V. I. Tolstikhin, A. Densmore, K. Pimenov, Y. Logvin, F. Wu, S. Laframboise, and S. Grabtchak, "Monolithically Integrated Optical Channel Monitor for DWDM Transmission Systems," *Optical Fiber Communications Conference*
Journal of Lightwave Technology, vol. 22, pp. 146-153, 2004.

[103] H. Wei, J. Yu, Z. Liu, X. Zhang, W. Shi, and C. Fang, "Signal bandwidth of general nXn multimode interference couplers," *Lightwave Technology, Journal of*, vol. 19, pp. 739-745, 2001.

[104] D. S. Levy, R. Scarmozzino, Y. M. Li, and R. M. Osgood, Jr., "A new design for ultracompact multimode interference-based 2X2 couplers," *Photonics Technology Letters, IEEE*, vol. 10, pp. 96-98, 1998.

[105] D. S. Levy, K. H. Park, R. Scarmozzino, R. M. Osgood, Jr., C. Dries, P. Studenkov, and S. Forrest, "Fabrication of ultracompact 3-dB 2X2 MMI power splitters," *Photonics Technology Letters, IEEE*, vol. 11, pp. 1009-1011, 1999.

[106] C. W. Hsu, H. L. Chen, and W. S. Wang, "Multimode interference couplers using polymeric optical waveguides," in *Optical Fiber and Planar Waveguide Technology, 13-15 Nov. 2001*
Proceedings of the SPIE - The International Society for Optical Engineering, Beijing, China, 2001, pp. 84-91.

[107] M. A. Fardad and M. Fallahi, "Sol-gel multimode interference power splitters," *IEEE Photonics Technology Letters*, vol. 11, pp. 697-699, Jun 1999.

[108] E. C. M. Pennings, R. van Roijen, M. J. N. van Stralen, B. H. Verbeek, J. M. M. van der Heijden, and T. van Dongen, "Spectral behavior of InP-based ring lasers employing multimode interference devices," in *Lasers and Electro-Optics Society Annual Meeting, 1993. LEOS '93 Conference Proceedings. IEEE*, 1993, pp. 617-618.

[109] L. B. Soldano, A. H. Devreede, M. K. Smit, B. H. Verbeek, E. G. Metaal, and F. H. Groen, "Mach-Zehnder Interferometer Polarization Splitter in Ingaasp/Inp," *IEEE Photonics Technology Letters*, vol. 6, pp. 402-405, MAR 1994.

[110] L. Schares, R. Paschotta, L. Occhi, and G. Guekos, "40-GHz mode-locked fiber-ring laser using a Mach-Zehnder interferometer with integrated SOAs," *Journal of Lightwave Technology*, vol. 22, pp. 859-873, Mar 2004.

[111] V. M. Menon, W. Tong, and S. R. Forrest, "Control of quality factor and critical coupling in microring resonators through integration of a semiconductor optical amplifier," *IEEE Photonics Technology Letters*, vol. 16, pp. 1343-1345, May 2004.

[112] H. Oohashi, Y. Shibata, H. Ishii, Y. Kawaguchi, Y. Kondo, Y. Yoshikuni, and Y. Tohmori, "46.7-nm Wavelength-Selectable Arrayed DFB Lasers with Integrated

MMI Coupler and SOA," in *13th International Conference on InP and Related Materials (13th IPRM)*, 2001, pp. 575-578.
[113] S. Y. Lee, S. Darmawan, C. W. Lee, and M. K. Chin, "Transformation between directional couplers and multi-mode interferometers based on ridge waveguides," *Optics Express*, vol. 12, pp. 3079-3085, Jul 12 2004.
[114] J. M. Heaton, R. M. Jenkins, D. R. Wight, J. T. Parker, J. C. H. Birbeck, and K. P. Hilton, "Novel 1-to-N way integrated optical beam splitters using symmetric mode mixing in GaAs/AlGaAs multimode waveguides," *Applied Physics Letter*, vol. 61, pp. 1754-1756, 12 October 1992.
[115] M. H. Ibrahim, S. Y. Lee, M. K. Chin, N. M. Kassim, and A. B. Mohammad, "Multimode interference wavelength multi/demultiplexer for 1310 and 1550 nm operation based on BCB 4024-40 photodefinable polymer," *Optics Communications*, vol. 273, pp. 383-388, May 2007.

Chapter 2

[1] O. Bryngdahl, "Image formation using self-imaging techniques," *Journal of the Optical Society of America*, vol. 63, pp. 416-19, 1973.
[2] H. F. Talbot, "Facts relating to optical science No. IV," *Philosophical Magazine*, vol. 9, pp. 401 - 407 1836.
[3] L. B. Soldano and E. C. M. Pennings, "Optical multi-mode interference devices based on self-imaging: principles and applications," *Lightwave Technology, Journal of*, vol. 13, pp. 615-627, 1995.
[4] M. Bachmann, P. A. Besse, and H. Melchior, "General Self-Imaging Properties in N X N Multimode Interference Couples Including Phase-Relations," *Applied Optics*, vol. 33, pp. 3905-3911, Jun 20 1994.
[5] R. Ulrich, "Image formation by phase coincidences in optical waveguides," *Optics Communications*, vol. 13, pp. 259-64, 1975.
[6] R. Ulrich and T. Kamiya, "Resolution of self-images in planar optical waveguides," *Journal of the Optical Society of America*, vol. 68, pp. 583-92, 1978.
[7] H. H. ElRiffaey and D. A. M. Khalil, "Rigorous modal analysis of multi-mode interference (MMI) structures by radiation spectrum method with multiple reflection," *Optics Communications*, vol. 144, pp. 306-314, Dec 15 1997.
[8] C. Themistos and B. M. A. Rahman, "Design issues of a multimode interference-based 3-dB splitter," *Applied Optics*, vol. 41, pp. 7037-7044, Nov 20 2002.
[9] M. Bachmann, P. A. Besse, and H. Melchior, "Overlapping-Image Multimode Interference Couplers with a Reduced Number of Self-Images for Uniform and Nonuniform Power Splitting," *Applied Optics*, vol. 34, pp. 6898-6910, Oct 20 1995.
[10] L. B. Soldano, F. B. Veerman, M. K. Smit, B. H. Verbeek, A. H. Dubost, and E. C. M. Pennings, "Planar Monomode Optical Couplers Based on Multimode Interference Effects," *Journal of Lightwave Technology*, vol. 10, pp. 1843-1850, DEC 1992.
[11] S. Adachi, "Material parameters of $In_{1-x}Ga_xAs_yP_{1-y}$ and related binaries," *Journal of Applied Physics*, vol. 53, pp. 8775-92, 1982/12/ 1982.
[12] R. J. Deri and E. Kapon, "Low-loss III-V semiconductor optical waveguides," *Quantum Electronics, IEEE Journal of*, vol. 27, pp. 626-640, 1991.l
[13] N. Yoshimoto, Y. Shibata, S. Oku, S. Kondo, and Y. Noguchi, "Design and demonstration of polarization-insensitive Mach-Zehnder switch using a lattice-matched InGaAlAs/InAlAs MQW and deep-etched high-mesa waveguide structure," *Lightwave Technology, Journal of*, vol. 17, pp. 1662-1668, 1999.
[14] J. M. Heaton, M. M. Bourke, S. B. Jones, B. H. Smith, K. P. Hilton, G. W. Smith, J. C. H. Birbeck, G. Berry, S. V. Dewar, and D. R. Wight, "Optimization of

deep-etched, single-mode GaAs-AlGaAs optical waveguides using controlled leakage into the substrate," *Lightwave Technology, Journal of*, vol. 17, pp. 267-281, 1999.
[15] S. Darmawan, S. Y. Lee, C. W. Lee, and M. K. Chin, "Transformation of directional couplers to multi-mode interferometers based on ridge waveguides and its applications," *Journal of Nonlinear Optical Physics & Materials*, vol. 14, pp. 221-235, JUN 2005.
[16] S. Y. Lee, S. Darmawan, C. W. Lee, and M. K. Chin, "Transformation between directional couplers and multi-mode interferometers based on ridge waveguides," *Optics Express*, vol. 12, pp. 3079-3085, Jul 12 2004.
[17] B. Broberg and S. Lindgren, "Refractive-Index of $In_{1-X}Ga_xAs_yP_{1-y}$ Layers and InP in the Transparent Wavelength Region," *Journal of Applied Physics*, vol. 55, pp. 3376-3381, 1984.
[18] P. Martin, E. M. Skouri, L. Chusseau, C. Alibert, and H. Bissessur, "Accurate Refractive-Index Measurements of Doped and Undoped Inp by a Grating Coupling Technique," *Applied Physics Letters*, vol. 67, pp. 881-883, Aug 14 1995.

Chapter 3

[1] E. C. M. Pennings, R. van Roijen, M. J. N. van Stralen, B. H. Verbeek, J. M. M. van der Heijden, and T. van Dongen, "Spectral behavior of InP-based ring lasers employing multimode interference devices," presented at Lasers and Electro-Optics Society Annual Meeting, 1993. LEOS '93 Conference Proceedings. IEEE, 1993.
[2] L. B. Soldano and E. C. M. Pennings, "Optical multi-mode interference devices based on self-imaging: principles and applications," *Lightwave Technology, Journal of*, vol. 13, pp. 615-627, 1995.
[3] M. Bachmann, P. A. Besse, and H. Melchior, "Overlapping-Image Multimode Interference Couplers with a Reduced Number of Self-Images for Uniform and Nonuniform Power Splitting," *Applied Optics*, vol. 34, pp. 6898-6910, 1995.
[4] L. B. Soldano, F. B. Veerman, M. K. Smit, B. H. Verbeek, A. H. Dubost, and E. C. M. Pennings, "Planar Monomode Optical Couplers Based on Multimode Interference Effects," *Journal of Lightwave Technology*, vol. 10, pp. 1843-1850, 1992.
[5] J. M. Heaton and R. M. Jenkins, "General matrix theory of self-imaging in multimode interference (MMI) couplers," *IEEE Photonics Technology Letters*, vol. 11, pp. 212-214, 1999.
[6] C. Vazquez, C. Aramburu, M. Galarza, and M. Lopez-Amo, "Experimental assessment of access guide first-order mode effect on multimode interference couplers," *Optical Engineering*, vol. 40, pp. 1160-1162, 2001.
[7] C. W. Lee and M. K. Chin, "Room-Temperature Inductively Coupled Plasma Etching of InP Using Cl2/N2 and Cl2/Ch4/H2," *Chin. Phys. Lett.*, vol. 23, pp. 903-906, 2006.
[8] H. Wei, J. Yu, Z. Liu, X. Zhang, W. Shi, and C. Fang, "Signal bandwidth of general n×n multimode interference couplers," *Lightwave Technology, Journal of*, vol. 19, pp. 739-745, 2001.
[9] S.-H. Fan, D. Guidotti, H.-C. Chien, and G.-K. Chang, "Compact polymeric four-wavelength multiplexers based on cascaded step-size MMI for 1G/10G hybrid TDM-PON applications," *Opt. Express*, vol. 16, pp. 12664-12669, 2008.
[10] M. A. Fardad and M. Fallahi, "Sol-gel multimode interference power splitters," *IEEE Photonics Technology Letters*, vol. 11, pp. 697-699, 1999.
[11] M. Kohtoku, T. Hirono, S. Oku, Y. Kadota, Y. Shibata, and Y. Yoshikuni, "Control of higher order leaky modes in deep-ridge waveguides and application to low-crosstalk arrayed waveguide gratings," *Lightwave Technology, Journal of*, vol. 22, pp. 499-508, 2004.

Chapter 4

[1] D. M. Mackie, T. J. Tayag, and T. E. Batchman, "Polarization separation/combination based on self-imaging," Optical Engineering, vol. 40, pp. 2265-2272, 2001.
[2] B. J. Li, S. J. Chua, C. W. Leitz, and E. A. Fitzgerald, "1x2 optical waveguide filters based on multimode interference for 1.3-and 1.55-mu m operation," Optical Engineering, vol. 41, pp. 723-727, 2002.
[3] K. C. Lin and W. Y. Lee, "Guided-wave 1.3/1.55 mu m wavelength division multiplexer based on multimode interference," Electronics Letters, vol. 32, pp. 1259-1261, 1996.
[4] M. R. Paiam, C. F. Janz, R. I. Macdonald, and J. N. Broughton, "Compact Planar 980/1550-Nm Wavelength Multi/Demultiplexer Based on Multimode Interference," IEEE Photonics Technology Letters, vol. 7, pp. 1180-1182, 1995.
[5] M. H. Ibrahim, S. Y. Lee, M. K. Chin, N. M. Kassim, and A. B. Mohammad, "Multimode interference wavelength multi/demultiplexer for 1310 and 1550 nm operation based on BCB 4024-40 photodefinable polymer," Optics Communications, vol. 273, pp. 383-388, 2007.
[6] L. Eldada and L. W. Shacklette, "Advances in polymer integrated optics," Selected Topics in Quantum Electronics, IEEE Journal of, vol. 6, pp. 54-68, 2000.
[7] T. D. C. Company, "Product Literature: CycloteneTM Advanced Electronic Resins," May 1999.
[8] W. C. Chuang, C. Y. Chang, C. C. Lai, and K. C. Lin, "Integrated-optics multimode-interference wavelength division multiplexer for optical communication," Fiber and Integrated Optics, vol. 18, pp. 93-104, 1999.
[9] D. X. Xu, A. Densmore, P. Waldron, J. Lapointe, E. Post, A. Delage, S. Janz, P. Cheben, J. H. Schmid, and B. Lamontagne, "High bandwidth SOI photonic wire ring resonators using MMI couplers," Optics Express, vol. 15, pp. 3149-3155, 2007.
[10] D. X. Xu, S. Janz, and P. Cheben, "Design of polarization-insensitive ring resonators in silicon-on-insulator using MMI couplers and cladding stress engineering," IEEE Photonics Technology Letters, vol. 18, pp. 343-345, 2006.
[11] D. G. Rabus and M. Hamacher, "MMI-coupled ring resonators in GaInAsP-InP," IEEE Photonics Technology Letters, vol. 13, pp. 812-814, 2001.
[12] D. G. Rabus, M. Hamacher, and H. Heidrich, "Resonance frequency tuning of a double ring resonator in GaInAsP/InP: Experiment and simulation," Japanese Journal of Applied Physics Part 1-Regular Papers Short Notes & Review Papers, vol. 41, pp. 1186-1189, 2002.
[13] L. Caruso and I. Montrosset, "Analysis of a racetrack microring resonator with MMI coupler," Lightwave Technology, Journal of, vol. 21, pp. 206-210, 2003.
[14] S. Darmawan, Y. M. Landobasa, P. Dumon, R. Baets, and M. K. Chin, "Resonance Enhancement in Silicon-on-Insulator-Based Two-Ring Mach-Zehnder Interferometer," *Photonics Technology Letters, IEEE,* vol. 20, pp. 1560-1562, 2008.
[15] S. Darmawan, Y. M. Landobasa, P. Dumon, R. Baets, and M. K. Chin, "Nested-Ring Mach-Zehnder Interferometer in Silicon-on-Insulator," *Photonics Technology Letters, IEEE,* vol. 20, pp. 9-11, 2008.
[16] D. S. Levy, Y. M. Li, R. Scarmozzino, and R.M. Osgood, Jr., "A multimode interference-based variable power splitter in GaAs-AlGaAs," *Photonics Technology Letters, IEEE,* vol. 9, pp. 1373-1375, 1997.
[17] D. S. Levy, K. H. Park, R. Scarmozzino, R. M. Osgood, Jr., C. Dries, P. Studenkov, and S. Forrest, "Fabrication of ultracompact 3-dB 2X2 MMI power splitters," *Photonics Technology Letters, IEEE,* vol. 11, pp. 1009-1011, 1999.
[18] D. S. Levy, R. Scarmozzino, Y. M. Li, and R. M. Osgood, Jr., "A new design for ultracompact multimode interference-based 2Xcouplers," *Photonics Technology Letters, IEEE,* vol. 10, pp. 96-98, 1998.

[19] D. S. Levy, R. Scarmozzino, and R. M. Osgood, Jr., "Length reduction of tapered NXN MMI devices," *Photonics Technology Letters, IEEE,* vol. 10, pp. 830-832, 1998.
[20] P. A. Besse, E. Gini, M. Bachmann, and H. Melchior, "New 2X2 and 1X3 multimode interference couplers with free selection of power splitting ratios," *Lightwave Technology, Journal of,* vol. 14, pp. 2286-2293, 1996.
[21] W. Bogaerts, D. Taillaert, B. Luyssaert, P. Dumon, J. Van Campenhout, P. Bienstman, D. Van Thourhout, R. Baets, V. Wiaux, and S. Beckx, "Basic structures for photonic integrated circuits in Silicon-on-insulator," Opt. Express, vol. 12, pp. 1583-1591, 2004.
[22] W. Bogaerts, R. Baets, P. Dumon, V. Wiaux, S. Beckx, D. Taillaert, B. Luyssaert, J. Van Campenhout, P. Bienstman, and D. Van Thourhout, "Nanophotonic waveguides in silicon-on-insulator fabricated with CMOS technology," Lightwave Technology, Journal of, vol. 23, pp. 401-412, 2005.
[23] W. Bogaerts, V. Wiaux, D. Taillaert, S. Beckx, B. Luyssaert, P. Bienstman, and R. Baets, "Fabrication of photonic crystals in silicon-on-insulator using 248-nm deep UV lithography," Selected Topics in Quantum Electronics, IEEE Journal of, vol. 8, pp. 928-934, 2002.
[24] W. Bogaerts, P. Dumon, D. Van Thourhout, D. Taillaert, P. Jaenen, J. Wouters, S. Beckx, V. Wiaux, and R. G. Baets, "Compact wavelength-selective functions in silicon-on-insulator photonic wires," IEEE Journal of Selected Topics in Quantum Electronics, vol. 12, pp. 1394-1401, 2006.
[25] Y. A. Vlasov and S. J. McNab, "Losses in single-mode silicon-on-insulator strip waveguides and bends," in *LEOS Topical Meeting on Photonic Crystals and Holey Fibers*, Vancouver, CANADA, 2003, pp. 1622-1631.
[26] M. A. Webster, R. M. Pafchek, A. Mitchell, and T. L. Koch, "Width dependence of inherent TM-mode lateral leakage loss in silicon-on-insulator ridge waveguides," *IEEE Photonics Technology Letters,* vol. 19, pp. 429-431, Mar-Apr 2007.
[27] S. Y. Lee, S. Darmawan, C. W. Lee, and M. K. Chin, "Transformation between directional couplers and multi-mode interferometers based on ridge waveguides," Optics Express, vol. 12, pp. 3079-3085, 2004.
[28] D. S. Levy, Y. M. Li, R. Scarmozzino, and R.M. Osgood, Jr., "A multimode interference-based variable power splitter in GaAs-AlGaAs," Photonics Technology Letters, IEEE, vol. 9, pp. 1373-1375, 1997.
[29] P. Dumon, W. Bogaerts, D. Van Thourhout, D. Taillaert, R. Baets, J. Wouters, S. Beckx, and P. Jaenen, "Compact wavelength router based on a Silicon-on-insulator arrayed waveguide grating pigtailed to a fiber array," Opt. Express, vol. 14, pp. 664-669, 2006.
[30] Q. Lai, M. Bachmann, W. Hunziker, P. A. Besse, and H. Melchior, "Arbitrary ratio power splitters using angled silica on silicon multimode interference couplers," *Electronics Letters,* vol. 32, pp. 1576-1577, 1996.
[31] R. van Roijen and E. C. M. Pennings, "Compact InP-based ring lasers employing multimode interference couplers and combiners," *Applied Physics Letters,* vol. 64, p. 1753, 1994.
[32] M. Bachmann, P. A. Besse, and H. Melchior, "Overlapping-Image Multimode Interference Couplers with a Reduced Number of Self-Images for Uniform and Nonuniform Power Splitting," *Applied Optics,* vol. 34, pp. 6898-6910, Oct 20 1995.

Chapter 5

[1] S. L. Chuang, *Physics of Optoelectronic Devices*. New York: John Wiley & Sons, Inc., 1995.

[2] G. L. Li and P. K. L. Yu, "Optical intensity modulators for digital and analog applications," *Lightwave Technology, Journal of*, vol. 21, pp. 2010-2030, 2003.
[3] G. L. Li, P. K. L. Yu, W. S. C. Chang, K. K. Loi, C. K. Sun, and S. A. Pappert, "Concise RF equivalent circuit model for electroabsorption modulators," *Electronics Letters*, vol. 36, pp. 818-820, 2000.
[4] T. Ido, H. Sano, S. Tanaka, D. J. Moss, and H. Inoue, "Performance of strained InGaAs/InAlAs multiple-quantum-well electroabsorption modulators," *Journal of Lightwave Technology*, vol. 14, pp. 2324-2331, 1996.
[5] T. Ido, S. Tanaka, M. Suzuki, M. Koizumi, H. Sano, and H. Inoue, "Ultra-high-speed multiple-quantum-well electro-absorption optical modulators with integrated waveguides," *Lightwave Technology, Journal of*, vol. 14, pp. 2026-2034, 1996.
[6] J. W. Shi, C. A. Hsieh, A. C. Shiao, Y. S. Wu, R. H. Huang, S. H. Chen, Y. T. Tsai, and J. I. Chyi, "Demonstration of a dual-depletion-region electroabsorption modulator at 1.55-mu m wavelength for high-speed and low-driving-voltage performance," *IEEE Photonics Technology Letters*, vol. 17, pp. 2068-2070, 2005.
[7] J. X. Chen, Y. Wu, W. X. Chen, I. Shubin, A. Clawson, W. S. C. Chang, and P. K. L. Yu, "High-power intrastep quantum well electroabsorption modulator using single-sided large optical cavity waveguide," *Photonics Technology Letters, IEEE*, vol. 16, pp. 440-442, 2004.
[8] Y. Hua, M. K. Chin, J. Zhou, S. Y. Lee, W. Chen, and H. Zhu, "A traveling-wave electroabsorption modulator with a large optical cavity and intrastep quantum wells," *Semiconductor Science and Technology*, vol. 23, pp. 105011, 2008.
[9] A. C. Crook, M. L. Osowski, G. M. Smith, J. Frame, M. Grupen, and T. A. DeTemple, "A universal optical heterostructure for photonic integrated circuits: a case study in the AlGaAs material system," *Selected Topics in Quantum Electronics, IEEE Journal of*, vol. 2, pp. 341-347, 1996.
[10] M. E. Chin and W. S. C. Chang, "Theoretical design optimization of multiple-quantum-well electroabsorption waveguide modulators," *Quantum Electronics, IEEE Journal of*, vol. 29, pp. 2476-2488, 1993.
[11] R. E. Bartolo, S. S. Saini, T. Ren, Y. Zhu, M. Dagenais, H. Shen, J. Pamulapati, W. Zhou, O. King, and F. G. Johnson, "Polarization-independent waveguide modulators using 1.57 μm-strained InGaAs-InGaAsP quantum wells," presented at Lasers and Electro-Optics, 1999. CLEO '99. Summaries of Papers Presented at the Conference on, 1999.
[12] Y. Zhu, S. Saini, R. Bartolo, T. Ren, M. Dagenais, F. Johnson, H. Shen, J. Pamulapati, and W. Zhou, "Polarization independent & strained InGaAs/InGaAsP quantum well waveguide modulator," presented at Lasers and Electro-Optics Society 1999 12th Annual Meeting. LEOS '99. IEEE, 1999.

Chapter 6

[1] T. Mei, H. S. Djie, C. Sookdhis, and J. Arokiaraj, "Low-loss waveguide fabrication using inductively coupled argon plasma enhanced quantum well intermixing in InP quantum well sample," in *Optoelectronic and Microelectronic Materials and Devices, 2002 Conference on*, 2002, pp. 311-314.
[2] L. Fu, P. Lever, H. H. Tan, C. Jagadish, P. Reece, and M. Gal, "Suppression of interdiffusion in InGaAs/GaAs quantum dots using dielectric layer of titanium dioxide," *Applied Physics Letters*, vol. 82, pp. 2613-15, 2003.
[3] O. Boon Siew, K. McIlvaney, M. W. Street, A. S. Helmy, S. G. Ayling, A. C. Bryce, J. H. Marsh, and J. S. Roberts, "Selective quantum-well intermixing in GaAs-AlGaAs structures using impurity-free vacancy diffusion," *IEEE Journal of Quantum Electronics*, vol. 33, pp. 1784-93, 1997.

[4] H. S. Djie, C. Sookdhis, T. Mei, and J. Arokiaraj, "Photonic integration using inductively coupled argon plasma enhanced quantum well intermixing," *Electronics Letters*, vol. 38, pp. 1672-1673, 2002.

[5] A. McKee, C. J. McLean, G. Lullo, A. C. Bryce, R. M. De La Rue, J. H. Marsh, and C. C. Button, "Monolithic integration in InGaAs-InGaAsP multiple-quantum-well structures using laser intermixing," *Quantum Electronics, IEEE Journal of*, vol. 33, pp. 45-55, 1997.

[6] Y. Wang, H. S. Djie, and B. S. Ooi, "Low-loss monolithic extended cavity laser by low-energy ion-implantation induced intermixing," *Electronics Letters*, vol. 42, pp. 699-701, 2006.

[7] C. D. Xu, T. Mei, and J. R. Dong, "Determination of diffusion lengths for intermixed quaternary quantum well with polarized edge-emitting photoluminescence," *Applied Physics Letters*, vol. 90, pp. 191111-3, 2007.

[8] C. D. Xu, T. Mei, M. K. Chin, J. R. Dong, and S. J. Chua, "Built-in electric field enhancement/retardation on intermixing," *Applied Physics Letters*, vol. 91, Oct 2007.

[9] T. Mei, "Interpolation of quaternary III-V alloy parameters with surface bowing estimations," *Journal of Applied Physics*, vol. 101, pp. 013520-6, 2007.

[10] T. Mei, "Fourier transform-based k·p method of semiconductor superlattice electronic structure," *Journal of Applied Physics*, vol. 102, pp. 053708-5, 2007.

[11] C. W. Lee and M. K. Chin, "Room-Temperature Inductively Coupled Plasma Etching of InP Using Cl2/N2 and Cl2/Ch4/H2," *Chin. Phys. Lett.*, vol. 23, pp. 903-906, 2006.

[12] G. L. Li, R. B. Welstand, W. X. Chen, J. T. Zhu, S. A. Pappert, C. K. Sun, Y. Z. Liu, and P. K. L. Yu, "Novel bias control of electroabsorption waveguide modulator," *Photonics Technology Letters, IEEE*, vol. 10, pp. 672-674, 1998.

[13] S. Charbonneau, E. S. Koteles, P. J. Poole, J. J. He, G. C. Aers, J. Haysom, M. Buchanan, Y. Feng, A. Delage, F. Yang, M. Davies, R. D. Goldberg, P. G. Piva, and I. V. Mitchell, "Photonic integrated circuits fabricated using ion implantation," *IEEE Journal of Selected Topics in Quantum Electronics*, vol. 4, pp. 772-793, Jul-Aug 1998.

Appendix A

The program code used in the Simwindows software is as follows:

```
grid length=1.500 points=200
grid length=0.050 points=50
grid length=0.162 points=500
grid length=0.010 points=100
grid length=0.400 points=200
grid length=1.100 points=300

structure material=gaas alloy=al length=1.500 conc=0
structure material=gaas alloy=al length=0.050 conc=0.4

repeat start

structure material=gaas alloy=al length=0.005 conc=0.0
structure material=gaas alloy=al length=0.013 conc=0.4

repeat=9

structure material=gaas alloy=al length=0.010 conc=0
structure material=gaas alloy=al length=0.400 conc=0.4
structure material=gaas alloy=al length=1.100 conc=0.4

doping length=1.500 Na=1e+18
doping length=0.050
doping length=0.162
doping length=0.010 Nd=5e+18
doping length=0.400
doping length=1.100 Nd=1e+18
```

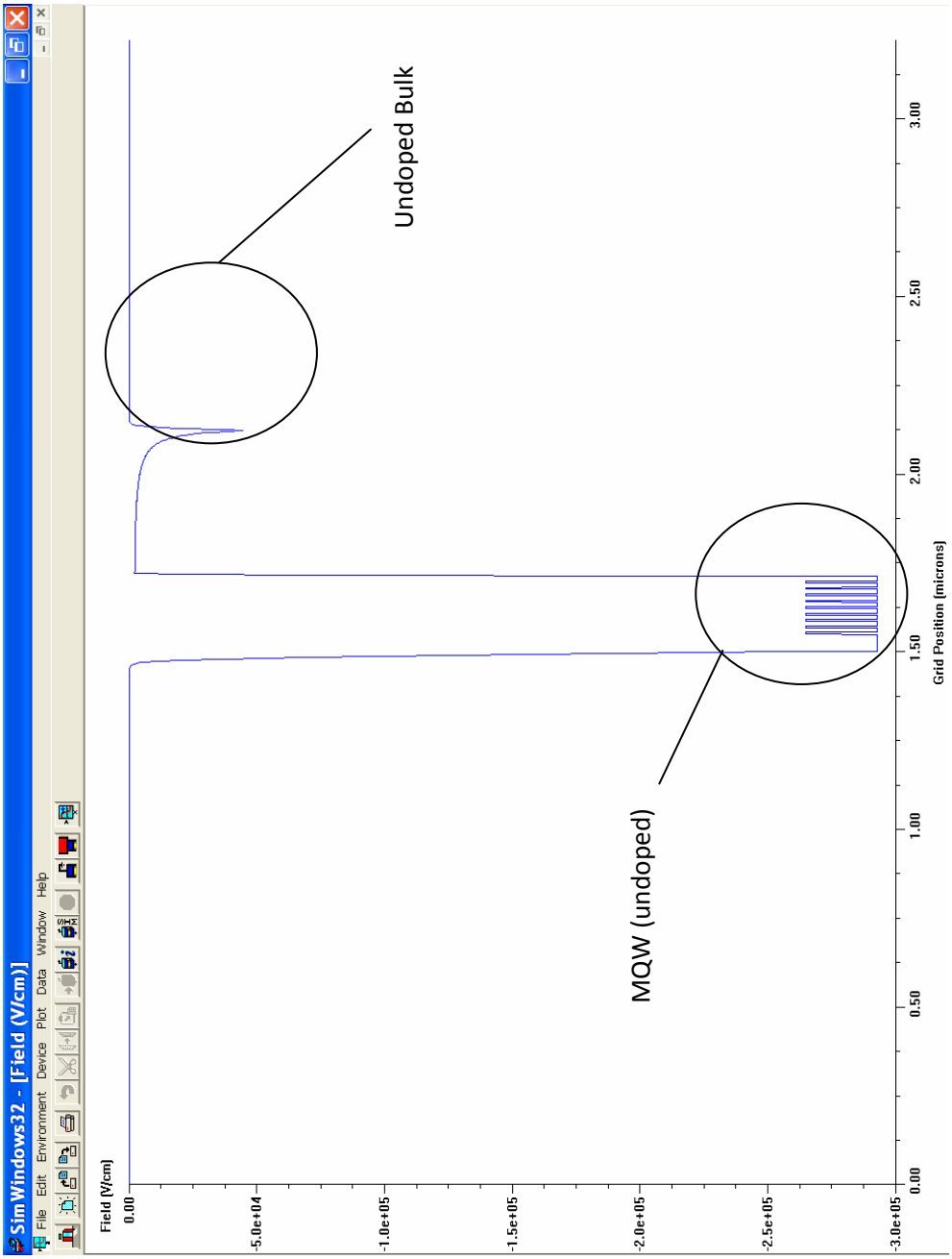

Fig.A1. Simulated Distribution of Electric field on dual depletion region

Appendix B

TABLE B1: Material Parameters for $In_{1-x}Ga_x As_yP_{1-y}$

Symbol	Parameter	$In_{1-x}Ga_x As_yP_{1-y}$	Unit
$Q_C : Q_V$	Band offset splitting ratio	0.6:0.4	-
$Eg(x, y)$	Energy band gap	1.35 - 1.17y + 0.668x-0.069xy + $0.18y^2$ + $0.03xy^2$ + $0.758x^2$ - $0.322x^2y$	eV
$\Delta_0(X)$	Spin-orbit splitting	0.34xy+0.43(1-x)y+0.10x(1-y)+0.10(1-x)(1-y)	eV
$m_C^*(X)$	Electron effective mass	0.0632xy+0.0213(1-x)y+0.17x(1-y)+0.077(1-x)(1-y)	m_e
$m_{\perp HH}^*(X)$	Heavy Hole effective mass perpendicular to QW layer	0.5xy+0.41(1-x)y+0.54x(1-y)+0.12(1-x)(1-y)	m_e
$m_{\perp LH}^*(X)$	Light Hole effective mass perpendicular to QW layer	0.088xy+0.024(1-x)y+0.16x(1-y)+0.12(1-x)(1-y)	m_e
$m_{\parallel HH}^*(X)$	Heavy Hole effective mass parallel/transverse to QW layer	0.11xy+0.031(1-x)y+0.19x(1-y)+0.15(1-x)(1-y)	m_e
$m_{\parallel LH}^*(X)$	Light Hole effective mass parallel/transverse to QW layer	0.23xy+0.082(1-x)y+0.34x(1-y)+0.29(1-x)(1-y)	m_e
a_0	Lattice constant	5.6533xy+6.0584(1-x)y+5.4512x(1-y)+5.8688(1-x)(1-y)	$\circ$ A
C_{11}	Elastic stiffness constant	11.8xy+8.329(1-x)y+14.12x(1-y)+10.22(1-x)(1-y)	10^{11} dyn/ cm^2
C_{12}	Elastic stiffness constant	5.38xy+4.526(1-x)y+6.253x(1-y)+5.76(1-x)(1-y)	10^{11} dyn/ cm^2
dEg / dP	Hydrostatic pressure coefficient	11.5xy+10.0(1-x)y+11.0x(1-y)+8.5(1-x)(1-y)	10^{-6} eV/bar
b	Shear deformation potential	-1.7xy-1.8(1-x)y-1.5x(1-y)-2.0(1-x)(1-y)	eV
ε_{static}	Dielectric function	0.11xy+0.031(1-x)y+0.19x(1-y)+0.150(1-x)(1-y)	ε_0
A	Renewed strength of E_0 and $(E_0 + \Delta_0)$ transitions	8.40-3.40y	-
B	Nondispersive contribution	6.60+3.40y	-

(m_e=0.91095x10^{-30}kg; ε_0 =8.85418x10^{-12}F/m)

Band Profile before intermixing

The energy bandgap of InGaAsP alloy with lattice matched to InP covers the range of 1.35eV to 0.75eV depending on the energy bandgap equation employed. These bandgap equations vary depending on the conditions applied and variations of methods used for instance, imposing bowing effects [1] upon the Vegard's Law [2]. The method employed here, where lattice mismatching of the different layers may occur due to interdiffussion at nonunity V/III diffusion length ratio, make use of molar fraction expressions to more accurately interpolate the quarternary III-V alloy parameters [2]. The material parameter function $Q(x, y)$ of a quarternary alloy (for example, the $In_{1-x}Ga_x As_yP_{1-y}$) can be plotted as a surface in a square domain enclosed by four boundaries Ga, In, As and P. These parameters can then reach the binary material parameters (B) at the four corners B_{GaAs}, B_{GaP}, B_{InAs}, B_{InP} and subsequently be reduced to the ternary parameter expressions with surface bowing parameters which can be estimated as:

$$C_{AsP} = xC_{GaAsP} + (1-x)C_{InAsP} - x(1-x)D_1,$$

$$C_{InGa} = yC_{InGaAs} + (1-y)C_{InGaP} - y(1-y)D_2,$$

(B1)

so that $Q(x, y)$ can be deduced to,

[2] Vegard's law is an approximate empirical rule which holds that a linear relation exists between the crystal lattice parameter of an alloy and the concentrations of the constituent elements. That is to say, if we are to take an example of a binary semiconductor compound (or alloy) A_xB_{1-x} where A and B are the assumed pure materials and x is the composition ratio of each material in the alloy, then, their associated lattice parameters, α, can be treated as:

$$\alpha_{AB} = x\alpha_A + (1-x)\alpha_B$$

This relation is often extended to determine the semiconductor bandgap energies (Eg (eV)) and is preferred by experimentalists who often use variations of this law in order to quickly estimate a property of a given alloy. The simplest variation consists of adding a quadratic term to the linear Vegard's law but this case is more successfully applied to ternary III-V material. In the case of quarternary III-V semiconductor compound, several more approaches were taken and the one which was employed here is to interpolate the quarternary III-V parameters with surface bowing estimations.

$$Q(x,y) = Q_0(x,y) + \Delta Q(x,y) \tag{B2}$$

which comprises a term of fundamental estimation,

$$\begin{aligned} Q(x,y) = {} & xyB_{GaAs} + x(1-y)B_{GaP} + (1-x)yB_{InAs} + (1-x)(1-y)B_{InP} \\ & -xy(1-y)C_{GaAsP} - (1-x)y(1-y)C_{InAsP} - x(1-x)yC_{GaInAs} \\ & -x(1-x)(1-y)C_{GaInP} \end{aligned} \tag{B3}$$

and a term of correction,

$$\Delta Q(x,y) = x(1-x)(1-y)\left[\frac{x(1-x)D_1 + y(1-y)D_2}{x(1-x) + y(1-y)}\right] \tag{B4}$$

This weighted-sum expression can effectively estimate the bandgap energy which closely follows the quick estimation of the energy bandgap before intermixing (the expression shown in the material parameter list given in Table B1). The various bowing parameters introduced can be obtained from refs. [1-4]. Further explanation regarding the derivation of $Q(x,y)$ can be obtained from ref. [2] where the bandgap calculation method was obtained from.

Fig.B1 shows one of five $In_{1-x}Ga_x\ As_yP_{1-y}$ quantum wells with $x = 0.4335$ and $y=0.96$ and a thickness of 5nm which is sandwiched between 10nm thick barriers $In_{1-x}Ga_x\ As_yP_{1-y}$ with the composition of $x = 0.24$ and $y=0.5106$. Table B2 gives a comparison of the bandgap calculated using equation (B2) as compared to the quick estimation obtained by the expression in Table B1.

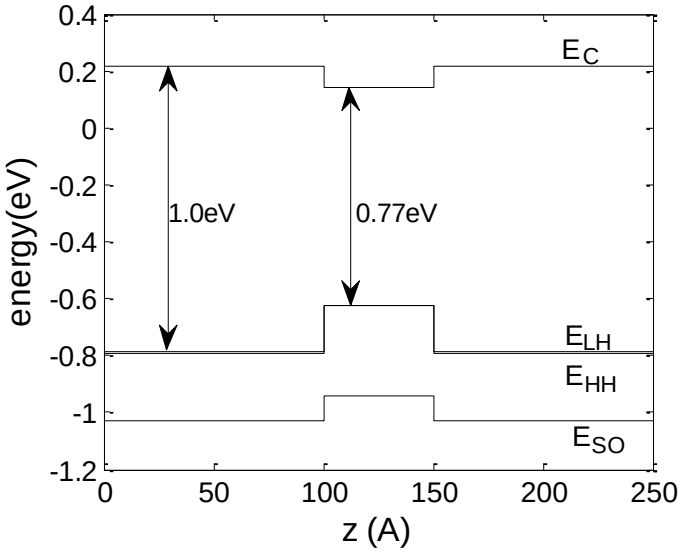

Fig.B1 Band profile of a 5nm InGaAsP quantum well with 10nm thick InGaAsP barriers before intermixing

TABLE B2: Comparison of Calculated Bandgap Energy for $In_{1-x}Ga_x As_yP_{1-y}$

Band	x	y	Eg(eV) based on expression in Table B1	Eg(eV) based on equation B2
well	0.4335	0.93	0.777	0.767 (HH), 0.767 (LH)
barrier	0.24	0.5106	0.987	1.006 (HH), 1.003 (LH)

Band Profile after intermixing

The intermixing (also known as the interdiffusion process) modifies the compositional profile of the as-grown MQW from abrupt QW band edges to change into graded profile. In the intermixing of both $A_xB_{1-x}C_{1-y}D_y$ and $A_xB_yC_{1-x-y}D$ type of III-V compounds, the interdiffussion processes can occur in both group III and group V atoms. For the case of $In_{1-x}Ga_x As_{1-y}P_y$, the interdiffussion analysis is done by grouping them into group III (In, Ga) and group V (As, P) materials, and by modifying their diffusion length ratio, characterized by $k=L_{dV}/L_{dIII}$, where L_{dIII} and L_{dV} denote the diffusion lengths of the group III and group V sublattices respectively, whereas for the $In_xGa_yAl_{1-x-y}As$ material which we have also intermixed, the approach adopted was to observer the *x* and *y* change brought on by the component shifts and to translate these values into bandgap shift and subsequently wavelength shift.

The interdiffused compositional profile shown in Fig.B2 is modeled by Fick's law[3] of diffusion. The analytical model used here is obtained from refs. [5-7]. The error function profile (*erf*) after interdiffusion process is obtained

[3] Fick's law of diffusion states that $\frac{\partial C}{\partial t_a} = D_{QW}\frac{\partial^2 C}{\partial z^2}$, where *C* is the concentration of one of the alloy, t_a is the interdiffusion time and *D* is the diffusion coefficient and *z* is the interdiffusion direction. The multiple cations interdiffusion for quarternary alloys is based on the expanded form of Fick's second law, $\frac{\partial C_i}{\partial t} = \sum_{j=1}^{n-1} D_{ij}\nabla^2 C_{ij}$

from summing the effects of a series of line sources representing an extended source of limited extent, each yielding a Gaussian distribution. An example of the expression used to express the group III concentration in the active layer profile after interdiffusion is given here as:

$$x(z,L_{dIII}) = x_{QB} + \frac{\Delta x_{QW}}{2}\left[2 - erf\left(\frac{z-c_1}{2L_{dIII}}\right) + erf\left(\frac{z-c_1}{2L_{dIII}}\right) + \sum_{n=1}^{N-1}\left[erf\left(\frac{z-a_i}{2L_{dIII}}\right) + erf\left(\frac{z-b_i}{2L_{dIII}}\right)\right]\right] \quad \text{(B5)}$$

where

$$c_1 = -c_2 = -\left(L_{QW}\frac{N}{2} + L_{QB}\frac{N-1}{2}\right); \qquad a(i) = c_1 + L_{QW} + (i-1)(L_{QW} + L_{QB}); b(i) = a_i + L_{QB} \quad \text{(B6)}$$

$x(z,L_{dIII})$ is the group III concentration, x_{QB} is the concentration at the quantum barrier, Δx_{QW} is the difference in the concentration between the QW and the barrier, L_{QW} is the QW width, is the barrier width, N is the QW layer number and z is the direction along QW growth (QW is assumed to be centered at z=0). The group V concentration can similarly be formulated using the analogy of (B5). With a given interdiffusion length and the group III and V concentrations (or x and y concentrations) the band edge interdiffusion profile can then be calculated. The interdiffusion of the QW shown in Fig.B1 is shown in Fig.B2. The concentrations remained the same and the interdiffusion lengths for group III and V adopted in this example are 15 and 16 respectively.

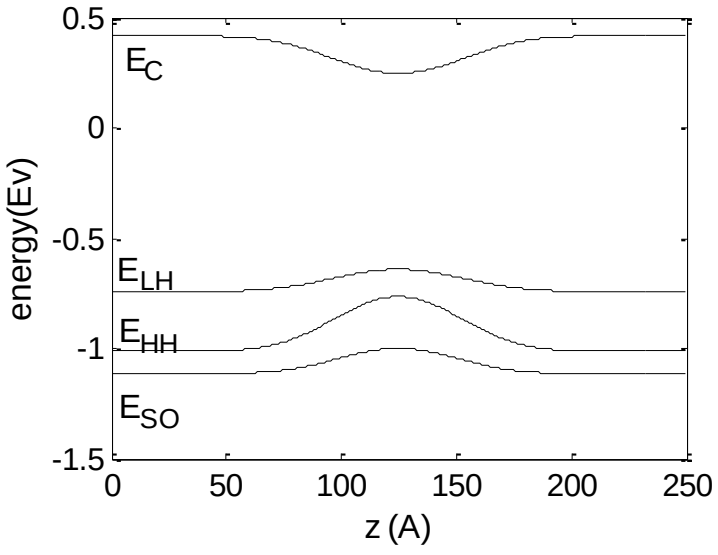

Fig.B2 Band profile of a 5nm InGaAsP quantum well with 10nm thick InGaAsP barriers after intermixing

The bandgap contour which changed as the III-V diffusion lengths were varied was mapped out in the contour graph in Fig.6.1.1(b). The bandgap calculation was found using the 8-band k·p method with finite difference detailed in ref. [8]. In this method, the band energy was simulated using plane wave expansion envelope wavefunction in k-space, Hermitian form. The finite difference equations generated from the mesh points is formed into a generalized eigen value Hamiltonian matrix equation and subsequently the eigen values of the matrix equation can be used to identify the interband transitions energy and the electron-hole transition energies. The wavelength shift contours shown in Fig. 6.1.5(c) and Fig. 6.1.5(d) were similarly obtained from the bandgap contour graphs generated.

References:

[1] I. Vurgaftman and J. R. Meyer, "Band parameters for nitrogen-containing semiconductors," *Journal of Applied Physics*, vol. 94, p. 3675, 2003.

[2] T. Mei, "Interpolation of quaternary III-V alloy parameters with surface bowing estimations," *Journal of Applied Physics*, vol. 101, pp. 013520-6, 2007.

[3] T. Ishikawa and J. E. Bowers, "Band lineup and in-plane effective mass of InGaAsP or InGaAlAs on InP strained-layer quantum well," *Quantum Electronics, IEEE Journal of*, vol. 30, pp. 562-570, 1994.

[4] G. P. Donati, R. Kaspi, and K. J. Malloy, "Interpolating semiconductor alloy parameters: Application to quaternary III-V band gaps," *Journal of Applied Physics*, vol. 94, p. 5814, 2003.

[5] H. S. Djie, T. Mei, J. Arokiaraj, C. Sookdhis, S. F. Yu, L. K. Ang, and X. H. Tang, "Experimental and theoretical analysis of argon plasma-enhanced quantum-well intermixing," *IEEE Journal of Quantum Electronics*, vol. 40, pp. 166-174, Feb 2004.

[6] H. S. Djie, C. Sookdhis, I. Mei, and J. Arokiaraj, "Photonic integration using inductively coupled argon plasma enhanced quantum well intermixing," *Electronics Letters*, vol. 38, pp. 1672-1673, Dec 2002.

[7] H. S. Djie, Y. Wang, B. S. Ooi, D. N. Wang, J. C. M. Hwang, X. M. Fang, Y. Wu, J. M. Fastenau, W. K. Liu, G. T. Dang, and W. H. Chang, "Wavelength tuning of InAs/InAlGaAs quantum-dash-in-well laser using postgrowth intermixing," *Electronics Letters*, vol. 43, pp. 33-34, 2007.

[8] T. Mei, "Fourier transform-based k·p method of semiconductor superlattice electronic structure," *Journal of Applied Physics*, vol. 102, pp. 053708-5, 2007.